

SYNTHESIS, CHARACTERIZATION AND LASER PATTERNING OF PULSED DC MAGNETRON SPUTTERED NiTi SHAPE MEMORY ALLOY AND TiN THIN FILMS

Thesis

Submitted in partial fulfillment of the requirements for the degree of

DOCTOR OF PHILOSOPHY

by

**JITHIN M. A.
(Reg. No: 145017 PH14P01)**



DEPARTMENT OF PHYSICS

NATIONAL INSTITUTE OF TECHNOLOGY KARNATAKA,
SURATHKAL, MANGALORE – 575 025

June 2021

SYNTHESIS, CHARACTERIZATION AND LASER PATTERNING OF PULSED DC MAGNETRON SPUTTERED NiTi SHAPE MEMORY ALLOY AND TiN THIN FILMS

Thesis

Submitted in partial fulfillment of the requirements for the degree of

DOCTOR OF PHILOSOPHY

by

JITHIN M. A.

(Reg. No: 145017 PH14P01)

Under the Guidance of

Prof. N. K. Udayashankar



DEPARTMENT OF PHYSICS

NATIONAL INSTITUTE OF TECHNOLOGY KARNATAKA,

SURATHKAL, MANGALORE – 575 025

June 2021

DECLARATION

I hereby *declare* that the Research Thesis entitled “**Synthesis, Characterization and laser patterning of pulsed DC magnetron sputtered NiTi shape memory alloy and TiN thin films**” which is being submitted to the National Institute of Technology Karnataka, Surathkal, in partial fulfillment of the requirements for the award of the **Degree of Doctor of Philosophy in Physics** is *a bonafide report of the research work carried out by me*. The material contained in this Research Thesis has not been submitted to any University or Institution for the award of any degree.



Mr. Jithin M. A.

(Reg. No. 145017 PH14P01)

Department of Physics

Place: NITK, Surathkal

Date: 15-06-2021

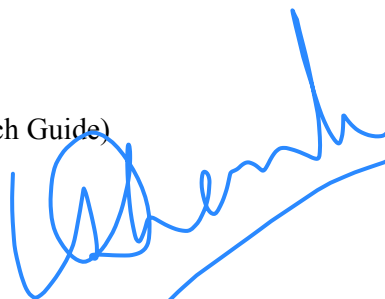
CERTIFICATE

This is to *certify* that the Research Thesis entitled “**Synthesis, Characterization and laser patterning of pulsed DC magnetron sputtered NiTi shape memory alloy and TiN thin films**” submitted by Jithin M. A. (Register Number 145017 PH14P01) as the record of the research work carried out by him, is accepted as the *Research Thesis* submission in partial fulfillment of the requirements for the award of degree of Doctor of Philosophy.



Prof. N. K. Udayashankar

(Research Guide)



Chairman-DRPC

Dedicated to Prof. S. Mohan...

Acknowledgments

On this happy occasion, I wish to express my deep sense of gratitude to my research supervisor, Prof. N. K. Udayashankar, Department of Physics, NITK Surathkal, for giving me the excellent opportunity of working with him. I am very much thankful for all his research guidance, timely decisions, routine discussions, and constant advice that have helped me complete my research work successfully. Other than being a scientific adviser, he has been moral support, and for this, I would be forever indebted to him. I thank him for the support, encouragement, and timely help he provided during my stay at NITK. Thank you, Sir.

I want to express my deep and sincere gratitude to Professor S. Mohan, Emeritus Professor at Centre for Nano Science and Engineering, Indian Institute of Science, for his excellent guidance, invaluable suggestions, and unwavering support. I am deeply grateful to him for allowing me to carry out this research work in his laboratory. Everything I know about research has come from him. His vast experience and creative nature helped me immensely along the way and were essential to completing this thesis. I feel privileged to be associated with a person like him during my life. Thank you so much for everything, Sir.

I want to thank the former and current chairpersons of CeNSE for allowing me to carry out my research work at CeNSE. I would also like to acknowledge the funding agencies; MHRD, MeitY, and DST Nano Mission through NNetRA for carrying out the thesis work. I am also thankful to the Director, NITK Surathkal, for initiating the CeNSE - NITK student program. I sincerely thank the former and current H.O.Ds of the Department of Physics, NITK, for their unconditional support during this research work. I would also acknowledge my RPAC members Dr. Partha Pratim Das, Department of Physics, NITK, and Dr. K. S. Ravishankar, Department of Metallurgical and Materials Engineering, NITK, for evaluating my research progress and giving valuable suggestions.

I would like to express my heartfelt gratitude to my long-time colleague Dr. K. L. Ganapathi, for his suggestions and guidance. I cannot describe the full depth of my feelings in a sentence for the fruitful discussions we had over the years. Despite his

busy activities as a DST Inspired Fellow at IIT Madras, he always found time to look into my thesis work and research papers. Similarly, I have profound regards to Dr. Deepa K. G. of the University of Kerala for her unconditional and magnanimous helps in analyzing and interpreting the data and her timely help in writing the research papers. Simply stated, I am here today only because of the unconditional and unwavering support from these two noble souls.

From the bottom of my heart, I sincerely thank Dr. K. R. Gunasekhar, Mr. M. Adinarayana Murthy, and Mrs. H. S. Vijaya for their guidance during my initial struggles on vacuum systems. I am incredibly grateful to Late Dr. C. L. Nagendra, Mr. Ajith Kumar, Mr. M. Viswanathan (all from LEOS - ISRO) for sparing time for the fruitful discussions and advice on various thin-film processes. Without their unselfish supports, I could not have felt the taste of vacuum and thin films. I thank Prof. S. Kasthuriangan and Mr. Raju H. S. for their timely support to maintain the Cryo pumping system that I depended entirely on to carry out this research work. I also thank the various vacuum companies based in Bangalore who timely supported the vacuum systems with minimum downtime.

I sincerely thank Dr. Balashanmugham, Mr. Niranjana, Mr. Jagdish, and Mr. Sunil of Central Manufacturing Technology Institute (CMTI) for providing access to the use of femtosecond laser facility. I acknowledge all my group members of Thin Films Lab, IISc and Nanomaterials Lab, NITK, for their motivation and cooperation.

The scientific and technical support from all the CeNSE centralized facilities MNCF, NNFC, MEMS packaging labs is greatly acknowledged. I have been fortunate to work with a few of the fabulous colleagues of these labs like Dr. Savitha, Dr. Vijayaraghavan, Sunanda Babu, Dr. Asis, Dwarakanath, Pradeep, Prahlada, Dr. Arunbabu, Venu, Avnish, Suma, Martina, Ambresh, Prakash, Ashwini, Archana, Manasa Jain, Dr. Sangeeth, Lavendra, Karthik, Vijay, Nizam, Reshma, Shreyas, Prashanth, Chandan, Madhuri, Manasa A. M., Deepu, Arjun, Littin, Veeramani, Pandian, Jayabal. I also thank the CeNSE utility team and admin staff for the timely support.

I sincerely thank my class teachers from Anganwadi to masters-level Mrs. Mani, Mrs. Suprabha, Late Mrs. Parvathi, Late Mrs. Balamani, Mrs. Leela, Mrs. Maggy, Mrs. Jessy, Late Mrs. Leela, Mrs. Shirley, Mr. James, Mrs. Mallika, Mrs. Nandini, Mr. Paul, Dr. Purushothaman and other Physics teachers like Mr. Anil, Mr. Murali, Mr. Rajeev, Mr. Varghese, Mr. Vasanthakumar for their blessings and guidance, and as I stand to receive my final degree few of their absence is my only regret.

I thank my Ph.D. batch mates of NITK Achyutha, Karthik, Varadharaj, Suchithra, Sibin, and Sowjanya for their support during my coursework period at NITK. I sincerely thank my Ph.D. colleagues at NITK, notably Manoj, Nimith, Siby Thomas, Sreejesh, Sripadaraja, Sterin, Brijesh, and Harsha, who made my stay at NITK a memorable one.

I was blessed with a great circle of friends and well-wishers who were always instrumental to my success. A very warm note of gratitude to Sumesh, Abhilash, Hari, Vinod, Sasi, Sriram, Venu, Harshan, Rajesh, Siju, Renil, Palash, Krishna Murthy, Sanjay John, Gopesh, Renjith, Santhosh, Anil, Ashwin, Siva Kumar, Pankaj, Deepak, Dileesh, Anoop, Anirudh, Ankit, Rama Satya, Makek, Ashraf, and I thank each of them personally for their affection and support. Many thanks to Prasanth and Linto, my best friends from school to master's level, for their constant encouragement throughout this endeavor.

Finally, family is the place where one starts learning. First, I must thank my parents, Aravindakshan and Bhageerathy, for their prayers, encouragement, support, and sacrifices with patience throughout my career. I would not have achieved anything in life without their love and support. Achan and Amma, this is to you. My younger sister, Jayalakshmi, was always with me during my ups and downs as an epitome of support. I also thank my in-laws for their love and understanding. At last, there are not enough words to express my gratitude to the two precious diamonds of my life - Sidhila (wife) and Shreeya (daughter) for their love, support, and understanding; they are the greatest strength in my life. Since it is impossible to express by words what they mean to me, I can only say that I thank them for making this journey possible.

Jithin M. A.

“You've got to have dreams to keep you going...”

~ Steve Waugh

ABSTRACT

The preparation, characterization, and applications of nickel-titanium (NiTi) shape memory alloy (SMA) and titanium nitride (TiN) thin films are investigated in this thesis. The vacuum diagnoses of the process chamber using a residual gas analyzer (RGA) and its importance in the high-quality thin film process environment have been discussed. An optical emission spectroscopy has been employed for analyzing the in-situ plasma characteristics of both pulsed DC magnetron sputter (PDCMS) deposition technique and the conventional DC magnetron sputter deposition (DCMS) techniques. The PDCMS NiTi plasmas exhibited higher intensity than the DCMS NiTi plasmas. The enhancements of the NiTi plasma and thin film properties of the PDCMS deposition technique over those of the conventional DCMS technique have been investigated. In the next attempt, the influence of deposition pressure and pulse frequencies on the NiTi thin films properties has been investigated. The NiTi films deposited at 10^{-3} mbar order pressure exhibited austenitic phase at room temperature, whereas the NiTi films deposited at 10^{-2} mbar order were in martensitic phase at room temperature. The NiTi films deposited at various pulse frequencies (50 to 350 kHz) did not significantly improve the film properties because the variation of pulse frequencies from 50 to 350 kHz was not adequate to impact the film properties substantially. The second material, TiN, has also been synthesized using the PDCMS technique. The electrical properties of the TiN thin films have been fine-tuned by varying their microstructures using various process adjustments like substrate temperature and nitrogen partial pressures. The TiN film with better electrical resistivity was chosen to fabricate micro-heaters. Focused Ion Beam (FIB) and Ytterbium fiber laser bulk micromachining techniques were utilized to fabricate the micro-heater patterns. By adjusting the input powers, the temperature attained was nearly 400 °C. Similarly, femtosecond laser and Ytterbium fiber laser bulk micromachining techniques were used to fabricate NiTi micro-devices, such as micro-cantilevers and micro-wrappers micro-combs, micro-mesh, etc. TiN micro-heaters were fabricated alongside the NiTi micro-devices to provide the required temperatures for actuation. Since both NiTi and TiN are biocompatible materials, these devices could be used in bio-friendly environments.

Keywords: *DC magnetron sputtering, Pulsed DC magnetron sputtering, Nickel-Titanium, Titanium nitride, Optical emission spectroscopy, Residual gas analyzer, MEMS, micro-heaters, femtosecond laser, Ytterbium fiber laser micromachining*

CONTENTS

LIST OF FIGURES.....	i
LIST OF TABLES	vii
ABBREVIATIONS.....	ix
NOMENCLATURE.....	xi

CHAPTER 1.....	1
-----------------------	----------

INTRODUCTION.....	1
--------------------------	----------

1. 1. Actuators.....	1
-----------------------------	----------

1. 2. Micro-actuators.....	2
-----------------------------------	----------

1. 2. 1. Applications of SMA micro-actuators.....	3
---	---

1. 3. Shape memory effect.....	4
---------------------------------------	----------

1. 4. Working of shape memory alloys.....	5
--	----------

1. 5. Hysteresis.....	6
------------------------------	----------

1. 6. Shape memory alloys.....	6
---------------------------------------	----------

1. 7. NiTi shape memory alloy.....	7
---	----------

1. 7. 1. Phase diagram.....	8
-----------------------------	---

1. 7. 2. Thin film NiTi shape memory alloys.....	8
--	---

1. 8. Literature review on NiTi Shape memory alloy thin films.....	9
---	----------

1. 8. 1. Properties required to exhibit shape memory effect.....	9
--	---

1. 8. 2. Processing of NiTi shape memory alloys thin films.....	9
---	---

1. 8. 3. Magnetron sputter deposition of NiTi shape memory alloy thin films... 10
--

1. 8. 4. DCMS deposition of NiTi shape memory alloy thin films..... 11

1. 8. 5. RFMS deposition of NiTi shape memory alloy thin films..... 14

1. 8. 6. Co-Sputter (RF & DC MS) deposition of NiTi shape memory alloy thin films..... 14

1. 8. 7. Advantages of PDCMS deposition technique..... 17
--

1. 8. 8. Patterning of NiTi thin films..... 17

1. 9. Importance of capping layer with NiTi thin films.....	18
--	-----------

1. 10. Titanium nitride thin films.....	19
--	-----------

1. 10. 1. Titanium nitride in MEMS.....	20
1. 11. Literature review on TiN thin films.....	20
1. 11. 1. Processing of TiN thin films.....	20
1. 11. 1. 1. DCMS Processing of TiN thin films.....	21
1. 11. 1. 2. RFMS Processing of TiN thin films.....	22
1. 11. 1. 3. PDCMS Processing of TiN thin films.....	22
1. 11. 2. Patterning of TiN thin films.....	24
1. 12. Scope of the work.....	24
1. 13. Objectives of the work.....	26
1. 14. Organization of the thesis.....	26
CHAPTER 2.....	29
EXPERIMENTAL DETAILS.....	29
2. 1. Introduction.....	29
2. 2. Deposition techniques.....	29
2. 2. 1. Physical vapor deposition.....	29
2. 2. 2. Chemical vapor deposition.....	30
2. 2. 3. Sputter deposition.....	30
2. 2. 4. Magnetron sputter deposition.....	31
2. 2. 4. 1. DC magnetron sputter deposition.....	33
2. 2. 4. 2. Pulsed DC magnetron sputter deposition.....	34
2. 2. 5. Sputtering yield.....	35
2. 2. 6. Sputter deposition from alloy target.....	36
2. 2. 7. Composition of the films.....	37
2. 2. 8. Reactive Pulsed DC magnetron sputter deposition.....	37
2. 3. Experimental Setup.....	38
2. 3. 1. Vacuum chamber.....	39
2. 3. 2. Pumping system.....	39
2. 3. 3. Vacuum gauges.....	40
2. 3. 4. Mass flow controller.....	40
2. 3. 5. Substrate holder cum heater.....	40

2. 3. 6. Magnetron sputter gun.....	41
2. 3. 7. Power supplies.....	41
2. 3. 8. Residual gas analyzer.....	41
2. 3. 9. Butterfly Valve.....	43
2. 3. 10. Gate valve.....	43
2. 3. 11. Bellows.....	43
2. 4. Deposition procedure.....	43
2. 4. 1. Selection of substrate.....	44
2. 4. 2. Substrate cleaning and loading.....	44
2. 4. 3. Chamber evacuation and vacuum diagnosis.....	45
2. 4. 4. Deposition and plasma diagnosis.....	45
2. 5. Characterization techniques.....	46
2. 5. 1. Optical emission spectroscopy (OES) - <i>In-situ</i> plasma studies.....	47
2. 5. 2. Thickness measurement by cross-sectional scanning electron microscopy.....	52
2. 5. 3. Microstructure characterization by X-ray diffraction (XRD).....	52
2. 5. 4. Phase transformation studies by high-temperature X-ray diffraction (HT- XRD).....	53
2. 5. 5. Surface morphology studies.....	54
2. 5. 5. 1. Atomic force microscopy.....	54
2. 5. 5. 2. Field emission scanning electron microscopy.....	54
2. 5. 6. Atomic composition studies by Energy Dispersive X-Ray Spectroscopy (EDS).....	55
2. 5. 7. Electrical resistivity studies by the four-probe measurement system ...	55
2. 6. Fabrication techniques.....	56
2. 6. 1. Focused ion beam milling.....	56
2. 6. 2. Femto second laser.....	57
2. 6. 3. Ytterbium fiber Laser micromachining.....	58
2. 6. 4. Reactive ion etching–Cl and TMAH etching of silicon.....	59
2. 6. 5. Wirebonding.....	60
2. 6. 6. Infrared thermal camera.....	61

CHAPTER 3.....63

INFLUENCE OF DCMS AND PDCMS PROCESSES ON NICKEL-TITANIUM THIN FILMS PROPERTIES.....63

3. 1. Introduction.....63

3. 2. Vacuum diagnose of process chamber using residual gas analyzer.....63

3. 3. Calibration of the experimental setup.....67

 3.3.1. Microstructure analysis.....68

 3.3.2. Surface topographic and compositional studies.....69

3. 4. Study of DCMS and PDCMS NiTi thin film properties.....71

 3. 4. 1. Microstructural studies.....73

 3. 4. 2. Surface topographic and compositional studies.....74

 3. 4. 3. Phase transformation studies.....79

3. 5. DCMS and PDCMS NiTi plasma diagnose using optical emission spectroscopy.....83

3. 6. Conclusion.....86

CHAPTER 4.....89

INFLUENCE OF VARIOUS PROCESS CONDITIONS ON THE PDCMS NiTi THIN FILM PROPERTIES.....89

4. 1. Introduction.....89

4. 2. Effect of deposition pressures on the PDCMS NiTi plasma and thin film Properties.....89

 4. 2. 1. Plasma diagnose by optical emission spectroscopy.....90

 4. 2. 2. Microstructure analysis.....92

 4. 2. 3. Surface topographic and compositional studies.....93

 4. 2. 4. Phase transformation studies.....96

4. 3. Study of PDCMS NiTi plasmas and thin films properties deposited at

various pulse frequencies	97
4. 3. 1. Plasma diagnose by optical emission spectroscopy.....	98
4. 3. 2. Microstructural studies.....	100
4. 3. 3. Surface, compositional studies.....	101
4. 4. Conclusion	104
CHAPTER 5	107
PULSED DC MAGNETRON SPUTTER (PDCMS) DEPOSITION OF TITANIUM NITRIDE THIN FILMS	107
5. 1. Introduction	107
5. 2. Calibration of the experimental setup	107
5. 2. 1. Vacuum diagnose of process chamber at various conditions using residual gas analyzer.....	107
5. 2. 2. TiN plasma diagnose using optical emission spectroscope.....	109
5. 3. Effect of substrate temperature on TiN thin film properties	113
5. 3. 1. Microstructural studies.....	114
5. 3. 2. Surface topographic and compositional studies.....	116
5. 3. 3. Electrical studies.....	118
5. 4. Effect of the nitrogen partial pressures on the TiN thin film properties ...119	
5. 4. 1. Microstructural studies.....	120
5. 4. 2. Surface topographic studies.....	122
5.4. 3. Electrical resistivity measurement.....	124
5.4. 4. Compositional and structural analysis with transmission electron microscopy.....	125
5. 5. Effect of differential pumping mechanism on PDCMS TiN plasma and structural properties	128
5. 5. 1. TiN plasma diagnose using optical emission spectroscope.....	129
5. 5. 2. Microstructural studies.....	131
5. 6. Conclusion	132
CHAPTER 6	135

FABRICATION OF NICKEL-TITANIUM AND TITANIUM NITRIDE MICROSTRUCTURES AND DEVICES.....135

6. 1. Introduction.....135

6. 2. Fabrication Methodology.....135

6. 3. Fabrication and characterization of TiN micro-heaters.....136

6. 3. 1. Focused ion beam micromachining of TiN micro-heaters.....136

6. 3. 1. 1. Fabrication.....136

6. 3. 1. 2. Characterization.....138

6. 3. 2. Laser *micromachining* of TiN micro-heater structures.....139

6. 3. 2. 1. Fabrication.....139

6. 3. 2. 2. Characterization.....141

6. 4. Micromachining of NiTi MEMS devices (Cantilevers and Wrappers) by femtosecond lasers.....142

6. 4. 1. Fabrication and integration of NiTi micro-cantilevers with TiN micro-heaters.....142

6. 4. 2. Fabrication and integration of NiTi micro-wrappers with TiN micro-heaters.....146

6. 5. Other NiTi micro-devices fabricated using laser micromachining.....149

6. 5. 1. Fabrication of NiTi micro-mesh by laser engraving technique.....149

6. 5. 2. Fabrication of NiTi micro-combs by laser machining technique.....152

6. 6. Conclusions.....153

CHAPTER 7.....155

SUMMARY, CONCLUSIONS, AND SCOPE OF FUTURE WORKS.....155

7. 1. Summary and conclusions.....155

7. 2. Future directions.....157

References.....159

List of publications.....181

Curriculum vitae.....183

LIST OF FIGURES.....

Figure 1.1	Two phases of shape memory alloys: (a) High-temperature austenite phase – cubic. (b) Low-temperature martensite phase monoclinic.....	4
Figure 1.2	Shape memory process shown microscopically: austenite (a) is cooled to form twinned martensite (b) without undergoing a phase change and then is deformed by moving twin boundaries (c). Heating either state (b) or (c) will return the originally austenitic structure and shape.....	5
Figure 1.3	Plot showing phase transformation Vs. temperature.....	6
Figure 1.4	Phase diagram of Nickel-Titanium SMA system.....	9
Figure 2.1	The effect of ion-solid interactions.....	31
Figure 2.2	Schematic of a magnetron housed in the sputter deposition chamber.....	33
Figure 2.3	DCMS deposition setup (schematic).....	34
Figure 2.4	PDCMS deposition setup (schematic and waveform).....	35
Figure 2.5	Schematic diagram of vacuum deposition unit.....	39
Figure 2.6	(a) SRS 200 RGA with differential pumping mechanism, (b) RGA integration with the process chamber.....	42
Figure 2.7	Schematic diagram of the mass spectrometer.....	42
Figure 2.8	Energy levels involved in typical OES experiments.....	48
Figure 2.9	Optical emission spectrometer and its incorporation with the process chamber between the magnetron gun and the substrate holder.....	49
Figure 2.10	Optical emission spectra of (a) DCMS and PDCMS NiTi plasmas, (b) TiN plasmas at various Ar:N ₂ ratios.....	50 - 51
Figure 2.11	Schematic diagram of the diffraction of X-rays from the atomic planes.....	53
Figure 2.12	Schematic of FIB column.....	57
Figure 2.13	Schematic of femtosecond laser system.....	58
Figure 2.14	Schematic of Ytterbium fiber laser system	59
Figure 2.15	Oxford reactive ion etching system.....	60

Figure 2.16	TPT wire bonder.....	60
Figure 2.17	Components of IR camera.....	61
Figure 3.1	Residual gas analyzer integration with process chamber. Isolation butterfly valve is highlighted with the marking.....	64
Figure 3.2.a	The vacuum diagnosis during chamber evacuation and baking using residual gas analyzer.....	65
Figure 3.2.b	The vacuum diagnosis during NiTi deposition using residual gas analyzer.....	67
Figure 3.3	The XRD spectra of DCMS NiTi thin films.....	69
Figure 3.4	Surface topography of DCMS NiTi thin films by AFM.....	69
Figure 3.5	The FE-SEM surface image of DCMS NiTi thin films.....	70
Figure 3.6	The cross-sectional SEM image of 880 nm. thick DCMS NiTi thin films.....	71
Figure 3.7	The thickness calibration curve of DCMS NiTi thin films.....	71
Figure 3.8	The room temperature XRD spectra of DCMS and PDCMS NiTi thin films at (a) 400, (b) 500, (c) 600 and (d) 650°C.....	73 - 74
Figure 3.9.a	AFM images of both DC and PDC NiTi thin films deposited at 400, 500, 600, and 650°C, respectively.....	75 - 76
Figure 3.9.b	Height profiles of both DC and PDC NiTi thin films deposited at 400, 500, 600, and 650°C, respectively.....	76
Figure 3.10.a	FE-SEM image of DCMS and PDCMS NiTi thin films, respectively, at 400°C.....	77
Figure 3.10.b	FE-SEM image of DCMS and PDCMS NiTi thin films, respectively, at 500°C.....	77
Figure 3.10.c	FE-SEM image of DCMS and PDCMS NiTi thin films, respectively, at 600°C.....	78
Figure 3.10.d	FE-SEM image of DCMS and PDCMS NiTi thin films, respectively, at 650°C.....	78
Figure 3.11	Cross-sectional FE-SEM images of DCMS and PDCMS NiTi thin films.....	79
Figure 3.12	The high-temperature XRD spectra of DCMS NiTi thin films.....	80
Figure 3.13	The high-temperature XRD spectra of PDCMS NiTi thin films.....	81

Figure 3.14	XRD profiles showing diffractions from martensite and austenite phases of PDCMS 600°C NiTi thin films as a function of temperature.....	82
Figure 3.15	Average crystallite size of PDCMS 600°C NiTi films during martensite-to-austenite phase transformation as a function of temperature	82
Figure 3.16	Wide spectra of both DCMS and PDCMS NiTi magnetron plasma...	84
Figure 3.17	Optical emission spectra of DCMS and PDCMS sputtered (a) titanium, (b) nickel, and (c) argon.....	85 - 86
Figure 4.1	PDCMS NiTi plasma characteristics at various deposition pressures.	91
Figure 4.2	The RT-XRD spectra of PDCMS NiTi thin films deposited at pressures 2.5×10^{-3} , 5×10^{-3} , 7.5×10^{-3} , and 1×10^{-2} mbar.....	93
Figure 4.3	Upper panel: The AFM images of PDCMS NiTi films deposited at (a) 2.5×10^{-3} mbar, (b) 5×10^{-3} mbar, (c) 7.5×10^{-3} mbar and (d) 1×10^{-2} mbar. Lower panel: Corresponding height profiles.....	94
Figure 4.4	The FE-SEM image and grain size details of PDCMS NiTi films deposited at 2.5×10^{-3} mbar, 5×10^{-3} mbar, 7.5×10^{-3} mbar and 1×10^{-2} mbar, respectively.....	95
Figure 4.5	The HT-XRD spectra of room temperature martensite phase NiTi thin films deposited at 1.00×10^{-2} mbar.....	97
Figure 4.6	Plot between pulse frequency Vs. duty cycle and pulse reversal time.....	98
Figure 4.7	Optical emission spectra of pulsed DC sputtered (a) titanium, (b) nickel, and (c) argon at various pulse frequencies.....	99-100
Figure 4.8	The RT-XRD spectra of PDCMS NiTi thin films at 600°C and 1.00×10^{-2} mbar at pulse frequencies 50, 100, 200 and 350 kHz.....	101
Figure 4.9	Upper panel: The AFM images of PDCMS NiTi thin films deposited at pulse frequencies 50, 100, 200, and 350 kHz. Lower panel: Corresponding height profiles.....	103
Figure 4.10	FE-SEM image and grain size details of PDCMS NiTi thin films deposited at pulse frequencies 50, 100, 200, and 350 kHz.....	104

Figure 5.1	Partial pressures of (a) major residual gases measured using residual gas analyzer.....	108
Figure 5.2	Partial pressures of both argon and nitrogen gases at different Ar:N ₂ ratios.....	109
Figure 5.3	OES spectral analysis of PDCMS TiN plasma.....	110
Figure 5.4	Wide range emission spectra of PDCMS TiN plasmas at various nitrogen flow rates.....	111
Figure 5.5	Elemental spectra of (a) titanium, (b) nitrogen, and (c) argon in PDCMS TiN plasmas at various nitrogen flow rates.....	112-113
Figure 5.6	XRD patterns of PDCMS TiN films deposited at substrate temperatures of RT, 100, 200 and 300°C.....	115
Figure 5.7	2D surface images of PDCMS TiN film deposited at RT, 100, 200, and 300°C. and corresponding height profiles.....	117
Figure 5.8	The FE-SEM images of PDCMS TiN films deposited at RT, 100, 200 and 300°C.....	118
Figure 5.9	SEM image of the fractured cross-section of TiN_RT films	118
Figure 5.10	Variation of electrical resistivity of PDCMS TiN thin films deposited at different substrate temperatures	119
Figure 5.11	XRD patterns of PDCMS TiN films deposited at Ar:N ₂ ratios of 20:20, 20:15, 20:10, 20:05.....	121
Figure 5.12	Upper panel: 2D surface topographies of the PDCMS TiN films deposited at Ar:N ₂ ratios 20:20, 20:15, 20:10, and 20:05. Lower panel: Corresponding height profiles	123
Figure 5.13	The FE-SEM images of PDCMS TiN films deposited at various Ar:N ₂ ratios	124
Figure 5.14	Images of the fracture surface of TiN_20:20 and TiN_20:05 thin films.....	124
Figure 5.15	Electrical resistivity of the TiN thin films at various Ar:N ₂ ratios....	125
Figure 5.16	TEM Diffraction pattern of 20:05 (Ar:N ₂) TiN film.....	126
Figure 5.17	(A) Cross-sectional STEM-HAADF micrograph of 20:05 (Ar:N ₂) TiN film and EDS elemental maps for (B) Si, (C) Ti, (D) N, (E) O, & (F) Pt.....	127

Figure 5.18	Counts of each element Si, Ti, N, and O obtained from EDS spectr.	128
Figure 5.19	Wide range emission spectra of PDCMS TiN plasmas recorded with RGA differential pumping mechanism ON and OFF.....	130
Figure 5.20	Elemental spectra of (a) titanium, (b) nitrogen and (c) argon in PDCMS TiN plasmas with and without RGA differential pumping mechanism.....	130-131
Figure 5.21	XRD spectra of PDCMS TiN films deposited at Ar:N ₂ ratios 20:20, 20:15, 20:10 and 20:05.....	132
Figure 6.1	Auto CAD design of the planned TiN micro-heater pattern.....	136
Figure 6.2	Auto CAD design of the Si (Black)/SiO ₂ (Green)/TiN (Yellow) stack.....	137
Figure 6.3	FIB image of the TiN micro-heater pattern.....	137
Figure 6.4	Packaged TiN micro-heater device.....	138
Figure 6.5	IR images of micro-heaters at (a) 0.18, (b) 0.7, (c) 1.56 & (d) 2.84..	138
Figure 6.6	Power Vs. heater temperature measurements of TiN micro-heaters..	139
Figure 6.7	Auto CAD design of the planned Si/SiO ₂ /TiN stack.....	139
Figure 6.8	Laser-patterned TiN thin film micro-heater patterns (a) 200 and (b) 400 μm.....	140
Figure 6.9	IR images of micro-heaters: (a) 200 μm, (b) 400 μm, and (c) 600 μm with their maximum temperatures.....	141
Figure 6.10	Performance of TiN micro-heaters with their dimensions at ~8 W...	141
Figure 6.11	Heating performance of TiN micro-heaters at different lengths.....	142
Figure 6.12	Auto CAD design of the planned NiTi micro-cantilever and TiN micro-heater structures.....	143
Figure 6.13	Top view of the Si/NiTi/TiN thin film stacks.....	143
Figure 6.14	Microscopic image of the femtosecond laser micropatterned Si/NiTi stack.....	144
Figure 6.15	Si/NiTi stack after femtosecond laser micropatterning (FE-SEM image).....	144
Figure 6.16	FE-SEM image of the released NiTi cantilever microstructures....	145

Figure 6.17	FE-SEM image of the micropatterned NiTi micro-wrapper and TiN micro-heater structures.....	145
Figure 6.18	Optical images showing the actuation of NiTi cantilevers upon heating: (a) at room temperature. (b) at temperatures of 150 - 170°C.....	146
Figure 6.19	Auto CAD design of the planned NiTi micro-wrapper and TiN micro-heater structures	147
Figure 6.20	Side view of the Si/NiTi/TiN thin film stacks.....	147
Figure 6.21	FE-SEM image of the femtosecond laser micropatterned Si/NiTi stack.....	148
Figure 6.22	FES-EM image of the released NiTi wrapper microstructures.....	148
Figure 6.23	FE-SEM image of the micropatterned NiTi micro-wrapper and TiN micro-heater structures.....	149
Figure 6.24	Auto CAD design of the planned NiTi micro-mesh structures.....	150
Figure 6.25	Auto CAD design of the Si/NiTi stack.....	150
Figure 6.26	Optical microscopic images of the laser patterned NiTi micro-meshes.....	151
Figure 6.27	Optical profiler 3D images of the laser micropatterned NiTi micro-meshes.....	151 - 152
Figure 6.28	Auto CAD design of the planned NiTi micro-mesh structures.....	152
Figure 6.29	Optical microscopic image of the NiTi micro-comb structures.....	153

LIST OF TABLES.....

Table 1.1	Comparison of various types of micro-actuators.....	2
Table 1.2	Some of the alloys exhibiting shape memory effect	7
Table 2.1	Characterization techniques used for studying NiTi and TiN film properties.....	46
Table 3.1	Process parameters of NiTi thin films deposited by DCMS.....	68
Table 3.2	Process parameters of NiTi thin films deposited by both DCMS and PDCMS techniques.....	72
Table 3.3	Crystallite size of both DCMS and PDCMS NiTi thin films deposited at 400, 500, 600 and 650°C.....	74
Table 3.4	Energy-dispersive spectroscopic analysis of both DCMS and PDCMS NiTi thin films	79
Table 4.1	Process parameters of PDCMS NiTi thin films deposited at various pressures.....	90
Table 4.2	Crystallite size of both PDCMS NiTi thin films deposited at pressures 2.5×10^{-3} , 5×10^{-3} , 7.5×10^{-3} and 1×10^{-2} mbar.....	93
Table 4.3	The elemental composition of PDCMS NiTi thin films deposited at 2.5×10^{-3} mbar, 5×10^{-3} mbar, 7.5×10^{-3} mbar, and 1×10^{-2} mbar	96
Table 4.4	Process parameters of PDCMS NiTi thin films deposited at pulse frequencies.....	98
Table 4.5	Crystallite size of both PDCMS NiTi thin films deposited at pressures 50, 100, 200, and 350 kHz.....	101
Table 4.6	The elemental composition of PDCMS NiTi thin films deposited at pulse frequencies (a) 50, (b) 100, (c) 200 and (d) 350 kHz.....	104
Table 5.1	Process parameters of PDCMS TiN thin films deposited at various substrate Temperatures.....	114
Table 5.2	Crystallite size and texture coefficient of TiN thin films deposited at various substrate temperatures, namely, RT, 100, 200, and 300°C....	116
Table 5.3	Process parameters of PDCMS TiN thin films deposited at different	

	Ar:N ₂ ratios	120
Table 5.4	Crystallite size and texture coefficient of TiN thin films deposited at Ar:N ₂ ratios of 20:20, 20:15, 20:10, and 20:05.....	122
Table 5.5	Process parameters of PDCMS TiN thin films deposited with and without RGA differential pumping system.....	129

ABBREVIATIONS.....

AFM	Atomic force microscopy
CMOS	Complementary metal oxide semiconductor
CVD	Chemical vapor deposition
DC	Direct current
DCMS	Direct current magnetron sputtering
DSC	Differential scanning calorimetry
EDX	Energy dispersive X-ray analysis
EM	Electromagnetic
ES	Electrostatic
FESEM	Field emission electron microscopy
FIB	Focused ion beam
FSL	Femtosecond laser
FWHM	full width half maxima
GIXRD	Grazing Incidence X-ray diffraction
HF	Hydrofluoric acid
IPA	Isopropyl alcohol
IR	Infrared
MB	Micro-bubble
MEMS	Micro-electromechanical system
NEMS	Nano-electromechanical systems
OES	Optical emission spectroscopy
PDCMS	Pulsed direct current magnetron sputtering
PE	Piezoelectric
PVD	Physical vapor deposition
RF	Radio frequency
RGA	Residual gas analyzer
RT	Room temperature
TC	Texture coefficient
SCCM	Standard cubic centimeter per minute

SMA	Shape memory alloy
SMA_s	Shape memory alloys
SME	Shape memory effect
SL	solid–liquid phase change
TC	Texture coefficient
TE	Thermal expansion
TEM	Transmission Electron Microscopy
TMAH	Tetramethyl ammonium hydroxide
TMP	Turbo molecular pump
TP	Thermo pneumatic
VL	Visible light
XRD	X-ray diffraction
Min	Minute
Hr	Hour

NOMENCLATURE.....

A_f	Austenite finish
A_s	Austenite start
M_f	Martensite finish
M_s	Martensite start
Ni	Nickel
NiTi/TiNi	Nickel titanium
Si₃N₄	Silicon nitride
SiO₂	Silicon dioxide
Ti	Titanium
TiN	Titanium nitride
λ	Wavelength
θ	Bragg angle
Ar	Argon
CO₂	Carbon dioxide
H₂	Hydrogen
H₂O	Water vapor
N₂	Nitrogen
O₂	Oxygen
I	Current
V	Voltage
W	Power
kHZ	Frequency in Kilo Hertz

Chapter 1

INTRODUCTION

It is well known that shape memory alloy actuators play a significant role in advanced actuator applications. NiTi shape memory alloys gained considerable attention because of their excellent properties, such as high mechanical output, large recovery force, high corrosion resistance, exceptional fatigue behavior, and high biocompatibility. This chapter gives an overview of thin film shape memory alloys (NiTi) and thin film micro-heaters (TiN) and the importance of their integration for advanced MEMS applications. The chapter concludes with the thesis's scope, objectives, and outlines.

1. 1. Actuators

Actuators are the muscle of mechatronic systems. They are the vital components of a machine responsible for moving and controlling a particular mechanism or system. Defined technically, actuators are devices that convert energy (thermal, electrical, etc.) to mechanical motion. Actuators can have two basic motions, linear, which converts energy into straightline motions, and rotary, which converts energy into rotatory motion. Actuator types can be electric or piezoelectric, thermal and magnetic (shape memory alloys), hydraulic and pneumatic, etc. But in all these cases, the output is mechanical. Actuators have a significant role in the emerging MEMS/NEMS domains. The performance of an actuator depends mainly on the selection of appropriate materials. There has been a search for new materials to fulfill the need for actuators with desired properties, resulting in the concept of new advanced composites materials. These materials have a wide range of uses in aerospace, medical technology, and other fields. These new materials are known as “smart” or “intelligent” materials. Smart materials are a class of materials, which are being widely used as piezoelectric actuators, magnetostrictive actuators, shape memory polymers, and shape memory alloys (SMAs) (Miyazaki et al. 2009).

1. 2. Micro-actuators

Technological advances cemented the requirement for actuators in micro-electro-mechanical systems (MEMS). Many types of materials have been explored for the fabrication of micro-actuators. The micro-actuators are classified into: (1) NiTi shape memory alloy (SMA), (2) solid-liquid phase change (SL), (3) thermo pneumatic (TP), (4) thermal expansion (TE), (5) electromagnetic (EM), (6) electrostatic (ES), (7) piezoelectric (PE), (8) muscle (M), (9) micro-bubble (MB), etc. Only the first three actuators can create significant forces across lengthy displacements among these actuators. In MEMS actuators, piezoelectric, electromagnetic, and shape memory alloys are widely used because of their high work output per unit volume. Among these, SMAs exhibit one order of higher work output per unit volume than others (Johnson et al. 1999, Miyazaki et al. 2009). SMA actuators can produce a large work output per unit volume over a range of reasonably high cycling frequencies. The work output per unit volume (W) can be defined as $W = Fu/v$, where F , u , and v are force, displacement, and volume, respectively.

Table 1.1: Comparison of various types of micro-actuators (Miyazaki et al. 2009)

Material/Properties	Piezoelectric	SMA	Electromagnetic
Maximum Recoverable Stress	40MPa	600 MPa	Less
Range of motion	0.1%	5%	Large
Frequency Response	10 kHz	20 Hz	3kHz
Work output/ volume	$1.2 \times 10^5 \text{ J/m}^3$	$2.5 \times 10^7 \text{ J/m}^3$	$1.8 \times 10^5 \text{ J/m}^3$
Voltage	20-30 V	1-3 V	60-400 V

Superior properties of SMA actuators compared with piezoelectric and electrostatic actuators are shown in Table 1. 1. High mechanical output, large recovery force, excellent range of motion, and voltage requirements make SMA actuators the best

choice compared to other actuators. In addition, some of the SMAs exhibit good corrosion resistance and biocompatibility. The only drawback of the thermal SMA system is its poor frequency response. This is an issue of concern for applying them as thermal SMAs with the faster-performing device actuators. To overcome this, magnetic SMAs have been put forward in the later years. In the magnetic SMA system, the phase change occurs with the variation in the magnetic field. The actuators made of magnetic SMAs are much faster than the thermal SMAs and can be deployed for strategic applications (Hakola et al. 2004). The main advantage of NiTi SMA actuators includes large displacement and actuation force, low operation voltage, etc.

1. 2. 1. Applications of SMA micro-actuators

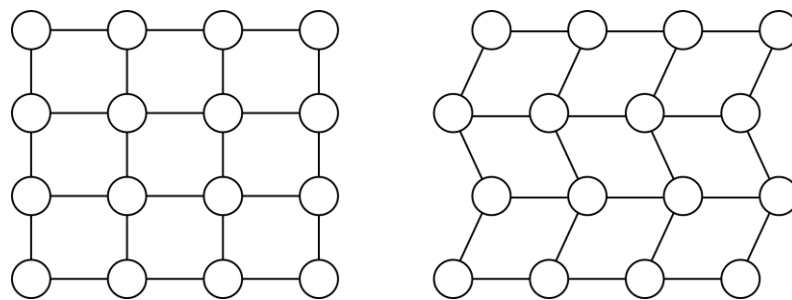
SMAs in MEMS also allow for mechanism simplicity and design freedom and the construction of clean, frictionless, and non-vibrating movements. NiTi MEMS actuators are sensitive to environmental changes, such as temperature, stress, magnetic fields, and electrical fields, making them excellent for microsensors. Since NiTi actuators provide these properties, most of their applications are focused on MEMS-based smart structures (Johnson et al. 1999). The better biocompatibility of NiTi MEMS devices finds various biological applications. NiTi-based micro-devices are used for grasping and manipulating small and micro-objects with high accuracy in microsurgery and drug injection micromanipulators for cells (Ryhanen et al. 1996, Mohammad et al. 2015).

The typical applications of SMA micro-actuators are in aerospace, optical sensing, electrical circuits, probe tips, automotive industry, micro-lense positioners, biomedical, etc. Thermal SMAs exhibiting a two-way shape memory effect (Eg. NiTiCu) are used to fabricate micro-sensors, micro-switches, and micro-positioners. In MOS devices, the NiTi electrodes are used to detect the temperature fluctuation by detecting the capacitance variations upon cooling and heating (Bendahan et al. 1999, Miyazaki et al. 2009). The NiTi shape memory micro-actuators also have a potential application in the fabrication of micro-diaphragms, micro-valves, micro-pumps, etc. (Shin et al. 2006). Another interesting application of NiTi SMAs is micro-grippers. These are used in biomedical applications as they have a good scope in drug delivery,

biopsy, and tissue sampling. Another application is to tag a device utilizing a micro-clipper with a tissue under treatment/investigation. Also, they are used for grasping and manipulating tiny micro-organisms in micro-manipulators (Sugawara et al. 2006, Gill et al. 2001, Takeuchi et al. 2000).

1. 3. Shape memory effect

The shape memory effect (SME) occurs when a material recovers its original size and shape when heated above a specific characteristic transformation temperature. It has a low-temperature phase and a high-temperature phase. The phase change occurs when atoms within the crystal lattice rearrange between two solid phases (Figure 1. 1). The low-temperature phase is martensite, B19' (named after German metallographer Adolf Martens), with a highly twinned crystalline structure. In contrast, the high-temperature phase is Austenite, B2 (named after William Chandler Austen, an English metallurgist) with a body-centered cubic structure. Austenite NiTi and martensite NiTi have several distinct characteristics.



(a) (b)

Figure 1.1: Two phases of shape memory alloys: (a) High-temperature austenite phase (B2) – cubic. (b) Low-temperature martensite phase (B19') – monoclinic.

On heating, the martensite phase will begin to transform into austenite (Figure 1. 2). The austenite-start temperature is the temperature at which the transformation begins (A_s). The austenite-finish temperature is the temperature at which the martensite-to-austenite transformation is complete (A_f). When austenite SMA is cooled, it starts to transform into martensite. The martensite-start temperature is the temperature at which the austenite-to-martensite transition begins (M_s). The martensite-finish

temperature is the temperature at which the austenite-to-martensite transition is complete (M_f) (Buehler et al. 1963, Miyazaki et al. 2009).

1. 4. Working of shape memory alloys

The shape memory effect is possible through a solid-state phase change, i.e., a molecular rearrangement in the shape memory alloys. Typically, when one thinks of a phase change, a solid-to-liquid or liquid-to-gas change is the first thing that comes to mind. A solid-state phase change occurs when an atomic rearrangement occurs, but the atoms remain closely packed so that the substance remains solid. In most SMAs, a temperature change of only about 10°C is necessary to initiate the phase change. Among the above-mentioned phases, martensite is a relatively softer and easily deformable phase of the SMAs, which forms at lower temperatures. The molecular structure in this phase is twinned (Figure 1. 2b). Upon deformation, this phase takes on the second form (Figure 1. 2c). Austenite is the stronger phase of the SMAs and occurs at higher temperatures. The austenite crystal structure is cubic (Figure 1. 2a). The un-deformed martensite phase is of the same size and shape as the cubic austenite phase on a macroscopic scale so that no change in size or shape is visible in shape memory alloys until the martensite is deformed.

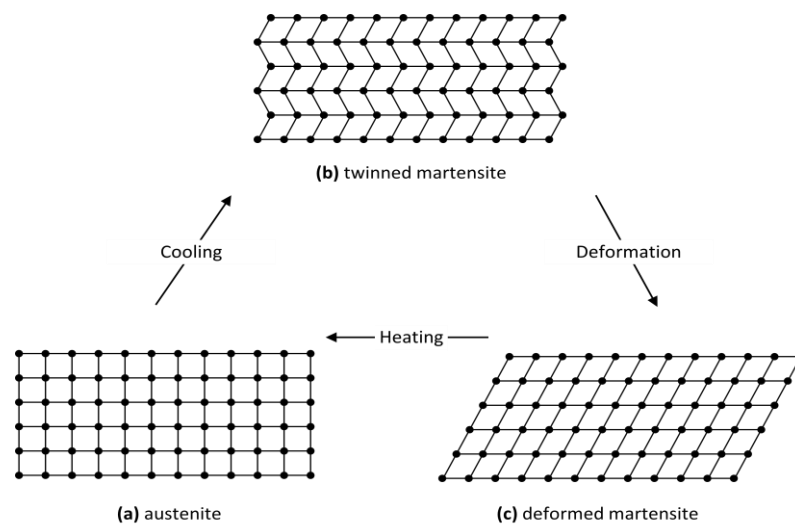


Figure 1.2: The shape memory process is shown microscopically: austenite (a) is cooled to form twinned martensite (b) without undergoing a phase change and then is deformed by moving twin boundaries (c). Heating either state (b) or (c) will return the original austenitic structure and shape. (Sumesh et al. 2005)

1. 5. Hysteresis

The temperature range for the heating-induced martensite-to-austenite transformation is slightly higher than that for the cooling-induced reverse transition (Figure 1. 3). Hysteresis is the difference between the transition temperatures for heating and cooling. Hysteresis is the difference between the temperatures when the material transforms to 50% austenite on heating and to 50% martensite on cooling. This temperature differential might range from 20 to 30 degree Celsius (Buehler et al. 1963).

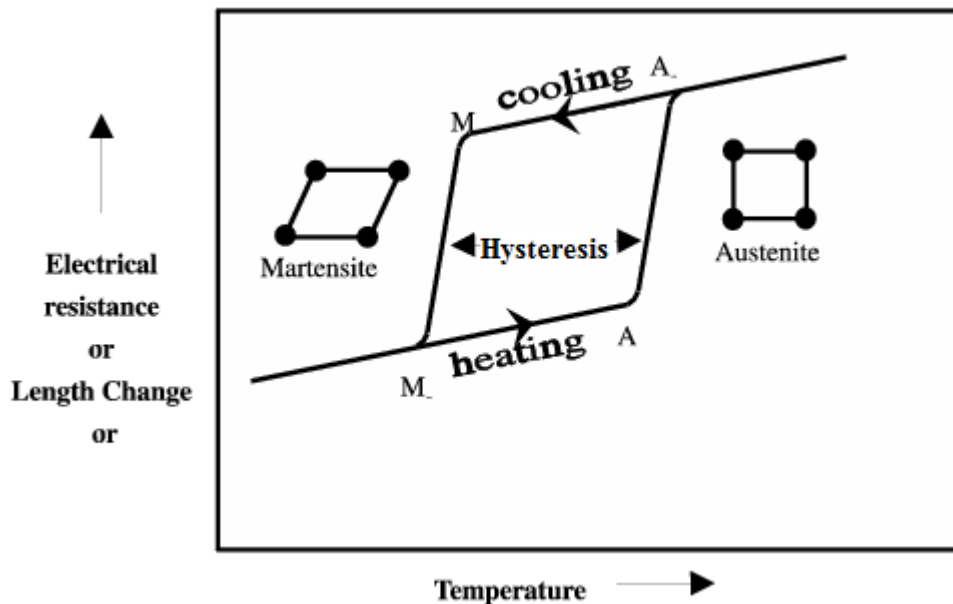


Figure 1.3: Plot showing phase transformation Vs. temperature

1. 6. Shape memory alloys

The term shape memory defines the property of certain materials to remember their original shape even after being severely deformed them, either mechanically or thermally. SMAs belong to the category of smart materials, and therefore, they are an important candidate in the actuator/sensor domain. The changes in geometries are realized by phase changes from the martensite-to-austenite phase of the material due to external mechanical or thermal stimulus (Miyazaki et al., 2009). The shape memory effect was first discovered in an alloy of Au 47.5% at.Cd in 1932, and the first commercial use of the same was in the fuel engine of the F-16 fighter jet. But Ni-Ti, Cu-Zn-Al, and Cu-Al-Ni alloys have gained more attraction commercially and

have undergone extensive research. The list of alloys exhibiting the shape memory effect is shown in Table 1. 2.

Table 1.2: Some of the alloys exhibit shape memory effect (Sumesh et al. 2005)

Alloys	Composition (At. or Wt. %)	Transformation Temp. Range (°C)
Ag – Cd	Ag-44/49 at.% Cd	-190 to -50
Au - Cd	Au-46.5/50 at.% Cd	30 to 100
Cu - Al - Ni	Cu-14/14.5 wt.% Al 3/4.5 wt/% Ni	-140 to 100
Cu – Sn	Cu-(approx.)15 at.% Sn	-120 to 30
Cu – Zn	Cu-38.5/41.5 wt.% Zn	-180 to -10
Cu - Zn - (Si, Sn, Al)	Cu-(1-10) wt.% of (Si, Sn, Al)	-180 to 200
In – Ti	In-18/23at.% Ti	60 to 100
Ni – Al	Ni-36/38at.% Al	-180 to 100
Ni-Ti	Ni-49/51at.% Ti	-50 to 110
Fe – Pt	Fe-(approx.) 25 at.% Pt	approx. -130
Mn - Cu	Mn-5/35at.% Cu	-250 to 180

1. 7. NiTi shape memory alloy

It has been reported that many alloys are exhibiting the shape memory effect. But the NiTi shape memory alloy system has received focused attention because of its enormous potential to be used as high-performance micro-actuators for MEMS applications. NiTi alloys have gained attention in the growing MEMS/NEMS sector due to their favorable features, such as high mechanical output, large recovery force, strong corrosion resistance, low fatigue, and high biocompatibility. The NiTi near equiatomic SMAs were discovered in 1962 by William. J. Buehler at the US Naval Ordnance Laboratory. Therefore, NiTi shape memory alloys are commercially known

as Nitinol (Ni-Ti Naval Ordnance Laboratory) (Wang et al. 1965, Kaufmann et al. 1997).

1. 7. 1. Phase diagram

The NiTi phase diagram is shown in Figure 1. 4, which explains the phase and precipitate formation in the NiTi SMA system. Equiatomic NiTi can exist in a solid state up to a temperature of 1310°C. It is clear from the phase diagram that for a slightly Ti-rich composition, the phases will be $Ti_2Ni + NiTi$, and for a Ni-rich composition, $NiTi + Ni_3Ti$. These precipitates play an important role in strengthening the Ni-rich NiTi alloys. The NiTi phase has a B2 (CsCl) type ordered structure with a lattice constant of 0.3015 nm at room temperature. The B2 phase is retained upon quenching or slow cooling to room temperature. This phase plays an essential role in the martensitic transformation and the associated shape memory effects (Philip et al. 1957). These phases are not equilibrium but influence the transformation temperature and shape memory behavior (Miyazaki et al. 2009).

The deviation in NiTi alloy composition causes significant effects on the shape memory effect. In the case of Ti-rich NiTi alloy, the precipitates have a significant impact on the hot workability of NiTi, particularly on the Titanium-rich side; they are brittle and often result in cracking. These precipitates ultimately change the transition temperatures of the alloy.

1. 7. 2. Thin film NiTi shape memory alloys

Unlike bulk SMAs, thin film SMAs provides a larger energy density, higher frequency response, and longer lifetime at micro-scales. Thin film SMAs have already established themselves as key actuating materials in micro-actuators, outperforming other micro-actuation mechanisms in work production per volume (Wolf et al. 1995). NiTi thin film SMAs have recently been recognized as promising and high-performance materials for MEMS applications.

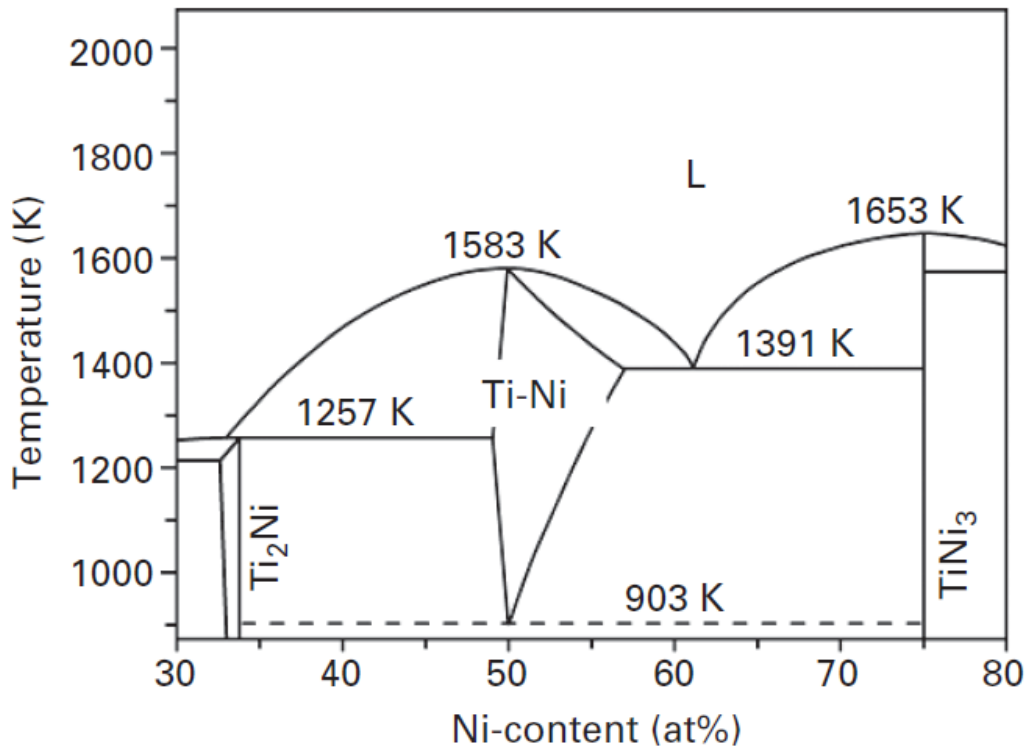


Figure 1.4: Phase diagram of Nickel-Titanium SMA system (Miyazaki et al. 2009)

1. 8. Literature review on NiTi Shape memory alloy thin films

1. 8. 1. Properties required to exhibit shape memory effect

The shape memory behavior, transition temperatures, and superelasticity of NiTi SMA thin films are affected by composition, microstructure, contamination, and other factors. These properties can be achieved and controlled using various process parameters (deposition pressure, substrate temperature, power, substrate – target distance, etc.). Hence, the deposition technique plays a pivotal role in achieving shape memory properties in NiTi thin films for use in MEMS applications (Loger et al. 2016, Tillmann et al. 2015, Kaur et al. 2013, Cha et al. 2012, Miyazaki et al. 2009, Arranz et al. 2005, Otsuka et al. 2005).

1. 8. 2. Processing of NiTi shape memory alloys thin films

Various processing techniques have been employed to produce NiTi SMA thin films with the required properties. These techniques mainly include ion beam deposition,

arc plasma ion plating, flash evaporation, laser ablation, etc. They have been used to synthesize NiTi thin films (Butt et al. 2014, Kong et al. 2014, Hou et al. 2014, He et al. 2000, Noh et al. 2000, He et al. 2000, Noh et al. 2000, Grummon et al. 1992). All these techniques have their own drawbacks, such as non-uniformity in the film thickness and composition, low deposition rate, MEMS process compatibility issues, etc. Magnetron sputtering has been widely accepted as one of the best techniques for depositing NiTi films (Loger et al. 2016, Cicek et al. 2015, Ohta et al. 2000). As sputter-deposited TiNi thin films, stable shape memory effect and superelasticity equivalent to bulk alloys have been produced (Miyazaki et al. 2009). Compared to previous methods, magnetron sputtering demonstrates the ability to create SMA films with good adhesion, hardness, repeatability, flexibility, and large-scale uniform coatings with a low/high density. Multi-component films, such as binary and ternary SMAs, can also be deposited using magnetron sputtering. Hence, sputtering has been used for most SMA thin film research (Choudhary et al. 2016, Cicek et al. 2015, Kabla et al. 2014).

1. 8. 3. Magnetron sputter deposition of NiTi shape memory alloy thin films

There are various issues associated with the sputter deposition of NiTi thin films. These issues need to be fixed to obtain the NiTi films with desired properties. The primary concern is the change in the sputtering yield of nickel and titanium under given power and processing conditions. Sputter deposition has the benefit of using a target with proper composition or individual targets of nickel and titanium to counter this issue. If the alloy target of NiTi is being used, the target property variation and related issues are to be carefully addressed. The composition of the film at various geometrical locations is a concern that needs to be carefully fixed with a proper substrate rotation mechanism. The minimum thickness requirement for the shape memory effect is also essential. Therefore, the sputter deposition technique lends higher deposition rates and can be used over other PVD techniques to deposit nickel-titanium thin films. Finally, the requirement of high temperatures for obtaining crystalline films, the NiTi thin films have to be deposited at higher substrate temperatures or post-deposition annealing (Tillmann et al. 2015, Tillmann et al. 2015, Miyazaki et al. 2009).

Magnetron sputter deposition of NiTi thin films with a single target (Ti-50at.%Ni) has been carried out by various research groups. Since nickel has a higher sputtering yield than titanium, some titanium patches (pieces) were kept on the target surface to make the titanium reach the near equiatomic composition. Some other groups have tried sputtering with titanium-rich targets (Ti- 55at.%Ni) with process optimization of target power, substrate-to-target distance, deposition pressures, etc. The other option is to employ co-sputtering, where more than one target is used. There are two ways for co-sputter deposition of NiTi thin films; either use a NiTi alloy target and another titanium target or use individual targets of nickel and titanium (Krulevitch et al. 1996, Ohta et al. 2000, Winzerk et al. 2004, Miyazaki et al. 2009). In most cases, NiTi thin films' sputter deposition has been carried out mainly with DC or RF magnetron techniques.

1. 8. 4. DCMS deposition of NiTi shape memory alloy thin films

There are literature reports on DCMS NiTi thin films deposited at room temperature followed by high-temperature annealing. The effects of annealing temperature on the structural, morphological, mechanical, and surface properties of near equiatomic DCMS NiTi thin films formed at ambient temperature were studied by Reddy et al. in 2017. Due to recrystallization, the degree of crystallinity increases up to 550°C but decreases around 650°C. Crystallization increases hardness and elastic modulus, but nucleation and grain development decrease due to recrystallization. The influence of annealing temperature on the structural, morphological, mechanical, and surface properties of intermetallic DCMS NiTi alloy thin films formed at room temperature was examined by Reddy et al. in 2016. On intermetallic NiTi thin films, the influence of annealing temperature was investigated. The average surface roughness values increased because of the increased grain development caused by annealing. Momeni et al. 2016 used DC magnetron sputtering to study the composite cavitation-resistant PVD coating of NiTi thin films. They employed a NiTi target with rich titanium content. Combining the superelasticity of sputtered NiTi thin films with the hardness of TiCN coatings, they investigated the fabrication of composite coatings. Individual layer thicknesses were varied to adjust the mechanical properties of the composite coatings. Wang et al. 2015 studied the transformation behaviors of DCMS NiTi thin

films on substrates and the thickness dependency of submicron Ni–50.5 at.%Ti thin films. To minimize grain-imposed restrictions, measurements were done on thin films with a microstructure consisting of pancake-like grains with aspect ratios above 50:1. Using various substrate materials with varying thermal expansion coefficients, the effect of residual stress on martensite transformation behavior was investigated. Tillmann et al. 2014 used DCMS to study the deposition of multilayer composite thin films comprised of NiTi and TiCN on Si (100) substrates. Nanoindentation, X-ray diffraction (XRD), scanning electron microscopy (SEM), and differential scanning calorimetry was used to explore the microstructures, mechanical characteristics, and shape memory behavior of these bilayers (DSC). The findings of this work indicated that adding a TiCN layer to a NiTi thin film changes its mechanical characteristics while keeping the shape memory effects. Habijan et al. 2012 reported on the preparation of NiTi thin films by DC magnetron sputter deposition. The target used was a cast-melted NiTi alloy disc. The substrate used was glass. The substrate was not heated during deposition, but post-deposition annealing was conducted at 650°C by rapid thermal annealing for 10 min. Following the films were annealed at 450°C for 10 min. Standard microfabrication techniques like photolithography and chemical wet etching techniques were used to fabricate different NiTi-based components. Chung et al. 2011 reported on the preparation of NiTi thin films by DC magnetron sputter deposition. The target used was NiTi alloy disc. Near equiatomic NiTi thin films were deposited on a glass substrate through patterned photoresists. Photolithography and chemical wet etching were used to produce NiTi microcantilever arrays with the desired dimension. The substrate was not heated during deposition but was conducted at 700°C for 30 min. post-deposition annealing. Phase transformation occurred on IR illumination and was well studied and reported.

Bayer et al. 2011 used a multi-gun sputter deposition technique to deposit DCMS NiTi thin films onto r-plane sapphire substrates at room temperature. They also reported the thermal interaction of SMA thin films with CNT forests to achieve quicker actuation frequencies of the SMA films through improved heat conduction via the CNTs. Chan et al. 2008 reported on the preparation of NiTi thin films by DC magnetron sputter deposition. The substrate was glass, and the target was an

equiatomic NiTi disc. The substrate was not heated during deposition but was conducted at 700°C for 30 min. post-deposition annealing. An array of NiTi microcantilevers was fabricated using photolithography and a chemical wet etching process. An optical imaging system for IR detection was integrated with the microcantilevers.

There are reports on the DCMS NiTi films deposited at higher temperatures. Magnetron sputtered near equiatomic NiTi thin films were deposited on Si (100) and hot work tool steel substrates, according to Momeni et al. 2017. The thin films were annealed *in-situ* at four different temperatures: 80°C, 305°C, 425°C, and 525°C. The impact of the *in-situ* annealing temperature on the film's microstructure, morphology, and mechanical and tribological properties was investigated. Tillmann et al. 2015 investigated how to crystallize DCMS NiTi thin films using two simple methods: (i) post-annealing and (ii) *in-situ* annealing during deposition. Each strategy keeps the annealing parameters (temperature and time) consistent. These thin films' microstructure, morphology, phase change behavior, and mechanical and tribological properties were studied. Sharma et al. 2013 studied the DCMS of NiTi from an equiatomic alloy target (Ni/Ti: 50/50 at.%). The films were applied to the substrates without intentionally heating them. The deposited sheets had a thickness of roughly 2 µm. The structure and morphology of NiTi films annealed at various temperatures were studied to understand better how annealing affects the films' physical properties. Energy-dispersive X-ray spectroscopy (EDS) and X-ray photoelectron spectroscopy (XPS) techniques were used to analyze the compositional examinations of new and annealed films. Choudhari et al. 2011 on the deposited NiTi thin films with DCMS technique at 550°C. They created an intelligent material by combining ferroelectric lead zirconate titanate (PZT) with ferroelectric lead zirconate titanate (PZT). The top NiTi films exhibited austenitic B2 structure with a preferred (110) orientation. The thickness of NiTi layers significantly influenced the NiTi/PZT/TiO_x heterostructure characteristics. These heterostructures had a layer of SMA material coupled to a ferroelectric material with a TiO_x layer underneath, and they are crucial for MEMS devices. Martins et al. 2009 reported on the preparation of NiTi thin films by DCMS deposition. The targets used were NiTi and Ti, and the substrates were Si (100) and Si (100)/SiO₂. The depositions were made at 450°C. The buffer layer of TiN was coated

with Ar:N₂ gas mixture from the Ti target. The RBS technique carried out the compositional studies of NiTi film. XRD studies of NiTi films deposited on Si (100) and Si (100)/SiO₂ were also reported.

1. 8. 5. RFMS deposition of NiTi shape memory alloy thin films

Ainslie et al. 2019 reported RF magnetron co-sputtered Ti-rich NiTi films onto (100) silicon wafers coated with a 5 nm thick Ru seed layer. Lower deposition temperatures (325°C) and sub-micron thin films (120 nm) with the necessary SME can be achieved using Ru as a seed layer. Yongqing et al. 2001 reported on the preparation of NiTi thin films by RF magnetron sputter deposition. The target was NiTi alloy disc, and the substrate was Si (100). The substrate was not heated during deposition, but post-deposition annealing was conducted at 650°C for 60 min. The composition of the films was studied using EDX, and the crystal orientation and phase change studies were carried out at lower and elevated temperatures. Microstructures like cantilevers and grippers were fabricated, and they tested the actuation at various temperatures. Ohta et al. 2000 reported a novel fabrication technique of NiTi SMA thin films by co-sputter deposition from individual Ni and Ti targets. The power applied at the target was RF. The substrates were Si (100) and Si (100)/SiO₂. The substrate temperature was not controlled and rose from RT to 107°C. A Dektak profiler was used to measure the thicknesses of the films. Electron probe microanalysis (EPMA) performed the compositional studies of NiTi thin films. DSC and XRD measurements were conducted for the phase transformation studies. The adhesion of NiTi thin films on Si (100), Si (100)/SiO₂, and photoresist was studied.

1. 8. 6. Co-Sputter deposition (DCMS and RFMS) of NiTi shape memory alloy thin films

Some groups have employed the magnetron co-sputtering method to deposit NiTi SMA films using the combination of DCMS and RFMS or both DCMS (RFMS has been used to sputter titanium).

Geetha et al. 2016 reported on the preparation of NiTi thin films by magnetron co-sputter deposition from Ni and Ti targets using DC and RF power, respectively. The substrates used were silicon (100) and quartz. The substrate was not heated during

deposition, but post-deposition annealing was conducted at 600°C before breaking the vacuum. The composition of the films was studied using EDX, and the crystal orientation and phase change studies were carried out using GIXRD. Surface topography studies were conducted using AFM. High-resolution TEM studies of the NiTi films were also carried out and reported. Tillmann et al. 2015 investigated the comparison of NiTi thin films sputtered from separate elemental targets and Ti-rich alloy targets. Employing Ti-rich alloy targets leads to faster formation of crystallized NiTi coatings. More homogeneity in the microstructure of NiTi coatings sputtered from alloy targets.

Behera et al. 2015 reported on the fabrication processes and the novel characterization techniques of the as-deposited and the annealed thin films. Deposition of single-bi-layer Ni-Ti thin film on Si(100) substrate has been done using DC and RF magnetron sputtering technique. The as-deposited thin films are amorphous and annealed at different temperatures (300, 400, 500, and 600°C) to induce the crystalline structure. Koker et al. 2013 reported on the preparation of NiTi thin films by magnetron co-sputter deposition from Ni and Ti targets. The substrate used was Silicon (100). The deposited films at room temperature were amorphous, and the specimen was heated for 30 min. at 650°C in a vacuum. The thicknesses of the films were measured using the Dektak surface profiler. The compositional studies were done by EDX. DSC and XRD techniques were used to conduct the phase transformation studies. SEM was used to study the surface morphology of the films.

Kumar et al. 2012 reported that the NiTi shape memory alloy thin films of different thicknesses have been grown on silicon (100) substrates using dc magnetron co-sputtering. Differences in microstructure such as crystallinity, grain size, grain size distribution, and surface roughness of these films were studied using an X-ray diffractometer (XRD) and atomic force microscope (AFM). The influence of film thickness on phase transformation behavior was studied using four-probe resistivity methods. Xu et al. 2011 reported on the preparation of amorphous NiTi thin films on Si₃N₄ by magnetron co-sputter technique from the combination of NiTi and Ti targets. During the deposition, the substrate was rotated to form uniform films of NiTi in composition. The specimen was annealed at 440°C for 30 min. in a vacuum post-

deposition. XRD was carried out to study the phase transformation studies. Mechanical properties like Young's modulus and hardness of the prepared NiTi films were measured at RT and 110°C. It was also reported that the phase transformation had a significant role in the mechanical properties of NiTi thin films. Geetha et al. 2010 reported on the preparation of NiTi thin films by magnetron co-sputter deposition from Ni and Ti targets using DC and RF power, respectively. The substrate used was silicon (100). The depositions were done at room temperature at 300°C. The composition of the films was studied using EDX, and the structure and phase change studies were carried out using GIXRD. Surface topography studies were performed using AFM. The hardness of the NiTi films was tested using a microhardness tester.

From the above literature, we can conclude that sputter deposition has been regarded as the most suitable technique for NiTi thin film processing, which helps to fabricate NiTi SMA devices for MEMS applications. Control over composition, faster growth rate, etc., are the advantages of magnetron sputter deposition. Most of the literature confirms that the DCMS technique has been widely used to process NiTi films. Of the two elements, titanium exhibits a very strong affinity toward oxygen. Since the DCMS process is continuous, the surface oxidation on the target is a major concern. The oxygen content in the NiTi thin film affects its shape memory property. This can be countered using RFMS, where the target polarity changes in regular intervals. But, as per the literature, compared to the DCMS technique, the RFMS is less explored. This might be due to the lower sputtering rate with RFMS than DCMS. One other reason might be that it is more expensive than the DCMS. The NiTi thin films need to meet certain thickness requirements to exhibit the shape memory effect. In some literature, the co-sputter deposition of NiTi films is wisely addressed with RF power sputter for titanium target. But employing a co-sputter deposition setup will double the cost as two magnetrons and power supplies are needed.

1. 8. 7. Advantages of PDCMS deposition technique

Another deposition method in the magnetron sputtering family, the PDCMS deposition technique, has not been explored for the deposition of NiTi thin films. However, it has several advantages compared to DCMS and RFMS. Compared to RFMS, PDCMS can achieve higher deposition rates using appropriate pulse

frequencies and duty cycles while avoiding arcing difficulties that degrade film quality. In addition, using pulsing frequency and switching dynamics (on-off times), the oxygen content in the plasma can be minimized, and films with a dense and void-free nature can be achieved. Bradley et al. 2002 suggest that the higher power pulsed DC plasma fluxes impart on the substrate can explain the reason behind dense, well-structured dielectric and metallic coatings.

In sputter deposition, when dealing with metals (e.g., titanium) that exhibit strong oxygen affinity, the charged layer formation on the target surface plays a significant role in deciding the deposition rate. The charged layer also results in arcing during the process and affects the film properties. The main advantage of the PDCMS technique over conventional DCMS is that it dramatically reduces or eliminates the formation of arcs by decreasing the chance of charged layer formation on the target surface (Kelly et al. 1995, Kelly et al. 2007, Kelly et al. 2009, Belkind et al. 2005). Lin et al. 2009 reported on the advantages of PDCMS over DCMS with CrN as a case study. PDCMS provides denser and ionized plasma, boosts adatom mobility and nucleation sites, and plugs void columnar grain borders by increasing ion bombardment. Pulsed CrN thin film coatings have a denser structure and finer grain size than DC coatings. The hardness and wear resistance of pulsed CrN coatings improved due to the enhanced microstructure. This thesis presents a comparative study of the NiTi thin film properties synthesized with PDCMS and DCMS deposition processes under the same processing conditions. Later, the studies on NiTi thin film properties with various process parameters such as deposition pressure and pulse frequencies were addressed.

1. 8. 8. Patterning of NiTi thin films

Lithography is the most common technique that has been used for the fabrication of NiTi SMA devices. However, it is an expensive and time-consuming process since many stages are involved in patterning NiTi thin films. Since NiTi needs high-temperature processing, the use of lithography procedures is limited. Laser cutting of NiTi is an alternative method for making NiTi SMA devices. Ultrafast Ytterbium and Nd:YAG lasers were used to fabricate the miniaturized NiTi structures (Mary et al. 2014, Haferkamp et al. 2001). These laser wavelengths were in the range of VL to IR

with various pulse energies, pulse repetition, and pulse durations for minimizing the heat-affected zones to avoid any degradation in the mechanical properties. Laser cutting of NiTi SMAs has been explored for biological applications like making cardiovascular stents and realizing smart sensing and actuating devices (Muhammad et al. 2017, Giorleo et al. 2016, Rohde et al. 1997). The emergence of advanced laser micromachining tools such as excimer and femtosecond lasers made the fabrication of NiTi SMA Devices much easier (Villiermaux et al. 1997, Hung et al. 2015, Kong et al. 2014). This study is focused on using femtosecond laser and Ytterbium fiber laser micromachining techniques to fabricate NiTi-based devices.

1. 9. Importance of capping layer with NiTi thin films

Of the two elements, Ti shows a high affinity towards oxygen, which concerns the stability of the NiTi-based MEMS devices. There is a good scope for surface engineering studies with NiTi thin films. The purpose of these surface engineering studies had their focused objectives. Tantalum and tantalum pentoxide surface coatings were used for reducing the nickel ion release from NiTi SMA thin films while used for biomedical applications (Li et al. 2010). Another study reveals that a thin layer of TiN over NiTi surgical tools enhances the biocompatibility of the same (Jin et al. 2013, Starosvetsky et al. 2001). The TiN layer with preferred orientations improves the mechanical properties of TiN MEMS devices (Kumar et al. 2009). In recent years, the TiN micro-heaters have been used in CMOS industries because of their remarkable properties over conventional gold or platinum-based micro-heaters (Creemer et al. 2008). As the NiTi system falls under thermal SMAs, the heating capability of TiN can be utilized for realizing the actuation of NiTi MEMS structures. In addition, since both NiTi and TiN are biocompatible materials, the devices fabricated combining these two can also be used for biological applications. Hence, the use of TiN enhances the mechanical properties of NiTi SMAs and offers an option as a heating element that can be utilized for realizing phase transformations (actuation).

1. 10. Titanium nitride thin films

Because of its exceptional qualities, titanium nitride is frequently utilized as a coating material. These features lend themselves to a wide range of beneficial applications.

These applications range from the diffusion barrier layer in microelectronics to the hard and protective coatings on mechanical tools. TiN exhibits infrared (IR) reflectivity qualities, reflecting in a spectrum comparable to elemental gold (Au), giving it a yellowish color. Because of this, it is widely used as a material for decorative coatings. It is an essential component of high-speed steel cutting tools due to its high hardness and corrosion resistance (Buhl et al. 1981). TiN has a significant role in the semiconductor industry because of its high conductivity and diffusion barrier properties (Wittmer et al. 1981). A thin layer of TiN is used as a protective layer in wavelength selective transparent optical thin film filters. Moreover, the better biocompatibility of TiN makes it a dominant coating material over the surfaces of medical devices such as micro-needles, etc. TiN layer improves NiTi-based micro-devices corrosion behavior used in the medical industry (Starosvetsky et al. 2001).

TiN is widely used as a coating material because of its remarkable properties. TiN, without any oxygen traces in it, exhibits golden color, and thus, it is used in decorative coatings (Roquiny et al. 1999). Based on its microstructural properties, it has a wide range of applications as a coating material with high hardness, corrosion resistance, and high conductivity (Peng et al. 2003, Patsalas et al. 2018). Its high chemical resistance and melting point make it a strong candidate in various cutting-edge research. It has been used as a suitable material in plasmonic and barrier layer applications (Patsalas et al. 2015, Faltermeier et al. 1997). Stoichiometric TiN has a rock-salt structure with a lattice parameter of 4.24 Å. These properties are satisfied if the TiN is synthesized with minimum oxygen and moisture contents. Since titanium exhibits a very affinity toward oxygen, a proper ambient process needs to be chosen to synthesize TiN (Jeyachandran et al. 2007, Ponon et al. 2015).

1. 10. 1. Titanium nitride in MEMS

The ability to control the electrical properties of TiN thin films by adjusting their micro-structural properties helps in various CMOS processes (Briggs et al. 2016). Its moderate heat (15 Wm⁻¹ K for bulk) and high electrical conductivity provide a strong window for using it in the microelectronics industry. TiN has the potential to withstand high temperatures because of its high melting point (2950⁰C). In addition, the TiN MEMS hotplates can reach higher temperatures quickly. Thus, TiN MEMS

hotplates outperform conventional Platinum heaters in MEMS structures (Creemer et al. 2008). These properties of TiN make it a potential applicant in MEMS and microelectronic industries. TiN acts as a barrier layer in miniaturized solar cell systems. TiN plays a barrier between the steel substrate and solar cells by stopping the iron diffusion (Seefeld et al. 1980).

1. 11. Literature review on TiN thin films

1. 11. 1. Processing of TiN thin films

TiN has been used as a protective, decorative, diffusion barrier layer coating for many years. Since it has a very high melting point and can have low electrical resistivity, TiN is also used in the microelectronics industry. Recently, the TiN films were used as heating elements for localized heating in MEMS applications. The tuning of electrical resistivity of TiN thin films is possible by playing with its microstructure orientations. Thus, a precise process needs to be optimized to grow the TiN thin films with preferred microstructures. In the synthesis of Titanium nitride films, though there are huge applications, there are also several difficulties with the coating of TiN thin films. To produce a TiN thin film with finer properties, suitable preparation methods and process parameters must be identified (Oettel et al. 1995). Conventional Chemical Vapor Deposition (CVD) has limitations in producing thin films as it needs a higher temperature ($\approx 800^{\circ}\text{C}$), uses toxic precursors (TiCl_4), and has poisonous exhausts (HCl , Cl). Among the other options, vacuum deposition by reactive evaporation can produce TiN films with poorer adhesion and limited optical, electrical, and mechanical properties.

Nonetheless, being a slower process than all the above-mentioned techniques, reactive magnetron sputter deposition has been successfully used to synthesize TiN thin films. The typical TiN formation features a NaCl-type crystal structure with a stoichiometry of around 1:1. The deposition factors, such as sputtering power density, nitrogen partial pressure, and deposition time, influence the crystallization behavior and chemical composition and microstructure of TiN films (Fang et al. 2001).

Many investigations have been made to understand the electrical, mechanical, optical, and surface properties of TiN thin films by tuning their microstructure by controlling

the energy of the sputtered species. The electrical resistivity of TiN films is very much dependent on their microstructures. Hence careful optimization of the deposition parameters has to be made to achieve TiN thin films with preferred electrical properties. The following literature survey consolidates earlier research on magnetron sputter deposited TiN thin films.

1. 11. 1. 1. DCMS Processing of TiN thin films

Some studies reveal that the DCMS technique from titanium target in reactive nitrogen gas with various flow rates results in stoichiometric TiN films. Variations in nitrogen partial pressure and their impact on stoichiometry, orientation, and morphology have been reported, with nitrogen-rich films exhibiting increased resistivity due to defects. It was also observed that minor traces of oxygen do not affect the film's resistivity (Lu et al. 2018, How et al. 2017, Ponon et al. 2015, Kim et al. 2012, Irudayaraj et al. 2008).

Some research groups have reported the impact of substrate temperature and post-deposition annealing on the structural, electrical, and mechanical properties of reactive DCMS deposited TiN thin films. The substrate temperature treatment has undoubtedly improved the properties of TiN thin films. Thermal treatment increased the sheet resistance of the TiN films. The oxidation during the annealing process has been suggested as a probable cause. But the devices made of these films were thermally stable at a higher temperature allowing them for use in high-temperature processes (Smith et al. 2018, Kearney et al. 2018, Ao et al., 2013).

Some literature reported on the synthesis of reactive DCMS deposition of TiN thin films under different argon flow rates keeping nitrogen flow rate constant. It was found that the mechanical and electrical properties improved with the increase in the argon flow rate (Khojier et al. 2013, Arshi et al. 2012).

Vipin et al. 2009 reported on the preparation of TiN thin films by reactive DCMS deposition on glass with various thicknesses. With increasing thickness, the microstructural orientations indicated the (200) preferred orientation up to 1.26 μm thickness, then changed into (220) and (200) peaks as thickness increased up to 2.83 μm . The hardness and roughness of TiN thin films as a function of thickness have

been reported. According to AFM images, the surface roughness of TiN films has grown slightly with film thickness. Creemer et al. 2008 reported on the preparation of TiN thin films by DCMS deposition on a thin titanium layer having better adhesion with Si₃N₄. The target used was titanium, and the gases were a mixture of argon and nitrogen. The TiN micro-heaters were patterned and compared their performance with conventional platinum heaters. The heat measurement studies have shown that TiN-based micro-heaters could outperform the platinum-based micro-heaters.

1. 11. 1. 2. RFMS Processing of TiN thin films

Cheng et al. 2013 reported on the thermal stability of Ti/TiN thin film stacks synthesized by reactive RFMS deposition. The Ti/TiN thin film resistor stacks were fabricated and subjected to their thermal stability tests. These stacks exhibited excellent thermal stability till 350°C. Takeo et al. 2008 reported on the preparation of TiN thin films by RFMS on a silicon substrate. The target used was titanium, and the gases were a mixture of argon and nitrogen. The effect of high vacuum range on the quality of deposited TiN films was investigated. To obtain high-quality TiN films, the process chamber should be free from oxygen content. Vasu et al. 2011 reported the effect of substrate temperature on the structure and composition variation of RFMS TiN thin films. It was observed that the composition of TiN_x films had changed to Ti₂N, and the crystal structure changed from tetragonal to cubic on increasing the substrate temperatures.

1. 11. 1. 3. PDCMS Processing of TiN thin films

Boonyawan et al. 2016 explored the bioactive TiN-HA thin films made by a reactive DC magnetron sputtering system with a co-axis target configuration on the polyetheretherketone (PEEK) bio-inert material. Optical emission spectroscopy was utilized to determine the optimal plasma conditions for depositing the TiN-HA layer on PEEK (OES). The correlation between plasma chemical composition, sputtering pressure, discharge voltage, duty cycle, and nitrogen gas content was studied. Qu et al. 2015 reported on the CrN/TiN superlattice coatings deposited using a combined DOMS (Deep oscillation magnetron sputtering) and pulsed dc magnetron sputtering (PDCMS) in a closed field unbalanced magnetron sputtering configuration. The Cr target was powered at 400 W by DOMS, and the Ti target was powered at 2000 W by

PDCMS. The negative substrate bias (V_s) ranged from 0 V to -100 V. As the V_s was increased, CrN/TiN superlattice coatings showed a single phase face-centered cubic structure with a strong (1 1 1) texture. The coatings exhibited a dense microstructure with well-defined interfaces between CrN and TiN layers. Chun et al. (2013) investigated the effect of pulse parameters on deposition rates, grain size, preferred orientation, resistivity, and hardness of TiN thin films using the PDCMS methodology. The duty cycle and pulse frequency were changed from 50 to 95% and 5 to 50 kHz. When the pulse frequency was raised, the deposition rate, grain size, and resistivity of pulsed dc sputtered films decreased, while the nano hardness of titanium nitride films increased. Asymmetric-bipolar pulsed dc sputtering can be used to create titanium nitride coatings with exceptional characteristics.

The influence of sputtering pressure on the characteristics of titanium nitride films produced by the PDCMS process was examined by Yeh et al. in 2008. When the sputtering pressure was reduced, the preferred orientation of titanium nitride films changed from (111) to (200). At the same time, film deposition rate and hardness increased, whereas titanium nitride film resistivities dropped. In comparison to films produced by DCMS processing, Kelly et al. 2007 observed that TiN coatings coated by PDCMS had much improved tribological properties, particularly a much lower coefficient of friction. In terms of tribological characteristics and tool life, the results showed that TiN coatings produced by pulsed processing consistently outperformed those produced by continuous processing. PDCMS (asymmetric bipolar, 20-kHz pulse frequency) and DCMS reactive sputtering were used to deposit titanium dioxide and titanium nitride coatings, according to Kelly et al. 2003. Scanning electron microscopy, electron probe microanalysis, X-ray diffraction, micro-hardness testing, scratch adhesion testing, wear testing, and surface profilometry were among the analytical and measurement techniques used to characterize the coatings in terms of their structures and properties. Both coating types had better optical and tribological performances when PDCMS was employed instead of continuous DCMS processing.

From the above literature, we can conclude that most researchers used the reactive magnetron sputter deposition technique for synthesizing TiN thin films. Feasibility of the microstructure tuning with proper process optimization helps to obtain preferred

electrical resistivities in the reactive magnetron sputter deposition technique. In magnetron sputtering, the DCMS process has problems with arcing or oxygen presence in the target surface following target poisoning issues. The deposition rate falls when the RFMS is employed to overcome this difficulty and is also a costlier process. At the same time, the exercise of TiN thin film deposition with the PDCMS process solves issues like target poisoning, arcing, deposition rate, etc., and is more economical than the RFMS. Hence, PDCMS can be used to produce TiN with better qualities with faster deposition rates.

1. 11. 2. Patterning of TiN thin films

The TiN thin films on Si or Si/SiO₂ substrates can be easily patterned using focused ion beam and laser micromachining techniques. These are mask-free fabrication techniques, and thus, there is no need for lengthy lithographic procedures to fabricate submicron-level MEMS structures. The FIB technique uses the kinetic energy of the focused ions to impart the TiN surface, resulting in the film's removal as per the selection area (Gao et al. 2003, Zintler et al. 2017). The engraving technique can make laser remelted tracks on the film surface. For years, laser engraving techniques have been utilized to create diverse microstructures on film surfaces, with laser power and speed controlled precisely (Lima et al. 2005).

1. 12. Scope of the work

From the literature survey, it is indisputably clear that the NiTi and TiN thin films are potential candidates for micro-actuator applications. Other than the actuator and sensing applications, these two materials have a wide range of applications in the medical industry because of their excellent biocompatibility. However, achieving pure NiTi thin films with high crystallinity and required stoichiometry are the critical challenges to realizing high-performance MEMS devices. The required properties of NiTi thin films can be achieved by controlling the process parameters and growth kinetics. Hence, the deposition method plays a pivotal role in developing NiTi thin film-based MEMS devices. The NiTi thin films are synthesized mainly by DCMS and RFMS or co-sputtering in magnetron deposition techniques. However, the deposition rates in RFMS are lower as compared to DCMS. It is difficult to control the oxygen concentration and achieve uniform deposition rates in DCMS due to target poisoning.

The employment of the PDCMS deposition technique, which has denser plasma characteristics, can result in higher deposition rates that may solve the associated problems while using DCMS and RFMS. Also, many process parameters (pulse frequency, on-off time, duty cycle, etc.), including substrate temperature and pressure, are available to control the growth kinetics. The sputter deposition techniques with an option for pulsing can provide better plasma properties and enhance the properties of the thin films. No report is available in the literature on the deposition of NiTi thin films using PDCMS though it has multiple advantages as compared to DCMS and RFMS. Therefore, a detailed study of NiTi thin film processing with the PDCMS technique was essential to realize high-performance NiTi-based MEMS devices. A plasma diagnosis tool (optical emission spectroscopy – OES) was employed to study the effect of deposition techniques under the same process condition. OES provides information on the plasma properties to correlate with the film properties.

It is clear from the literature that the NiTi MEMS devices need external stimuli for performing the actuation. These external stimuli can be either mechanical or thermal. Focusing on the thermal actuation, the SMA devices need a heating element to provide the temperature for the actuation. As NiTi-based SMA devices are already employed for many biological applications, the heating element should also be biocompatible. TiN has been used with NiTi as a protective layer and is well known for enhancing the mechanical properties and biocompatibility. TiN is also used with NiTi-based surgical tools in biomedical applications. However, their heating capability with NiTi devices has not been reported. Therefore, a detailed study was undertaken on the synthesis of TiN films with preferred structural and electrical properties.

The heating capabilities of TiN-based micro-heaters can be utilized for the actuation in NiTi MEMS devices that are fabricated alongside. These types of MEMS device combinations are ideal for potential applications in various fields such as optical, microelectronics and biomedical, etc. Therefore, a study on the fabrication and integration of NiTi and TiN microstructures is considered very much useful in the rapidly advancing MEMS domain. With this background and motivation, the objectives of this thesis were finalized.

1. 13. Objectives of the work

1. Selection of a suitable sputter deposition method from among DCMS and PDCMS techniques based on plasma characteristics that helps to get high-quality crystalline NiTi thin films with the required properties for SMA applications.
2. Investigate the influence of PDCMS process parameters on the properties of NiTi thin films, which exhibit the shape memory effect.
3. To investigate the influence of PDCMS process parameters on TiN thin film properties, including the structural and electrical properties.
4. Fabrication and characterization of NiTi and TiN MEMS structures
5. Integration and testing of NiTi micro-cantilevers and TiN micro-heaters.

1. 14. Organization of the thesis

This thesis comprises seven chapters. A brief outline of each of these chapters is given below.

Chapter 1: This chapter starts with an introduction to shape memory alloys with a brief discussion on the working of SMAs. In addition, this chapter briefly discusses the importance of TiN thin films as MEMS hotplates with NiTi micro-devices. An overview of the literature survey on NiTi and TiN thin films is also given in this chapter. This chapter concludes with the scope and objective of the proposed research work.

Chapter 2: This chapter describes the detailed experimental setup and methods used to deposit NiTi and TiN thin films. Secondly, the characterization technique used to analyze the plasma, microstructure, surface topography, phase transformation, and electrical properties of the NiTi and TiN has been discussed. A brief discussion on the laser patterning and micro-fabrication techniques that were used for the fabrication NiTi and TiN micro-structures is presented in this chapter.

Chapter 3: This chapter starts with the details related to the conditioning of the process chamber, i.e., vacuum diagnosis using a residual gas analyzer, followed by the optimization of the deposition rate of NiTi. The main focus of this chapter is the study of DCMS and PDCMS NiTi plasma characteristics and thin film properties under the same processing conditions for the selection of a suitable process technique.

Chapter 4: This chapter focuses on the PDCMS NiTi plasma and thin film properties deposited under various deposition pressures and pulse frequencies. The objectives of these experiments are to grow the NiTi thin films that exhibit the martensite phase at room temperature.

Chapter 5: This chapter presents the studies related to the PDCMS deposition of TiN thin films. The TiN plasma characteristics and thin film properties are discussed in detail. Optimization of the preferred microstructure and electrical properties of TiN thin films are also discussed.

Chapter 6: This chapter discusses the fabrication and testing of TiN and NiTi microstructures. The TiN micro-heaters were tested for different dimensions to achieve better heating performances. The fabrication, integration, and testing of the TiN micro-heater with the NiTi micro-cantilevers were also presented.

Chapter 7: In this chapter, an overall summary of the results, which are described in the previous chapters, is presented. This chapter concludes with some future work propositions.

CHAPTER 2

EXPERIMENTAL DETAILS

2. 1. Introduction

This chapter gives the relevant details of the techniques that have been employed for the synthesis, characterization, and fabrication of the NiTi and TiN thin films. Various components of the sputter deposition system and their specifications have been presented. Substrate cleaning and deposition procedures etc. used in this thesis have been described. Critical issues involved in the deposition of multicomponent thin films by alloy targets have also been discussed. The employment of *in-situ* process monitoring tools, which ensure the production of films with repeatable properties, has been presented in detail. The characterization techniques adopted for studying the structural, surface, compositional, thickness, phase and electrical properties of the NiTi and TiN thin films are described. Finally, a brief discussion on the micromachining techniques that have been used for the fabrication of NiTi and TiN-based MEMS structures is also presented.

2. 2. Deposition techniques

Physical vapor deposition (PVD), which includes both evaporation and sputtering, as well as chemical vapor deposition (CVD), have been used to make thin films of amorphous alloys, semiconductors, oxides, and chalcogenide glasses (Ohring et al. 1992). This thesis mainly focus on the physical vapor deposition (PVD) process, especially sputtering, the most widely used method for depositing NiTi and TiN thin films. NiTi was synthesized by both DCMS and PDCMS techniques, whereas the PDCMS technique synthesized the TiN with nitrogen as the reactive gas.

2. 2. 1. Physical vapor deposition (PVD)

The physical vapor deposition process involves the following steps,

- ✓ Reliance on solid or molten sources
- ✓ Generation of atom/molecular species by which source atoms enter the gas phase

- ✓ Transportation of the gaseous species with the kinetic energy associated with the vapor
- ✓ Condensation of the same to a surface (substrate)

In this method, the material to be deposited is kept in a clean vacuum environment. The substrate is kept in the line of sight of the source to form a film (Ohring et al. 1992, Chapman et al. 1980).

2. 2. 2. Chemical vapor deposition (CVD)

The chemical vapor deposition technique is one of the most promising methods widely used in thin film industries. CVD is chemically reacting a volatile compound of a material to be deposited with other gases to produce a non-volatile solid that deposits atomistically on a suitably placed substrate. This method produces films and coatings of metals, semiconductors, and compounds in either crystalline or vitreous form with high perfection, purity, and required stoichiometry (Ohring et al. 1992).

2. 2. 3. Sputter deposition

Sputtering is the removal of atoms when ions collide on solid surfaces. It is a momentum transfer technique. The factors influencing the sputtering process are the type of ion (mass, charge), the nature of the surface atom involved, and most importantly, the ion energy. The higher the energy better the adhesion of the films on the substrates. The sputter deposition technique is a promising PVD technique widely used in synthesizing thin films with specific properties (Maissel et al. 1970, Ohring et al. 1992, Chopra et al. 1966). The sputter deposition technique makes the synthesis of alloys easier than the evaporation techniques due to the simplicity of control over the composition. The interaction of energetic ions and solid surfaces is summarized in Figure 2. 1.

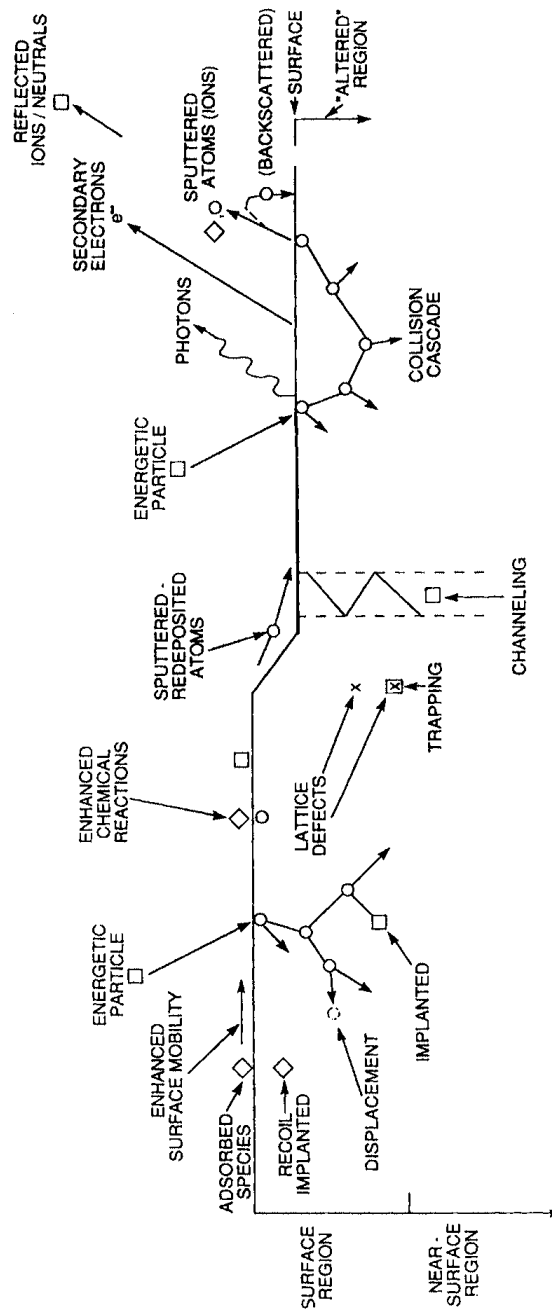


Figure 2.1: The effect of ion-solid interactions (Ohring et al. 1992)

2. 2. 4. Magnetron sputter deposition

Unlike the DC diode sputtering, a magnetron can be considered a ring magnet source; the width and diameter mainly depend on the pole strength and alignment of the permanent magnet in the target assembly (Rao, G. M., 1990). The width and diameter

of the erosion track determine the spatial distribution of the sputtered particles and thus play an essential role in deciding the thickness uniformity of deposition. In a 3” (7.62 cm) diameter target, the diameter of the ring source will be effectively 2” (5.08 cm). Therefore, the substrate uniformity that can be expected to be only 2”. In magnetron sputtering, a magnetic field is also applied in addition to the electric field. This causes the superimposition of magnetic and electric fields by which the electrons feel Lorentz force, which is given by Eq. 2.1,

$$F = m \frac{dv}{dt} = -q (\varepsilon + v \times B) \dots \dots \dots (\text{Eq. 2.1})$$

Where,

q - Electron charge

m - Mass of electron

v - Velocity of electron

If the velocity vector and the magnetic field are parallel, the term $v \times B$ becomes zero, and thus the electron does not experience any force known as Lorentz force. Suppose the electron is launched from the cathode at a velocity of v at an angle θ with respect to B ; in that case, it will experience a force $qvB\sin\theta$ in a direction perpendicular to the magnetic field B . It results in the motion of the electrons in a circular path, the radius of which is decided by the balance between the centrifugal force $m\frac{(v \sin\theta)^2}{r}$ and the Lorentz force. i.e., $r = \frac{mv\sin\theta}{qB}$.

The electrons in the magnetron do not reach the anode but will get trapped near the target, thereby enhancing the ionization efficiency in the near-target region. A magnetic field parallel accomplishes this to the target and perpendicular to the electric field. Magnetron gun produces a dense plasma in the vicinity of the target even at low pressures ($<1 \times 10^{-3}$ mbar). Other than the magnetron source, two parameters that control deposition uniformity are the pressure and substrate-to-target distance (STD). It has been understood that, in magnetron sputtering, the thickness uniformity is less if substrates are kept near the target. It improves with an increase in STD as described by the cosine distribution of the sputtered particles. The pressure plays a vital role in the deposition process as it decides the degree of scattering of the sputtered species

before they reach the substrate (Maissel et al. 1970, Ohring et al. 1992). The magnets arranged in a magnetron sputter source are shown in Figure 2. 2.

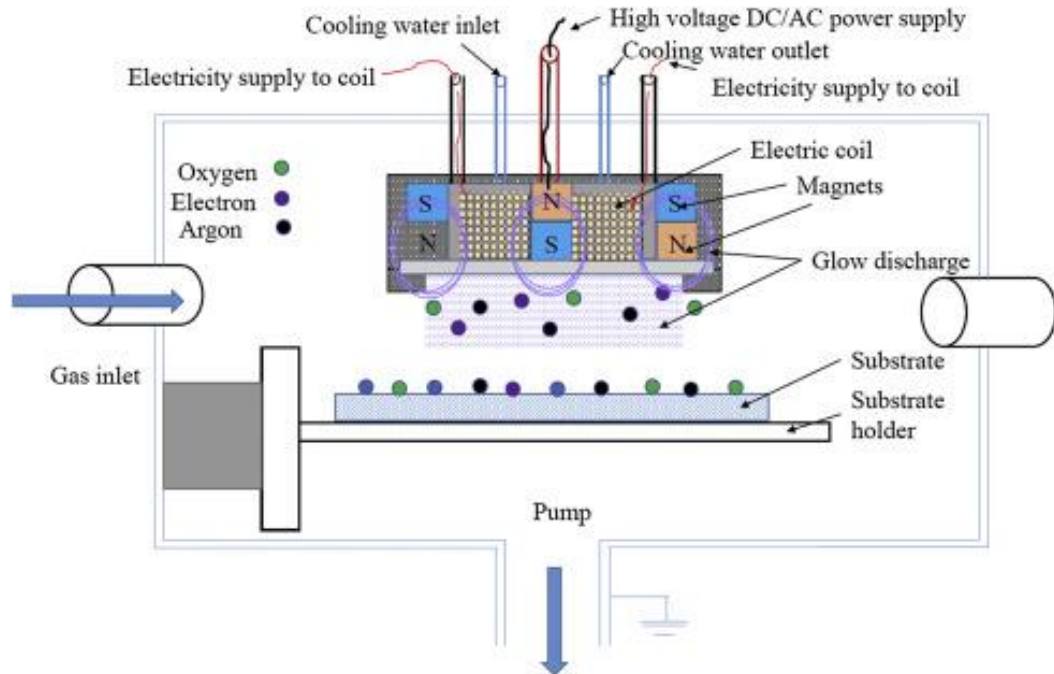


Figure 2.2: Schematic of a magnetron housed in the sputter deposition chamber

2. 2. 4. 1. DC magnetron sputter deposition (DCMS)

In DCMS, the cathode is connected to a DC power supply which acts as the source for the sputtering process. As the DC process is less suitable for dielectrics, its applications are limited to metals and alloys (Ohring et al. 1992). A typical schematic of the DCMS setup is shown in Figure 2. 14. At the same time, working with materials that exhibit a strong affinity towards oxygen, such as titanium, the positively charged layer formation on the surface of the target (which is at a negative potential) causes a decrease in the deposition rate as the tendency of the positive ion to move to the target decreases.

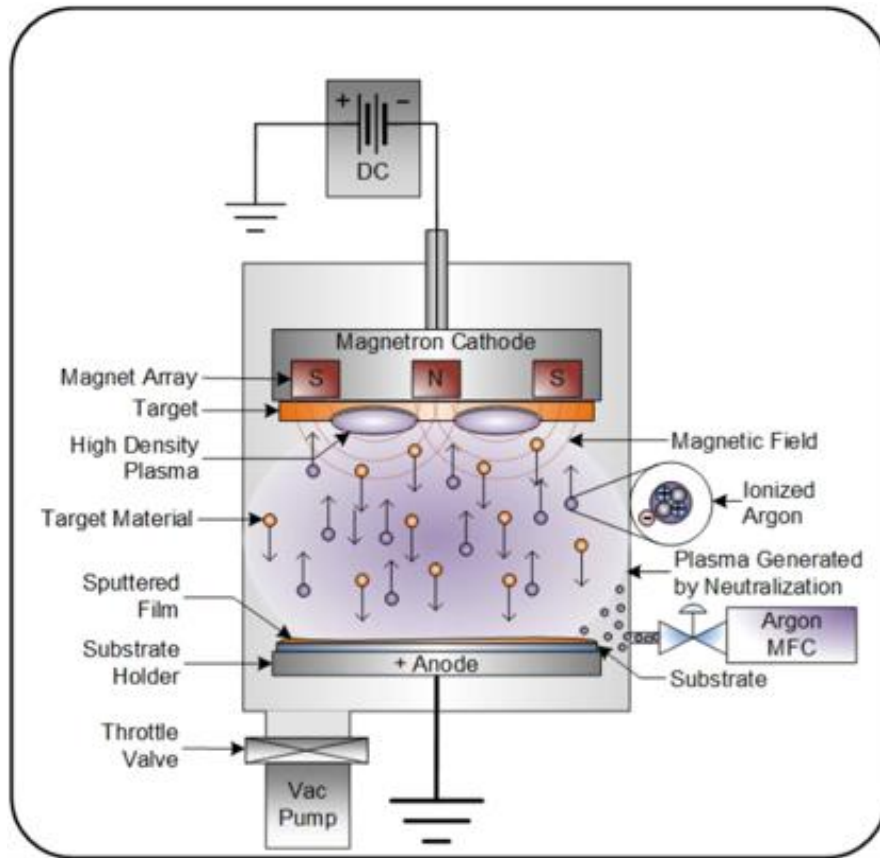


Figure 2.3: DCMS deposition setup (schematic)

2. 2. 4. 2. Pulsed DC magnetron sputter deposition (PDCMS)

To counter the positive charge build-up on the target surface and improve the plasma characteristics, the PDCMS deposition technique has been employed. In PDCMS, the power is applied to the target material for τ_{on} (on-time). The negative voltage is applied to the target material by several hundred volts. At the end of on-time, the voltage switches to positive polarity with less amplitude (about 20 volts). The applied voltage remains at this voltage for τ_{off} (off-time). This is also called “reverse time” (τ_{rev}) because of the polarity inversion of the applied voltage in the “off-time” interval. The charged layer formed at the target surface during the on-time discharges at off-time. Usually, the “off-time” interval is 1/10 of the “on-time” interval. The time it takes for plasma to form and stabilize depends on various factors, including pulse duration, pulse frequency, power, and pressure. A typical schematic of the DCMS setup and the waveform is shown in Figure 2. 4.

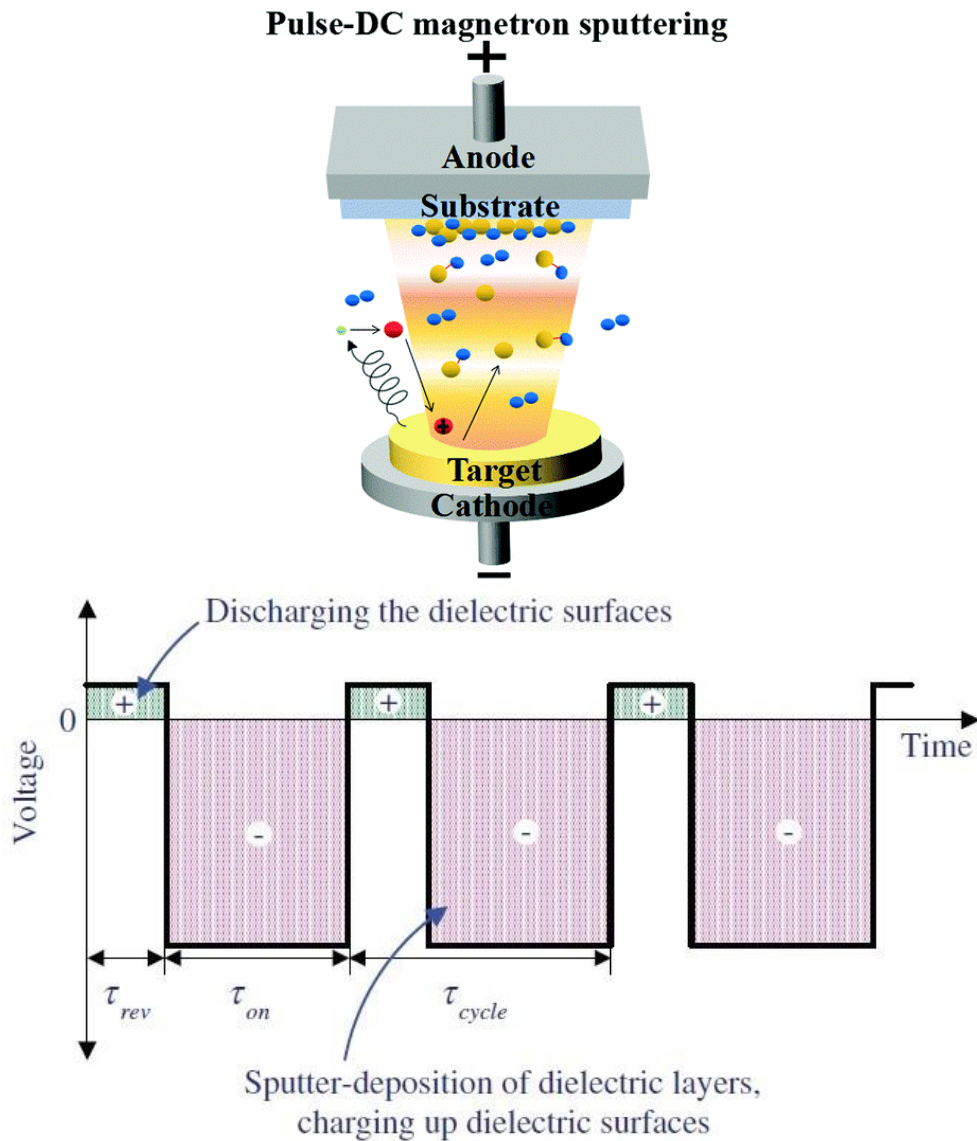


Figure 2.4: PDCMS deposition setup (schematic and waveform)

The pulse parameters can be calculated from the following Eq. 2.2,

$$\eta = f \times T_{on} = 1 - f \times T_{off} \dots \dots \dots \text{(Eq. 2.2)}$$

(Where, η – duty cycle, f – pulse frequency, T_{on} – on-time, T_{off} – off-time)

2. 2. 5. Sputtering yield

The number of atoms ejected from the target surface per each energetic ion, called sputtering yield, is a measure of the efficiency of the sputtering and determines the resultant composition and deposition rate of the process (Ohring et al. 1992). Sputtering yield, S , is calculated for planar targets as shown in Eq. 2.3,

$$S = \frac{3\alpha\lambda E}{4\pi^2 U_0} \dots\dots\dots (Eq. 2.3)$$

Where,

α - Function of (M_2/M_1) , a ratio of masses of the colliding atoms

E – Kinetic energy transferred to the atom

U_0 - Surface barrier energy which can be taken as the heat of sublimation

$$\lambda = \frac{4M_1M_2}{(M_1+M_2)^2}$$

2. 2. 6. Sputter deposition from alloy targets

Often multi-component thin films are required in the thin film industry, and these can be alloys, compounds, or a mixture of both. Sputtering is a suitable process to deposit alloy films because it can provide reasonable composition control compared to the evaporation technique. These thin films can be obtained by sputtering from a single target or several targets simultaneously or by reactive sputtering or a combination these techniques. The sputtered films carry an almost similar composition to the target used. This is the primary reason for using the sputtering process to deposition the alloy films. However, each component has its sputtering yields (Ohring et al. 1992). The composition of the sputtered atoms in multi-component deposition varies as the sputtering yields and the atomic masses of each element are different. In addition, with time, the target compositions also get altered due to the sputter source effect and gas-phase effect during sputtering. This can be quantitatively explained as follows.

Consider a binary alloy target surface containing a number of A atoms (n_A) and B atoms (n_B), such that the total number is $n = n_A + n_B$. The target concentrations are $C_A = n_A / n$ and $C_B = n_B / n$, with sputter yields S_A and S_B . Initially, the ratio of the sputtered atom fluxes (ψ) is given by Eq. 2.4,

$$\frac{\Psi_A}{\Psi_B} = \frac{S_A C_A}{S_B C_B} \dots\dots\dots (Eq. 2.4)$$

If n_g is the sputter gas atoms impinge on the target, the total number of A and B atoms ejected are $n_g C_A S_A$ and $n_g C_B S_B$, respectively. Then, the target surface concentration ratio can be modified as shown in Eq. 2.5,

$$\frac{C'_A}{C'_B} = \frac{C_A (1 - n_g S_A / n)}{C_B (1 - n_g S_B / n)} \dots\dots\dots(\text{Eq. 2.5})$$

Instead of C_A/C_B , if $S_A > S_B$, the surface is enriched with B atoms, which now begin to sputter in greater profusion; i.e.,

$$\frac{\Psi'_A}{\Psi'_B} = \frac{S_A C'_A}{S_B C'_B} = \frac{S_A C_A (1 - n_g S_A / n)}{S_B C_B (1 - n_g S_B / n)} \dots\dots\dots(\text{Eq. 2.6})$$

The regular change in the target surface composition alters the sputtered flux ratio where it is equal to C_A/C_B , which is the same as the original target composition. Simultaneously, the target surface reaches the value $C'_A/C'_B = C_A S_B / C_B S_A$, which is maintained thereafter. In the present case, the sputtering yield of Ni and Ti are 0.7 and 0.2 atoms/ions, respectively (with 200 eV Ar ions impinging normal to the surface (Maissel et al. 1970)).

Despite these constraints, the sputter deposition technique has been successfully employed for depositing multi-component thin films. The ability to control the process parameters, such as deposition pressure and pre-sputtering of the target, allows depositing the films of similar composition on the target. An alloy target has often been used to deposit multi-component thin films with required stoichiometry.

2. 2. 7. Composition of the films

The composition of the films formed will often be the same as that of the target, even if the components of the system differ considerably in their relative sputtering rates unless a significant amount of re-sputtering occurs. The following are the reasons for the deviation in the composition of the films from that of the target,

1. High target temperature
2. Oxidation effects of the component(s)
3. Re-sputtering from the targets

2. 2. 8. Reactive Pulsed DC magnetron sputter deposition

The reactive magnetron sputter deposition technique deals with synthesizing thin films of compounds by sputtering from metallic (not-nonmetallic) targets in a reactive

gas generally mixed with an inert working gas (often Ar). The most common compounds reactively sputtered and the reactive gases employed are briefly listed:

1. Oxides (oxygen) - Al_2O_3 , In_2O_3 , SnO_2 , SiO_2 , Ta_2O_5 , etc.
2. Nitrides (nitrogen, ammonia) - TaN, TiN, AlN, Si_3N_4 , CN_x , etc.
3. Carbides (methane, acetylene, propane) -- TiC, WC, SiC, etc.
4. Sulfides (H_2S) - CdS, CuS, ZnS, etc.
5. Oxycarbides and oxynitrides of Ti, Y, Al, Si, etc.

Depending on the power supply used to power the cathode, the reactive magnetron sputtering can be classified as reactive RF/DC/PulsedDC/Hi-PIMS deposition techniques. While dealing with reactive magnetron sputter depositions, the deposition rates of metals drop dramatically when compounds form on the target surfaces. The effect of deposition rate is very much dependent on reactive gas pressure. Sputtering effectively halts at high gas pressures in DC discharges, but the limits are also influenced by the applied power. Conditioning of the target in pure Ar is essential to restore the pure-metal surface and desired deposition rates (Ohring et al. 1992, Musil et al. 2005).

2. 3. Experimental Setup

Figure 2. 5. shows the schematic of the experimental setup used to deposit the NiTi and TiN thin films. The details of the vacuum deposition system components are discussed in the following sections.

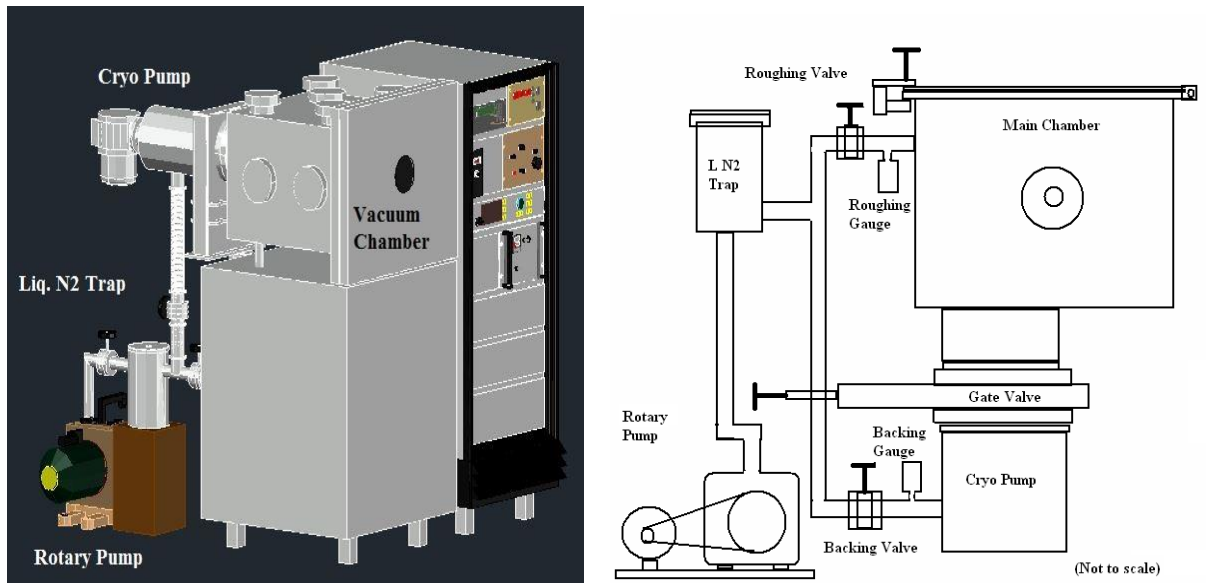


Figure 2.5: Schematic diagram of the vacuum deposition unit

2. 3. 1. Vacuum chamber

The vacuum chamber with dimensions of 60 mm × 50 mm × 45 mm (LBH) with a hinged door mechanism and a sufficient number of connection ports were designed to house the accessories like magnetron, substrate holder-cum-heater, shutter assembly with Wilson's seal, optical emission spectroscopy probe, residual gas analyzer, electrical feed-throughs, etc. The volume of the chamber is 135 liters without accessories. A viewport with tuffen glass was fixed on the chamber door for viewing the process inside the chamber *in-situ*.

2. 3. 2. Pumping system

The vacuum chamber was evacuated by combining the rotary (low vacuum) and cryopumps (high vacuum). An ISO-200 CF F (8") cryo pump (CryoTorr 8) supplied by the CTI Cryogenics Inc. was mounted on the rear side of the vacuum chamber. The cryopump was driven by a helium compressor (Helix), forming a closed-cycle refrigerator. The pump has a pumping speed of 1200 l/sec for argon, 2500 l/sec for hydrogen, 1500 l/sec for air, and 4000 l/sec for water vapor. The cryopump cannot be started directly from the atmospheric pressure. The roughing pressure required for cryo can take over pumping is 10^{-1} mbar or lower. This pressure was achieved by a rotary pump (Hind High Vacuum, Bangalore) having a pumping speed of 200 l/min.

The base pressure of 1.5×10^{-6} mbar is achieved routinely within 90 min. after exposing the chamber with the cryopump by opening the gate valve.

2. 3. 3. Vacuum gauges

The pressure (cryo roughing pressure) in the cryopump side is measured using a Leybold make Pirani gauge (Model: TTR-91), which can measure pressures at lower vacuum ranges ($1000 - 1 \times 10^{-3}$ mbar). The pressure inside the vacuum chamber was again measured by a Leybold make full range gauge (Pirani + Penning) (Model: PTR - 90), which can measure pressure over a range ($1000 - 1 \times 10^{-9}$ mbar). The gauge has a digital read-out with a two-channel display always indicating the readings from TTR-91 and PTR-90. A separate gauge, the capacitance gauge, which provides more accurate measurements of 10^{-3} and 10^{-4} mbar range pressures, was used to monitor the deposition pressure during the depositions.

2. 3. 4. Mass flow controller

The flow of the argon and nitrogen gases into the chamber was regulated using a flow control setup, called a mass flow controller (Eureka Hightech - Bronkhorst). The controller can control the flow rates in the range of 2 - 100 sccm for argon and 1 - 50 for nitrogen. The flow display was given by a digital read-out monitor (Eureka Hightech) and can also be interfaced with a PC. The pressure inside the chamber was controlled by adjusting the flow rate and throttling the gate valve to achieve the desired working pressures.

2. 3. 5. Substrate holder-cum-heater

The substrate on which the film needs to be coated is clamped to a substrate holder mechanism. A heating mechanism is housed in the substrate holder, allowing the films to be heated to a maximum temperature of 850°C . The temperature was measured using a K-type thermocouple, whose output was used to monitor and control the temperature using a PID (Proportional-Integral-Derivative) controller with a negative feedback loop. The substrate temperature could be maintained at the desired temperature with a maximum fluctuation of $\pm 1^{\circ}\text{C}$. Ramp rate control was another feature of the heater system, facilitating the heating and cooling rate control.

2. 3. 6. Magnetron sputter gun

Two 76 mm (3") dia. magnetron sources were used for sputtering the NiTi and Ti Target. The magnetron gun is housed in a cylindrical ring magnet, which provides the magnetic field for confining the plasma to the center. An external manually adjustable type substrate holder was used for shuttling between the two magnetrons. The magnetron and target were cooled by circulating chilled water through the axle to the backing plate on which the target material is pasted. The magnets and the sealing components like Teflon rings are cooled with chilled water. But there are no contacts between the target and backing plate and the magnetron body. The chilled water flow was maintained at a flow rate of 4 l/min. to provide sufficient cooling to the target and related accessories.

2. 3. 7. Power supplies

The target was powered by a 1 kW power supply (MDX 1K, Advanced Energy) for DCMS, and a 5 kW power supply (Pinnacle Plus, Advance Energy) for PDCMS. The MDX DC power supply can be operated in three modes of regulation: voltage mode, current mode, and power mode. The Pinnacle Plus pulsed DC power supply also can be performed in these modes. In addition, it has options to vary the pulse frequency, pulse reversal time, etc.

2. 3. 8. Residual gas analyzer

Stanford Research Systems residual gas analyzer model 200 (SRS RGA 200) is used for the partial pressure measurement of the gases (Figure 2.6.a.). This RGA is capable of measuring atomic mass units from 1 to 200. The RGA head is interfaced with an electronics control unit (ECU). The ECU is a complete box of electronics directly connected to the RGA head. The ECU is connected to a computer through RS 232 cable. In the case of magnetron sputtering, the chamber pressures during the deposition need to be maintained in the range of 10^{-2} to 10^{-3} mbar, because at lower pressures, the plasma cannot be sustained. But the RGAs can work in the pressures at 10^{-4} mbar or lower. Because the RGA filament, one of the important parts of the RGA setup, can work only at 10^{-4} mbar or lower vacuum levels. Therefore, a differentially pumped system is used to maintain the lower vacuum level in the RGA head region. In this case, the RGA head region was pumped using a turbomolecular pump and

rotary pump, as shown in Figure 2.6.b. It is essential to quantify the partial pressures of the contaminant gases and vapors *in-situ* before and during the depositions for producing thin films with reliable, reproducible, and stable characteristics. The RGAs work on the principle of mass spectrometry. The RGAs consist of the following parts, as shown in Figure 2. 7.



Figure 2.6: (a) SRS 200 RGA with differential pumping mechanism, (b) RGA integration with the process chamber

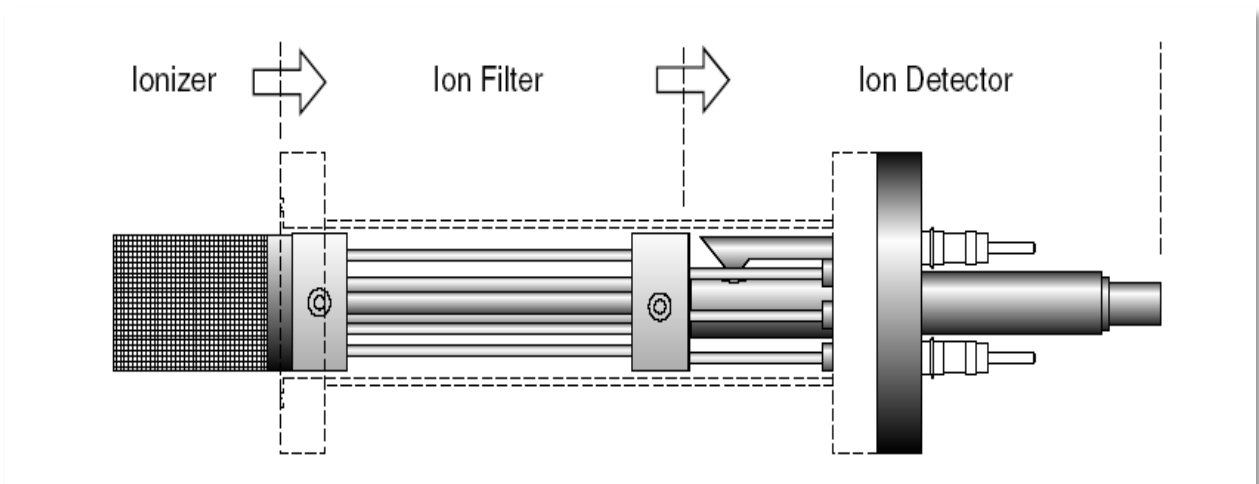


Figure 2.7: Schematic diagram of the mass spectrometer

The current measured represents the number of ions collected, and thus the pressure of the respective gas. The radius of curvature (**R**) in centimeters, magnetic field (**B**) in Gauss, atomic mass (ionized atom) (**M**)’ and acceleration voltage (**V**) is related by Eq. 2.7:

$$R = \frac{144}{B(MV)^{1/2}} \dots \dots \dots (Eq. 2.7)$$

The working principle of RGA is as follows:

1. **Ion generation:** A thermionic filament is used to generate electrons. When these electrons strike the gas molecules, the ions are produced.
2. **Ion separation** (mass filter/resonator): These ions are accelerated through the quadrupole rods and separated depending on the mass-to-charge ratio (M/e).
3. **Detector:** The ions that come out of the mass filter are collected by Faraday Cup. A sensitive ammeter measures the resulting current.
4. **Signal amplifier:** The current produced by ions by Faraday Cup is very small. The Faraday Cup output is connected to an extremely sensitive secondary electron multiplier (SEM).

2. 3. 9. Butterfly Valve: Two numbers of butterfly-type valves with KF-25 fittings at the ends were used as the isolation between the rotary pump with the chamber and cryopump during forevacuum creation.

2. 3. 10. Gate valve

A manually operated hand wheel type ISO-200 CF F gate valve (VAT –8”) was fixed between the vacuum chamber and the cryopump. The gate valve isolates the cryopump and the vacuum chamber during the cryo running-up. It also acts as the control valve for adjusting the pressure inside the vacuum chamber by throttling the pumping of the gas molecules.

2. 3. 11. Bellows

Bellows are flexible vacuum pipelines connecting the forevacuum pump (rotary pump) with the vacuum chamber and cryopump. Their flexible nature avoids the vibrations caused by rotary pumps to the chamber and high vacuum pumps.

2. 4. Deposition procedure

A detailed procedure followed for the deposition of NiTi SMA and TiN thin films is presented in this section.

2. 4. 1. Selection of substrate

It is important to consider the following criteria before selecting the substrates for the film deposition. These are:

- Surface finish
- Requirement of the characterization techniques

In this thesis, we have used two kinds of substrates: Si (100) and Si/SiO₂. The latter is used for the electrical characterization of the TiN thin films to precisely calculate the resistivities by eliminating the effects from Si substrates.

2. 4. 2. Substrate cleaning and loading

The surface of any substrate will have dust particles, organic contaminants, oxide layers, etc. These contaminants will influence the adhesion and purity of the coating. In addition, native oxide formed on the surface of the silicon substrates tends to native oxide layer formation, which can degrade the shape memory property of the NiTi thin films. Hence, following a standard procedure for cleaning the Si wafer before loading it into the process chamber is important. The procedure which we followed is as follows:

1. The 3” dia. silicon wafers were cut into pieces (10 mm × 10 mm) using a diamond tip cutter.
2. These silicon substrates were kept in de-ionized water for 10 min.
3. Then these silicon substrates were subjected to ultrasonic cleaning for about 8 – 10 min. in an acetone bath to remove the organic contaminants from the surface.
4. In the next step, after dipping in the de-ionized water, the silicon substrates were dipped in a diluted HF solution for about 1 min. to remove the oxide layer on the surface.
5. The cleaned silicon substrates were dipped in de-ionized water for about 2 seconds and dried using nitrogen gas purging.
6. The silicon substrates were immediately loaded onto the substrate holder inside the deposition chamber without exposing much to the atmosphere.

2. 4. 3. Chamber evacuation and vacuum diagnose

Before starting the cryopump, a forevacuum of $<2.5 \times 10^{-2}$ mbar was created using the rotary pump. A liquid nitrogen trap was used between the rotary pump and the

cryopump to ensure that vapors of the rotary oil were not contaminating the adsorbers inside the cryopump. There was no continuous backing requirement for the cryopump as in the diffusion and turbomolecular pumps. The cooldown of cryo arrays from 300 to 15 K takes approximately 2 – 3 hrs. During this time, the sample cleaning and loading procedures were done. The chamber pressure was brought to $<2.5 \times 10^{-2}$ mbar or below using the same rotary pump. Once the cryo cold head temperature reached 15 K, the gate valve was opened, and the cryopump was exposed to the chamber. The cryopump evacuates the process chamber to a base pressure of 1.5×10^{-6} mbar or below from this stage.

Using a residual gas analyzer, the vacuum diagnosis was carried out to study the presence and quantification of the partial pressures of the residual gases. A detailed study of the same is discussed in Chapter 3, Section 3.2.

2. 4. 4. Deposition and plasma diagnose

When the chamber was evacuated to the base pressure and the vacuum diagnosis was completed, high purity Ar (99.999%) gas was passed at a flow rate of 25 sccm using a mass flow controller. In the case of reactive sputtering, nitrogen gas was also passed into the deposition chamber using a separate mass flow controller. The sputter and reactive gas's pumping speed was controlled by throttling the manually operated gate valve fixed at the pump mouth to maintain the desired deposition pressures. Using DC (or pulsed DC) power supplies, the target was then powered. The target was pre-sputtered for about 15 - 20 min. keeping the shutter closed to remove the contaminations on its surface and reduce the oxygen gas traces present in the chamber by the Ti gettering. The pressure inside the chamber was maintained constant with minimal variation in the decimal points. Depositions were carried out at constant power (100W) both in DC and pulsed DC cases. The substrate temperatures were raised as per the process requirements. The deposition parameters were varied from cycle to cycle to optimize the films with the desired properties. The plasma diagnosis was carried out using an optical emission spectroscope to correlate the plasma properties with the film properties. A detailed study of the same is discussed in Chapter 3, Chapter 4, and Chapter 5 based on the variations in the process parameters.

2. 5. Characterization techniques

For developing an ideal thin film process, the films need to be characterized and evaluated for their repeatability, reliability, etc. In the case of thin films, the properties are determined by their processing conditions, microstructure, thickness, composition, surface topography, phase behavior, etc. It is important to correlate the processing conditions and film properties to obtain films with the desired characteristics. In this section, brief descriptions of the different characterization techniques that have been used are given. Table 2.1 shows different analytical techniques that were used for studying different film properties.

Table 2.1: Characterization techniques used for studying NiTi and TiN film properties

S. No.	Plasma/Film Property	Measurement Technique
1.	Plasma	Optical emission spectroscopy
2.	Thickness	Cross-sectional SEM
3.	Microstructure	X-ray Diffraction (XRD)
4.	Phase Transformation	High-temperature X-ray Diffraction (HT-XRD)
5.	Surface Morphology	Atomic Force Microscope (AFM) Scanning Electron Microscope (SEM)
6.	Composition	Energy-dispersive X-ray spectroscopy (EDS)
7.	Electrical	Four probe electrical resistivity measurement

2. 5. 1. Optical emission spectroscopy (OES) - *In-situ* plasma studies

Process control is essential in plasma applications to ensure the reliability and quality of the process. In the case of vacuum deposition by magnetron sputtering, the process needs to be real-time monitored to ensure the plasma conditions and to realize the changes instantaneously (Bendahan et al. 1996, Wu et al. 2000). Optical emission spectroscopy (OES) analyzes light emitted from a medium without external optical

excitation. Optical emission is significant in plasma-assisted processing, such as plasma-assisted etching and deposition and sputter deposition techniques, since collisions with energetic electrons push gas-phase species to excited electronic states. These excited states relax to lower levels by spontaneous emission, which may be the ground electronic states. This released radiation is then detected after being spectrally scattered. Plasma-induced emission is another name for optical emission from plasma (PIE). While optical emission occurs between vibration levels in the same electronic state, it is weaker and less attractive (Herman et al. 1996).

The emission process in OES is represented in Figure 2. 8. Because OES detects only excited species in plasmas, the observed spectrum gives information about the excited-state density and does not directly reflect the ground-state population profile. When such emission is present, OES is a powerful yet simple diagnostic tool useful for practical real-time monitoring. The absence of an external excitation source makes OES an inexpensive and robust candidate for real-time control, but it limits the versatility of this method. Nonetheless, OES is probably the most widely used optical probe of plasma-assisted processing (Herman et al. 1996).

The mechanism of the plasma excitation and optical emission spectroscopy can be explained as occurring with various excitation processes, such as,

- i) **Electron impact excitation - $A + e^- \rightarrow A^* + e^-$**
- ii) **Electron impact dissociation - $AB + e^- \rightarrow A^* + B + e^-$**
- iii) **Ion impact - $A^+ + e^- (M^+) \rightarrow A^* (+M)$**

Where A and B are atoms, radicals, or molecules, and AB is a molecule. The asterisk (*) indicates the excited species that emits light, and $e^- (+ M)$ may be either a neutral species, a negative ion or an electron plus a third body (M), or a surface (Phelps 1990).

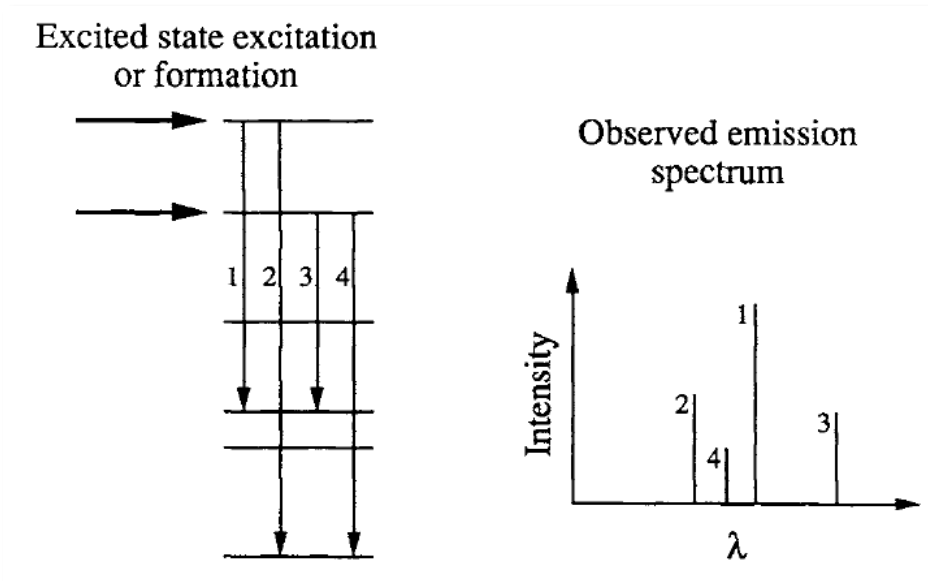


Figure 2.8: Energy levels involved in typical OES experiments

This work uses a Plasus Emicon system with the vacuum deposition system to record the *in-situ* plasma characteristics. The emission spectra between the wavelength (200–1100 nm) from a plasma source can be real-time monitored and recorded with this setup. The deployment of the OES sensor in the process chamber is shown in Figure 2. 9. The OES is connected to the PC using RS 232 interface. The optical fiber from the sensor is connected to the computer through a KF-25 port having vacuum-sealed connectors on both sides. The in-vacuum components include plasma characteristics acquiring optics and the related fiber cables. The ex-vacuum components, like the power connection and computer interface, were connected through the above-mentioned port. The analysis of the plasma characteristics can be carried out by loading the recorded spectra with the library data provided in the plasus software. The process optimization can be easily executed by real-time monitoring of the plasma process by taking advantage of the instant system response to parameter changes. In the present study, an investigation of OES of the nickel-titanium and titanium nitride sputter plasma radicals was performed to clarify the relationship between the plasma properties, sputtering conditions, and properties of the thin films. The broad spectra obtained from the nickel-titanium and titanium nitride plasmas are shown in Figure 2. 10. (a.& b).



Figure 2.9: Optical emission spectrometer and its incorporation with the process chamber between the magnetron gun and the substrate holder

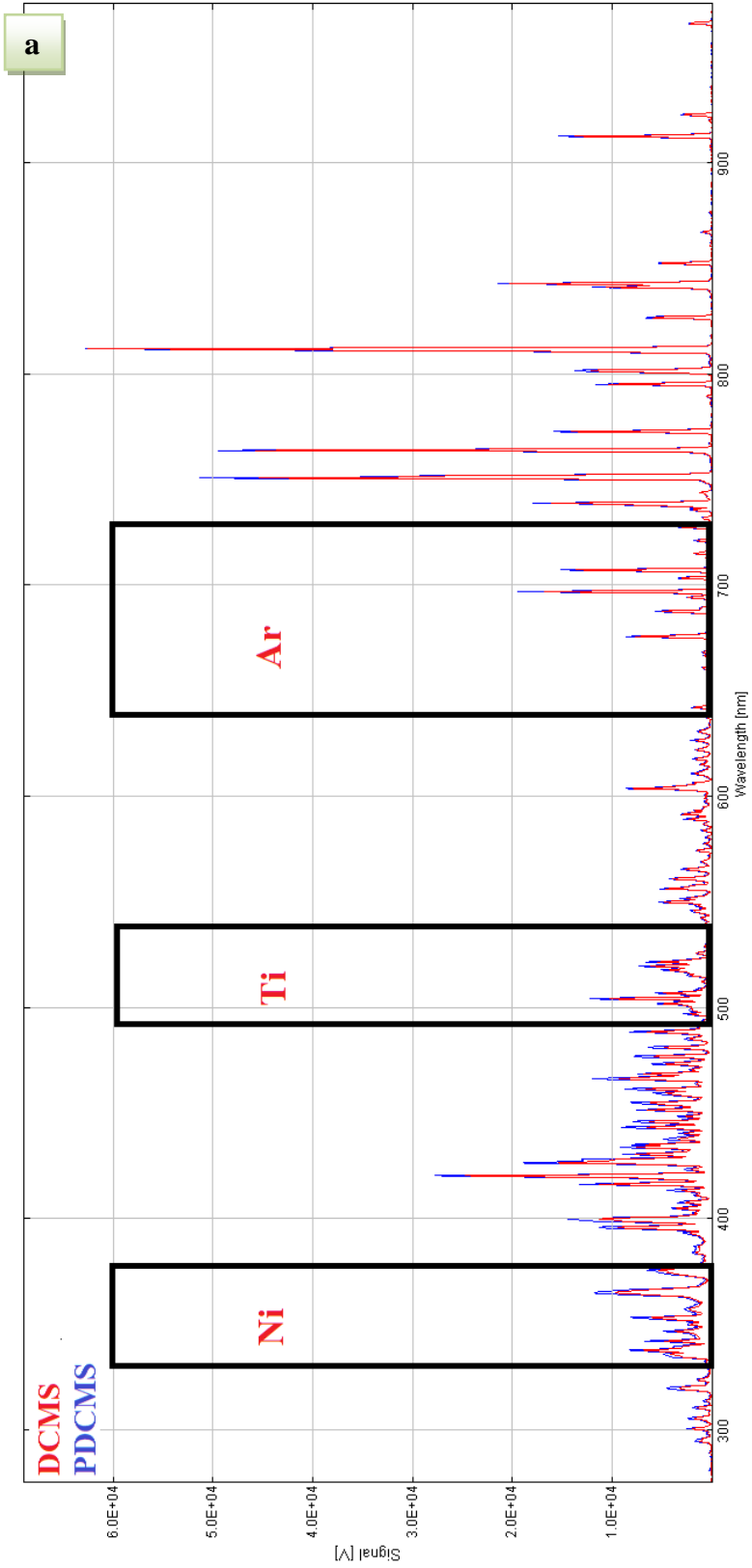


Figure 2.10 (a): Optical emission spectra of DCMS and PDCMS NiTi plasmas

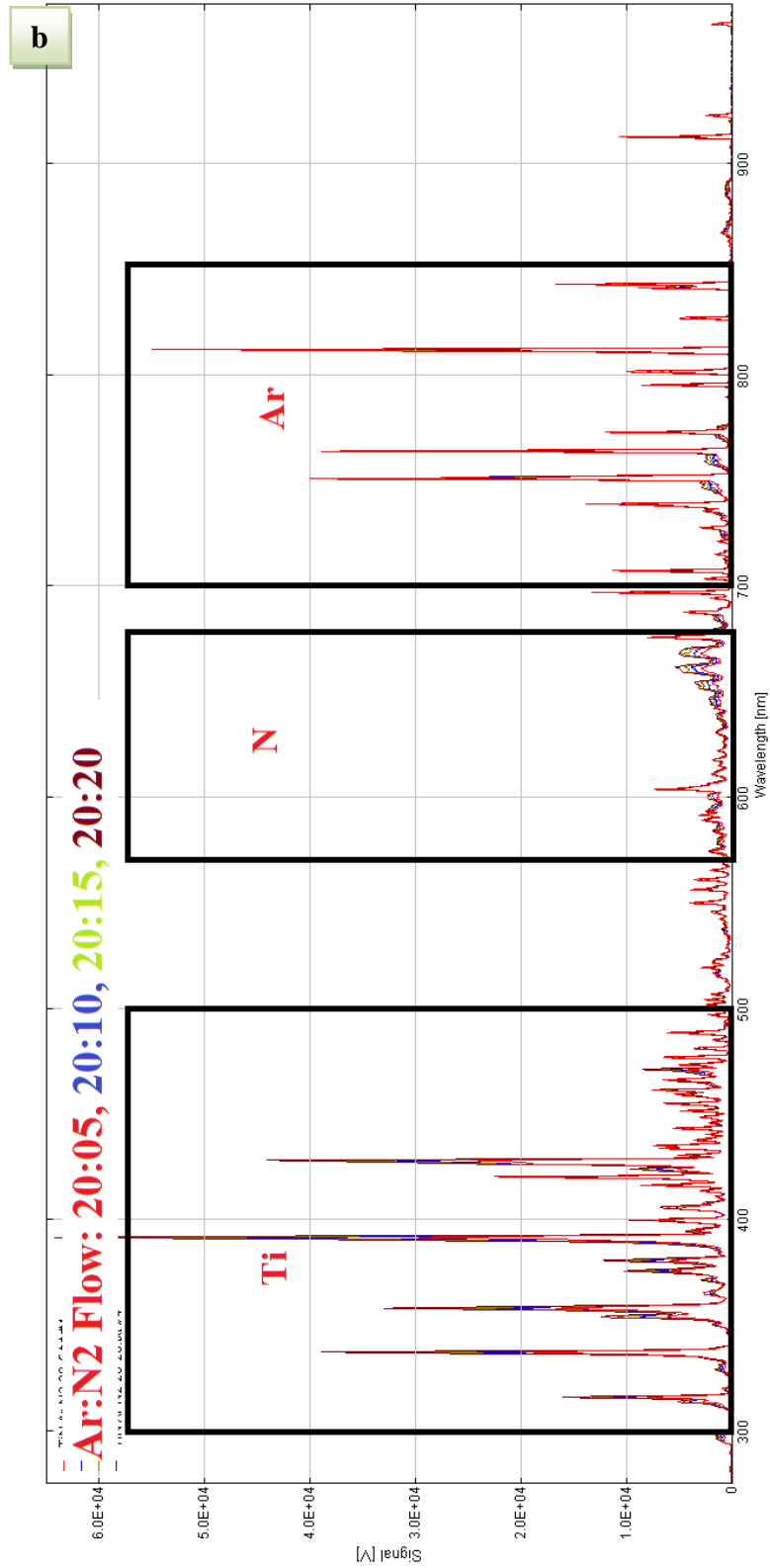


Figure 2.10 (b): Optical emission spectra of TiN plasmas at various Ar:N₂ ratios

2. 5. 2. Thickness measurement by cross-sectional scanning electron microscopy

Thickness plays an important role in deciding the properties of the film. The thickness of the film needs to be tuned with respect to the specific applications. The thickness of the films can be measured either by *in-situ* or by post-deposition measurement techniques. In general, quartz crystal and optical monitors are used for *in-situ* thickness monitoring. Post-deposition thickness measurement techniques include optical profiler, surface profiler, ellipsometer, gravimetric method, etc. Some of these techniques are destructive. Hence, an appropriate selection of thickness measurement techniques is required, which depends on the material's nature, deposition technique, application, etc. The nature of the material and selected technique play an important role in the accuracy of film thickness measurement. Direct thickness measurement of the thick and non-dielectric films can be easily measured without any charging difficulties during SEM imaging (Ding et al. 1992). In this case, the cutting effect of the film-substrate interface needs to be taken care of to avoid difficulty in the measurements. In this study, the NiTi and TiN thin film thicknesses have been measured by cross-sectional SEM imaging using the fractured edge of the film-substrate interface.

2. 5. 3. Microstructure characterization by X-ray diffraction (XRD)

The crystal structure studies of the NiTi and TiN thin films have been carried out using the X-ray diffraction technique. X-ray diffractometry is a non-destructive characterization technique used to determine the bulk and thin film materials' crystalline structure, chemical composition, etc. The XRD analysis gives information about lattice parameters, crystal structure, orientation, grain size, and stresses present in the films. Figure 2.11 represents the interaction of X-rays inside the crystal. XRD works based on Bragg's law, Eq. 2.8(Cullity, 1956).

$$n\lambda = 2d \sin\theta \dots \dots \dots (\text{Eq. 2.8})$$

Where 'θ' is the diffraction angle, 'λ' the wavelength of X-rays, and 'n' the diffraction order. The structural parameters, such as grain size, internal stress, and dislocation density, have been calculated from the XRD data using appropriate

relations. The crystallite size of the material can be approximated from the XRD data using the Scherrer formula, Eq. 2.9 (Cullity, 1956).

$$\text{Particle Size} = T = \frac{K\lambda}{\beta \cos\theta} \dots \dots \dots (\text{Eq. 2.9})$$

Where $\lambda = 1.54060 \text{ \AA}$ (in the case of $\text{CuK}\alpha 1$) so, $\Theta = 2\theta/2$ (in the example = $20/2$), K is a dimensionless shape factor with a value close to unity, and β = Full-width at the half-maximum intensity of the peak (in Rad). In general, the dominating peak is used to calculate the crystallite size. Rigaku SmartLab is used for the XRD analysis of the samples in this work. The measurement capabilities of this system are phase identification, crystallize size, and chemical composition.

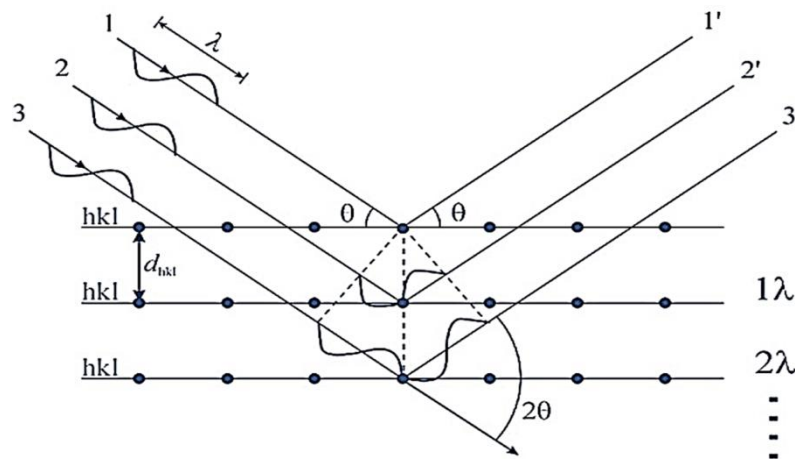


Figure 2.11: Schematic diagram of the diffraction of X-rays from the atomic planes

The preferred orientation can be quantified by calculating the texture coefficient of the films using the following equation (Eq. 2.10).

$$TC(hkl) = \frac{\frac{I(hkl)}{I_0(hkl)}}{\frac{1}{n} \sum_{i=1}^n \frac{I(hkl)}{I_0(hkl)}} \dots \dots \dots (\text{Eq. 2.10})$$

2. 5. 4. Phase transformation studies by high-temperature X-ray diffraction (HT-XRD)

A locally developed sample heating stage was incorporated with the same X-ray diffraction setup. A maximum temperature of 250°C can be reached by controlling using a PID controller without much fluctuation in the set and actual values of the

temperatures. The NiTi films were subjected to high-temperature X-ray diffraction studies to study their phase transformation behavior.

2. 5. 5. Surface morphology studies

2. 5. 5. 1. Atomic Force Microscopy (AFM)

Atomic force microscopy (AFM) is a powerful tool, which detailed information about the surface morphology and the roughness of the sample surfaces. The basic principle involved in the AFM technique is the interaction between a sharp tip having atomic dimensions and the sample surfaces. This technique can be used to determine the topography of almost all kinds of surfaces. The critical part of the AFM is the force sensor, which transforms the force interaction over the tip-sample junction into an electrical signal. The probe is connected to a cantilever tip, and a laser beam is used to measure the deflection of the cantilever tip. Even angstrom level deflection of the cantilever can be identified by the laser and is recorded by a photo diode to generate a corresponding surface image of the sample (Binnig et al. 1986, Giessibl et al. 2003). This work studied the surface morphologies and roughness of the NiTi and TiN thin films with a scanned area of $5 \mu\text{m}^2$ using tapping mode AFM (Bruker) with a tip size of 10 nm.

2. 5. 5. 2. Field emission scanning electron microscopy (FESEM)

Field emission electron microscopy (FESEM) is used to study the morphology of the sample surfaces. In FESEM, electrons are produced either by thermionic or field emission, which is used to scan the samples. These electrons have a higher current density and can be used for better imaging. Compared to normal SEM, the field emission SEMs are more effective for the higher resolution. The incident electrons interact with the sample atoms, resulting in signal production, containing information about the sample's surface topography. In the case of thin films, the SEM is used to mainly study the surface topography and grain size (Smith et al. 1955, Bogner et al. 2007). In the present study, the field emission scanning electron microscope (Gemini technology Zeiss FE-SEM) has been used to investigate the surface topographies of NiTi and TiN thin films. The resolution of this instrument is approximately 0.8 nm at 300 KX magnification. The tool is capable of achieving 25 lakh magnification. SEM

has wide applications in various areas, such as life sciences, materials science, earth sciences, etc.

2. 5. 6. Atomic composition studies by Energy Dispersive X-ray Spectroscopy (EDS)

Energy-dispersive X-ray spectroscopy (EDS) is widely used as a chemical characterization tool for elemental analysis and compositional studies materials. When the high-energy electrons fall onto the sample surface, secondary electrons, Auger electrons, X-rays, and photons are produced. The X-rays carry vital information about the elemental composition of the material's surface. Each element has its unique properties, which describe the intensity of the X-rays emitted. The intensity of these X-rays at the detector determines the elemental compositions. EDAX provides the atomic percentage of the materials and the weight percentage of the atoms present. This characterization technique is based on the fundamental principle that each element has a unique atomic structure and emits rays that are characteristic of its own. The relative intensities of the X-rays are a measure of the ratio of elements present in the sample (Goldstein et al. 2003). In the present study, the composition of NiTi thin films has been determined using the EDAX technique combined with the FESEM.

2. 5. 7. Electrical resistivity studies by the four-probe measurement system

A four-point probe is a simple apparatus for measuring the sheet resistance of semiconductor samples. Passing a current through two outer probes and measuring the voltage through the inner probes allows the measurement of the sample sheet resistance. The sheet resistance (R_s) measurement can be formulated (Smits, 1958) as shown in Eq. 2.11,

$$R_s = \frac{\pi}{\ln 2} \frac{V}{I} \dots\dots\dots \text{(Eq. 2.11)}$$

Where $(\pi/\ln 2)$ is a correction factor, V and I are the voltage and current, respectively. If the thickness (t) of the film is known, the electrical resistivity (ρ) of the film can be calculated from the expression (Eq. 2.12),

$$\rho = R_s \times t \dots\dots\dots \text{(Eq. 2.12)}$$

In this study, the four-probe measurement was used to measure the electrical properties (sheet resistance) of the TiN thin films. The TiN films for electrical studies were deposited onto Si/SiO₂ substrates for measurement accuracy. The SiO₂ layer acts as an insulator for taking measurements only from the TiN layer.

2. 6. Fabrication techniques

In this section, the microfabrication techniques that were used for fabricating the NiTi and TiN MEMS structures are discussed. In this study, the micromachining of the NiTi and TiN MEMS structures has been carried out using laser patterning and focused ion beam milling. Conventional lithography techniques were not used here because the requirement of high-temperature processing of crystalline NiTi and TiN thin films hinders the employment of lithography procedures. The techniques used to fabricate NiTi and TiN MEMS structures are briefly discussed below.

2. 6. 1. Focused ion beam machining (FIB)

Focused ion beam machining is a non-contact method used to remove the material from the sample surface by transferring the kinetic energy of the ions to the sample atoms. It can machine the materials at submicron levels and do the process without residual stresses. As it is not a chemical process, any solid material can be machined. With the emergence of micro/nanodomains, FIB machining has become a powerful tool because of its ability to remove the precise amounts of material with minimum damage (Lindquist et al. 1993, Friedensen et al. 2017). FIB is also used in the sample preparation for TEM. In this work, a Helios NanoLAB 600i FIB system has been used to pattern the TiN microheater structures. Figure 2. 12 shows the major components of the FIB column. The ion column is usually kept at $\sim 10^{-7}$ mbar pressure to have a larger mean free path to the ions. However, the sample chamber is usually kept at a 10^{-5} mbar pressure.

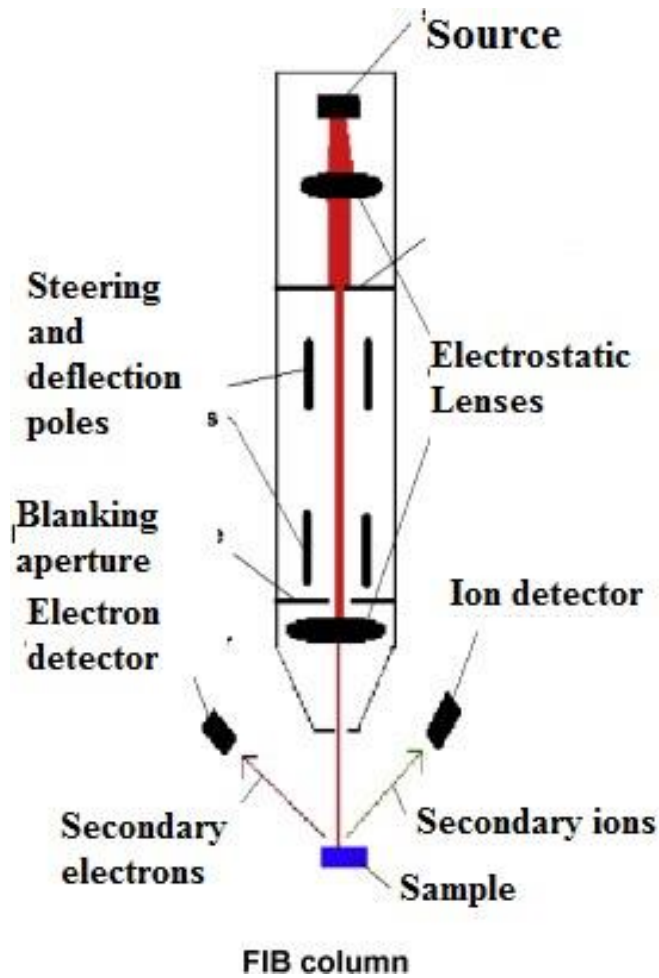


Figure 2.12: Schematic of FIB column

2. 6. 2. Femto second laser

Laser micromachining techniques are mainly used for miniature machining components and small micro-features of sizes ranging from 1 μm to even up to 1 mm using different materials, such as plastic, glass, ceramics, metals, diamond, etc. Lasers for micromachining are characterized by short pulse lengths from the millisecond range for applications in micro-welding to the pico and femto second area for ablation of materials. The energy from the pulsed laser is absorbed by the lattice of the machined material, and the atomic bonds are broken. There is no time for melting due to short pulses, no recast layer is formed, resulting in excellent features. The other features of these types of laser micromachining are that it can machine at the submicron level resolution without any micro-splatter, micro-cracks, delaminations, etc. (Osellame et al. 2012). This work used a Clark MXR Inc. femtosecond laser setup to machine the NiTi and TiN MEMS structures. The wavelength of the FSL was 775

± 2 nm with a resolution of 1 nm having a 1 W later output. The pulse width ranges from 10 ps to 150 fs, and the pulse repetition rate is from 1 Hz to 2 kHz. Figure 2. 13 shows a schematic diagram of the femtosecond laser setup.

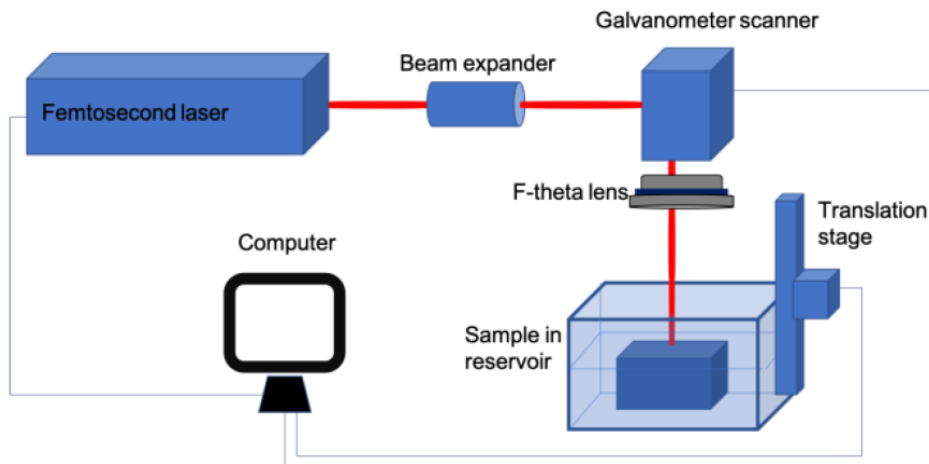


Figure 2.13: Schematic of the femtosecond laser system

2. 6. 3. Ytterbium fiber laser micromachining

Figure 2. 14 shows the Raycus Ytterbium fiber laser micromachining system that has been used in this work for patterning NiTi and TiN microstructures. This tool is capable of marking or machining various metal and non-metal surfaces. Raycus pulsed laser is a specially designed laser marking system with high speed and efficiency. It is an ideal high-power laser source for industrial laser marking systems and other applications. Compared with conventional lasers, the pulsed laser has some unique advantages in accelerating the conversion efficiency of the pump light over 10 times higher, its automated design in low power consumption, and being proper for operating both inside and outside of the lab. Besides, it is exquisite and convenient for its independence in placement, free time in use, and facility in connecting to equipment directly. The device can emit 1060~1085 nm wavelength pulsed light under the control of an industrial laser's standard interface driven by a 24V DC power source. It is a 30 W fiber laser setup with a single pulse energy of 1 mJ at a pulse frequency range (20 – 60 kHz).



Figure 2.14: Schematic of Ytterbium fiber laser system

2. 6. 4. Dry (RIE-Cl) and Wet (TMAH) etching of silicon

Reactive Ion Etching (RIE) is an etching technology used in micro-and nano-fabrication. RIE uses chemically-reactive plasma to remove material from wafers. The RF plasma is generated under low pressures by applying a strong RF electromagnetic field, typically set at 13.56 MHz with a few hundred Watts of power. High energy ions from the plasma attack the wafer surface and react with it to remove the film. RIE of silicon is independent of crystal planes, which making fabrication of any shape easier than anisotropic wet etching. The process parameters, such as pressure, gas, and RF power, play an important role in the etching characteristics. In this work, Oxford Instruments made PlasmaLab system 100 ICP 380 (Figure 2. 15) was used to etch the bottom silicon to make freestanding NiTi/TiN MEMS structures.

Tetramethylammonium hydroxide (TMAH, $(\text{CH}_3)_4\text{NOH}$) is a popular etchant that has been used in micro-fabrication procedures regularly. TMAH is widely used in the microelectronics industry because of its compatibility with the CMOS processes. It is effortless to handle and has low toxicity. The etching rate of TMAH depends upon temperature, chemical concentration, and orientation of the silicon. There is no doubt that TMAH is a suitable etchant for the anisotropic etching of silicon (100). In this work, the TMAH was used to etch the bottom silicon for making the free-standing NiTi structures like micro-meshes and micro-combs.



Figure 2.15: Oxford reactive ion etching system

2. 6. 5. Wirebonding

Wirebonding was employed for the interconnections between semiconductor devices. The fabricated device should have a minimum of $100 \times 100 \mu\text{m}^2$ area for contact pads to perform the wirebonding. Bond wires usually consist of these materials: aluminum, copper, gold, and silver. The wire diameters start from $15 \mu\text{m}$ and can be several hundred micrometers. Based on the power to be utilized with the device, the diameter of the wire should be fixed. In this work, a TPT wirebonder was used to make electrical contacts of $200 \times 200 \mu\text{m}^2$ TiN electrodes. Figure 2. 16 shows the TPT wirebonder used in this work.



Figure 2.16: TPT wirebonder

2. 6. 6. Heat measurements by thermal infrared camera

An infrared camera works on the principle of detecting and measuring the infrared energy of objects. Each object emits infrared energy, known as the object's heat signature. The processor in the infrared camera converts detected infrared data into an electronic image and then showed the visible surface temperature of the object being measured. An infrared camera contains an optical system that focuses infrared energy onto a special detector chip, a sensor array that includes thousands of detector pixels arranged in a grid. Each pixel in the sensor array reacts to the infrared energy focused on it and produces an electronic signal. Each temperature value is assigned a different color. The instrumentation of the IR camera is given in Figure 2. 17.

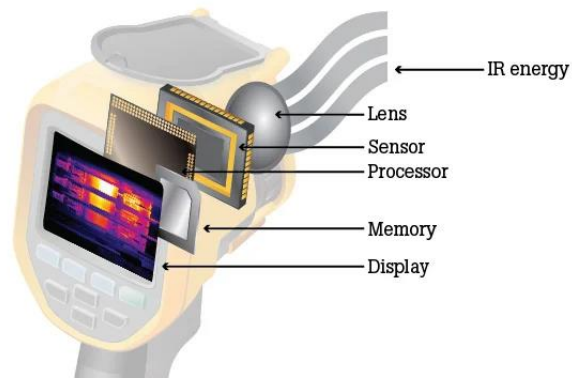


Figure 2.17: Components of IR camera

CHAPTER 3

INFLUENCE OF DCMS AND PDCMS PROCESSES ON NICKEL-TITANIUM THIN FILMS PROPERTIES

3. 1. Introduction

This chapter discusses the experiments and results of nickel-titanium (NiTi) thin films deposited by DCMS and PDCMS techniques. Among the two elements, titanium exhibits more affinity toward residual gases such as water vapor, oxygen, hydrogen, etc. The Ti-based alloy films need to be synthesized under clean and contamination-free process conditions. In addition, to exhibit the shape memory effect (SME), the NiTi thin films need to be prepared under contamination-free process conditions. The contaminant gases in the process chamber react with the sputtered atoms, degrading the film's shape memory property. This chapter starts with the vacuum diagnosis of the process chamber to study the presence of residual gases with their concentrations. In the following section, the calibration of the experimental setup, such as the stability of the process and deposition rate, and other details are explained. In the latter part of this chapter, the improvements in the NiTi thin film properties achieved using the PDCMS process over the DCMS process are discussed. Subsequently, these films were characterized for studying their microstructural, surface topographic, and phase transformation properties. The structural studies of the NiTi films were carried out by X-ray diffraction (XRD), while the surface topographic studies were conducted by atomic force microscopy (AFM) and scanning electron microscopy (SEM), and the thicknesses were measured using a cross-sectional SEM. The phase transformation properties of the films were studied by high-temperature X-ray diffraction (HT-XRD). In the final section, the NiTi plasma characteristics achieved using DCMS and PDCMS processes are studied and correlated with the characterization results.

3. 2. Vacuum diagnosis of process chamber using residual gas analyzer

The quality of the high vacuum depends on various residual gases in the process chamber. The contaminant gases, such as oxygen, carbon dioxide, water vapor, etc., degrade the shape memory property of nickel-titanium thin films. In addition, while

working with titanium-based alloys, the major concern is the presence of residual gases like moisture and oxygen in the process chamber. Since titanium possesses more affinity to moisture and O_2 , surface oxidation of the films is possible. The oxygen content in the NiTi SMA film will degrade the SME property (Otubo et al. 2008, Mehrpouya et al. 2016). Therefore, it is important to measure the partial pressure of the gases present in the process chamber during high vacuum conditions (Pathan et al. 2012, Watanabe et al. 1996). By *in-situ* monitoring of the process chamber, one can reduce the significant contaminant gases by chamber baking, titanium getter exercises, etc. (Fedchak et al. 2018, Bourim et al. 2018). In this study, the gases explored are from 1 to 64 amu as the major contaminants lie in the range of 1 – 64 amu. The analyzed residual gases were H_2 , O_2 , N_2 , CO_2 , H_2O , etc.

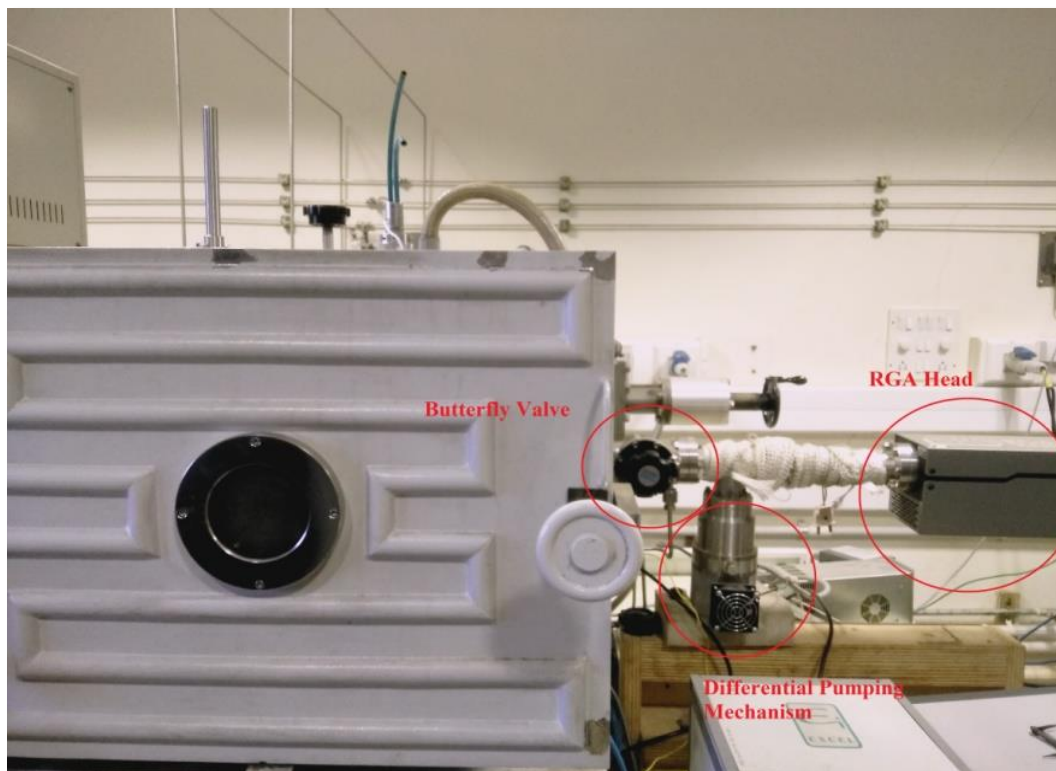


Figure 3.1: Residual gas analyzer integration with process chamber. An isolation butterfly valve is highlighted by the marking

Initially, the RGA head was isolated from the chamber using a butterfly valve, as shown in Figure 3.1. The partial pressures of various gases were recorded without exposing the chamber to the RGA head. This is considered as the background data

before the analysis of the process chamber. Then the process chamber was exposed to the RGA head by opening the butterfly valve, and the data was acquired. Then the substrate temperature was raised using a resistive heater set-up from room temperature to 600°C in increments of 200°C. With an increase in temperature, the degassing began, and some residual gases' partial pressures were increased. The variations in the partial pressures of the residual gases with chamber baking are shown in Figure 3.2.a.

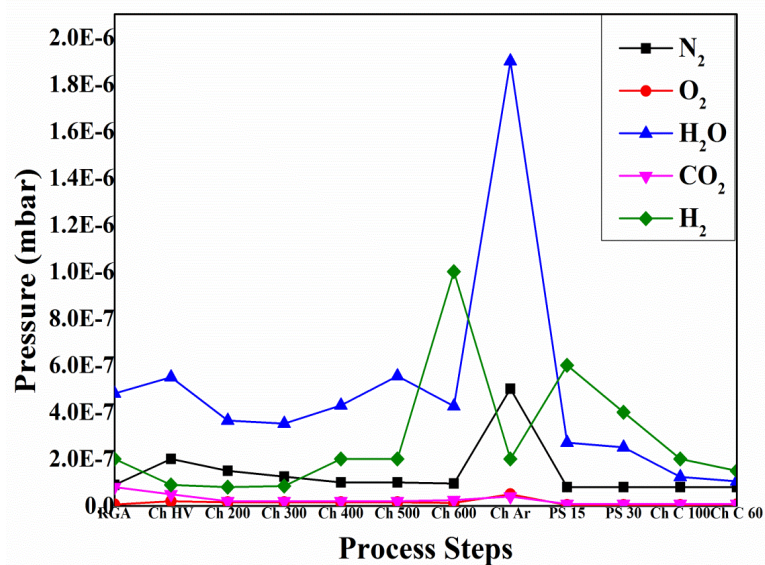


Figure 3.2.a: Vacuum diagnosis during chamber evacuation and baking using the residual gas analyzer

RGA → Data recorded in the RGA background – 5×10^{-7} mbar

Ch HV → Data recorded in chamber (high vacuum – 1.5×10^{-6} mbar)

Ch HV 200 → Data recorded in chamber (high vacuum at 200°C – 2.5×10^{-6} mbar)

Ch HV 300 → Data recorded in chamber (high vacuum at 300°C – 3×10^{-6} mbar)

Ch HV 400 → Data recorded in the chamber (high vacuum at 400°C – 3.5×10^{-6} mbar)

Ch HV 500 → Data recorded in the chamber (high vacuum at 500°C – 3×10^{-6} mbar)

Ch HV 600 → Data recorded in the chamber (high vacuum at 600°C – 2.5×10^{-6} mbar)

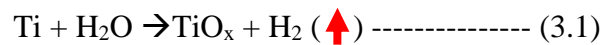
Ch Ar → Data recorded after passing argon gas at 600°C – 1.5×10^{-3} mbar

PS 15 → Data recorded after (pre-sputtering of 15 min. at 600°C– 5×10^{-3} mbar)

PS 30 → Data recorded after (pre-sputtering of 30 min. at 600°C– 5×10^{-3} mbar)

Ch C 100 → Data recorded in chamber (high vacuum at 100°C– 2×10^{-6} mbar)

Ch C 60 → Data recorded in chamber (high vacuum at 60°C– 1.7×10^{-6} mbar)



The sputter gas (argon 99.999% pure) was admitted into the chamber. When the argon gas was admitted, there was a sudden rise in the moisture levels observed. This moisture is the impurity from the process gas cylinder. The titanium pre-sputtering was carried out for half an hour to reduce the moisture level. It was found that the moisture, hydrogen, and oxygen contents in the process chamber were decreased after the titanium pre-sputtering. This was due to the gettering capability of titanium. The sputtered titanium atoms react with the residual gases and form the respective molecules before settling down on the shutter plate (Stout et al. 1955). Then the actual sputtering was carried out by opening the shutter plate between the target and substrate. After the completion of the deposition, the chamber was subjected to cooling to room temperature from 600°C. The partial pressures of the major contaminant gases, such as H₂, O₂, H₂O, N₂, and CO₂ were recorded during each step and tabulated. The characteristics of the residual gases during the deposition process are given below in Figure 3.2.b. The increase in hydrogen gas partial pressure is because of the chemical reaction between the sputtered Ti atoms and the water vapor, as shown in equation 3.1.

PS START → Data recorded in the chamber during the (pre-sputtering began at 600°C and Ar gas – 5×10^{-3} mbar)

PS END → Data recorded in the chamber during the (pre-sputtering completed at 600°C and Ar gas – 5×10^{-3} mbar)

NiTi Depn → Data recorded in the chamber during the (NiTi deposition at 600°C and Ar gas – 5×10^{-3} mbar)

Ch C 100 → Data recorded in the chamber (after cooled to 100°C post deposition)

Ch C 60 → Data recorded in the chamber (after cooled to 60°C post deposition)

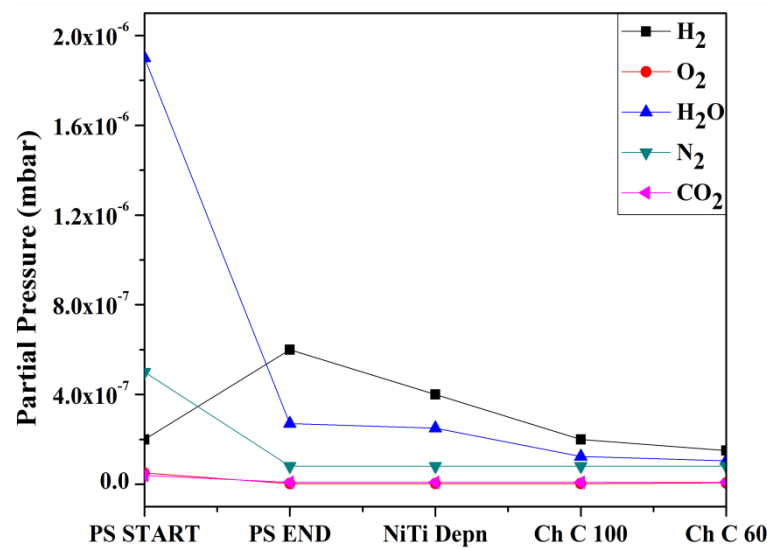


Figure 3.2.b: Vacuum diagnosis during NiTi deposition using residual gas analyzer

3. 3. Calibration of the experimental setup

The nickel-titanium thin films were deposited by DC magnetron sputtering (DCMS) on silicon (100) substrates for preliminary studies. The Si substrates were pre-cleaned with deionized water rinse before the deposition, followed by acetone ultrasonication to remove the organic contaminants. Then the Si wafer was dipped in a diluted hydrogen fluoride solution to remove the native oxygen layer. A Ni-45at%Ti alloy target was used for depositing the films. The process chamber was evacuated to a base pressure of 1.5×10^{-6} mbar using a combination of rotary and cryopumps. Argon gas was used as the sputter gas in all the experiments. The substrate-to-target distance was kept at 9 cm as better uniform films with 3" magnetrons are obtained between 7 and 12 cm (Maissel et al. 1970).

To exhibit the shape memory effect, the NiTi SMA thin films need to be synthesized in the thickness ranges of 1 μm or above. The transformation strain and residual strain show a maximum around the thickness of 1–2 μm . In addition, the transformation temperatures were also found to be affected by surface oxidation if the thickness is less than 1 μm . For Ti-rich films, surface oxidation is a cause of concern, as the film surface gets oxidized easily, resulting in the degradation of shape memory property (Ishida et al. 2003). Also, the NiTi films need to be in crystalline form to exhibit the

shape memory effect. Thus, the NiTi thin films were normally deposited or post-deposition annealed at high temperatures for crystallization. The minimum temperature at which the NiTi films undergo crystallization is (475–550°C) (Busch et al. 1990, Otsuka et al. 2005, Arranz et al. 2005). In this study, the target power was kept constant at DC=100 W, and the duration of deposition was varied (15, 30, 45, and 60 min) to reach the required thicknesses in short-duration depositions. To ensure NiTi films' crystalline behavior, the deposition was carried out at 400°C though the substrate heater could attain much higher temperatures. The deposition pressure was kept constant at 5×10^{-3} mbar. The process parameters are listed in Table 3.1.

Table 3.1: Process parameters of NiTi thin films deposited by DCMS

Process parameter	DCMS
Base pressure	1.5×10^{-6} mbar
Target	Ni-45at%Ti alloy - 99.99% pure
Substrate	P-type Silicon (100)
Sputter gas	Argon
Deposition pressure	5×10^{-3} mbar
Substrate temperature	400°C
Substrate-to-target distance	9 cm
DC power	100 W
Deposition duration	1 hr

3.3.1. Microstructural analysis

The microstructural study was carried out by X-ray diffraction, shown in Figure 3.3. The films appeared to be in an amorphous state without any sharp peaks. The films need to be deposited at higher temperatures and post-deposition annealed.

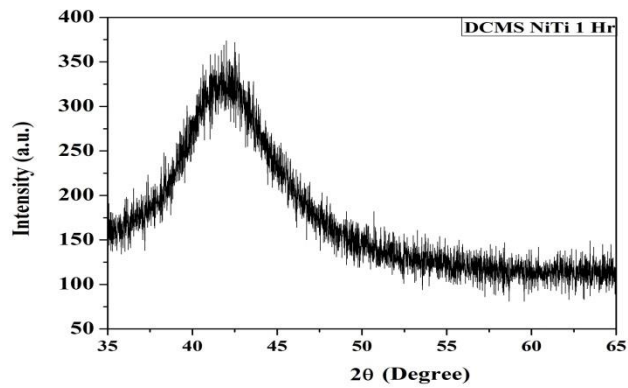


Figure 3.3: The XRD spectra of DCMS NiTi thin films

3.3.2. Surface topographic and compositional analyses

The surface topography of the NiTi films was studied by atomic force microscopy (AFM). Figure 3.4. shows the 3D topography of the DCMS NiTi thin film deposited at 400°C with a scan area of (5×5) cm². The film appears to be smoother, with a roughness value of 0.554 nm. The surface morphology of the NiTi films was carried out by field emission scanning electron microscopy (FESEM) and is shown in Figure 3.5. The composition of the film was determined by energy dispersive spectroscopy (EDS) and was found to be Ni-44.57at%Ti.

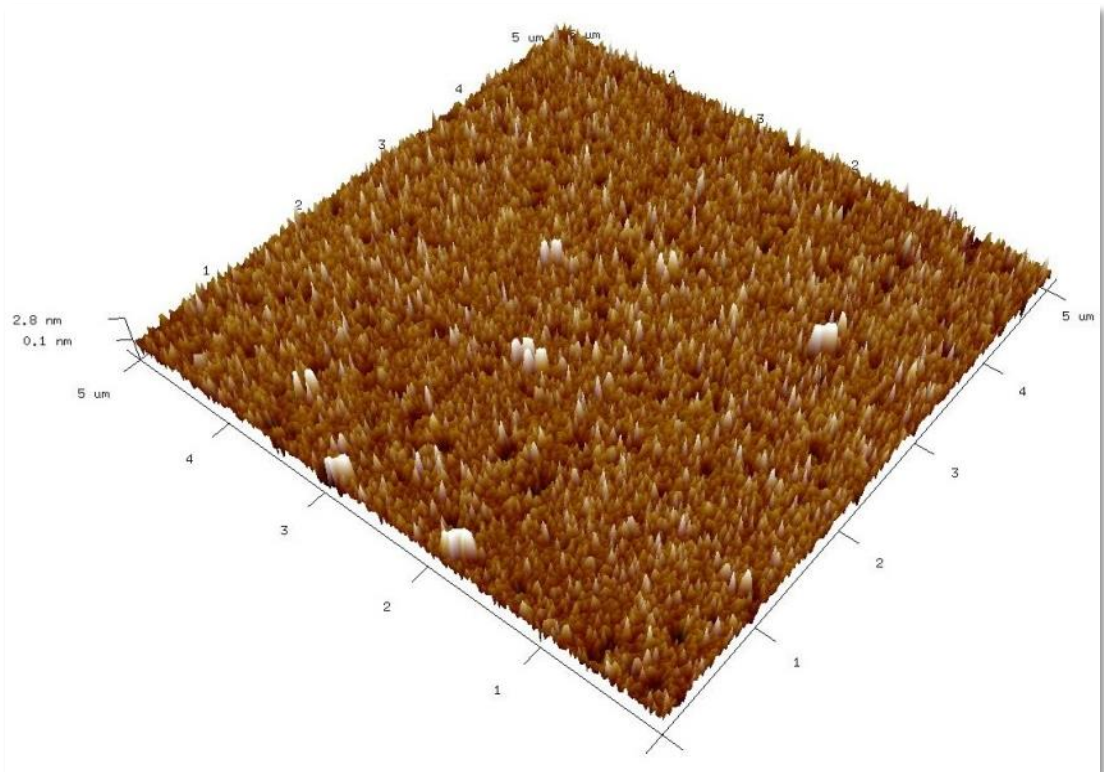


Figure 3.4: Surface topography of DCMS NiTi thin films by AFM

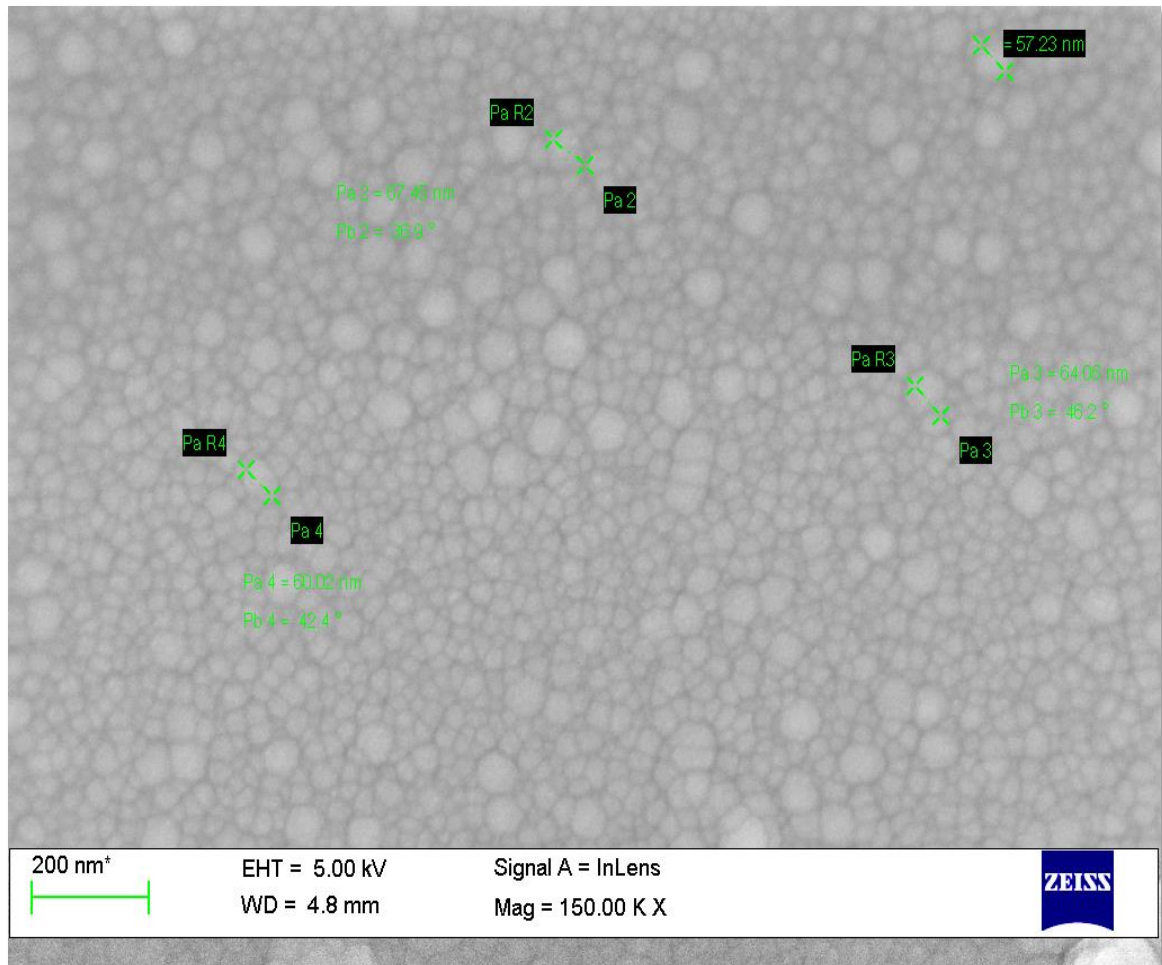


Figure 3.5: The FE-SEM surface image of DCMS NiTi thin films

The NiTi thin film thickness was measured by cross-sectional scanning electron microscopy. The cross-sectional SEM image of the NiTi film deposited for one hour is shown in Figure 3.6. The rate of deposition graph was plotted as deposition duration vs. thickness and is shown in Figure 3.7.

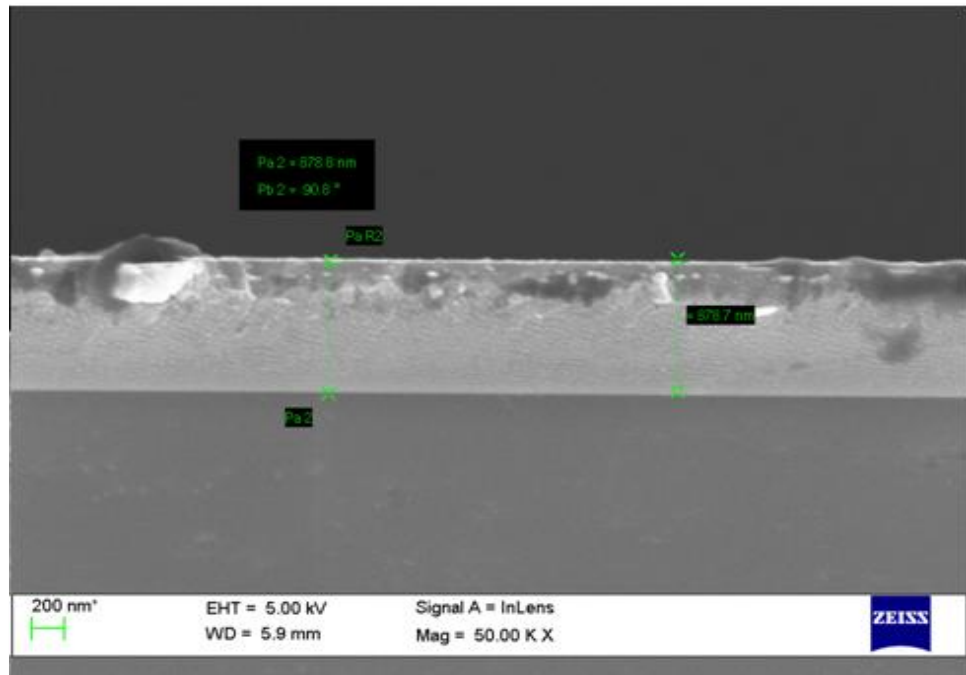


Figure 3.6: Cross-sectional SEM image of DCMS NiTi thin films

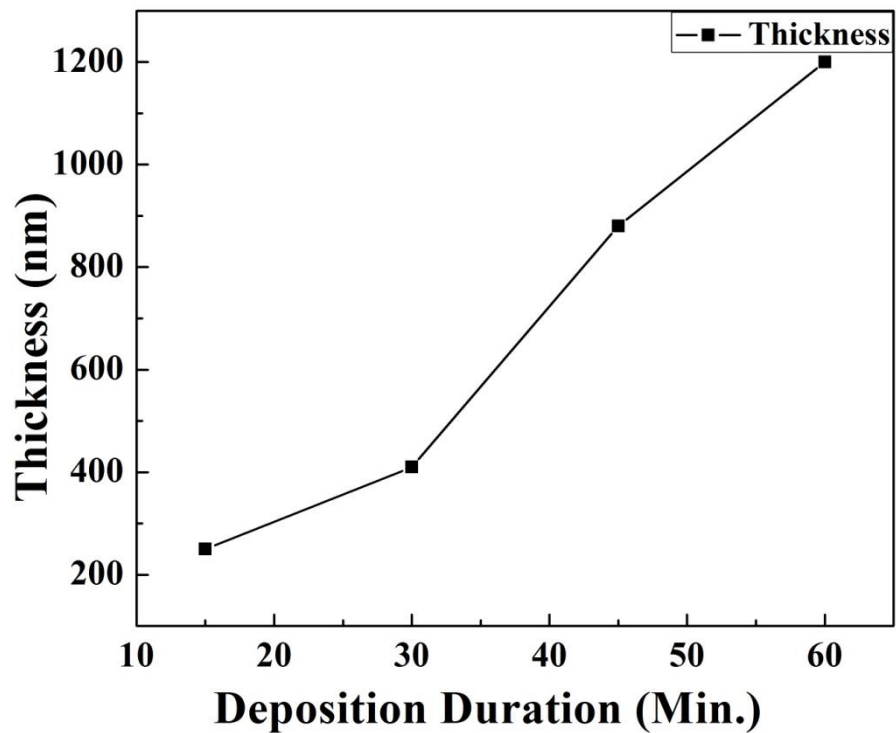


Figure 3.7: Thickness calibration curve of DCMS NiTi thin films

3. 4. Study of DCMS and PDCMS NiTi thin film properties

As the target is Ti-rich, the oxygen layer formation and target poisoning are a concern. This will result in variations in the deposition rate and lead to considerable

amounts of oxygen in the sputtered films. These constraints lead to difficulties in reproducing films having the same properties. The advanced pulsed DC magnetron sputtering (PDCMS) technique needs to be deployed to overcome this difficulty. In PDCMS, the periodic polarity reversals contain the arc formation at the target and provide long-term process stability. Thus, pulsing the magnetron discharge in this frequency range also strongly modifies the deposition plasma, raising the time-averaged electron temperature and the energy flux delivered to the substrate compared to continuous DC processing (Kelly et al. 2009). The denser plasma can produce better crystalline thin films and can also eliminate the lengthy annealing processes.

In this study, nickel-titanium alloy thin films were deposited onto silicon substrates by both DCMS and PDCMS techniques. This study aims to prove the improvements in the NiTi film properties deposited by PDCMS over the conventional DCMS process. The detailed process parameters are given in Table 3.2.

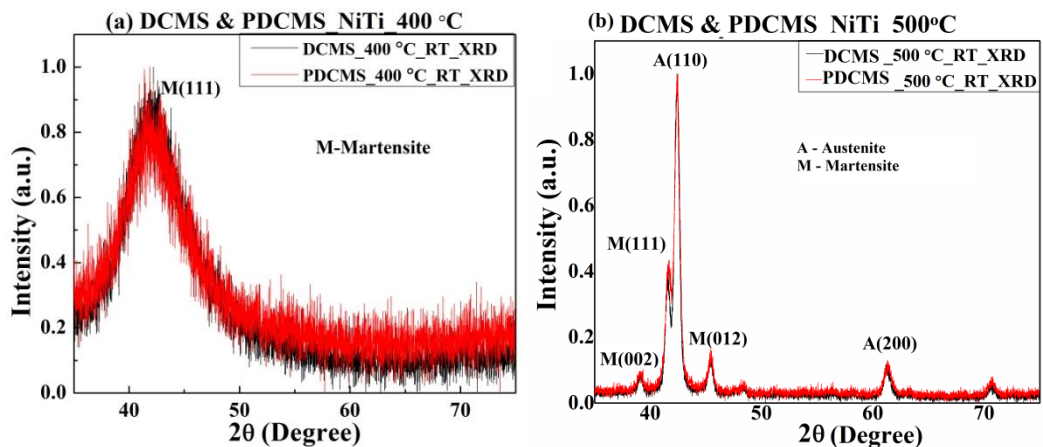
Table 3.2: Process parameters of NiTi thin films deposited by both DCMS and PDCMS techniques

Process parameters	DCMS	PDCMS
Base pressure	1.5×10^{-6} mbar	1.5×10^{-6} mbar
Target	Ni-45at%Ti alloy - 99.99% pure	Ni-45at%Ti alloy - 99.99% pure
Substrate	P-type Silicon (100)	P-type Silicon (100)
Sputter gas	Argon	Argon
Deposition pressure	5×10^{-3} mbar	5×10^{-3} mbar
Substrate temperature	600°C	600°C
Substrate-to-target distance	9 cm	9 cm
Pulsed DC power	100 W	100 W
Pulse frequency	NA	200 kHz
Pulse reversal time	NA	1.0 μ s
Deposition duration	1 hr	1 hr

3. 4. 1. Microstructural studies

The DCMS and PDCMS NiTi thin films have been subjected to X-ray diffraction (XRD) to study the microstructural orientations. To avoid the diffracted signals from the Si substrate, the grazing angle used was 0.5 degree. The film deposited at 400°C shows an amorphous nature in DCMS and PDCMS cases, whereas the films deposited at 500, 600, and 650°C show a crystalline nature as NiTi thin film's crystallization temperature is (475 – 550°C) (Otsuka et al. 2005, Arranz et al. 2005). These films exhibit an austenite phase at room temperature with a major (110) orientation at 42.6°. In addition, minor (200) orientations at 61.2° of the austenite phase were also observed in these films. There were small martensitic traces observed at orientations (002), (111), and (012) at 39.2°, 41.7°, and 45.4°, respectively (Uchil et al. 2007, Cha et al. 2012 and Koker et al. 2013, Daneshvar et al. 2020). The XRD spectra of both DCMS and PDCMS NiTi thin films deposited at 400, 500, 600, and 650°C are shown in Figure 3.8. These films are expected to be transformed completely to austenite upon heating and martensite upon cooling to room temperature.

By calculating the full-width half-maxima (FWHM) from the XRD spectra, the crystallite size can be calculated using the Scherrer formula (Eq. 2.9). The calculated and average crystallite sizes of DCMS and PDCMS NiTi films deposited at various substrate temperatures are tabulated in Table 3.3.



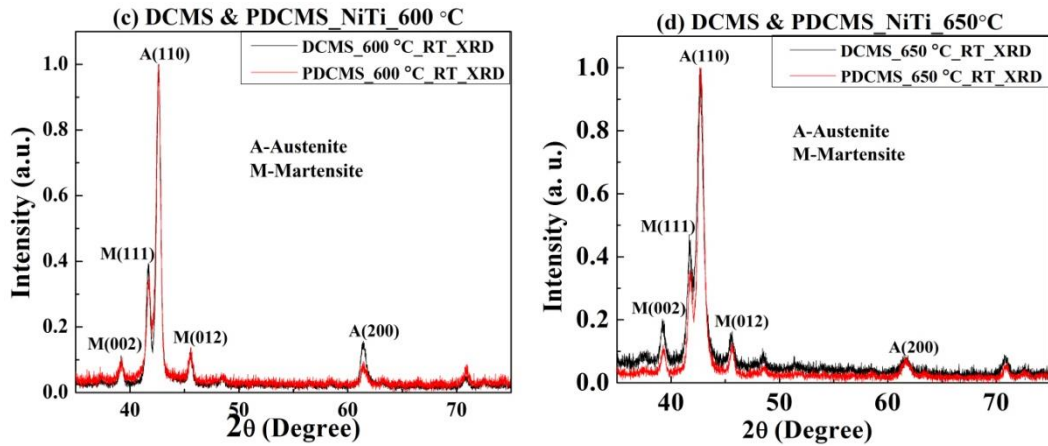


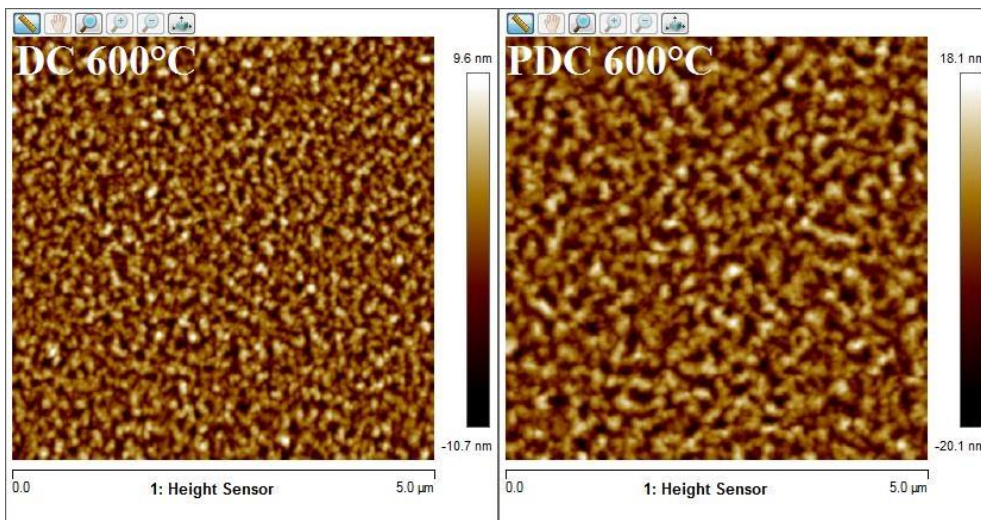
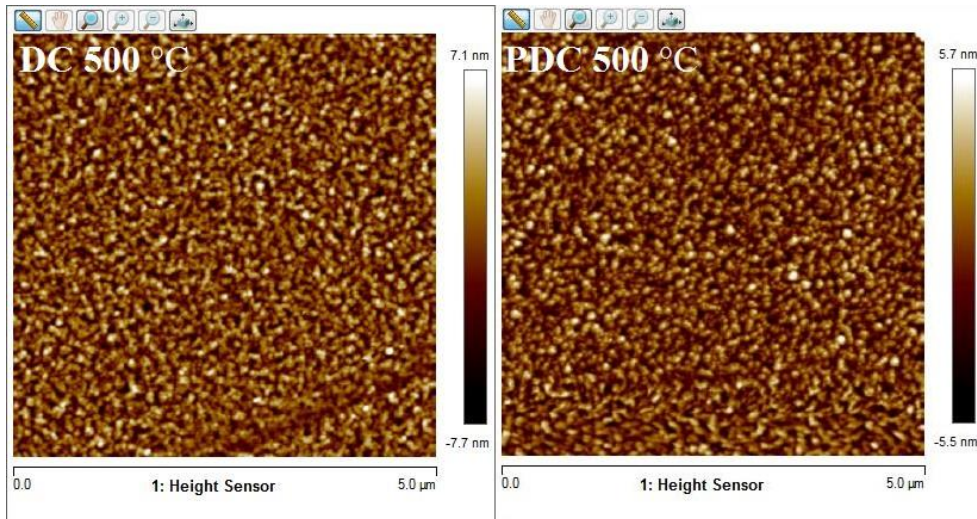
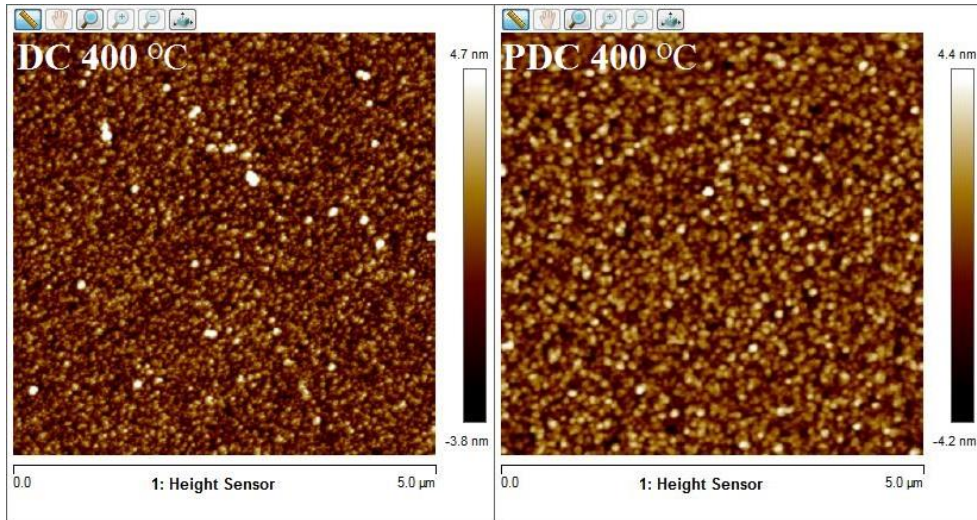
Figure 3.8: The room temperature XRD spectra of DCMS and PDCMS NiTi thin films at (a) 400, (b) 500, (c) 600, and (d) 650°C

Table 3.3: Crystallite size of both DCMS and PDCMS NiTi thin films deposited at 400, 500, 600, and 650°C

Substrate temperature (°C)	M(111)		A(110)		Average crystallite size, D (nm)	
	DCMS	PDCMS	DCMS	PDCMS	DCMS	PDCMS
400	---	---	---	---	---	---
500	15.9	13.5	16.8	15.5	16.4	14.5
600	17.7	13.7	18.3	18.3	18	16
650	15.5	16.7	12	13.3	13.8	15

3. 4. 2. Surface topographic and compositional studies

Figure 3.9. depicts the AFM images and corresponding height profiles of the DCMS and PDCMS NiTi thin film deposited at 400, 500, 600, and 650°C, respectively, with a scan area of (5×5) cm². In both cases, the surface roughness of the films showed an increasing with increasing the substrate temperature increases, except for the PDCMS 600 and 650°C films. Barring the 600°C deposited film, all the other DCMS sputtered films have shown higher surface roughness than PDCMS sputtered ones. The height profiles plotted in the lower panel indicate that the PDCMS films exhibit lower roughness than the DCMS films. It is reported that the PDCMS process provides dense, smooth films as compared to the DCMS process and is used widely for obtaining better physical and tribological properties (Kelly et al. 2007).



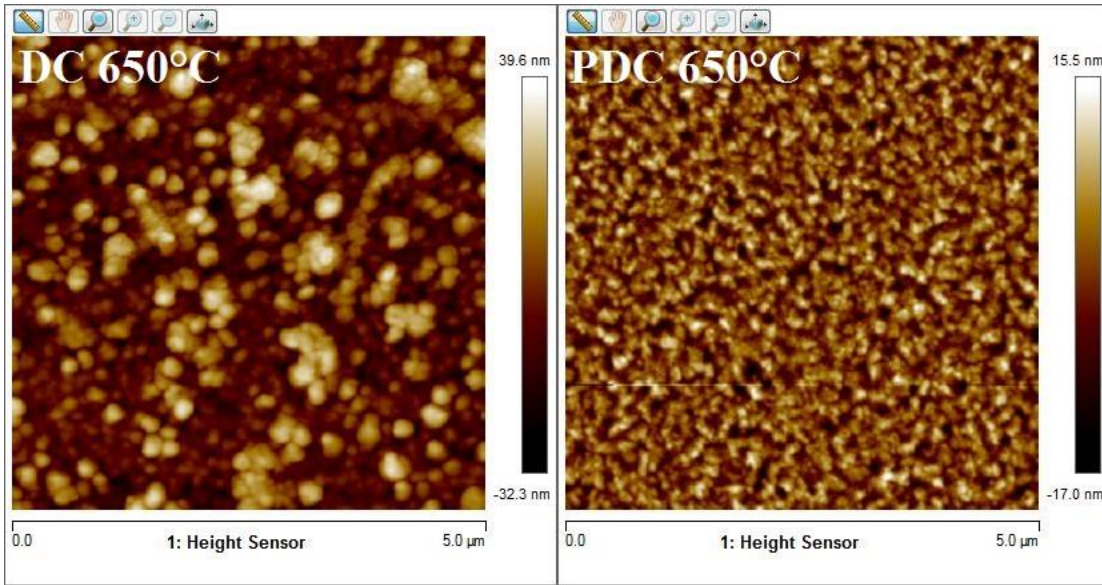


Figure 3.9.a: AFM images of DC and PDC NiTi thin films deposited at 400, 500, 600, and 650°C, respectively.

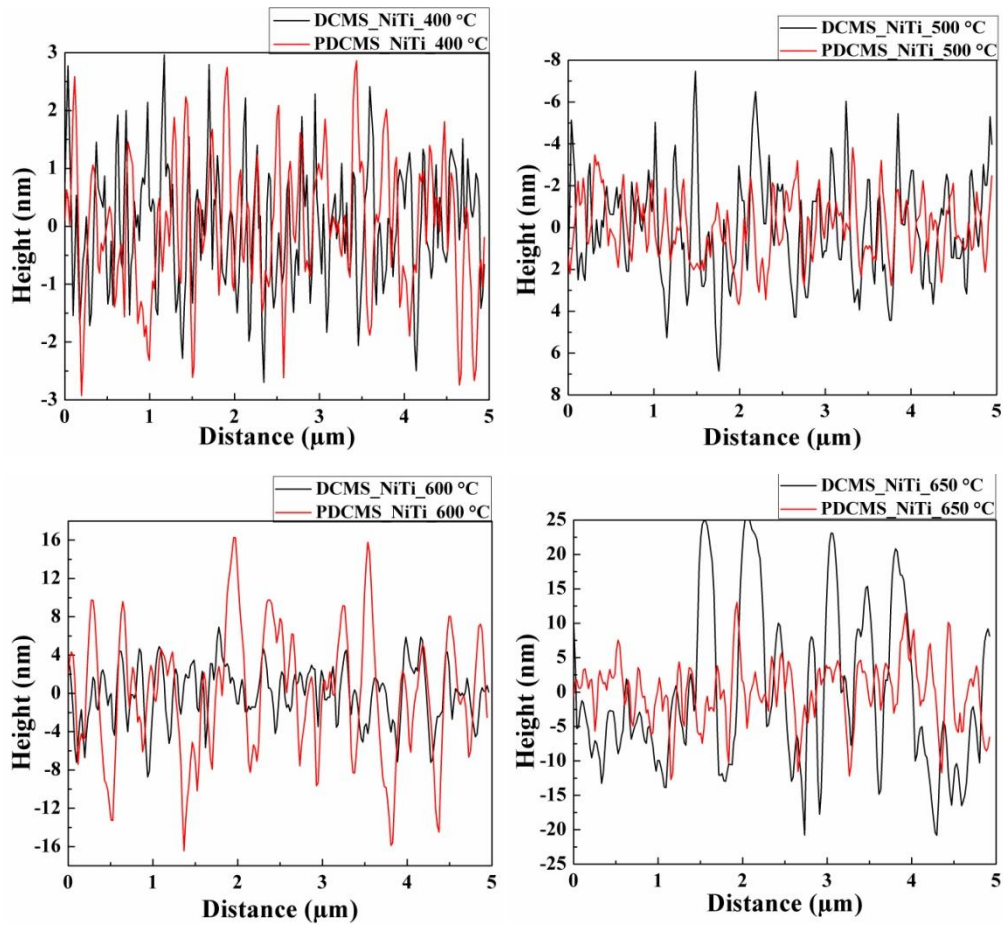


Figure 3.9.b: Height profiles of DC and PDC NiTi thin films deposited at 400, 500, 600, and 650°C, respectively.

The FE-SEM images of both DCMS and PDCMS NiTi films deposited at 400, 500, 600, and 650°C, respectively, are shown in Figure 3.10. As indicated in the XRD spectra, the film deposited at 400°C film shows amorphous nature with no grains found, as shown in Figure 3.10.a. The average grain sizes measured from the FE-SEM image for films deposited at 500°C (Figure 3.10.b.) by DCMS and PDCMS NiTi thin films were ~65 nm and 140 nm, respectively. For NiTi thin films deposited at 600°C, the average grain sizes are ~70 nm and 120 nm, respectively, as shown in Figure 3.10.c. In the case of films deposited at 650°C, the grain sizes were ~150 nm and 160 nm, respectively (Figure 3.10.d.). Therefore, in the case of 500 and 600°C films, there is a considerable increase in the grain sizes. Not much difference has been observed in the grain size of the films grown at 650°C. The rise in grain sizes must be due to the greater plasma density of the PDCMS process. The crystallization behavior of the NiTi thin films between substrate temperatures of 400 and 500°C explains the effect of crystallization temperature (Otsuka et al. 2005, Arranz et al. 2005). The SEM results corroborate the XRD and AFM findings.

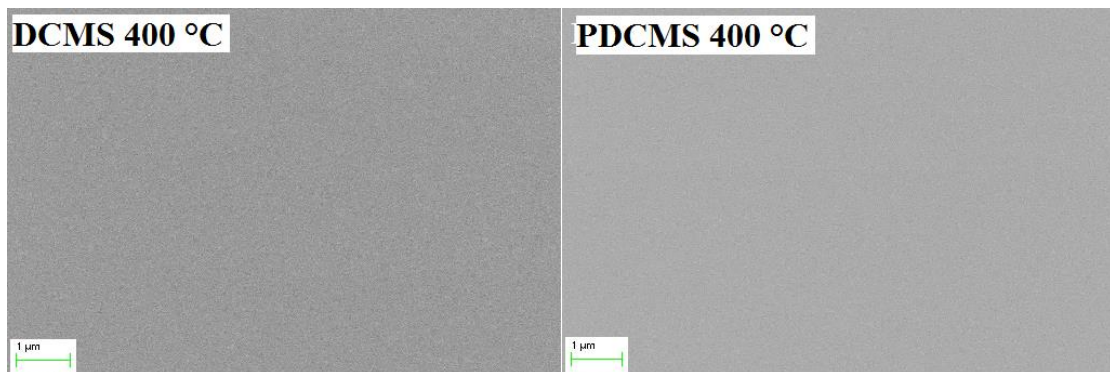


Figure 3.10.a: FE-SEM image of DCMS and PDCMS NiTi thin films, respectively, at 400°C

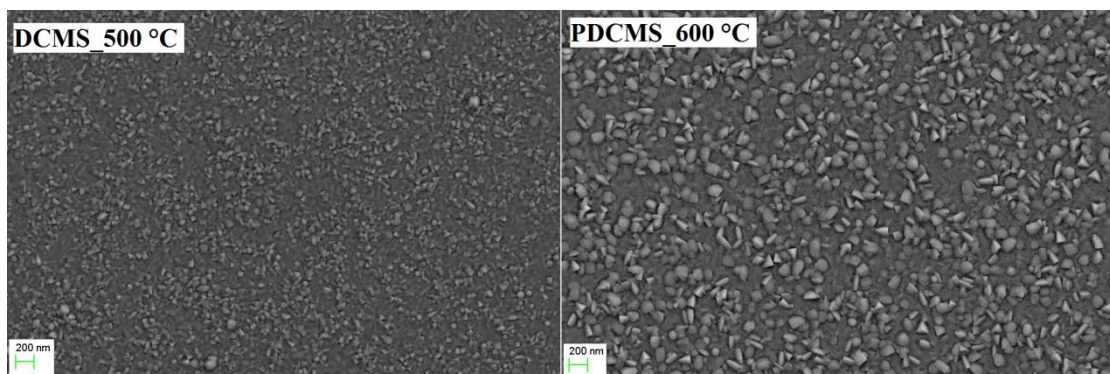


Figure 3.10.b: FE-SEM image of DCMS and PDCMS NiTi thin films, respectively, at 500°C

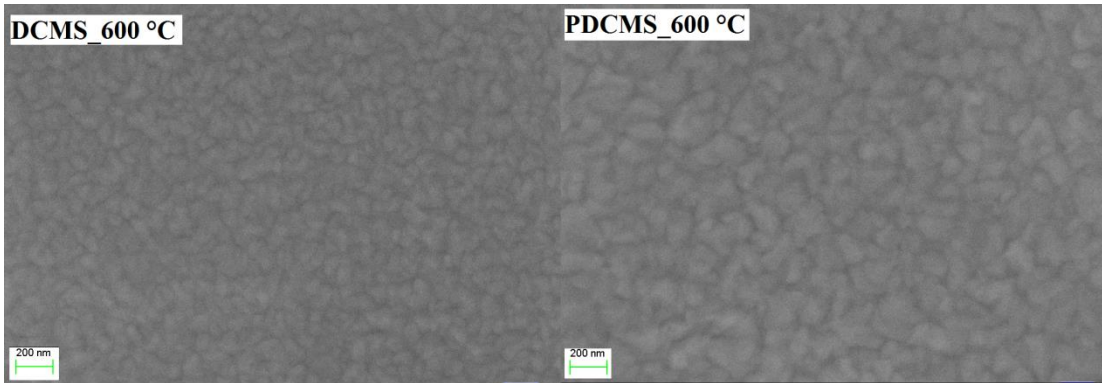


Figure 3.10.c: FE-SEM image of DCMS and PDCMS NiTi thin films, respectively, at 600°C

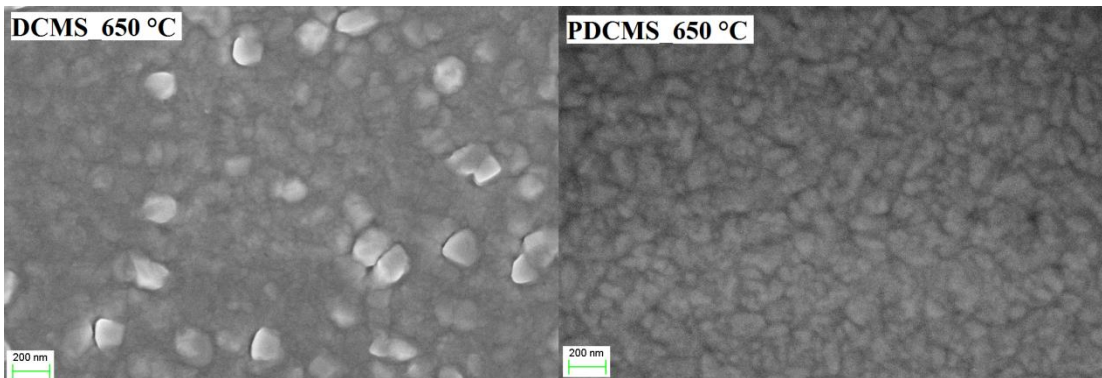


Figure 3.10.d: FE-SEM image of DCMS and PDCMS NiTi thin films, respectively, at 650°C

The thickness of the NiTi films measured from FE-SEM imaging of fractured cross-sectional samples is $\approx 1.3 - 1.5 \mu\text{m}$ by cross-sectional FE-SEM, as shown in Figure 3.11. Using this, the deposition rate of the films was calculated to be $\sim 25 \text{ nm/min}$. The PDCMS NiTi films are found to be approximately 100 nm less in thickness as compared to the DCMS films. This is expected as the PDCMS process undergoes pulse reversal for about a few microseconds and thereby exhibits a slightly lower deposition rate as compared to the DCMS process. The NiTi thin films' chemical composition was analyzed by EDS and is tabulated in Table 3.4.

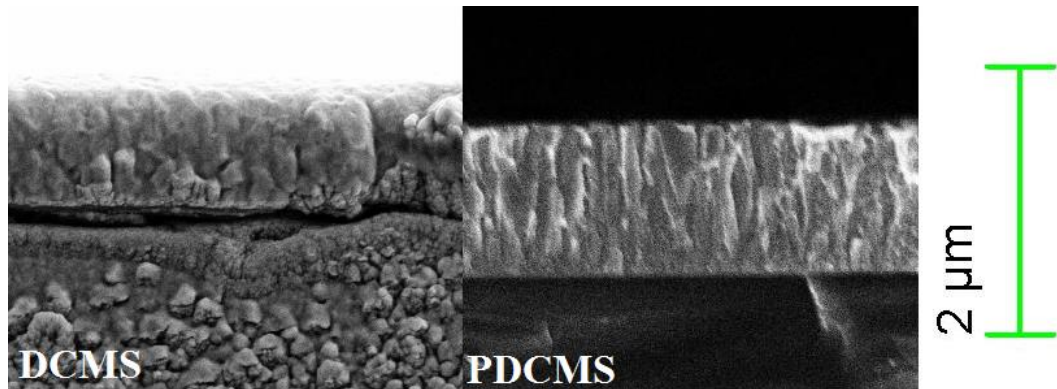


Figure 3.11: Cross-sectional FE-SEM images of DCMS and PDCMS NiTi thin films

Table 3.4: Energy dispersive spectroscopic analysis of both DCMS and PDCMS NiTi thin films

Deposition temperature (°C)	DCMS (Ti:Ni)	PDCMS (Ti:Ni)
400	55.09:44.91	55.41:44.59
500	56.54:43.46	56.94:43.06
600	56.08:43.92	55.56:44.44
650	56.81:43.19	55.96:44.04

3. 4. 3. Phase transformation studies

The phase transformation studies are generally conducted by differential scanning calorimetry (DSC) or high-temperature XRD (HT-XRD). In HT-XRD, by observing the changes in crystal orientations with variations in the temperature, the phase transformations are studied. The phase transformations in NiTi thin films were investigated by varying the sample stage temperature in the XRD system using a resistive heater set-up. The XRD spectra of DCMSNiTi thin films are shown in Figure 3.12. No changes were observed in the peaks at room temperature (25°C) and elevated temperature (120°C). The martensite peaks, which were supposed to disappear (or lower their intensity) at high temperatures, were still present in the spectra. This might be due to the lack of crystalline nature of the films.

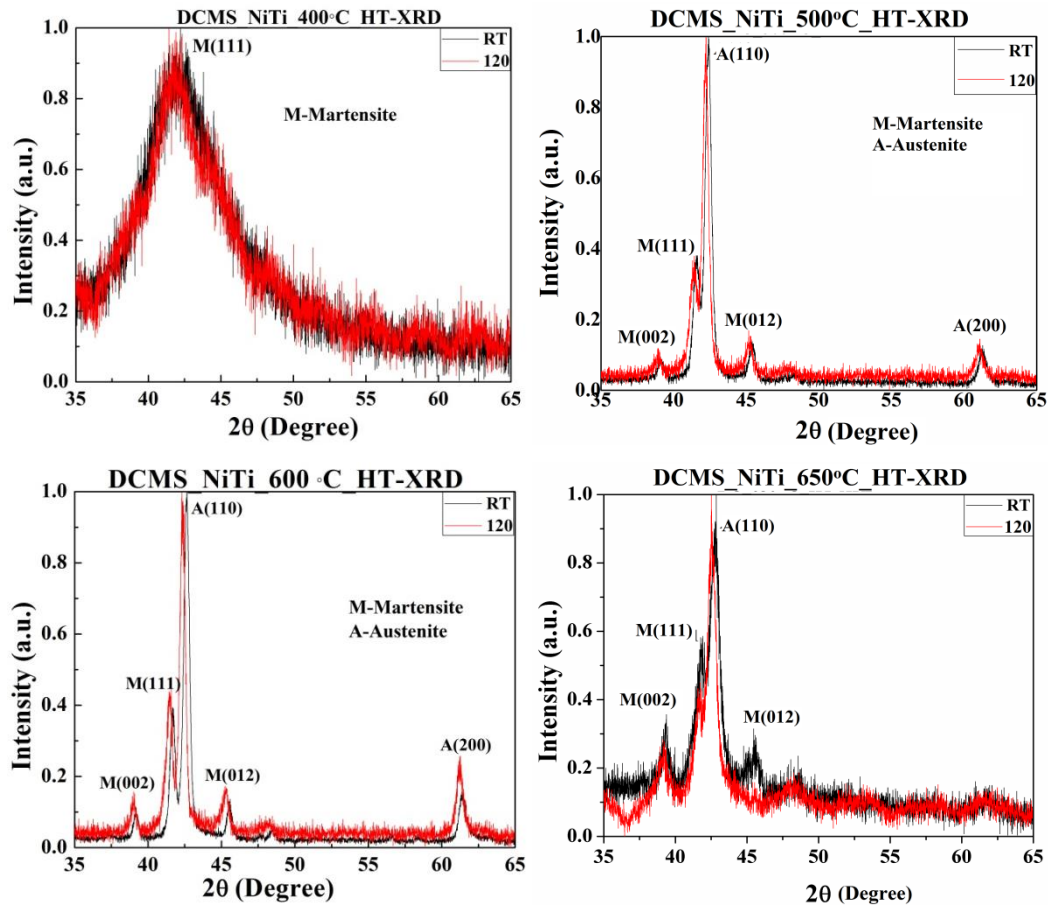


Figure 3.12: The high-temperature XRD spectra of DCMS NiTi thin films

On the other hand, the PDCMS NiTi films deposited at 600°C exhibited phase transformation on raising the temperature. The films deposited at 400, 500, and 650°C substrate temperatures did not show any phase transformation upon increasing the XRD stage temperature to 120°C. But, the 600°C films exhibited the reverse martensite-to-austenite ($B19' \rightarrow B2$) phase transformation upon heating (up to 120°C). As there was no cooling mechanism with the XRD set-up, only the reverse transformation ($M \rightarrow A$) is considered. With an increase in the temperature, the intensities of the martensite phase with orientations (002), (111), and (012) appeared to be decreasing, whereas the austenite peak (110) at 42.6° intensity remained the same. The peak intensity of the austenite phase with (200) orientation at 61.2° was also found to decrease. This might be because the film was more oriented toward the (110) plane at higher temperatures (Reddy et al. 2020, Tillmann et al. 2015, Koker et

al. 2013, Uchil et al. 2007). The HT-XRD spectra of PDCMS films are shown in Figure 3.13.

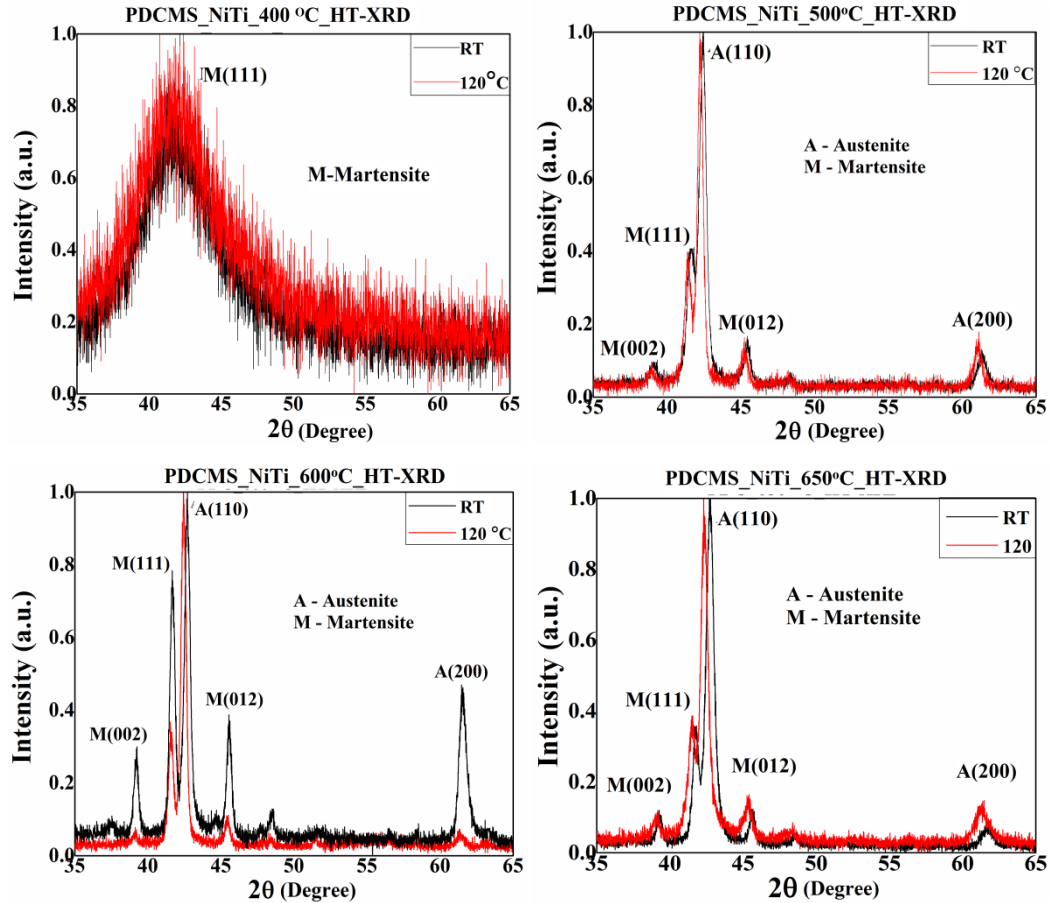


Figure 3.13: The high-temperature XRD spectra of PDCMS NiTi thin films

A detailed study of the phase transformation behavior of PDCMS NiTi has been carried out by varying the XRD sample stage temperature and is represented in Figure 3.14. The crystallite size of the PDCMS NiTi films was calculated using Scherrer's equation (2) and is shown in Figure 3.15. With an increase in temperature, the average crystallite size of the martensite phase decreased, whereas it increased in the case of the austenite phase. Earlier studies reported that this is due to increasing austenite volume caused by the martensite-to-austenite phase transformation (Koker et al. 2013).

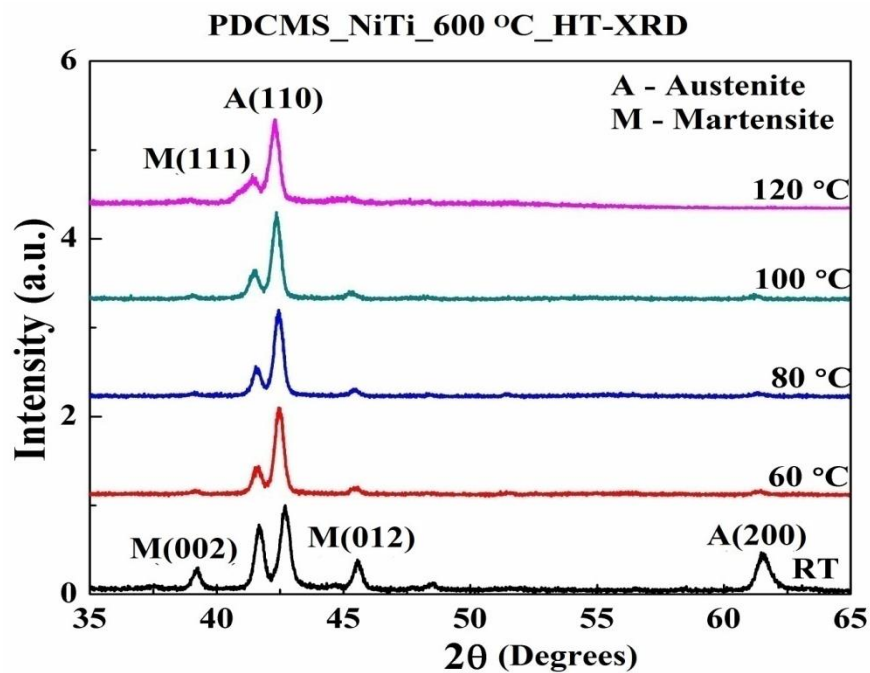


Figure 3.14: XRD profiles showing diffractions from martensite and austenite phases of PDCMS 600°C NiTi thin films as a function of temperature

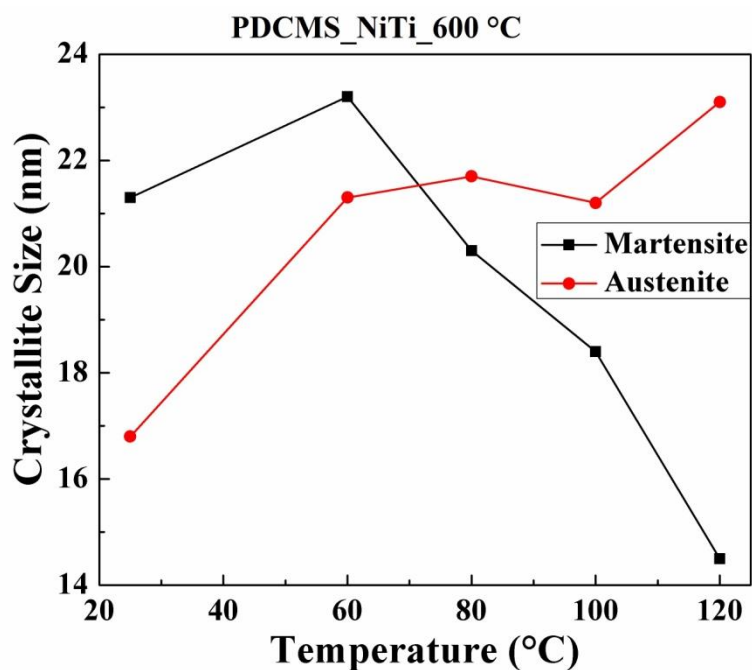


Figure 3.15: Average crystallite size of PDCMS 600°C NiTi films during martensite-to-austenite phase transformation as a function of temperature

3. 5. DCMS and PDCMS NiTi plasma diagnose using optical emission spectroscopy

Optical emission spectroscopy (OES) has been widely used to monitor plasma, especially while dealing with multi-component materials. In this study, the OES is mainly used for characterizing the excited nickel and titanium species in the plasma by analyzing the spectra obtained. While dealing with NiTi thin films for shape memory applications, composition control is very important and must be addressed (Wu et al. 2000, Bendahan et al. 1996).

The optical emission spectroscopy data have been collected as the emission spectra intensities against the wavelength of NiTi DCMS and PDCMS plasmas. In this study, the NiTi DCMS and PDCMS plasma characteristics were recorded and correlated with the corresponding film properties, shown in Figure 3.16. The plasma properties of nickel's emission spectra are generally collected in the region of 340 – 370 nm. Similarly, titanium and argon emission spectra are collected from 490 – 530 nm and 640 -720 nm, respectively, as shown in Figure 3.17. (Salhi et al. 2017, Swindells et al. 2006).

The discharge power was kept at 100 W with the chamber pressure at 5×10^{-3} mbar. The intensity of titanium, I_{Ti} at 503.9, 519.4, and 521.2 nm was found more for PDCMS atoms than DCMS atoms. Similarly, the nickel intensity, I_{Ni} at 341.8, 352.9, and 365 nm, was observed more for PDCMS atoms than DCMS atoms. Compared to I_{Ti} and I_{Ni} , the argon lines were more intense (I_{Ar}). This is because of the large concentration of excited argon atoms in the plasma. Titanium and nickel require much higher energy to be formed, so they are weak concentrations and peak intensities (Bendahan et al. 1995, Salhi et al. 2017). Thus, it is confirmed that the PDCMS plasma has a higher intensity than that of DCMS plasma in the cases of Ti, Ni, and Ar. The OES findings are in good agreement with the XRD, AFM, and SEM results. Hence, the reason behind the better film qualities for PDCMS NiTi films is much more enhanced plasma conditions than that of DMCS.

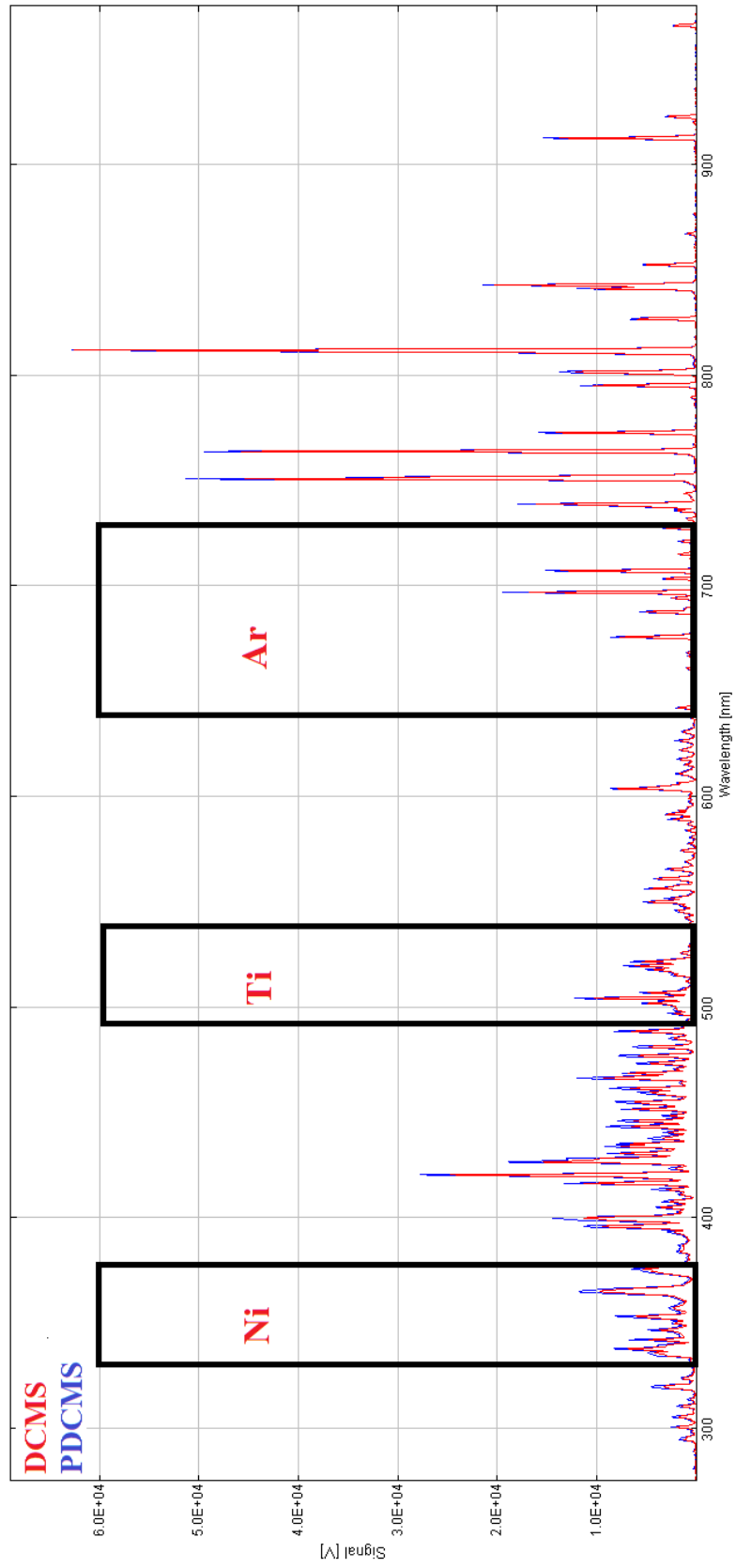
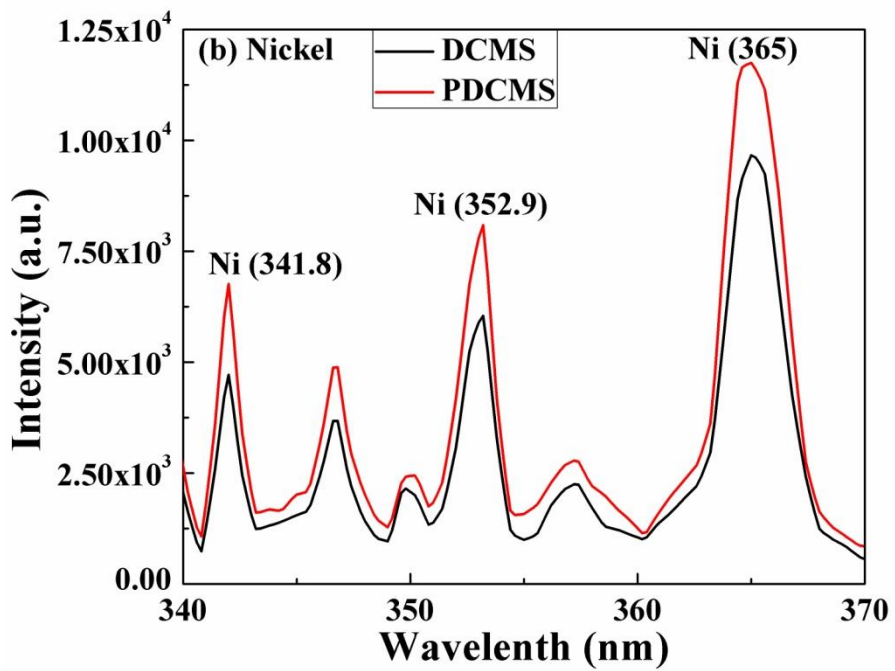
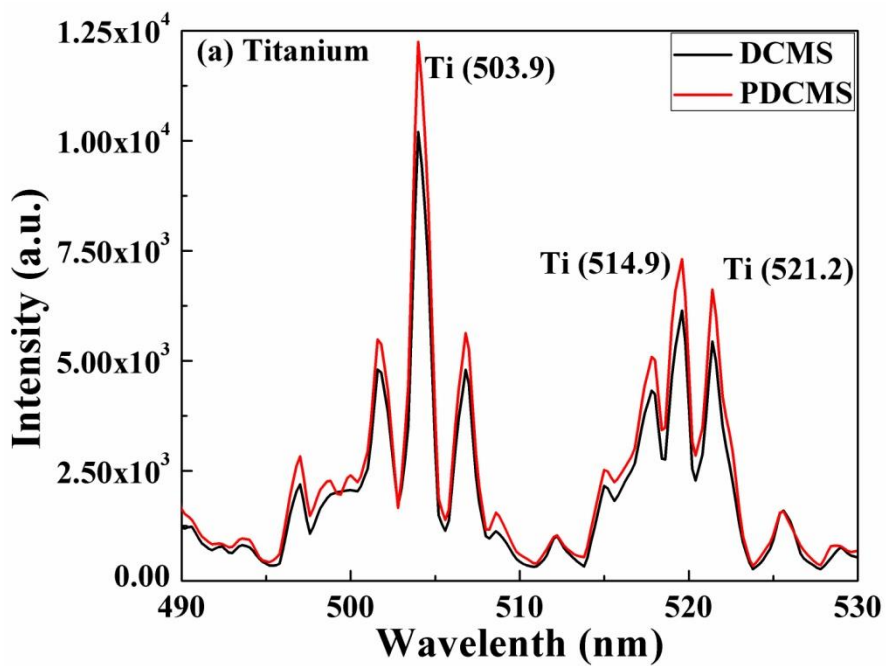


Figure 3.16: Wide spectra of both DCMS and PDCMS NiTi magnetron plasma



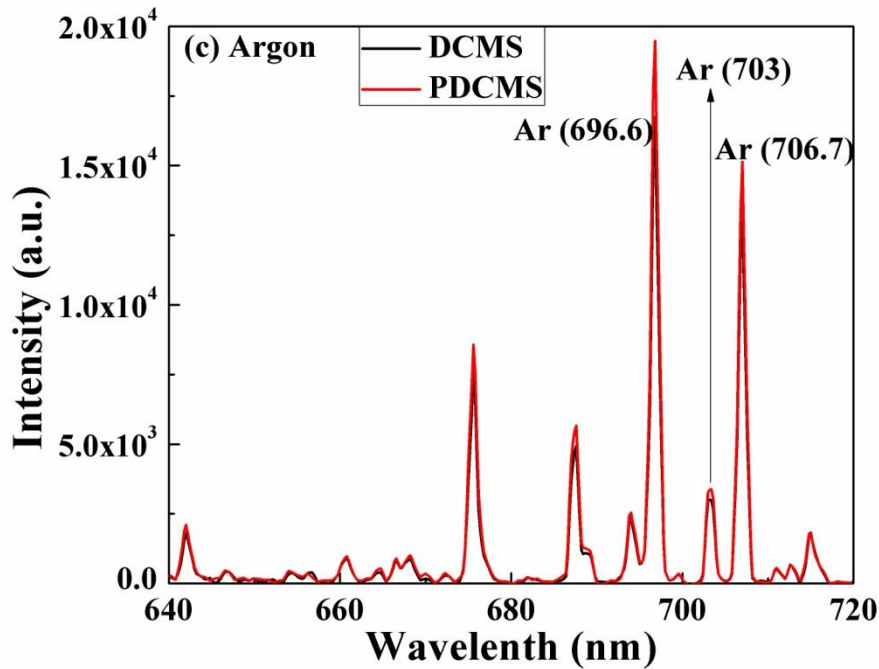


Figure 3.17: Optical emission spectra of DCMS and PDCMS sputtered (a) titanium, (b) nickel, and (c) argon.

3. 6. Conclusions

The process chamber's vacuum diagnosis was initially carried out using a residual gas analyzer to ensure the optimum vacuum condition for processing high-quality films with repeatable properties. To begin with, the NiTi thin films were deposited by the conventional DCMS technique. The deposition rate is stable with the process and meets the minimum thickness requirement to exhibit the shape memory effect. The DCMS-deposited NiTi thin films need to be deposited at further elevated temperatures or post-deposition annealed to obtain the crystalline films. To study the impact of the PDCMS process on the plasma behavior and film properties, a comparative study of the same was carried out along with DCMS under similar processing conditions. The microstructure, surface topography, and phase change studies of the NiTi films have been investigated. It was observed that the substrate temperature during film growth plays a significant role in the crystallization behavior of NiTi thin films. It has also been observed that the PDCMS NiTi thin film exhibited better crystalline properties. To study this behavior, the plasma properties of both the deposition processes were *in-situ* monitored by an optical emission spectroscopy

(OES). The PDCMS plasma was found to be more intense than that of the DCMS under the same deposition conditions. The OES findings were recorded and correlated with the film properties.

CHAPTER 4

INFLUENCE OF VARIOUS PROCESS CONDITIONS ON THE PDCMS NiTi THIN FILM PROPERTIES

4. 1. Introduction

This chapter deals primarily with the PDCMS deposition of NiTi thin films under various processing conditions. The experiments were carried out under optimal deposition pressures and pulse frequencies etc. Subsequently, these films were characterized for studying their microstructural, surface topographic, and phase transformation properties. The structural studies of the NiTi films were carried out by X-ray diffraction (XRD), the surface topographic studies were conducted by atomic force microscopy (AFM) and scanning electron microscopy (SEM), and the thickness was measured using cross-sectional SEM. The phase transformation properties of the films were studied by high-temperature X-ray diffraction (HT-XRD). Finally, the properties of the NiTi films were analyzed and explained in detail.

4. 2. Effect of deposition pressures on the PDCMS NiTi plasma and thin film properties

In this study, nickel-titanium alloy thin films were deposited onto silicon substrates in a pure argon gas atmosphere by the PDCMS technique at various deposition pressures. Optical emission spectroscopy was used to characterize the excited nickel and titanium species in the plasma. The plasma characteristics have been correlated with the film properties. This study aimed to investigate the crystal structure of the NiTi films deposited at various pressures and their influence on the phase formation of NiTi films. The substrate temperature was set as 600°C and was chosen from the previous set of experiments as there was no significant change between the 600 and 650°C NiTi films. The detailed process parameters are given in Table 4.1.

Table 4.1: Process parameters of PDCMS NiTi thin films deposited at various pressures

Base pressure	1.5×10^{-6} mbar
Target	Ni-45at%Ti alloy - 99.99% pure
Substrate	P-type Silicon (100)
Sputter gas	Argon
<i>Deposition pressure</i>	2.5×10^{-3} mbar, 5×10^{-3} mbar, 7.5×10^{-3} mbar, 1×10^{-2} mbar
Substrate temperature	600°C
Substrate-to-target distance	9 cm
Pulsed DC power	100 W
Pulse frequency	200 kHz
Pulse reversal time	1.0 μ s
Deposition duration	1 hr

4. 2. 1. Plasma diagnose by optical emission spectroscopy

The NiTi plasma characteristics at various deposition pressures (2.5×10^{-3} , 5×10^{-3} , 7.5×10^{-3} , and 1×10^{-2} mbar) were *in-situ* recorded and analyzed through an optical emission spectrometer. Figure 4.1. shows the characteristics of optical emission spectra of individual elements (a) titanium (490 – 530 nm), (b) nickel (340 – 370 nm), and (c) argon (640 – 720 nm), respectively. The intensities of titanium, I_{Ti} , at 503.9, 519.4, and 521.2 nm, and nickel, I_{Ni} , at 341.8, 352.9, and 365 nm are steadily increasing with increasing deposition pressures. When the deposition pressure rises, the number of ions takes part in the reaction increases. The reason for the rise in plasma intensities is that a large number of particles are contributing to the reaction. This was verified by using the microstructure and surface analysis of the NiTi films. Compared to I_{Ti} and I_{Ni} , the argon lines (I_{Ar}) are more intense at 696.6, 703.1, and 706.7 nm because of the presence of a large concentration of excited argon atoms in the plasma. In addition, titanium and nickel require much higher energies for excited species formation, and that is the reason for their poor concentrations and peak intensities (Bendahan et al. 1995, Sahli et al. 2017).

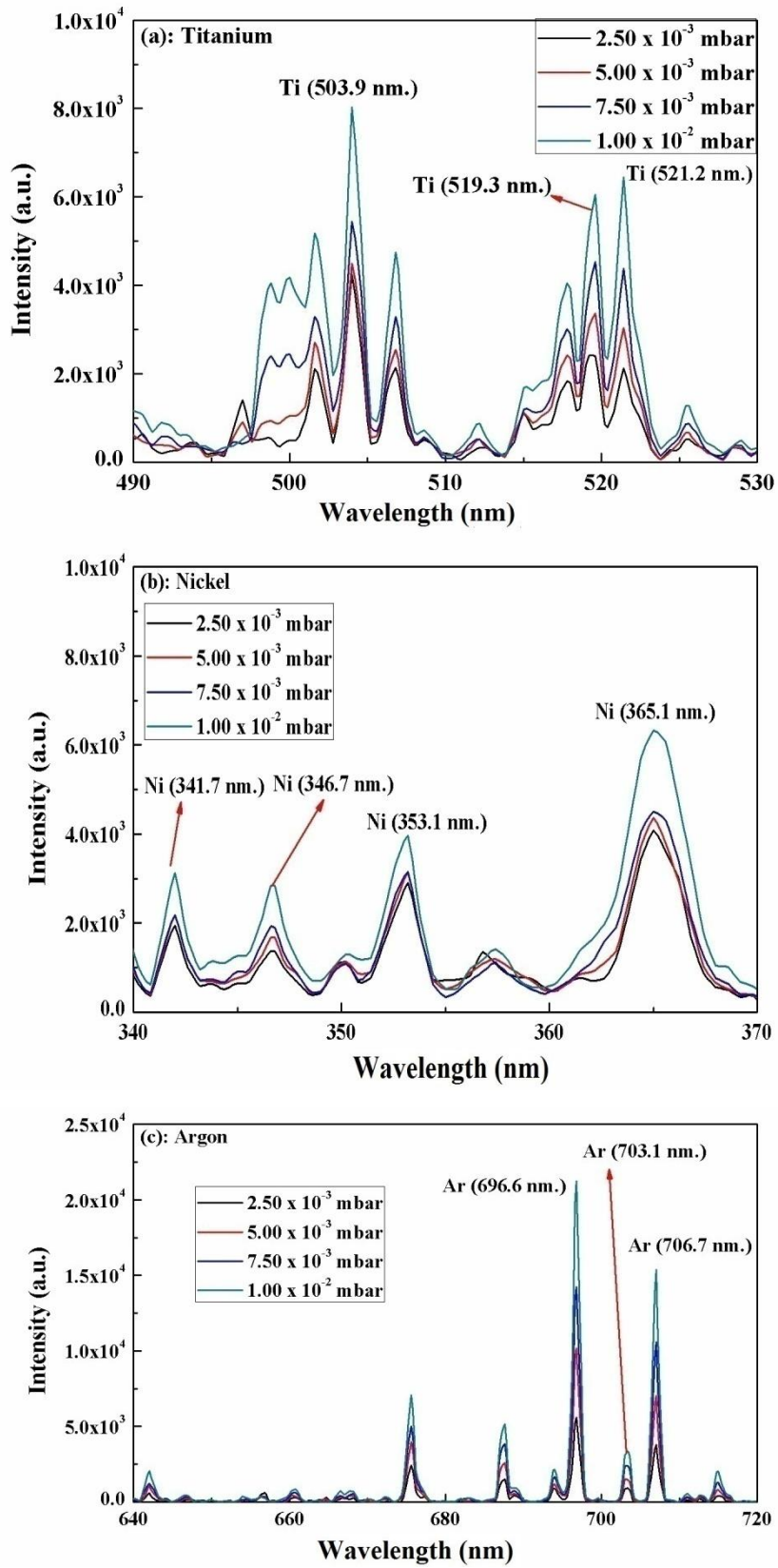


Figure 4.1: PDCMS NiTi plasma characteristics at various deposition pressures

4. 2. 2. Microstructural analysis

The room temperature XRD spectra of PDCMS NiTi thin films are shown in Figure 4.2. The XRD results reveal that the NiTi films deposited at 600°C with deposition pressures, 2.5×10^{-3} , 5×10^{-3} , and 7.5×10^{-3} mbar, are in polycrystalline nature and are in a mixed-phase at room temperature with a predominant austenitic phase (B2). The peak at 41.7° corresponds to the martensitic phase (B19') for (111) orientation. The strong peak at 42.6° corresponds to the austenitic phase (B2) for (110) orientation. But the NiTi deposited at the depositing pressure of 1×10^{-2} mbar shows the martensitic phase at room temperature. The peak at 41.7° corresponds to the martensitic phase (B19') for (111) orientation (Uchil et al. 2007, Fu et al. 2001, Ismail et al. 2012, Reddy et al. 2017). At lower deposition pressures, the mean free path of the sputtered atoms increases, which also enhances the energy of the sputtered atoms impinging at the substrates favoring the close-packed structure, which results in the austenitic phase at room temperature. But increasing the deposition pressure reduces the mean free path of the sputtered atoms. As a result, the energy of the sputtered atoms impinging on the substrate is also reduced (Weng et al. 2020). This results in the formation of the martensitic phase at room temperature (Chargui et al. 2020, Kabla et al. 2014). It is reported that, at higher temperatures ($>500^\circ\text{C}$), the enhanced activity of absorbed atoms on the substrate accelerates the migration of the atoms to favorable energy positions. As a result, it favors the formation of a close-packed structure to reduce the grown film's surface energy, which leads to the development of a strong (110) plane texture (Kumar et al. 2009, Murray et al. 1987, Saburi et al. 1986).

By calculating the full-width half-maxima (FWHM) from the XRD spectra, the crystallite size can be calculated using the Scherrer formula (Eq. 2.9). The calculated and average crystallite sizes of NiTi films deposited at various pressures are tabulated in Table 4.2.

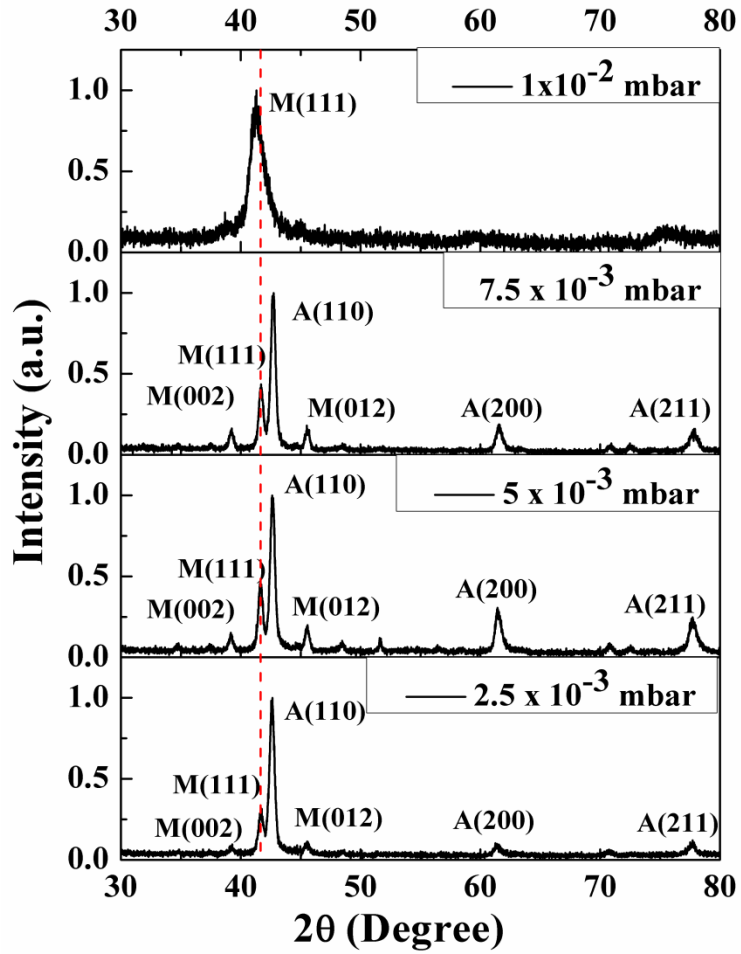


Figure 4.2: The RT-XRD spectra of PDCMS NiTi thin films deposited at pressures 2.5×10^{-3} mbar, 5×10^{-3} mbar, 7.5×10^{-3} mbar, and 1×10^{-2} mbar.

Table 4.2: Crystallite size of both PDCMS NiTi thin films deposited at pressures 2.5×10^{-3} mbar, 5×10^{-3} mbar, 7.5×10^{-3} mbar, and 1×10^{-2} mbar

Deposition Pressure (mbar)	M(111)	A(110)
2.5×10^{-3}	15.3	16.9
5×10^{-3}	17.7	17.5
7.5×10^{-3}	16.7	17.6
1×10^{-2}	5.32	---

4. 2. 3. Surface topographic and compositional studies

From the AFM results, it is clear that the roughness of the PDCMS NiTi thin films showed an increasing trend with the increase in the deposition pressure. Figure 4.3. shows the 3D images of the NiTi film surfaces by tapping mode AFM. The increase in the surface roughness can be attributed to the linear increase of the grain size as

well as the crystallinity of NiTi thin films with respect to the deposition pressures (Melo et al. 2004, Perron et al. 2008).

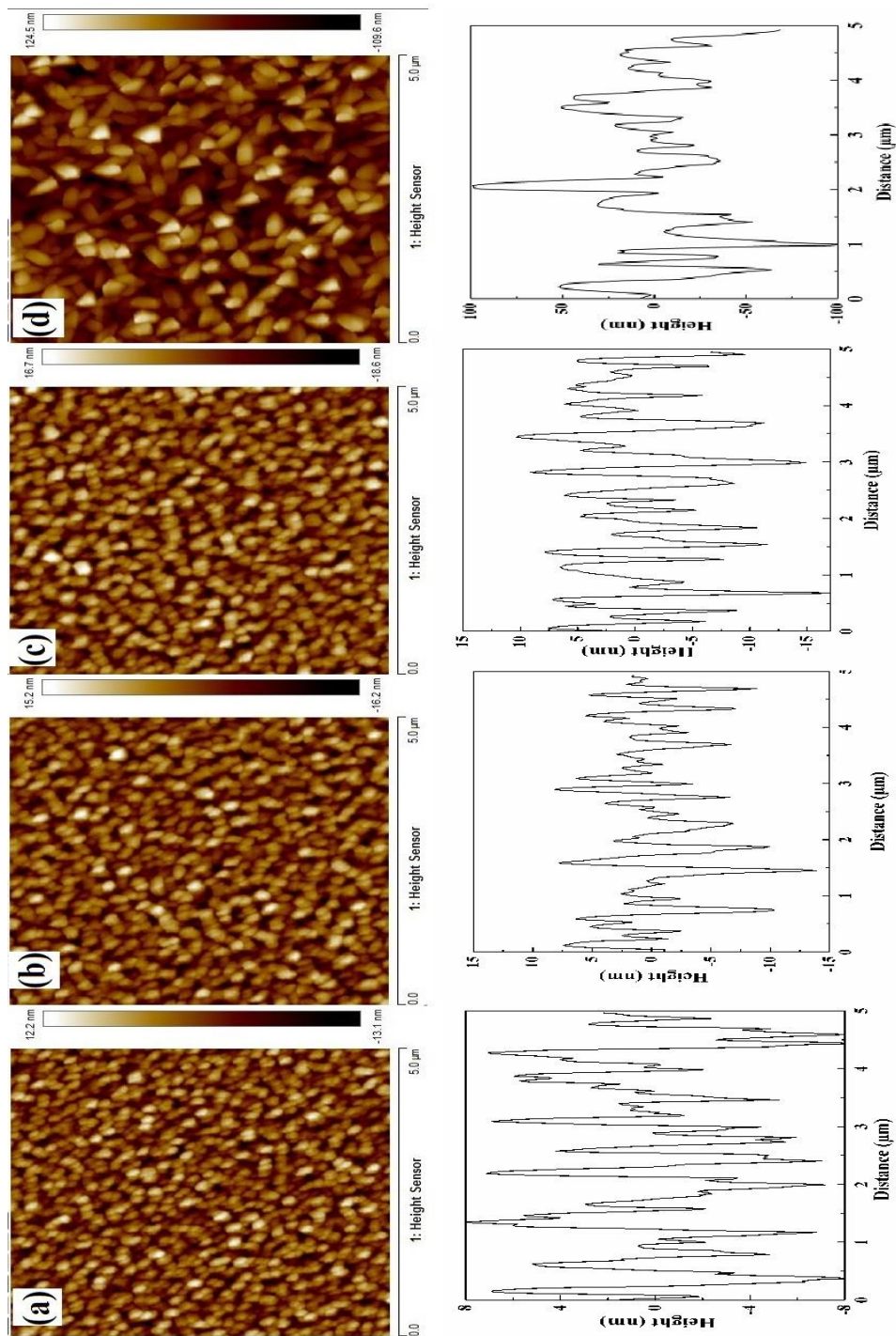


Figure 4.3: Upper panel: The AFM images of PDCMS NiTi films deposited at (a) 2.5×10^{-3} mbar, (b) 5×10^{-3} mbar, (c) 7.5×10^{-3} mbar, and (d) 1×10^{-2} mbar. Lower panel: Corresponding height profiles.

The SEM images are shown in Figure 4.4. reveal that the PDCMS NiTi thin films are crystalline. The grain sizes of the NiTi thin films increased with the deposition pressures (Kumar et al. 2009). Grain sizes of the NiTi thin films are under 100 nm for films deposited at pressures 2.5×10^{-3} and 5×10^{-3} mbar and are slightly higher than 100 nm for the films deposited at 7.5×10^{-3} mbar. But the NiTi film deposited at 1×10^{-2} mbar has grain sizes of nearly 200 nm. It has been reported that the phase transformation temperatures are directly proportional to the grain size of the NiTi films. Films with larger gains exhibit phase transformation at higher temperatures, whereas those with smaller grains exhibit phase transformation at lower temperatures (Wang et al. 2013, Ainslie et al. 2019). Earlier studies reported that films with higher grain sizes (>100 nm) are required for the growth of the martensite (B19') phase near room temperature. However, the martensitic transformation temperatures of the films with smaller grain sizes (<100 nm) are significantly lower, even below room temperature (Kumar et al. 2009, Ahadi et al. 2013). The SEM results are in good agreement with the XRD and AFM results. Table 4.3 contains the compositional analysis of the NiTi thin films deposited at various pressures by EDS measurements.

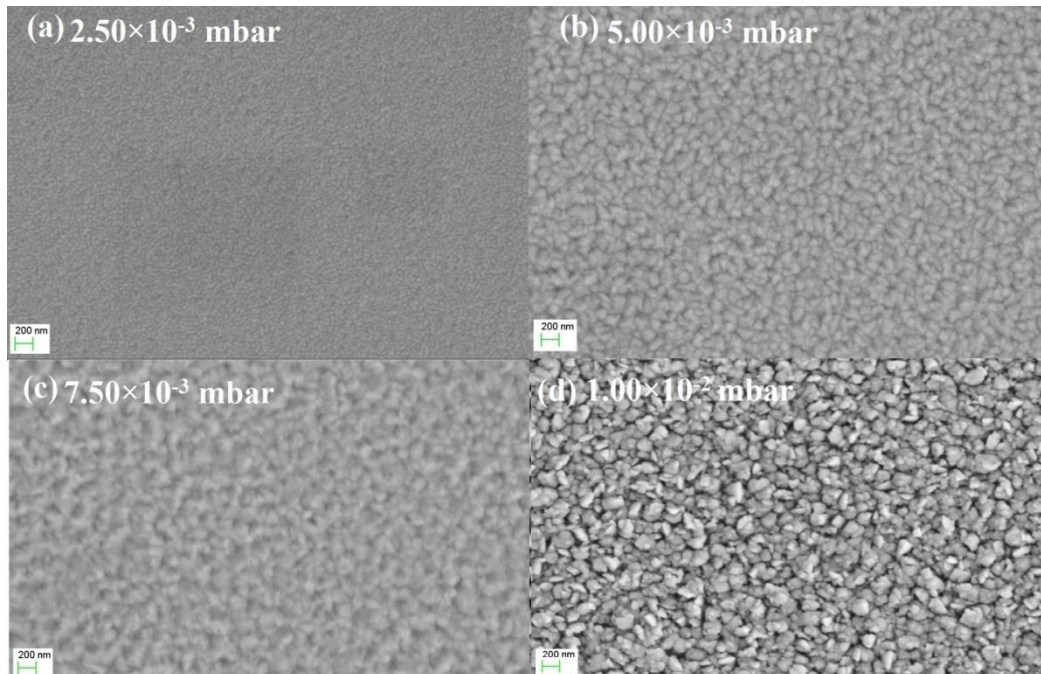


Figure 4.4: The FE-SEM image and grain size details of PDCMS NiTi films deposited at 2.5×10^{-3} mbar, 5×10^{-3} mbar, 7.5×10^{-3} mbar, and 1×10^{-2} mbar, respectively.

Table 4.3: The elemental composition of PDCMS NiTi thin films deposited at 2.5×10^{-3} mbar, 5×10^{-3} mbar, 7.5×10^{-3} mbar, and 1×10^{-2} mbar, respectively.

Deposition pressure (mbar)	Composition (Ni:Ti)
2.5×10^{-3}	56.29: 43.71
5×10^{-3}	54.38: 45.62
7.5×10^{-3}	57.08: 42.92
1×10^{-2}	55.87: 44.13

4. 2. 4. Phase transformation studies

The PDCMS deposited NiTi thin films at 1×10^{-2} mbar exhibited martensite phase at room temperature and have been chosen for phase transformation studies. The XRD stage temperature was increased, and the measurements were carried out. High-temperature XRD spectra exhibiting martensite-to-austenite phase transformation are shown in Figure 4.5. The XRD results show that the film exhibits the phase transformation from martensite-to-austenite on raising the stage temperature. The peak corresponding to the martensite phase (111) disappeared, and austenite's (110) orientation peak appeared. Besides, the (200) orientation of the austenite peak also appeared as the temperature was increased. This reveals the existence of the phase transformation in the NiTi thin films (Fu et al. 2001, Fu et al. 2006). For studying the phase transformations in the films deposited at pressures 2.5×10^{-3} , 5×10^{-3} , and 7.5×10^{-3} mbar, the XRD sample holder stage needed cooling. This study was not taken up as the interest was to fabricate devices performing at higher temperatures.

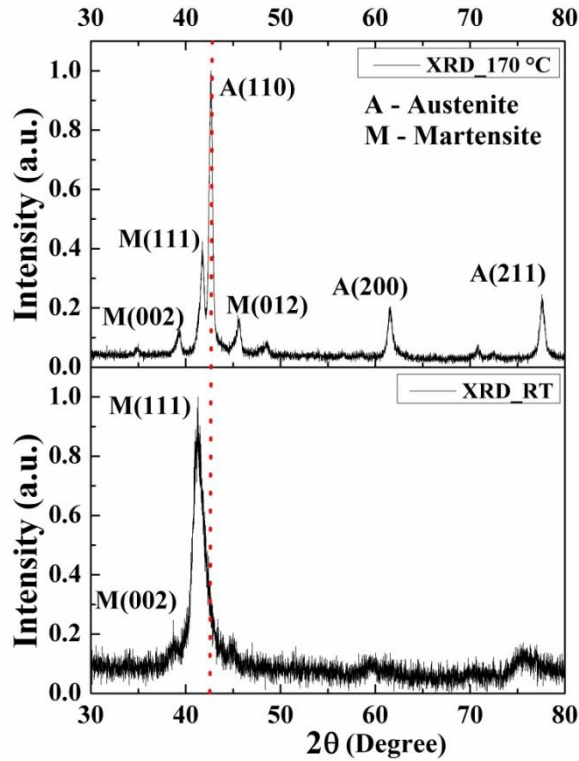


Figure 4.5: The HT-XRD spectra of room temperature martensite phase NiTi thin films deposited at 1×10^{-2} mbar

4. 3. Study of PDCMS NiTi plasmas and thin films properties deposited at various pulse frequencies

In this study, nickel-titanium alloy thin films were deposited onto silicon substrates in pure Argon gas ambient by PDCMS technique at various pulse frequencies. The optical emission spectroscopy was used to characterize the excited nickel and titanium species in the plasma. The plasma characteristics have been correlated with the film properties. This study aimed to investigate the changes in the properties of NiTi films deposited at various pulse frequencies. From the previous experiments, the substrate temperature was set as 600°C , and the deposition pressure was set as 1×10^{-2} mbar. The detailed process parameters are given in Table 4.4. The pulse frequencies used were 50, 100, 200, and 350 kHz. With changes in the pulse frequencies, the pulse reversal times were also varied by default. The details of the pulse frequency Vs. duty cycle and pulse reversal time are shown in Figure 4.6.

Table 4.4: Process parameters of PDCMS NiTi thin films deposited at pulse frequencies

Base pressure	1.5×10^{-6} mbar
Target	Ni-45at%Ti alloy - 99.99% pure
Substrate	P-type Silicon (100)
Sputter gas	Argon
Deposition pressure	1×10^{-2} mbar
Substrate temperature	600°C
Substrate-to-target distance	9 cm
Pulsed DC power	100 W
Pulse frequency	50, 100, 200 & 350 kHz
Deposition duration	1 hr

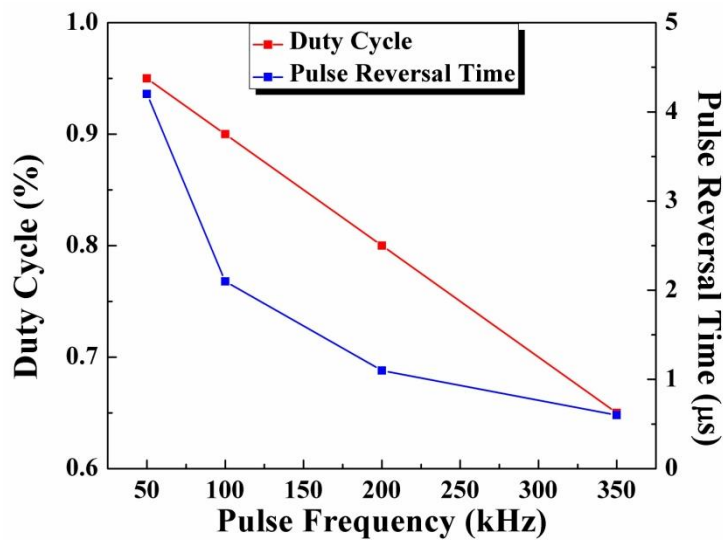
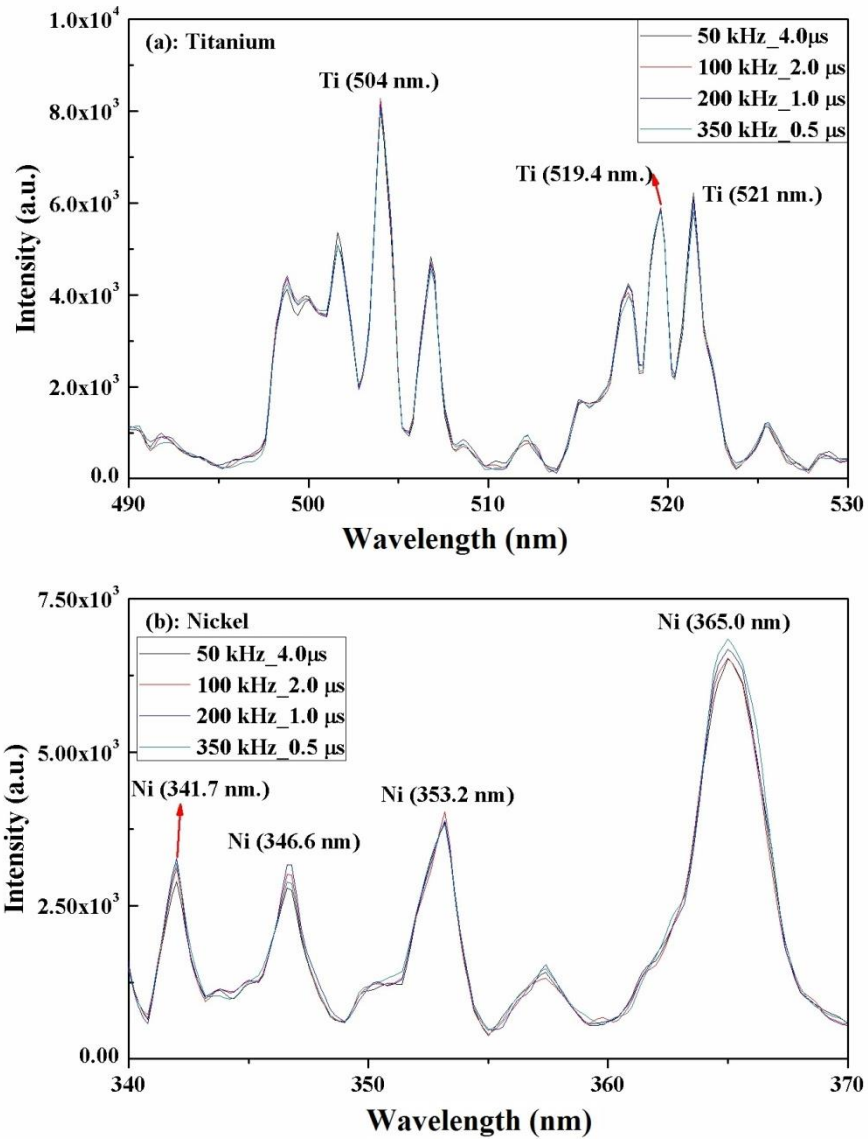


Figure 4.6: Plot between pulse frequency Vs. duty cycle and pulse reversal time

4. 3. 1. Plasma diagnose by optical emission spectroscopy

The emission spectra of PDCMS NiTi plasmas at various pulse frequencies (50, 100, 200, and 350 kHz) have been monitored, recorded, and plotted as spectral intensities Vs. wavelength plots. Figure 4.7. shows the characteristics of optical emission spectra of individual elements (a) titanium (490 – 530 nm), (b) nickel (340 - 370) and (c) argon (640 - 720) respectively. The intensities of titanium (I_{Ti} at 503.9, 519.4, and 521.2 nm) and nickel (I_{Ni} at 341.8, 352.9, and 365 nm) showed a minor increase with

the increase of pulse frequencies. These minor variations in the plasma intensities might not influence the NiTi film properties. As in the earlier cases, the argon lines (I_{Ar}) were more intense than those of I_{Ti} and I_{Ni} , because of the large argon concentration in the plasma (Bendahan et al. 1995, Sahli et al. 2017).



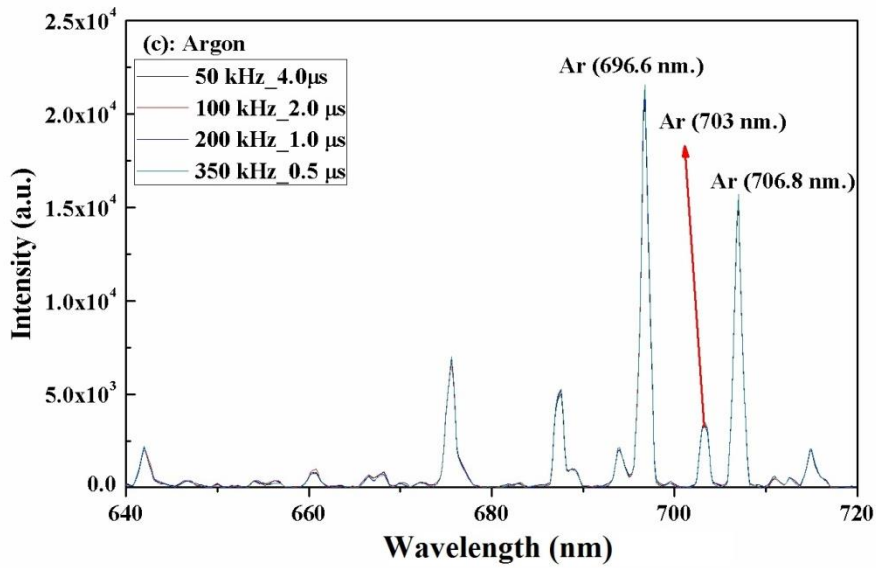


Figure 4.7: Optical emission spectra of pulsed DC sputtered (a) titanium, (b) nickel, and (c) argon at various pulse frequencies

4. 3. 2. *Microstructural studies*

The XRD spectra of PDCMS NiTi thin films are shown in Figure 4.8. From the spectra, it is clear that all the NiTi films deposited at 600°C and 1×10^{-2} mbar at pulse frequencies 50, 100, 200, and 350 kHz showed martensite phase (B19') at room temperature with a predominant peak at 41.7° corresponding to (111) orientation (Fu et al. 2001, Uchil et al. 2007). There was no significant variation in the peak intensities and crystalline nature of the NiTi films with change in the pulse frequencies. These films are expected to transform into an austenite phase upon external mechanical or thermal stimulus.

By calculating the full-width half-maxima (FWHM) from the XRD spectra, the crystallite size can be calculated using the Scherrer formula (Eq. 2.9). The calculated and average crystallite sizes of NiTi films deposited at various substrate temperatures are tabulated in Table 4.5.

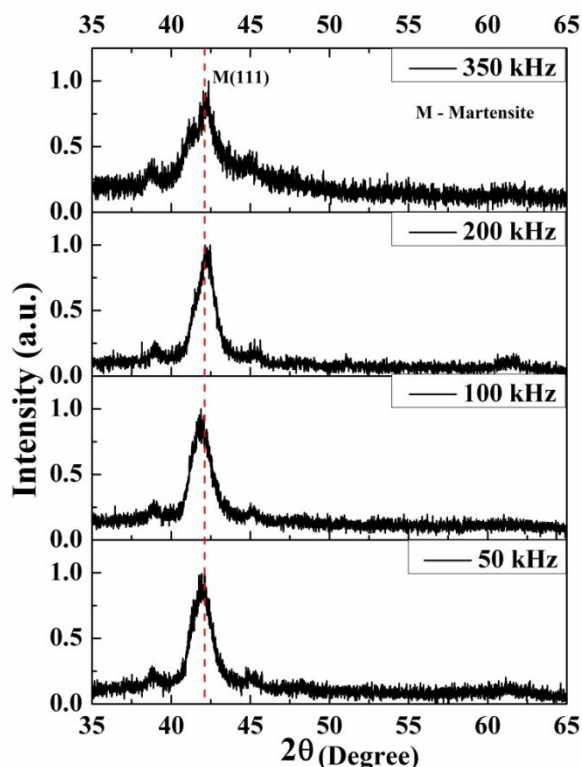


Figure 4.8: The RT-XRD spectra of PDCMS NiTi thin films at 600°C at pulse frequencies 50, 100, 200, and 350 kHz and 1×10^{-2} mbar

Table 4.5: Crystallite size of both PDCMS NiTi thin films deposited at pressures 50, 100, 200, and 350 kHz

Pulse frequency (kHz)	Crystallite size (nm) M(111)
50	5.3
100	5.4
200	5.6
350	2.3

4. 3. 3. Surface, compositional studies

Generally, PDCMS sputtered films exhibit lower surface roughness compared to those deposited by DCMS due to the influence of pulse parameters. For better smooth films PDCMS technique is preferred to DCMS. In this case, from the AFM results, it is clear that the roughness of the PDCMS NiTi thin films shows a decreasing trend with an increase in the pulse frequencies (Brien et al. 2001, Kelly et al. 2007, Kelly et al. 2009). Figure 4.9 shows the AFM images of the NiTi film surfaces by tapping mode AFM and corresponding height profiles. The decrease in the surface roughness

is due to the effect of pulse parameters. It is reported that the PDCMS films are smoother than those deposited by other magnetron sputtering techniques because of the pulse parameter effects (Brien et al. 2001, Kelly et al. 2007).

The SEM images shown in Figure 4.10 reveal that the NiTi thin films are crystalline. There were fewer variations in the grain sizes of the NiTi thin films with an increase in the pulse frequencies. However, they have shown a decreasing trend with increased pulse frequencies. It is reported that the film produced by the PDCMS deposition technique generally exhibits smoother surfaces (Kumar et al. 2009). The SEM results are in good agreement with the XRD and AFM results. Table 4.6 contains the compositional analysis of the NiTi thin films deposited at different pulse frequencies.

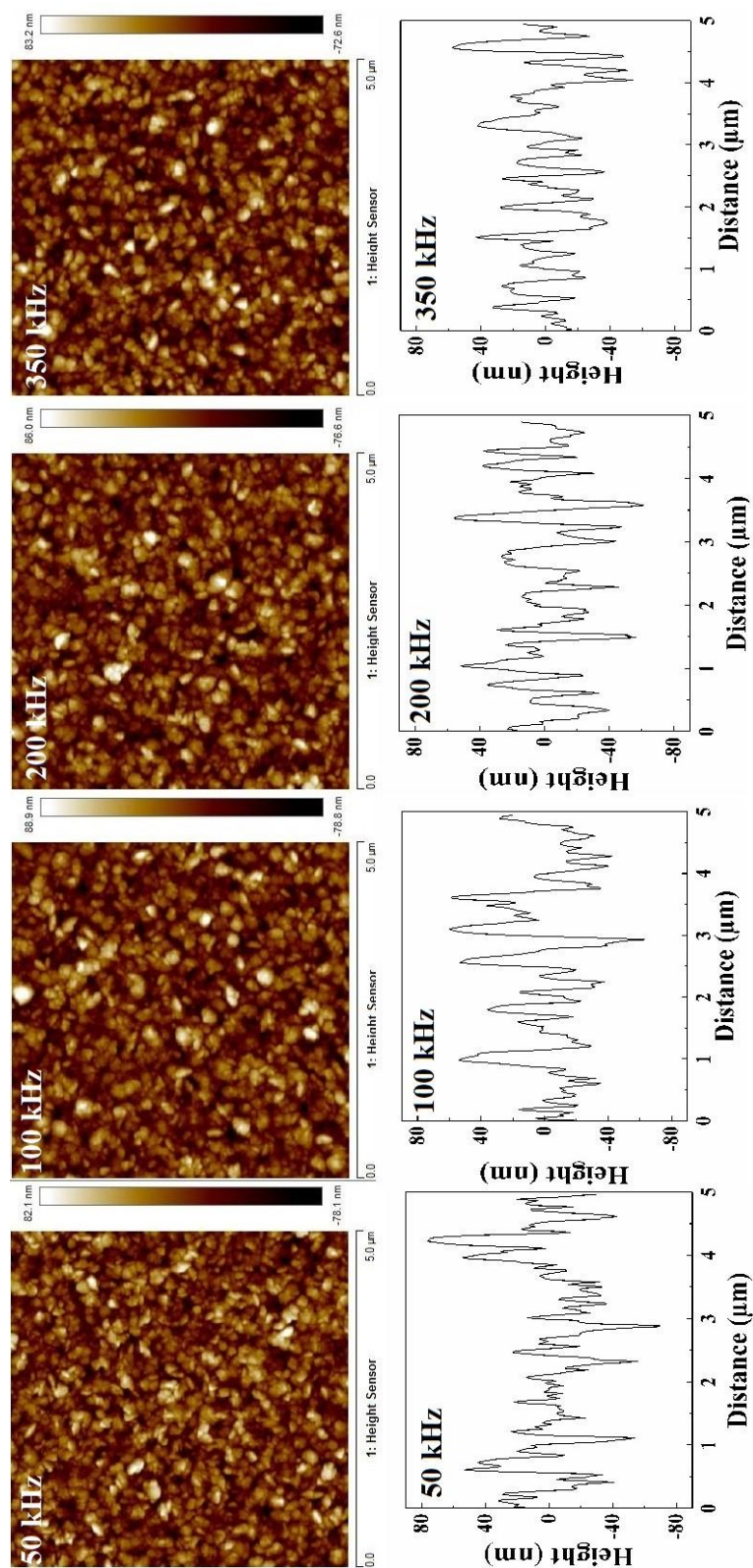


Figure 4.9: Upper panel: The AFM images of PDCMS NiTi thin films deposited at pulse frequencies 50, 100, 200, and 350 kHz. Lower panel: Corresponding height profiles.

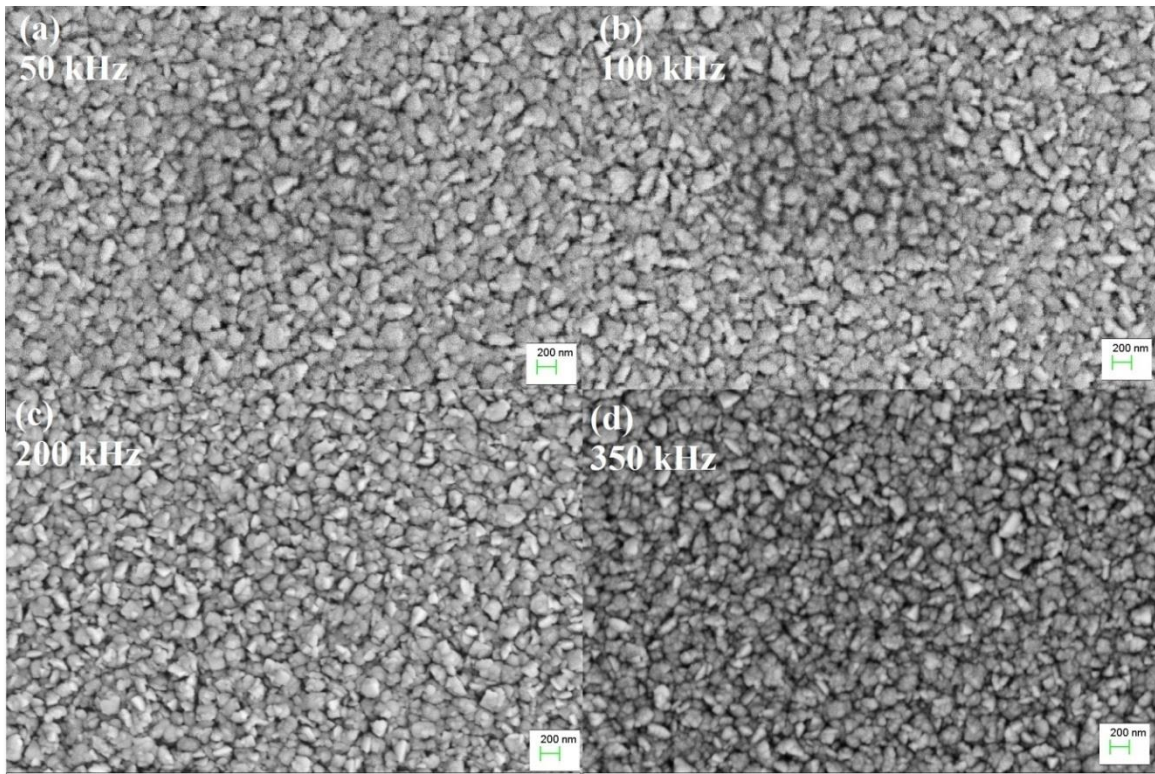


Figure 4.10: FE-SEM images and grain size details of PDCMS NiTi thin films deposited at pulse frequencies 50, 100, 200, and 350 kHz

Table 4.6: The elemental composition of PDCMS NiTi thin films deposited at pulse frequencies 50, 100, 200, and 350 kHz

Pulse frequency (kHz)	Composition (Ni:Ti)
50	53.2:46.8
100	52.8:47.2
200	54.4:45.6
350	52.6:47.4

4. 4. Conclusions

The NiTi films have been prepared using the PDCMS technique under optimal deposition pressures and pulse frequencies. The plasma characteristics of the films deposited at various deposition pressures and pulse frequencies were *in-situ* recorded. It was observed that, with the increase in the deposition pressure, the plasma density and sputtering fluxes were found to increase. The increases in the plasma density led

to the improvement in the NiTi film's crystalline nature. The influence of the deposition pressures, on the plasma characteristics, structural, surface, and phase transformation properties, have been investigated and correlated. It was also observed that the films deposited at 1×10^{-2} mbar exhibited martensite phase at room temperature, whereas all the other films deposited at lower pressures exhibited austenite phase. At higher deposition pressures, the probability of collisions between the atoms that travel towards the substrate increases, which decreases the mean free path and incident energy of the adatoms reaching the substrate. The disordered martensite phase can be formed by reducing the impact energy of the deposited atoms. The phase transformation studies of the NiTi films deposited at 1×10^{-2} mbar were carried out, and were observed that with an increase in the temperature, the NiTi films transformed into the austenite phase. However, the NiTi films deposited at various pulse frequencies have shown similar properties. This is due to the smaller variations in the duty cycles with pulse frequencies and pulse reversal times that could not significantly impact the plasma strengths at the given power, 100W. There were no considerable variations in the OES spectra with changes in the duty cycles. The surface roughness and grain size have shown a decreasing trend with increased pulse frequencies as expected with the PDCMS processes.

CHAPTER 5

PULSED DC MAGNETRON SPUTTER (PDCMS) DEPOSITION OF TITANIUM NITRIDE THIN FILMS

5. 1. Introduction

Generally, the Ti-rich nickel-titanium (NiTi) films easily undergo surface oxidation as Ti exhibits a very strong oxygen affinity. Hence, a capping layer on the NiTi thin films will be an ideal solution for overcoming this problem. The titanium nitride (TiN) thin layer on NiTi films is better for a capping layer because of its excellent mechanical and biocompatibility features. In addition, TiN films with specific crystal orientations result in the enhanced mechanical properties of the NiTi-based thin film structures. In this chapter, apart from the above-mentioned uses, we explored the heating capabilities of TiN films as MEMS hotplates for inducing the phase transformations in the NiTi-based MEMS devices. This chapter discusses the experiments and results of PDCMS titanium nitride thin films deposited under various process conditions.

5. 2. Calibration of the experimental setup

5. 2. 1. Vacuum diagnose of process chamber at various conditions using residual gas analyzer

The quality of the high vacuum is analyzed using a residual gas analyzer fixed with the process chamber. As Ti easily reacts with oxygen, TiO_xN_y can be formed easily which will degrade the properties of the films. Therefore, the residual gas analysis is necessary while dealing with high-quality TiN films with repeatable properties. The diagnosis procedure followed was similar as discussed in Chapter 3, Section 3.3. Partial pressures of the residual gases measured at various stages are shown in Figure 5.1. This chapter describes the studies on the TiN thin films deposited at various substrate temperatures and Ar:N₂ ratios. The partial pressures of argon and nitrogen gases at different Ar:N₂ ratios in the process chamber are shown in Figure 5.2.

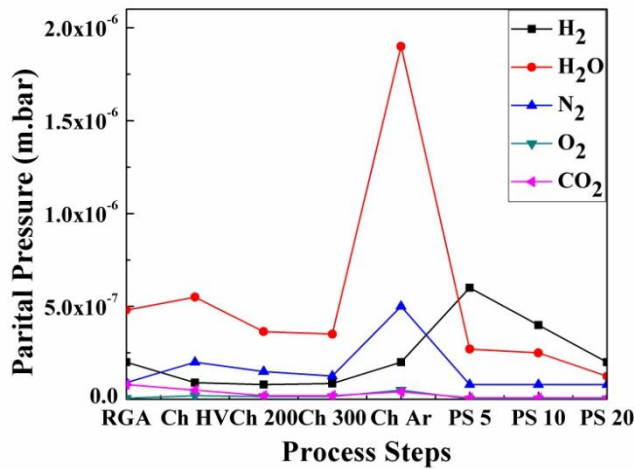


Figure 5.1: Partial pressures of major residual gases measured using a residual gas analyzer.

RGA → Background data recorded in RGA head - 5×10^{-7} mbar – Without exposing to the main process chamber.

Ch HV → Data recorded in the chamber during high vacuum – 1.5×10^{-6} mbar at room temperature.

Ch HV 200 → Data recorded in chamber high vacuum – 2.5×10^{-6} mbar at 200°C

Ch HV 300 → Data recorded in chamber high vacuum – 3×10^{-6} mbar at 300°C

Ch Ar → Data recorded after flowing argon gas (20 sccm) into the chamber. Moisture and nitrogen levels were found to increase with argon flow. Argon gas partial pressure is eliminated from the plot to highlight the residual gases.

PS 5 → Data recorded after titanium pre-sputtering for 5 min. 5×10^{-3} mbar and 300°C

PS 10 → Data recorded after titanium pre-sputtering for 10 min. 5×10^{-3} mbar and 300°C

PS 20 → Data recorded after titanium pre-sputtering for 20 min. 5×10^{-3} mbar and 300°C

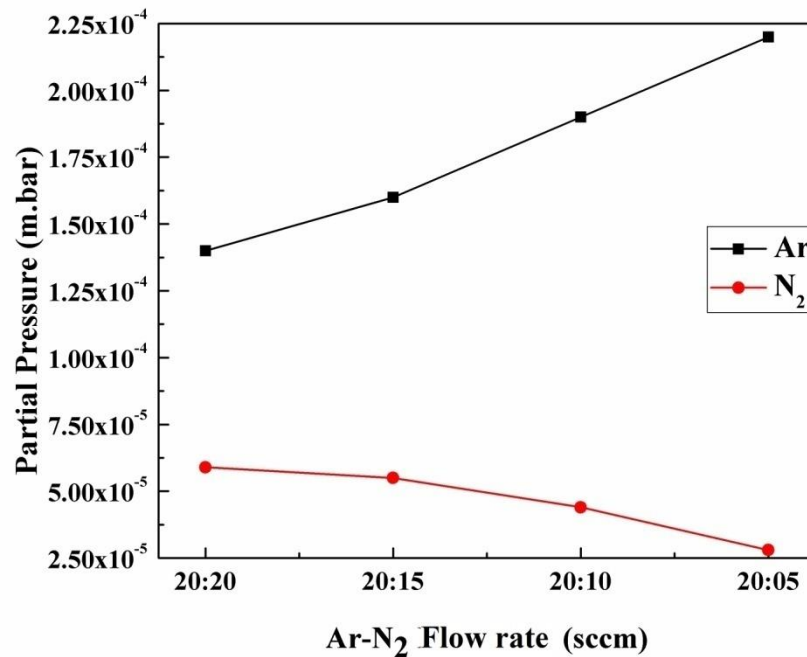


Figure 5.2: Partial pressures of both argon and nitrogen gases at different Ar:N₂ ratios

5. 2. 2. TiN plasma diagnose using optical emission spectroscope

Optical spectroscopy is widely used to monitor plasma, especially while dealing with the reactive processing of materials. The OES is used to study the TiN *in-situ* plasma concentration by analyzing the spectra obtained. While dealing with TiN thin films, monitoring the concentration of nitrogen plasma is important as the reactive nitrogen species can influence the structural properties of the TiN films (How et al. 2017).

In this study, the TiNPDCMS plasma characteristics were recorded and are shown in Figure 5.3. The plasma properties of titanium's emission spectra are generally collected in the region of 300 – 500 nm. Similarly, nitrogen and argon emission spectra are collected from 575 – 675 nm and 700 - 850 nm, respectively (Nafarizal et al. 2009, How et al. 2018, NIST Database). The detailed studies on the TiN plasma characteristics with variation in the process parameters are discussed below.

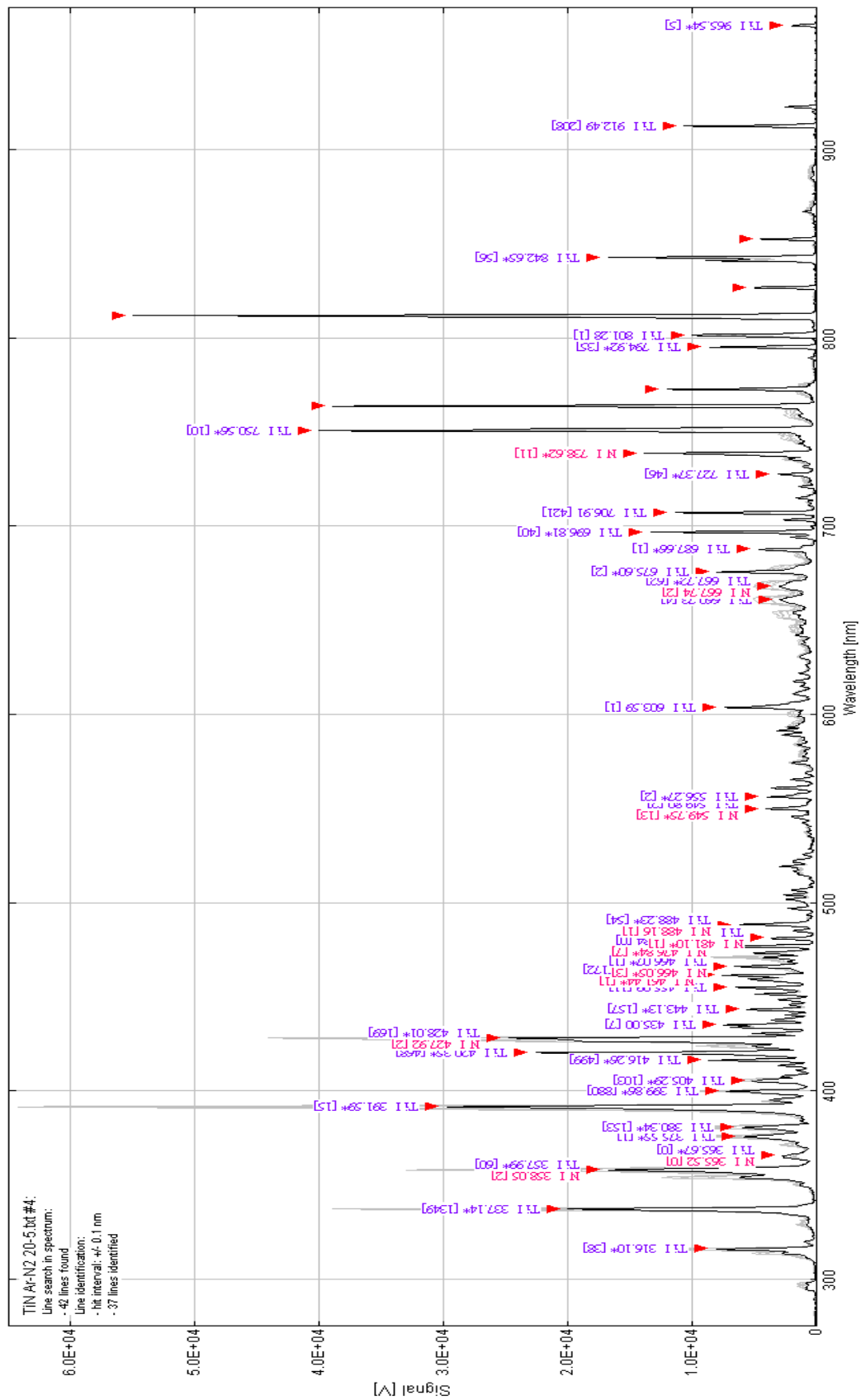


Figure 5.3: OES spectral analysis of PDCMS TiN plasma

Typical emission spectra of PDCMS TiN plasmas from the Ti target are shown in Figure 5.4. The nitrogen flow was varied between 0 and 20 sccm with an increment of 5 sccm.

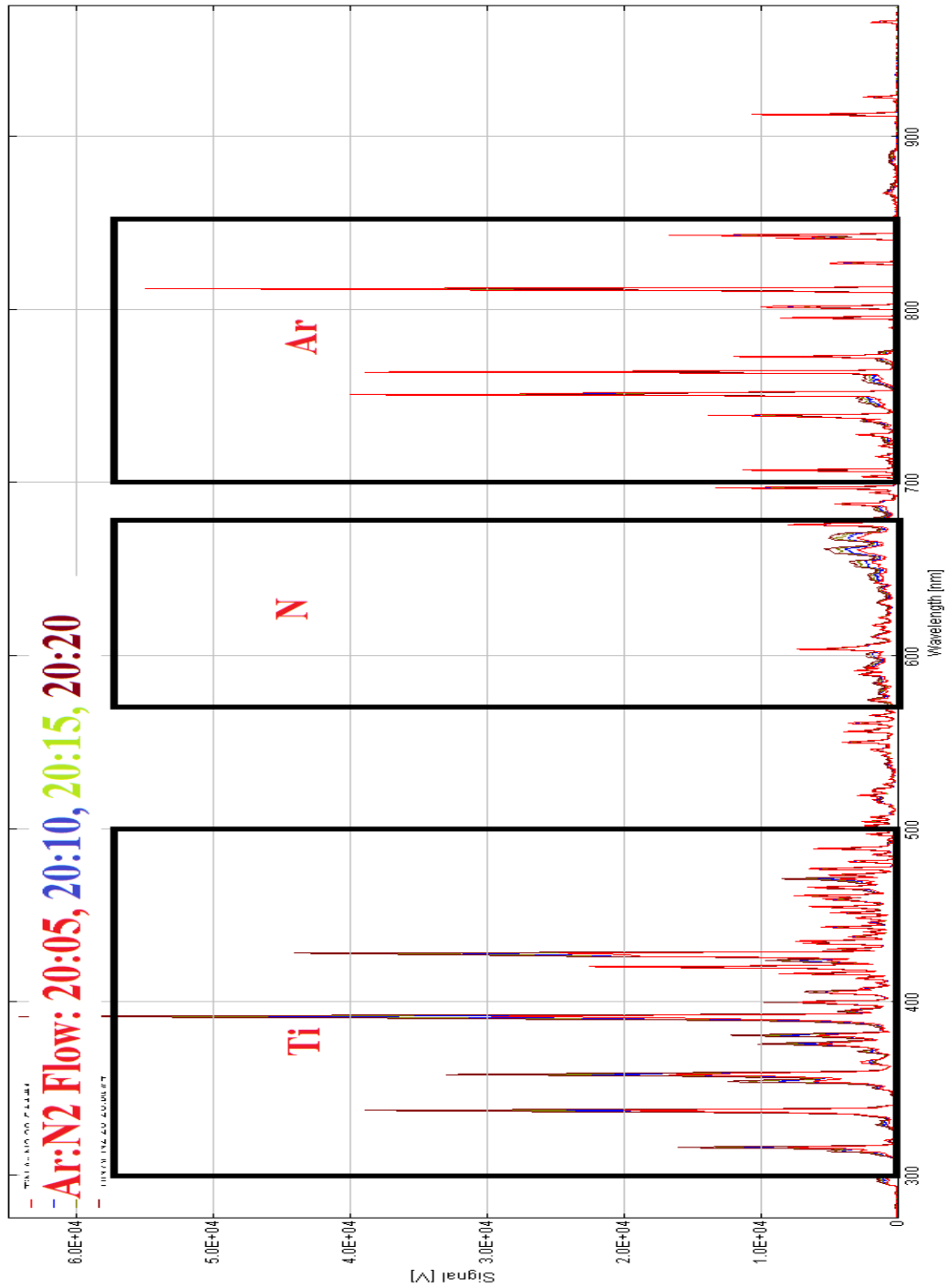
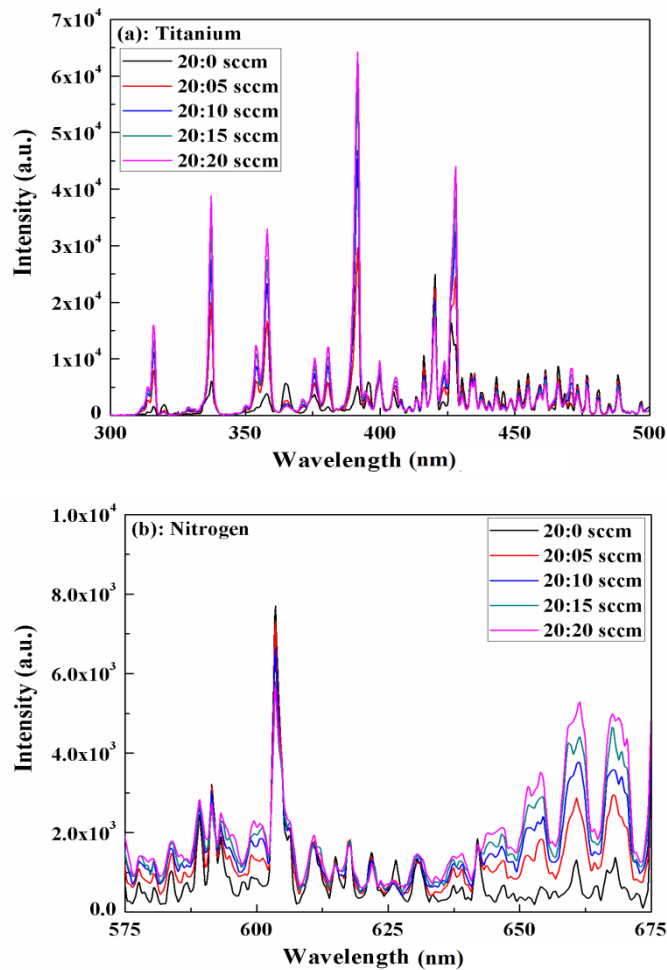


Figure 5.4: Wide range emission spectra of PDCMS TiN plasmas at various nitrogen flow rates.

From the NIST database, each of the elemental emission spectra was confirmed. Figure 5.5. shows the elemental spectra of (a) titanium, (b) nitrogen, and (c) argon metastables and ions (How et al. 2017, Hafiz et al. 2018, NIST 2019). The intensities of titanium and nitrogen emissions increased with the increase in the nitrogen flow rate. While the argon emission intensities were found to decrease with an increase in the nitrogen flow rates. This can be explained by correlating with the RGA findings shown in Figure 5. 2. The nitrogen partial pressures increased and dominated their presence in the process chamber with an increase in the nitrogen flow rates. Consequently, the partial pressure of argon gas was found to decrease. Hence, the intensities of argon-excited species decreased with an increase in the intensities of excited nitrogen species in the plasma.



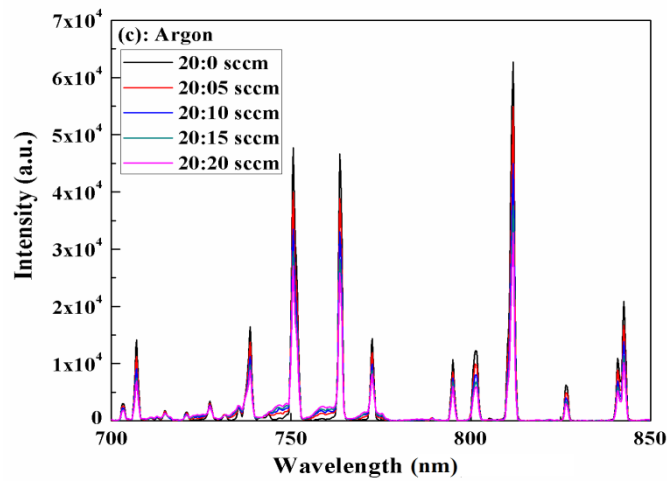


Figure 5.5: Elemental spectra of (a) titanium, (b) nitrogen, and (c) argon in PDCMS TiN plasmas at various nitrogen flow rates.

5. 3. Effect of substrate temperature on TiN thin film properties

TiN thin films were deposited by pulsed DC magnetron sputtering (PDCMS) on silicon (100) substrates. Before the deposition, the Si substrates were pre-cleaned by using deionized water followed by acetone ultrasonic sonication to remove the organic contaminants. Then the Si wafers were dipped in diluted hydrogen fluoride solution to remove the native oxygen layer. The process chamber was evacuated before the deposition using a rotary - cryogenic pumping combination to a base pressure of 1.5×10^{-6} mbar. The target used was a 99.99% pure Titanium disc of 76.2 mm diameter. Argon gas was used as the sputter gas, and the flow rate of the sputter gas was maintained at 20 sccm in all the experiments. Nitrogen gas was used as the reactive gas, and its flow rate was maintained at 5 sccm. The depositions were carried out at varied substrate temperatures between room temperatures and 300°C in increments of 100 using a resistive heater setup. Initially, the Ti target was pre-sputtered for about 20 min. with only argon gas to avoid oxidation at the target surface. The reactive gas (nitrogen) was admitted into the chamber in the next step. The chamber working pressure was maintained constant at 5×10^{-3} mbar using a manually operated gate valve after argon and nitrogen gases were passed into the chamber. The target was powered using a pulsed DC power supply (Pinnacle plus) with a power at 100W, pulsed frequency at 200 kHz, and a time reversal of 1.0 μs . Later, a 200 nm thick SiO_2 layer was thermally grown on Si. The substrate-to-target

distance was kept at 9 cm as a 3” target gives better uniformity between STD 7 – 12 cm (Maissel et al. 1970). The details of the process parameters are listed in Table 5.1.

Table 5.1: Process parameters of PDCMS TiN thin films deposited at various substrate temperatures

Process parameters	PDCMS
Base pressure	1.5×10^{-6} mbar
Target	Ti - 99.99% pure
Substrate	P-type Silicon (100)& Si/SiO ₂
Sputter gas flow	Argon – 20 sccm
Reactive gas	Nitrogen – 5 sccm
Deposition pressure	5×10^{-3} mbar
Substrate temperature	RT, 100, 200, and 300°C
Substrate-to-target distance	9 cm
Pulsed DC power	100 W
Pulse frequency	200 kHz
Pulse reversal time	1.0 μ s
Deposition duration	40 min.

5.3.1. Microstructural studies

XRD spectra of the films (Figure 5.6) deposited at room temperature (TiN_RT), 100°C (TiN_100), 200°C (TiN_200), and 300°C (TiN_300) show that the films are polycrystalline. However, as the temperature increases, the crystallinity of the film increases. This is due to improved adatom mobility induced by thermal energy at higher temperatures (Thompson et al. 2000). TiN_RT shows only peaks corresponding to (111) and (220) orientations of TiN at 36.7° and 61.8°, respectively. The films TiN_100, TiN_200, and TiN_300 show additional peaks at 42.7°, which correspond to a (200) orientation of TiN, and its intensity increases with an increase in substrate temperature. This is not prominent in the TiN_100 film (Ponon et al. 2015, Ao et al. 2013, Arshi et al. 2012, Meng et al. 1997, Pelleg et al. 1991).

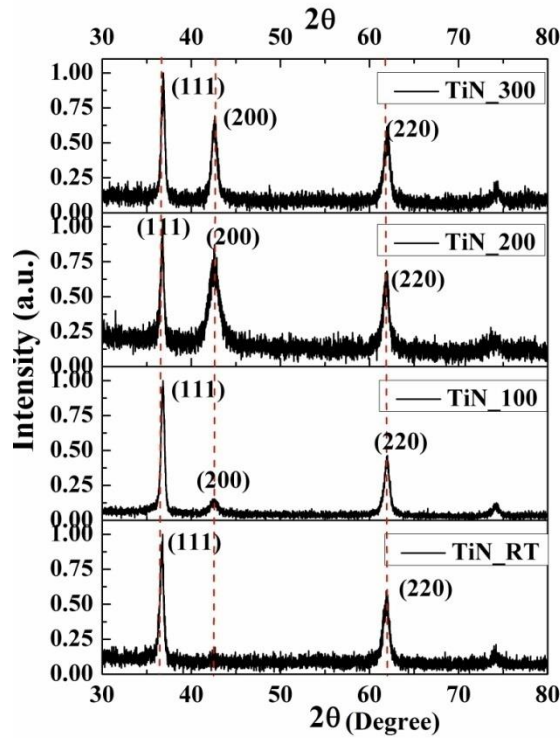


Figure 5.6: XRD patterns of PDCMS TiN films deposited at substrate temperatures of RT, 100, 200, and 300°C

By calculating the full-width half-maxima (FWHM) from the XRD spectra, the crystallite size can be calculated using the Scherrer formula (Eq. 2.9). The calculated and average crystallite sizes of TiN films deposited at various substrate temperatures are tabulated in Table 5.2. There was less variation in the crystallite size with a change in the deposition temperature. This might be due to the similar thicknesses of the TiN films in all the cases. In general, TiN grows in (111) orientation, although (200) and (220) orientations are also reported (Sundgren et al. 1985). Recent studies reveal the effect of the process conditions on the development of preferred orientation in TiN coatings (Ponon et al. 2015).

The texture coefficient of TiN thin films was calculated using Eq. 2. 10 and is shown in Table 5.2. The texture coefficient can quantify the preferred orientations in TiN thin films from their respective X-ray diffraction profiles. Where N is the number of diffraction peaks, and $I(h\ k\ l)$ and $I_o(h\ k\ l)$ are the measured and corresponding recorded intensities, respectively, given in the JCPDS data (Sharma et al. 2016). The

table shows that the texture coefficient of (200) orientation increases with substrate temperatures.

Table 5.2: Crystallite size and texture coefficient of TiN thin films deposited at various substrate temperatures, namely, RT, 100, 200, and 300°C.

Substrate Temperature (°C)	(111)		(200)		(220)		Average crystallite size (nm)
	D (nm)	TC	D (nm)	TC	D (nm)	TC	
RT	14.7	2.04	---	---	10.9	1.5	12.8
100	16.9	2.10	7.5	0.22	12.5	1.21	12.3
200	16.8	1.33	5.4	0.76	11.2	1.1	11.13
300	16.3	1.46	10.8	0.66	10.8	1.1	12.63

5. 3. 2. Surface topographic and compositional studies

The surface topography (2D) of the TiN films and the corresponding height profiles are shown in Figure 5.7. The surface roughness of the films deposited at higher temperatures shows an increasing trend with substrate temperature. However, the roughness decreased with an increase in the substrate temperature from room temperature to 100°C. This could be because of the origin of a (200) peak at higher deposition temperatures. From the XRD pattern, it is clear that though the room temperature film is crystalline, as the deposition temperature increases, the (200) plane appears, resulting in more crystallinity of the film. This might be the reason for the increase in surface roughness with the deposition temperature. Further investigation is needed to be carried out to understand this behavior.

The FE-SEM images of TiN films deposited at room temperature, 100, 200, and 300°C are shown in Figure 5.8. There was no considerable difference observed in the grain size of the films grown at different temperatures, and it is clear that all the films are crystalline. This is corroborated by the XRD analysis. The thickness of the TiN films measured from SEM imaging of fractured cross-sectional samples (Figure 5.9. for TiN_RT) is about $\sim 277 \pm 10$ nm. Using this, the deposition rate of the films can be calculated to be about ~ 7 nm/min.

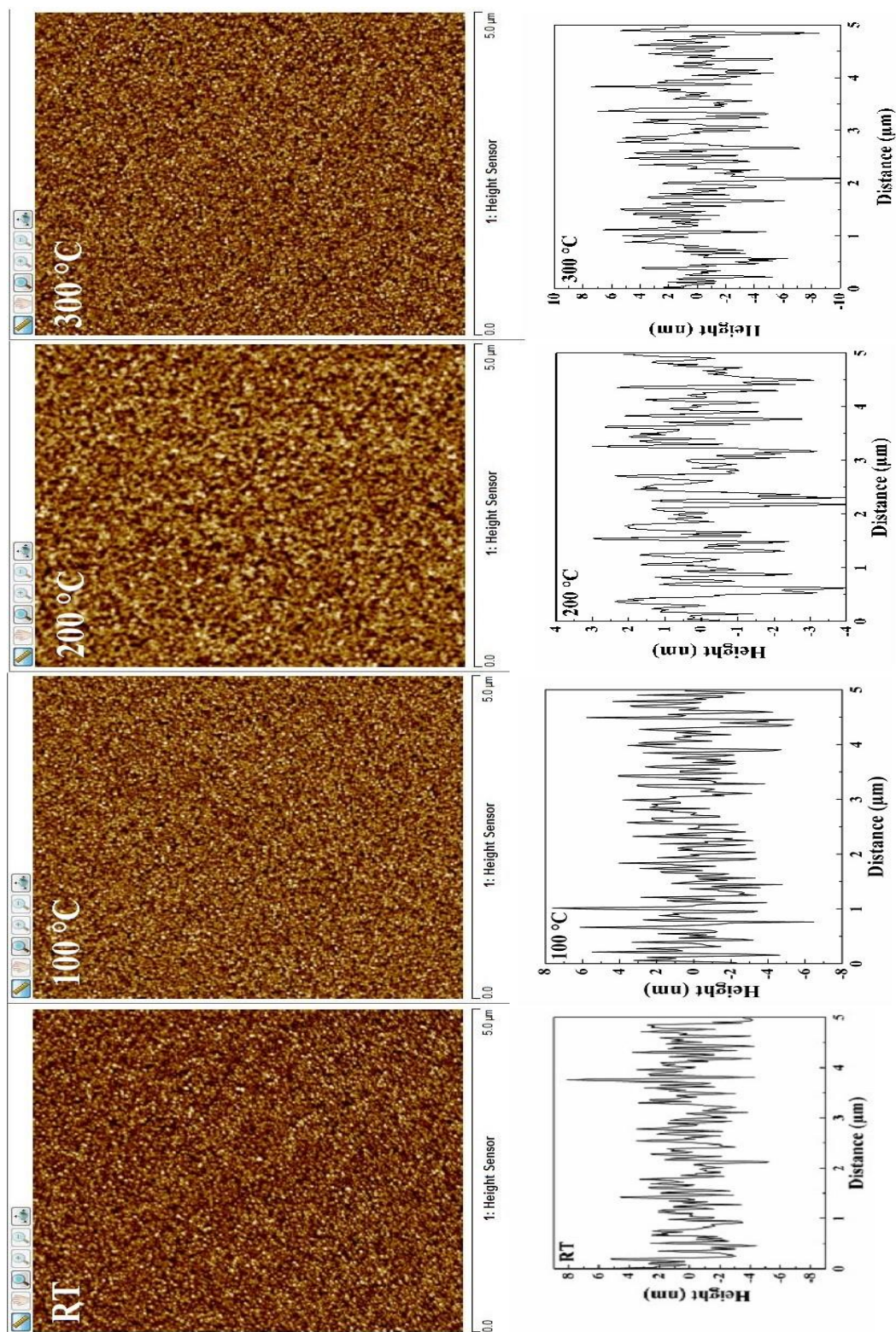


Figure 5.7: 2D surface images of PDCMS TiN film deposited at substrate temperatures of RT, 100, 200, and 300°C and corresponding height profiles.

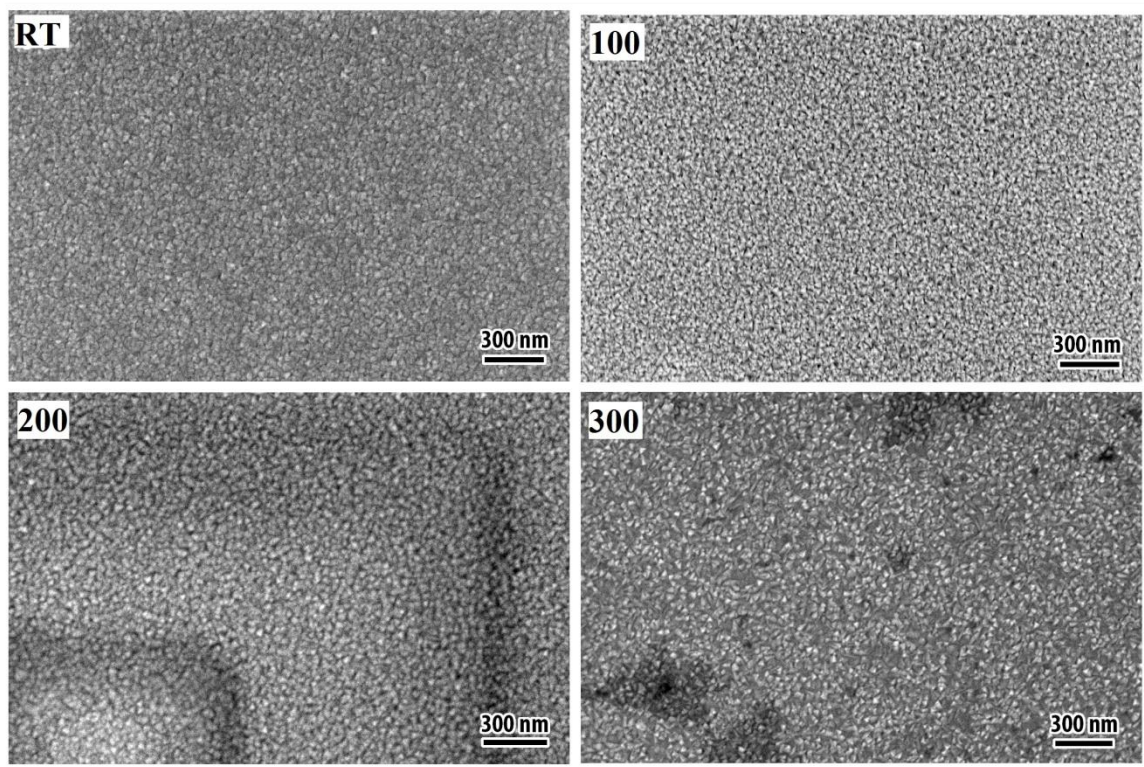


Figure 5.8: The FE-SEM images of PDCMS TiN films deposited at substrate temperatures of RT, 100, 200, and 300°C

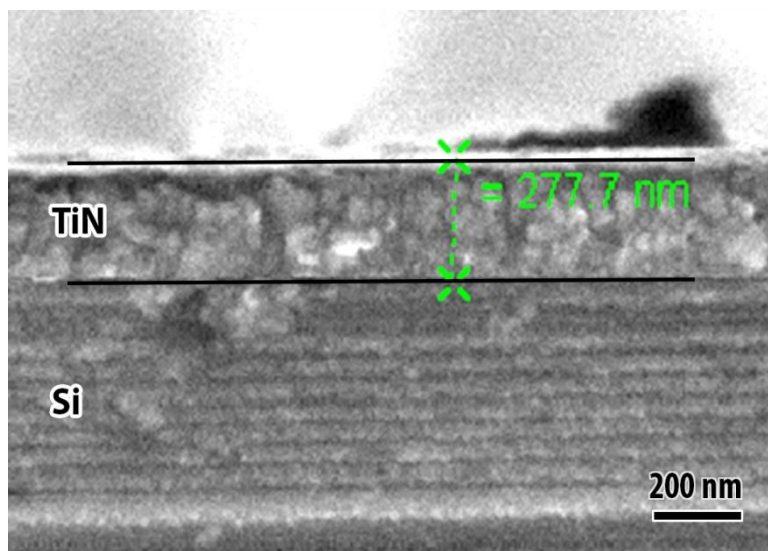


Figure 5.9: SEM image of the fractured cross-section of TiN_RT films

5. 3. 3. *Electrical studies*

The sheet resistance of the films TiN_RT, TiN_100, TiN_200 and TiN_300 are 30.29, 20.50, 15.94 and 11.10 Ω /Sq., respectively. The electrical resistivity of the TiN films

is calculated by multiplying the sheet resistance with the thickness of the films. Figure 5.10 shows the variation of resistivity of TiN film w.r.t. substrate temperature. From Figure 5.10, it is observed that the resistivity decreases with an increase in substrate temperature. It is reported that the TiN film with a high (200) diffraction peak intensity has a lower electrical resistivity (Arshi et al. 2012, Meng et al. 1995, Meng et al. 1997) compared to other-oriented planes. The XRD results (Figure 5.6) have shown that the intensity of the TiN (200) peak has increased with the increase in substrate temperature. Hence, the decrease in electrical resistivity with an increase in substrate temperature can be attributed to the presence of (200) planes in the TiN films deposited at higher substrate temperatures ($T > 200^{\circ}\text{C}$).

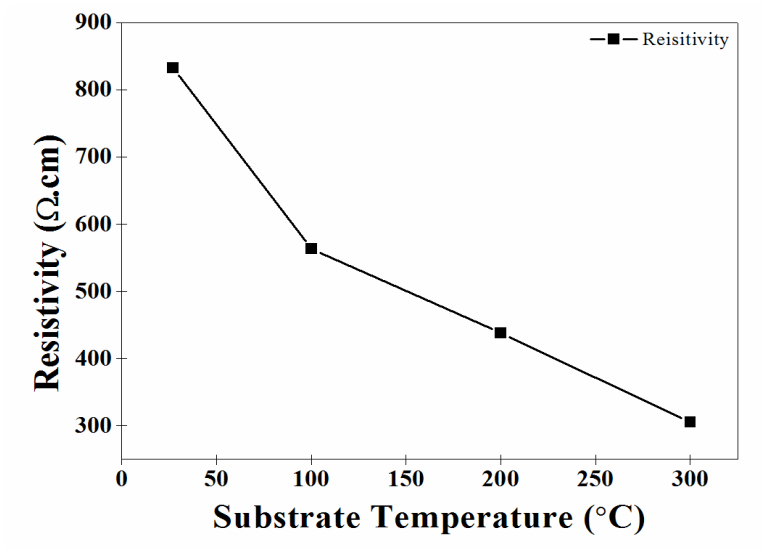


Figure 5.10: Variation of electrical resistivity of PDCMS TiN thin films deposited at different substrate temperatures

5. 4. Effect of the nitrogen partial pressure on the TiN thin film properties

From the previous section of this chapter, it may be recalled that the details regarding the TiN thin films deposited by the PDCMS technique at various substrate temperatures and with a 20:05 Ar:N₂ ratio were given. The process temperature (300 $^{\circ}\text{C}$), which yielded better electrical resistivity, has been kept constant, and further investigations were carried out by varying the nitrogen partial pressures. The duration of the depositions was varied to obtain films with approximately the same thickness (Lou et al. 1997). The details of the process parameters are listed in Table 5.3.

Table 5.3: Process parameters of PDCMS TiN thin films deposited at different Ar:N₂ ratios

Process parameters	PDCMS
Base pressure	1.5×10^{-6} mbar
Target	Ti - 99.99% pure
Substrate	P-type Silicon (100)& Si/SiO ₂
Sputter gas	Argon – 20 sccm
Reactive gas	Nitrogen – 20, 15, 10, 5 sccm
Deposition pressure	5×10^{-3} mbar
Substrate temperature	300°C
Substrate-to-target distance	9 cm
Pulsed DC power	100 W
Pulse frequency	200 kHz
Pulse reversal time	1.0 μ s
Deposition duration	Varied to achieve ~275 nm thickness

5.4.1. Microstructural studies

The PDCMS TiN thin films were deposited at different Ar:N₂ ratios and were subjected to X-ray diffraction studies (Figure 5.11). The XRD patterns show that the films deposited at 300°C with Ar:N₂ ratios of 20:20, 20:15, 20:10, and 20:5 were polycrystalline. The peaks were indexed using JCPDS powder diffraction files, and the peaks were well matched with the TiN phase of TiN films (JCPDS Card Nos. 38–1420 and 23–1455). The TiN films deposited at Ar:N₂ ratios of 20:5, 20:10, and 20:15 show the prominent (111) orientation at 36.7°. In addition, these films show the (200) and (220) orientations at 42.8° and 61.9°, respectively (Meng et al. 1997, Penilla et al. 2008, Saoula et al. 2009, Ao et al. 2013, Kumar et al. 2020). It has been observed that, with the increase in nitrogen partial pressure, the intensity of the (200) plane is also found to be increasing with the TiN_{20:20} film exhibiting predominantly (200) orientation. It has been reported that the increase of nitrogen content in the titanium nitride thin film causes defects and leads to the prominence of the (200) plane (Meng et al. 1997, Cuong et al. 2006, Chawla et al. 2009, Ponon et al. 2015).

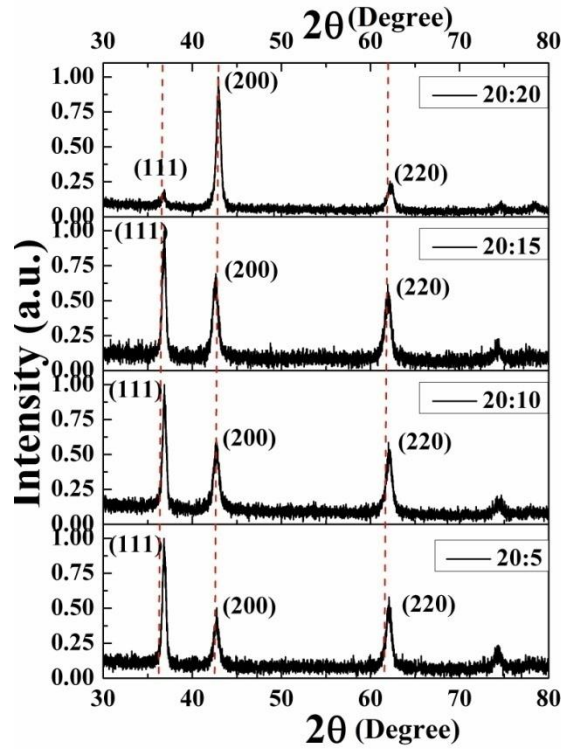


Figure 5.11: XRD patterns of PDCMS TiN films deposited at Ar:N₂ ratios of 20:20, 20:15, 20:10, 20:05

By calculating the full-width half-maxima (FWHM) from the XRD spectra, the crystallite size of TiN thin films was calculated from (111), (200), and (220) peaks using Scherrer's formula (Eq. 2.9), and the values are presented in Table 5.4. Irrespective of the variation in the orientations of the TiN films, the crystallite sizes were almost similar, which might be due to the similar thicknesses of the films. The most commonly observed orientation of TiN thin films was (111), although (200) and (220) orientations were also reported (Sundgren et al. 1985). More recently published reports discuss the effect of the process conditions on the development of preferred orientation in TiN coatings (Ponon et al. 2015).

The preferred orientations in the TiN thin films can be quantified by calculating the texture coefficient from their respective X-ray diffraction profiles using Eq. 2.10, shown in Table 5.4. Here N is the number of diffraction peaks, and $I(h\ k\ l)$ and $I_o(h\ k\ l)$ are the measured and corresponding recorded intensities, respectively, given in the JCPDS data (Sharma et al. 2016). From the table, it is clearly observed that the texture coefficient of (200) orientation increases with the increase of nitrogen partial pressure.

As per the literature, film orientation can influence resistivity, with (111) oriented films more resistive than (200) oriented films (Ponon et al. 2015).

Table 5.4: Crystallite size and texture coefficient of TiN thin films deposited at Ar:N₂ ratios of 20:20, 20:15, 20:10, and 20:05

Ar:N ₂ ratio (sccm)	(111)		(200)		(220)		Average crystallite size (nm)
	D (nm)	TC	D (nm)	TC	D (nm)	TC	
20:20	13.7	0.47	13.9	1.55	12.2	0.72	13.3
20:15	15.2	1.47	10.1	0.68	11.4	1.10	12.2
20:10	16.5	1.54	11.4	0.62	11.8	1.12	13.2
20:05	16.3	1.59	10.8	0.54	10.8	1.14	12.6

5.4. 2. Surface topographic studies

The AFM 2D images and their corresponding height profiles of the PDCMS TiN thin films deposited at 20:20, 20:15, 20:10, and 20:05 Ar:N₂ ratios of the substrate temperature of 300 °C are shown in Figure 5.12. The surface roughness of the films deposited at various Ar:N₂ ratios at 300 °C shows an increasing trend with a decrease in nitrogen flow rates, which is in good agreement with the previously reported results (Vaz et al. 2005, Ponon et al. 2015). However, there are a fewer variations in the roughness of the films. The average roughness lies between 1.6 and 3.0 nm for all the films. This might be because all the depositions were carried out at the same substrate temperature of 300 °C.

The FE-SEM images of PDCMS TiN films deposited at various Ar:N₂ ratios are shown in Figure 5.13. Less difference was observed between the grain sizes of the films grown at different Ar:N₂ ratios. Also, it is clear from the images that all the films are crystalline. This corroborates the microstructural XRD studies. The thickness of the TiN films measured from SEM imaging of the fractured surface of samples (Figure 5.14.) is about $\sim 250 \pm 10$ nm and $\sim 275 \pm 10$ nm for 20:20 and 20:05, respectively. The thicknesses were maintained approximately equal by varying the deposition duration to compare the electrical resistivity more precisely (Berg et al. 1986).

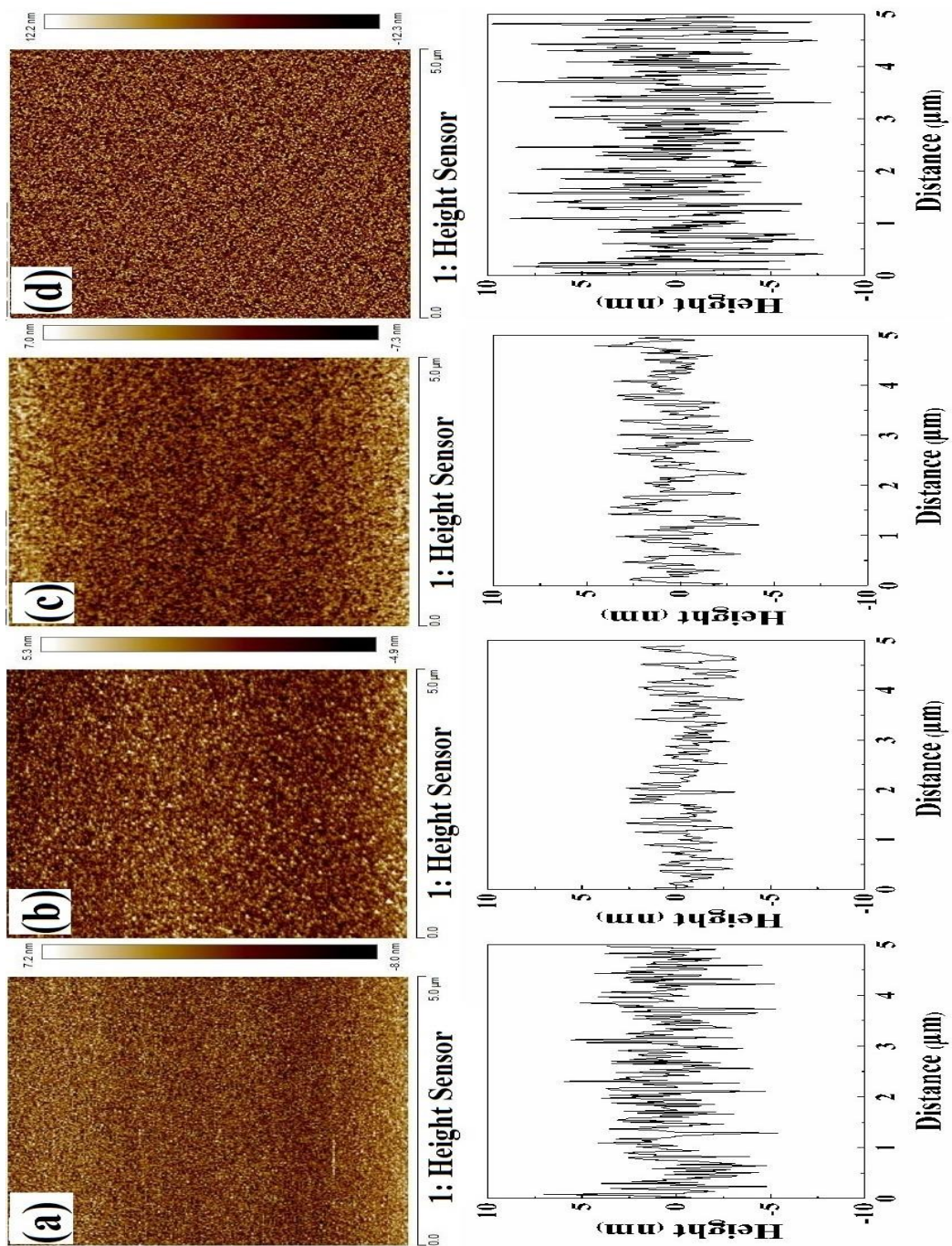


Figure 5.12: Upper panel: 2D surface topographies of the PDCMS TiN films deposited at Ar:N₂ ratios (a) 20:20, (b) 20:15, (c) 20:10, and (d) 20:05. Lower panel: Corresponding height profiles.

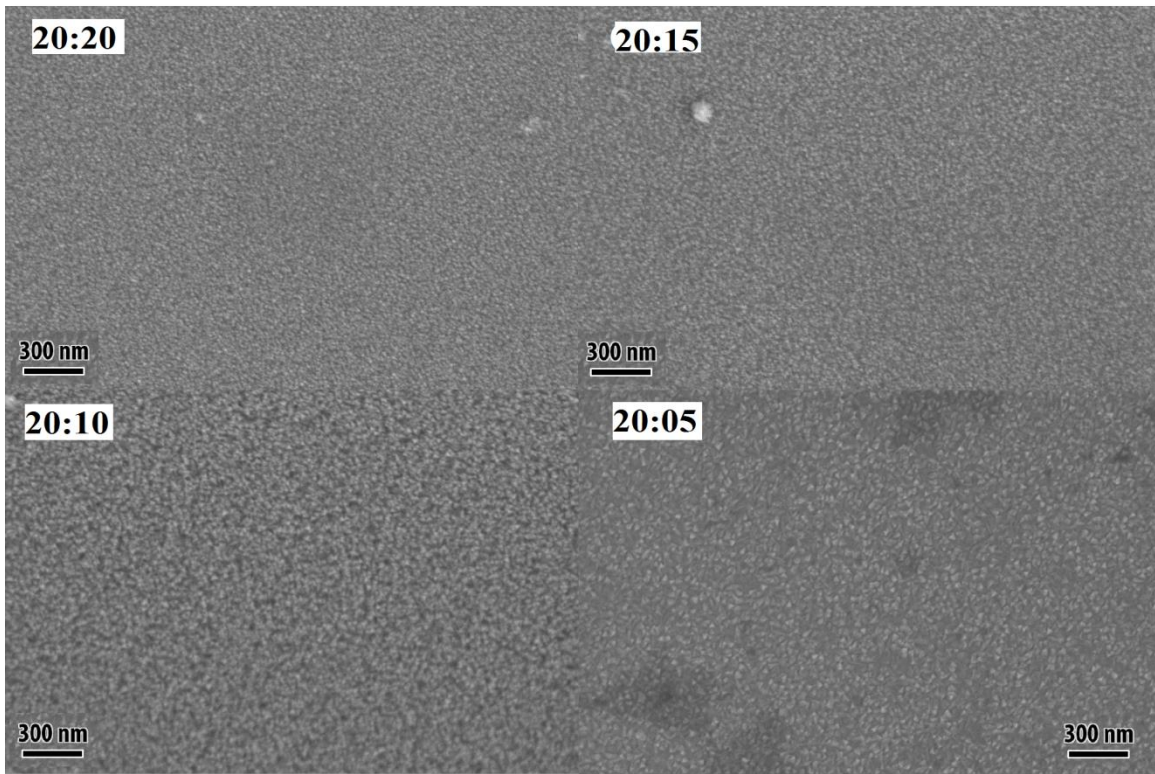


Figure 5.13: The FE-SEM images of PDCMS TiN films deposited at various Ar:N₂ ratios

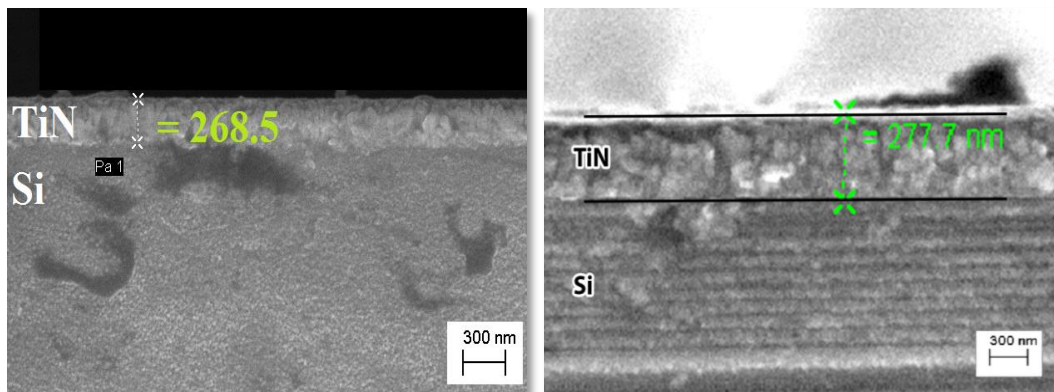


Figure 5.14: Images of the fracture surface of TiN_{20:20} and TiN_{20:05} thin films

5.4. 3. *Electrical resistivity measurement*

The sheet resistance of the films TiN_{20:20}, TiN_{20:15}, TiN_{20:10} and TiN_{20:05} was measured as 50.06, 24.61, 18.87 and 11.10 Ω /Sq., respectively. The electrical resistivity of the TiN films was calculated by multiplying the sheet resistance with the thickness of the films. The resistivity of the films are 1376.65, 676.78, 518.93 & 305.25 $\mu\Omega$.cm , respectively (Figure5.15).

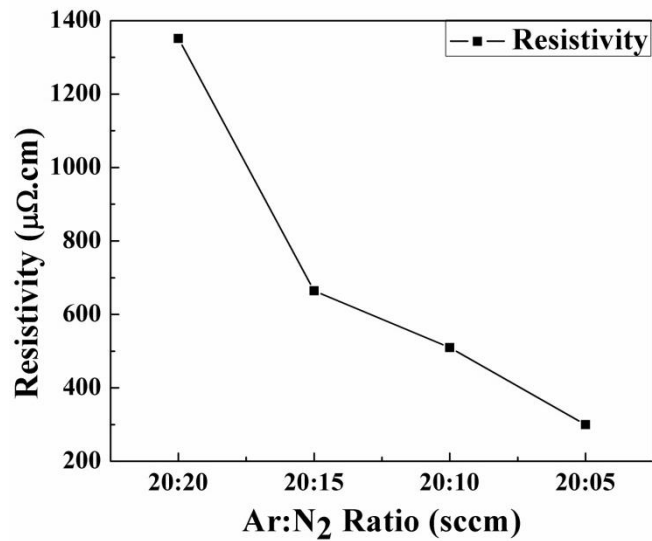


Figure 5.15: Electrical resistivity of the TiN thin films at various Ar:N₂ ratios

From Figure 5.15, it is observed that the electrical resistivity increases with an increase in the nitrogen gas partial pressure, which can be attributed to the dominance of the (200) plane as compared to the (111) plane. The increase of (200) orientation leads to defect in the TiN film, which cause a reduction in electrical conductivity (Meng et al. 1995, Ponon et al. 2015, Sundgren et al. 1983, Sundgren et al. 1982). The increase in the nitrogen partial pressure during the deposition provides a more intense (200) peak but results in higher electrical resistivity. This can be attributed to the hyperstoichiometry with defects in the TiN films. Earlier studies reported that, in hyperstoichiometric compositions, the electrical resistivity increases much faster than that for the substoichiometric compositions because the scattering power of the N-vacancies is different from that of the Ti-vacancies (De Maayer et al. 1975). Hence the crystal structures can play an important role in controlling the electrical properties of TiN films which are crucial for making electrical devices, including MEMS microheaters.

5.4. 4. Compositional and structural analysis with transmission electron microscopy

Figure 5.16. shows the TEM cross-sectional image of the TiN film and the selected area diffraction pattern presenting continuous diffraction rings, indicating the random orientation of the grains. The TEM diffraction pattern shows a polycrystalline TiN pattern in agreement with the XRD results. Figure 5.17. depicts the elemental area mapping of PDCMS TiN thin film deposited at 20:05 Ar:N₂ ratio acquired through

energy-dispersive spectroscopy (EDS) and corresponding spectrum imaging. The TiN layer formed on the Si substrate and the Pt protection layer deposited during the FIB sample preparation process is vividly observed. While Ti and N signals dominate, trace oxygen contents above the background (as estimated from the spectrum collected from the substrate) are also observed. This oxygen contamination contributes to the increase in the electrical resistivity of TiN thin films. Figure 5.18 shows the counts of each element, i.e., Si, Ti, N, and O, obtained from EDS. The net oxygen counts integrated over a representative area (150 nm x 100 nm) in the TiN layer (black) are larger than the background oxygen counts from Si of the same area, showing that the film is slightly oxidized.

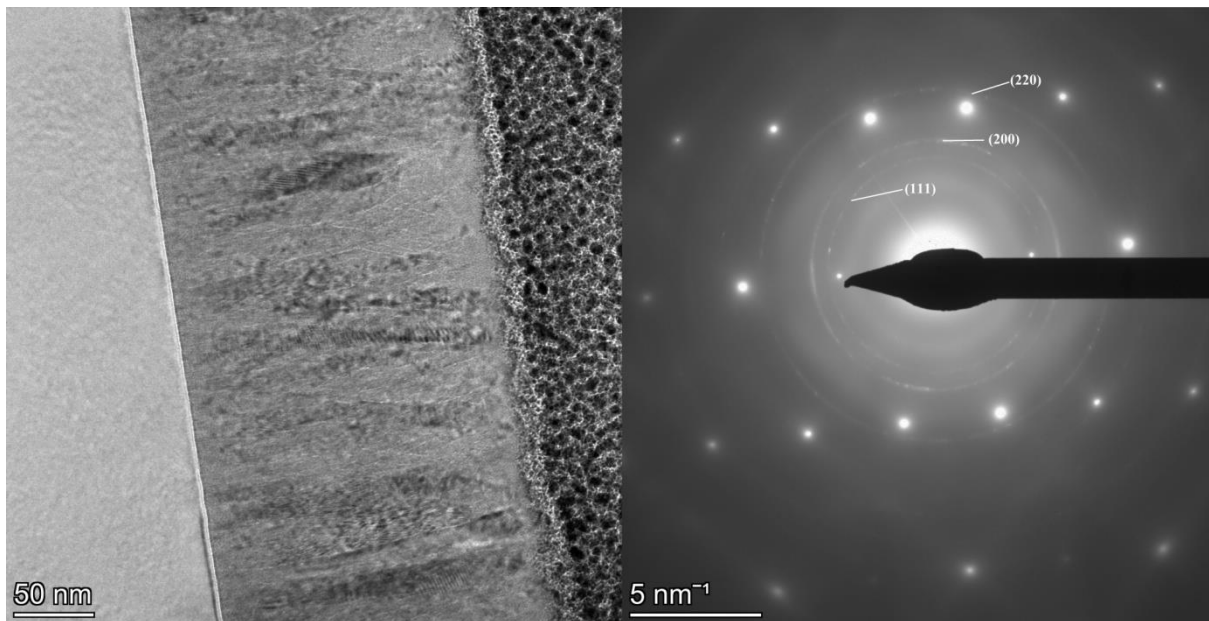


Figure 5.16: TEM Diffraction pattern of 20:05 (Ar:N₂) TiN film

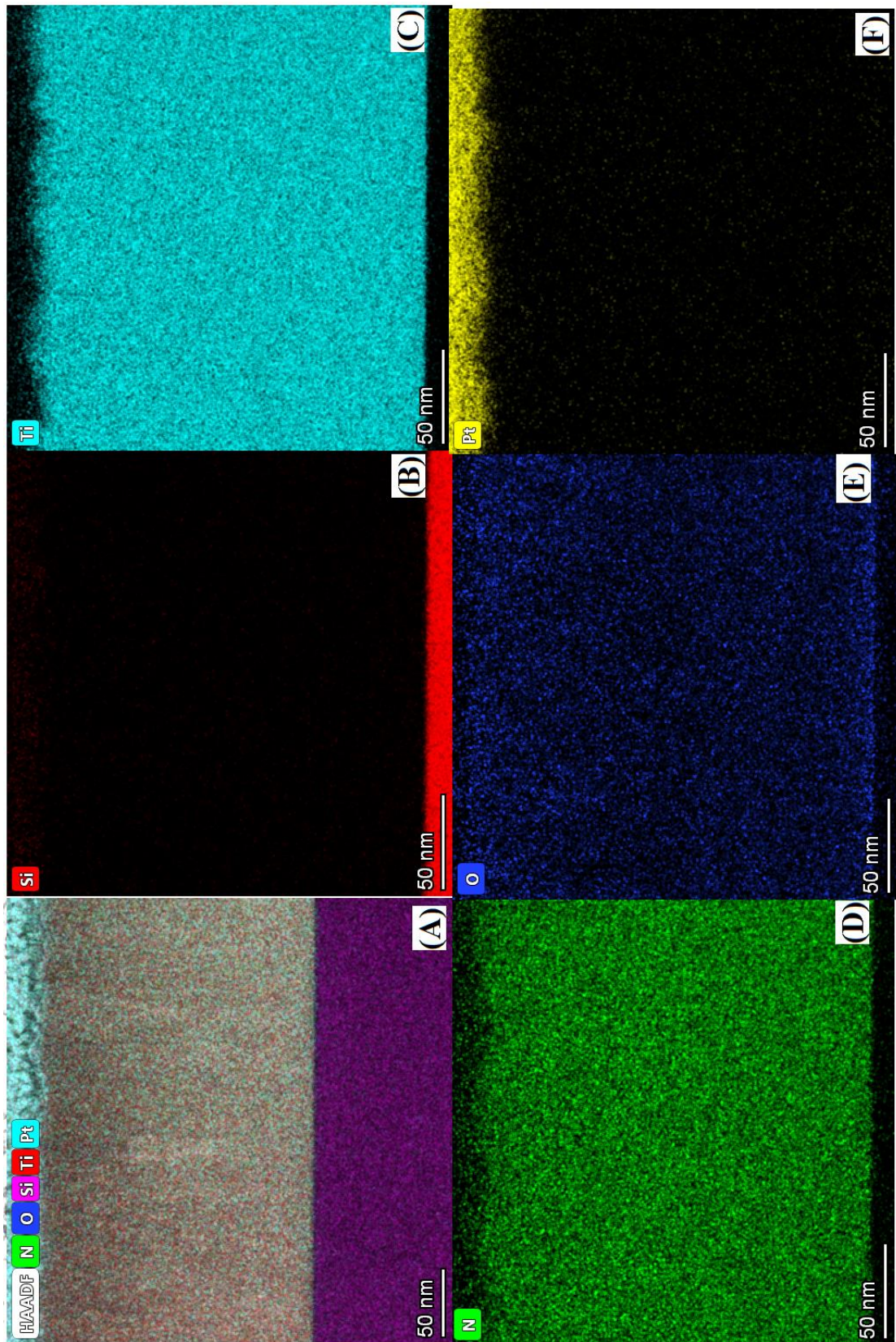


Figure 5.17: (A) Cross-sectional STEM-HAADF micrograph of 20:05 (Ar:N₂) TiN film and EDS elemental maps for (B) Si, (C) Ti, (D) N, (E) O, and (F) Pt.

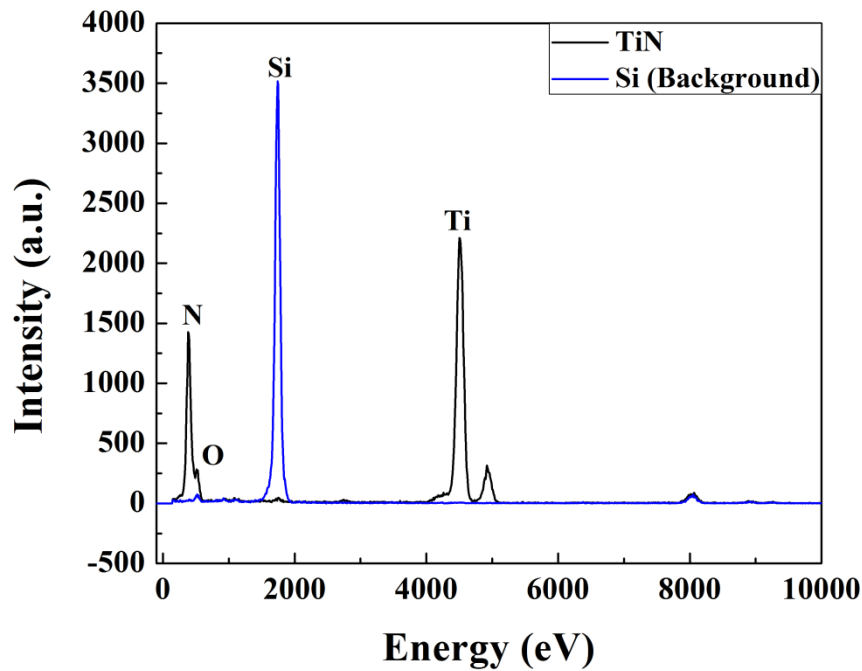


Figure 5.18: Counts of each element Si, Ti, N, and O obtained from EDS spectra

5. 5. Effect of differential pumping mechanism on PDCMS TiN plasma and structural properties

This study is an accidental observation of the effect of differential pumping mechanism on the TiN crystal orientations. TiN thin films were deposited by PDCMS on silicon (100) substrates. The deposition conditions were similar, as mentioned in Section 5.3 of this chapter. The TiN films were deposited in the same process conditions. The only difference between the two experiments was that one deposition was carried out with RGA differential pumping, while the other was without RGA differential pumping. As the structural properties of TiN films were influenced by the process conditions, such as substrate temperature and nitrogen plasma flux, differential pumping also plays a role in films' structural properties because the gas molecules' pumping directions vary. The presence of nitrogen gas molecules in the process chamber with and without differential pumping was monitored using OES after striking the TiN plasma. The findings from the OES were studied and correlated with the XRD results. The details of the process parameters are listed in Table 5. 5.

Table 5.5: Process parameters of PDCMS TiN thin films deposited with and without RGA differential pumping system

Process parameters	Differential pumping open	Differential pumping closed
Base pressure	1.5×10^{-6} mbar	1.5×10^{-6} mbar
Target	Ti - 99.99% pure	Ti - 99.99% pure
Substrate	P-type Silicon (100)	P-type Silicon (100)
Sputter gas	Argon – 20 sccm	Argon – 20 sccm
Reactive gas	Nitrogen – 5 sccm	Nitrogen – 5 sccm
Deposition pressure	5×10^{-3} mbar	5×10^{-3} mbar
Substrate temperature	300°C	300°C
Substrate-to-target distance	9 cm	9 cm
Pulsed DC power	100 W	100 W
Pulse frequency	200 kHz	200 kHz
Pulse reversal time	1.0 μ s	1.0 μ s
Deposition duration	40 Min.	40 Min.

5.5.1. TiN plasma diagnose using optical emission spectroscopy

Figure 5.19 shows the typical emission spectra of PDCMS TiN plasmas from the Ti target. The plasma was recorded with an RGA differential pumping mechanism closed and open. From the NIST database, each of the elemental emission spectrums was confirmed. Figure 5.20. shows the elemental spectra of (a) titanium, (b) nitrogen, and (c) argon metastables and ions (How et al. 2017, Hafiz et al. 2018, NIST 2019). The intensities of titanium, nitrogen, and argon emissions were observed to increase with the differential pumping mechanism. These increases in the intensities caused the variations in the structural properties of TiN thin films.

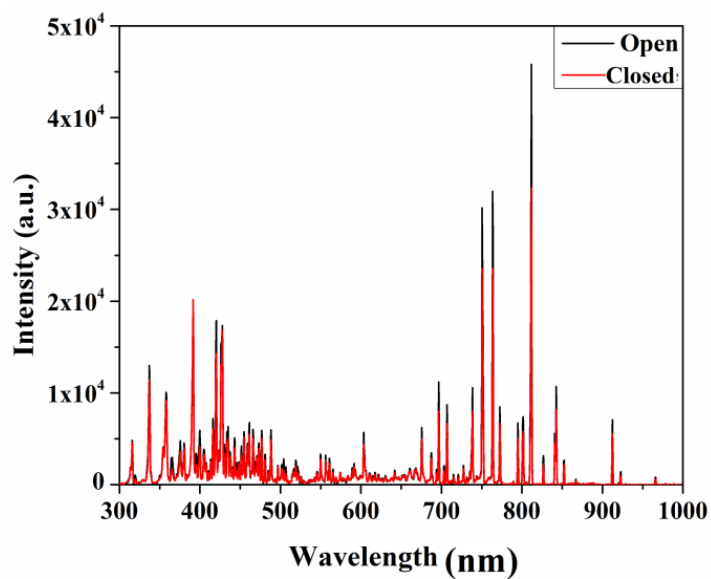
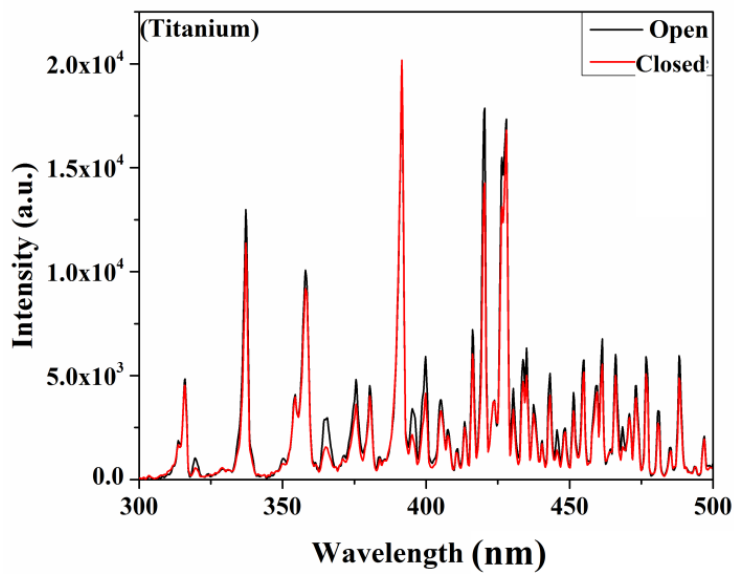


Figure 5.19: Wide range emission spectra of PDCMS TiN plasmas recorded with RGA differential pumping mechanism ON and OFF



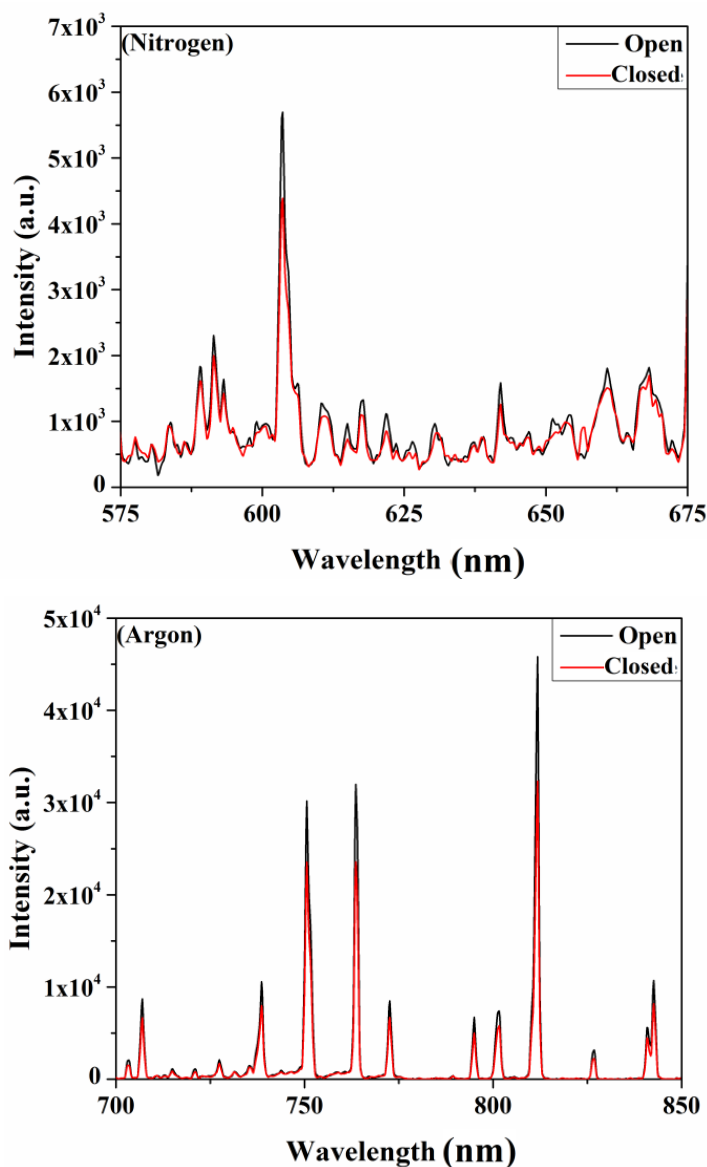


Figure 5.20: Elemental spectra of (a) titanium, (b) nitrogen, and (c) argon in PDCMS TiN plasmas with and without RGA differential pumping mechanism

5.5.2. Microstructural studies

The PDCMS TiN thin films deposited with the RGA differential pumping mechanism closed and open were subjected to X-ray diffraction studies (Figure 5.21). The peaks were indexed using JCPDS powder diffraction files, and the peaks were well matched with the TiN phase of TiN films (JCPDS Card Nos. 38–1420 and 23–1455). The XRD pattern shows that the films deposited without the RGA differential pumping mechanism exhibited predominant orientation towards the (111) plane at 36.7° (Meng et al. 1997, Penilla et al. 2008, Chawla et al. 2009, Saoula et al. 2009). However, the

films deposited with the RGA differential pumping mechanism exhibited predominant orientation towards the (200) plane at 42.8° . This is due to the increase in the concentration of nitrogen gas molecules in the target premises. This leads to more ionization of the nitrogen gas species in the plasma. An increase in the nitrogen ions results in a slightly nitrogen-rich TiN films causing orientation towards the (200) plane. It has been reported that the increase in nitrogen content in the titanium nitride thin film causes defects and leads to the prominence of the (200) plane (Meng et al. 1997, Cuong et al. 2006, Ponon et al. 2015).

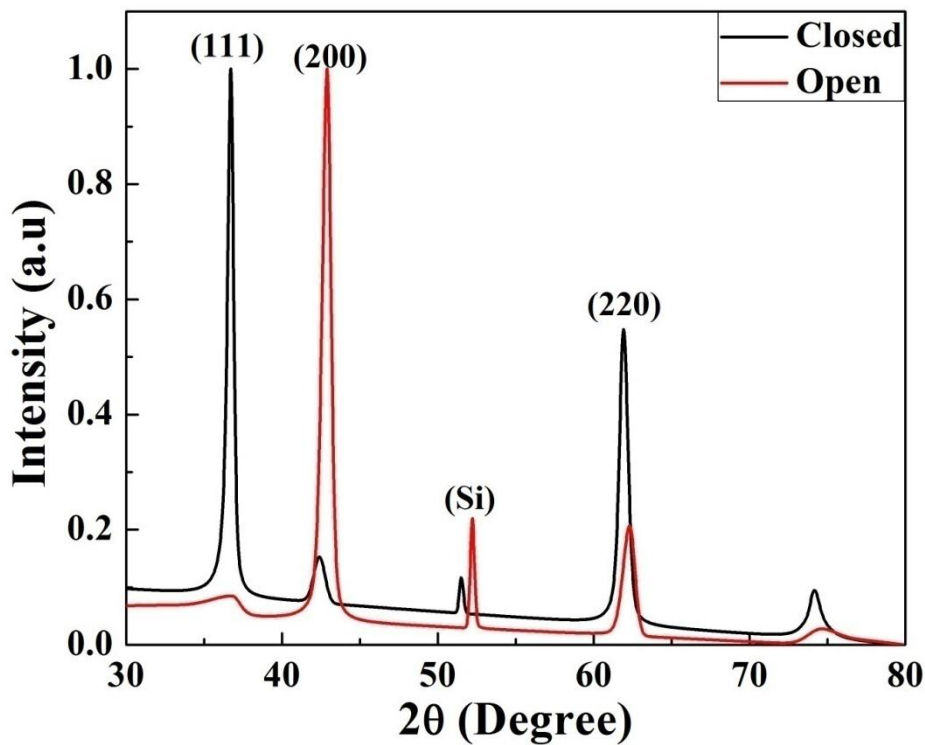


Figure 5.21: XRD patterns of PDCMS TiN films deposited with and without RGA differential pumping mechanism

5. 6. Conclusions

The influence of process parameters in PDCMS, such as substrate temperature and argon to nitrogen ratio at fixed pulse parameters, on the structural, morphological, and electrical properties of TiN thin films have been investigated. The plasma characteristics for the films deposited at various nitrogen partial pressures were *in-situ* recorded using an optical emission spectroscope. It was observed that the TiN films were found to grow in (200) orientation with an increase in the substrate temperature

and nitrogen partial pressure. The elevated temperature provides extra energy for growing the TiN films, resulting in the formation of (200) orientation. But the increase in the nitrogen plasma flux with the nitrogen partial pressure might induce defects in TiN thin films, which results in the growth towards (200) orientation. The electrical resistivity of the TiN films was measured and correlated with the microstructural orientations of the same. The electrical resistivity of the TiN films was found to decrease with an increase in substrate temperature due to the dominance of the (200) orientation. But the increase in the nitrogen partial pressures beyond a level caused an increase in the electrical resistivity. This is due to defects in the TiN films with the appearance of (200) plane. The effect of RGA's differential pumping on the TiN film structural properties was observed and then investigated. The TiN films appeared with (111) and (200) orientations with RGA open and closed conditions, respectively. During the RGA pumping open condition, the increase in the nitrogen flux was observed through OES. This had caused the growth towards (200) orientation. Therefore, differential pumping systems have a significant influence on the film properties.

CHAPTER 6

FABRICATION OF NICKEL-TITANIUM AND TITANIUM NITRIDE MICROSTRUCTURE AND DEVICES

6. 1. Introduction

In general, an external stimulus is required for realizing actuations in NiTi-based MEMS devices. The external stimulus can be either mechanical or thermal; hence a MEMS hotplate setup alongside the thermal NiTi shape memory micro-devices is essential. TiN can be used as a MEMS hotplate, and it can serve as a capping layer to avoid the surface oxidation of NiTi thin film microstructure. Moreover, TiN is suitable for fabricating NiTi-based biomedical devices because of its biocompatibility. In this chapter, the fabrication of NiTi and TiN-based MEMS devices such as micro-cantilevers, micro-wrappers, micro-combs, micro-heaters, etc., and their characterization are discussed. TiN MEMS hotplates were fabricated alongside these NiTi micro-devices, and their heating performance was evaluated. This chapter also includes the studies related to the fabrication of NiTi-based micro-mesh and micro-comb structures by laser bulk micromachining technique.

6. 2. Fabrication Methodology

The PDCMS NiTi thin films, which exhibit a martensitic phase at room temperature (pulse frequency - 200 kHz, deposition pressure – 1×10^{-2} mbar, substrate temperature - 600°C), have been chosen for the fabrication of MEMS devices. The PDCMS TiN thin films with the lowest electrical resistivity (deposited at the substrate temperature of 300°C and an argon:nitrogen ratio of 20:5) were selected for the micro-heater fabrication. This TiN thin film is directly deposited onto the Si/NiTi stack. The NiTi micro-cantilever and micro-wrapper MEMS structures have been micromachined using femto second laser bulk micromachining technique (Li et al. 2006, Quintino et al. 2013, Biffi et al. 2017). But, the NiTi-based micro-mesh and micro-comb MEMS structures have been patterned using the Ytterbium fiber laser micromachining technique (Fu et al. 2014, Shiva et al. 2015). The TiN micro-heaters were fabricated

using focused ion beam and laser micromachining techniques (Gao et al. 2003, Massl et al. 2009, Giorleo et al. 2016, Zintler et al. 2017). The micromachined NiTi micro-cantilever and micro-wrapper structures were made free-standing by dry etching of bottom silicon using Reactive Ion Etching (RIE-Cl) chemistry (Jansen et al. 1996, Kiihamaki et al. 1999, Rosli et al. 2006, Wu et al. 2010, Morozov et al. 2017). The bottom silicon beneath these micro-mesh and micro-comb structures was etched by chemical wet etching using tetramethyl ammonium hydroxide (TMAH) (Thong et al. 1997, Tang et al. 2014, Robbins et al. 2016, Swarnalatha et al. 2017).

The NiTi and TiN MEMS structures fabrication process flow is listed below.

6. 3. Fabrication and characterization of TiN micro-heaters

6. 3. 1. Focussed ion beam micromachining of TiN micro-heaters

6. 3. 1. 1. Fabrication

- i. An Auto CAD design of the planned micro-heater device was drawn. The drawing file could be loaded with the FIB system software for fabrication (Figure 6.1.). The dimensions of the contact pads for taking the electrical contacts of micro-heater patterns were $200 \times 200 \mu\text{m}^2$.

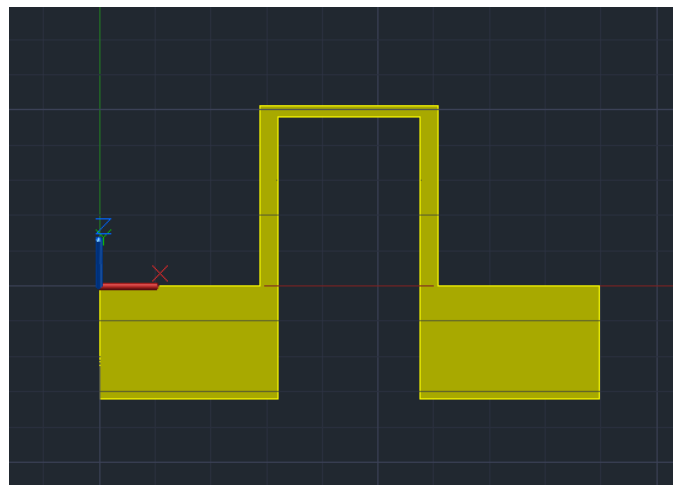


Figure 6.1: Auto CAD design of the planned TiN micro-heater pattern

- ii. A silicon (100) wafer of 10 mm X 10 mm size was chosen as the substrate for the micro-heater fabrication. This Si wafer was pre-cleaned using standard acetone and HF.
- iii. The SiO_2 layer (1 - 2 μm) has been thermally grown on the Si wafer to form the Si/ SiO_2 stack for using as an electrical-cum-thermal barrier to TiN micro-heaters.

- iv. The TiN thin films were deposited using the PDCMS technique onto the Si/SiO₂ stacks to complete the Si/SiO₂/TiN stack (Figure 6.2.).

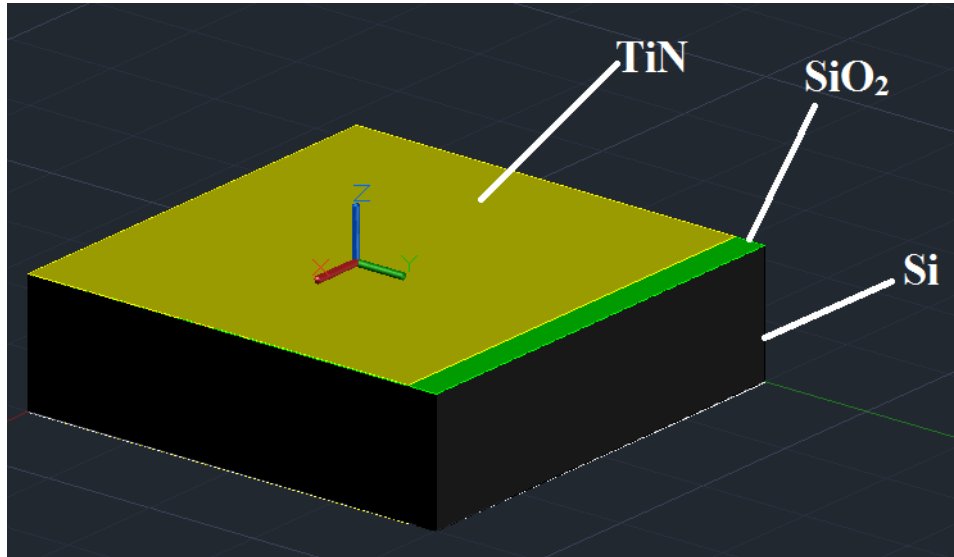


Figure 6.2: Auto CAD design of the Si (Black)/SiO₂ (Green)/TiN (Yellow) stack

- v. TiN films were micro-patterned using a focused ion beam technique to form a micro-heater structure (Figure 6.1.). The depth of the micro-patterning was set at 1 μm as the TiN film thickness was ~ 275 nm to make sure the micro-heater structure pattern was not shorting anywhere. The SEM image of the micro-patterned TiN micro-heater structure is shown in Figure 6.3.

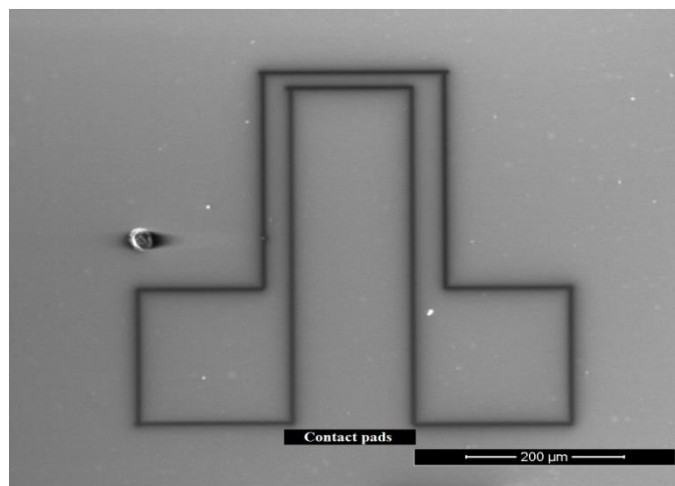


Figure 6.3: FIB image of the TiN micro-heater pattern

- vi. The silicon wafer containing the micro-heater structures was packaged for making easy contacts (Figure 6.4.). The electrical connections to the micro-heater structures were made using the wire bonding technique.

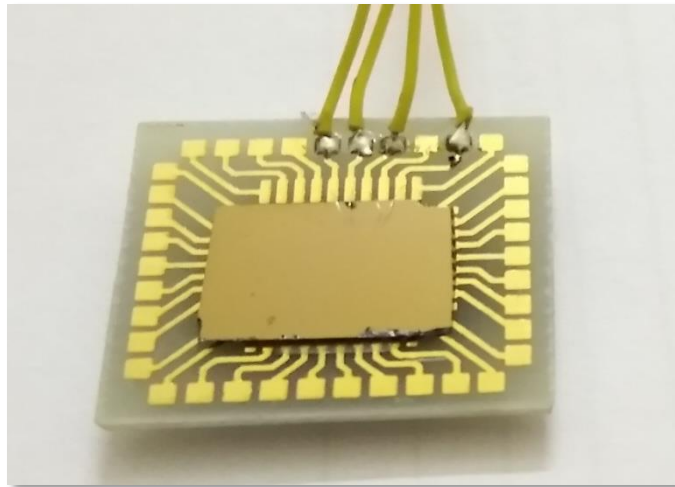


Figure 6.4: Packaged TiN micro-heater device

6. 3. 1. 2. Characterization

The heating capacity of the micro-heater was measured at various input powers. The measured heater resistance was $\sim 16 \Omega$. Figure 6.5 shows the thermal images of the heater at various powers captured using a Fluke IR thermal camera.

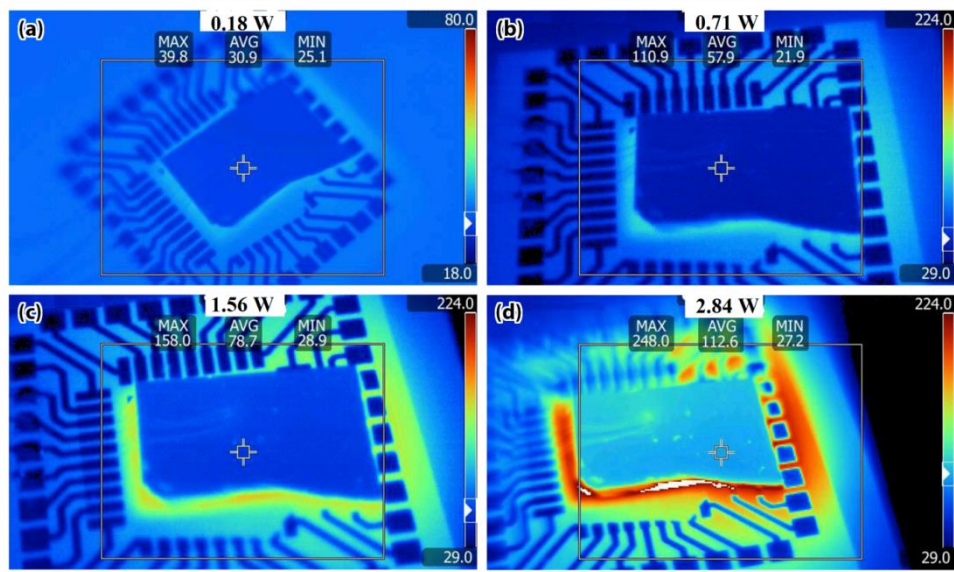


Figure 6.5: IR images of micro-heaters at (a) 0.18, (b) 0.7, (c) 1.56 & (d) 2.84

Figure 6.6 shows the performance of the heater at various input powers. From the Figure, it can be observed that the temperature of the heater increases nearly linearly with increasing power. A maximum temperature of 250°C was achieved by applying a power of 2.8W within 1 min. duration. This range of temperature is sufficient for the actuation of NiTi micro-devices.

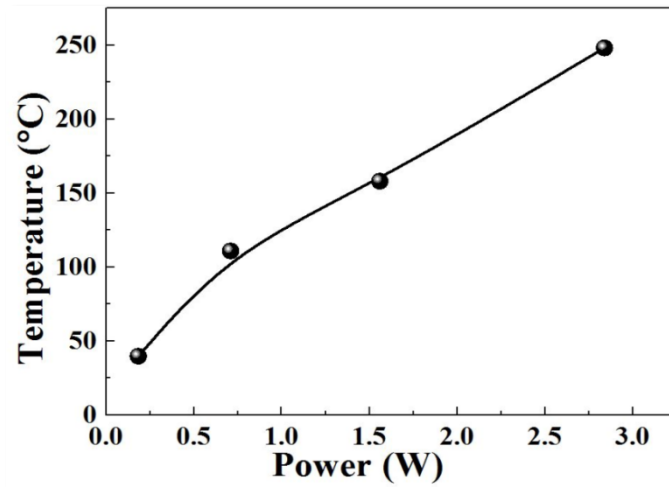


Figure 6.6: Power vs. heater temperature measurements of TiN micro-heaters

6. 3. 2. *Laser micromachining of TiN micro-heater structures*

Though the focused ion beam technique suits well for micropatterning MEMS structures, it is a very costly technique. Devices in micron dimensions can be patterned using fairly cheaper techniques, like laser bulk micromachining. For the fabrications such as heater patterns, the laser machining technique can be used for making boundary cuts without any difficulties.

6. 3. 2. 1. *Fabrication*

- i) The Auto CAD design of the planned micro-heater patterns was drawn (Figure 6.7.) and loaded to the software for the micro-machining of the TiN microstructures. The contact pad (electrodes) sizes were maintained at $500 \times 500 \mu\text{m}^2$ for probing the electrical contacts.

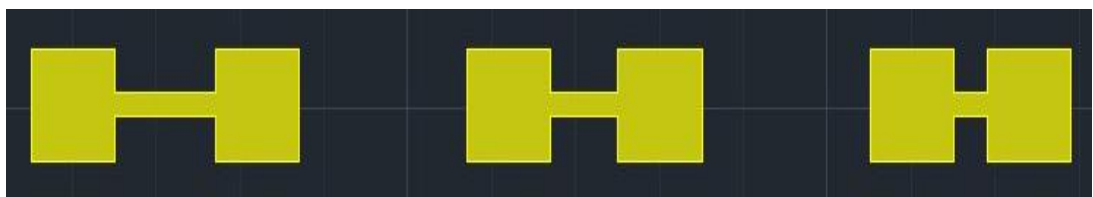


Figure 6.7: Auto CAD design of the planned Si/SiO₂/TiN stack

- ii) A silicon (100) wafer of 10 mm×10 mm size was chosen as the substrate for the micro-heater fabrication. This Si wafer was pre-cleaned using standard acetone, HF cleaning procedure.
- iii) The SiO₂ layer (1 - 2 μm) was thermally grown on the Si wafer to form the Si/SiO₂ stack for using as an electrical-cum-thermal barrier to TiN micro-heaters.

- iv) The TiN thin films were deposited onto the Si/SiO₂ stacks to complete the Si/SiO₂/TiN stack (Figure 6.2.).
- v) TiN films were micro-patterned using the laser micro-machining technique to form a micro-heater structure as designed in the Auto CAD (Figure 6.7.). The heater dimensions (lengths) were varied as 200, 400, and 600 μm to study their heating capabilities with the lengths. The depth of the micro-patterning was set as 1 μm as the TiN film thickness was ~275 nm to make sure the micro-heater structure pattern was not shorting anywhere. The optical microscopic image of the micro-patterned TiN micro-heater structure is shown in Figure 6.8.

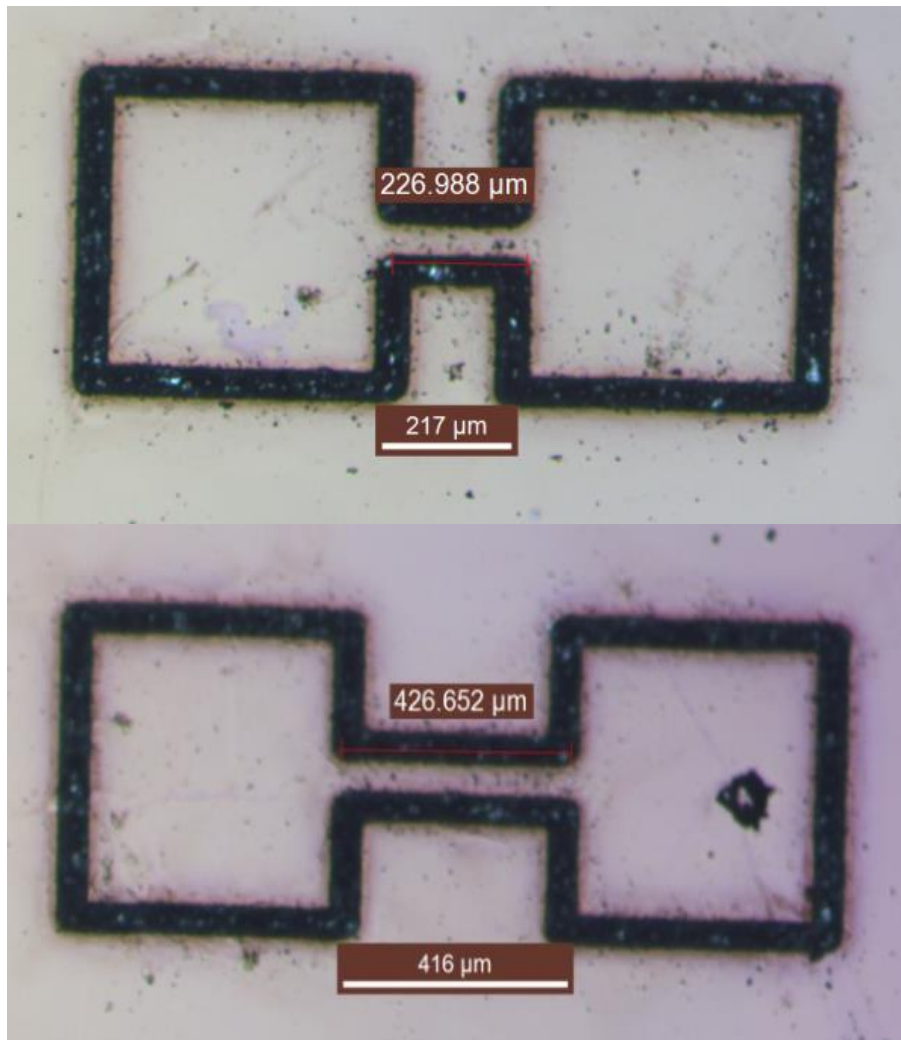


Figure 6.8: Laser-patterned TiN thin film micro-heater patterns: (a) 200 and (b) 400 μm.

6. 3. 2. 2. Characterization

The heating capacity of the micro-heater was measured at various input powers. The IR thermal camera images showing the direct heat measurements are shown in Figure 6.9. The heating capabilities of the TiN micro-heaters with respect to their lengths (200, 400, and 600 μm) at a power of $\sim 8\text{W}$ are shown in Figure 6.10. It is found that, with an increase in the heater dimensions, the heating capabilities of the TiN heaters also increased for the same power input.

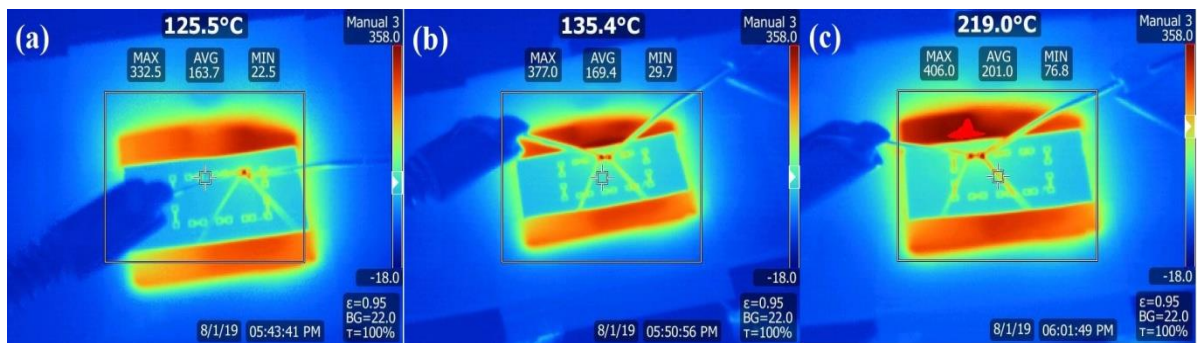


Figure 6.9: IR images of micro-heaters: (a) 200 μm , (b) 400 μm , and (c) 600 μm with their maximum temperatures.

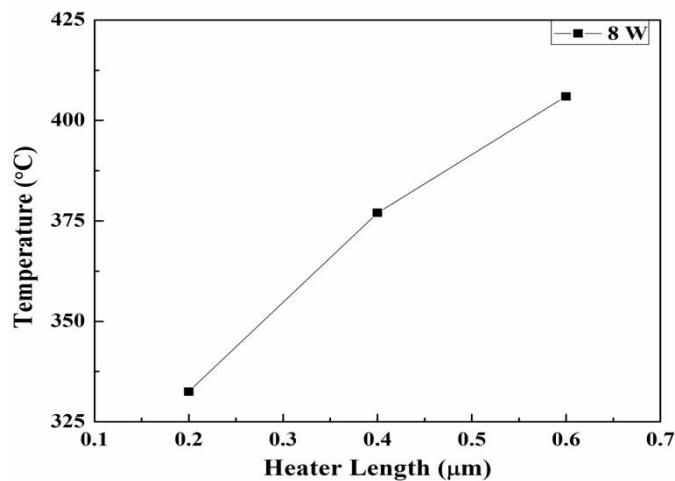


Figure 6.10: Performance of TiN micro-heaters with their dimensions at $\sim 8\text{ W}$

The micro-heaters with various dimensions (lengths) were fabricated to study the heating efficiency with specific input powers. As resistance and length are directly proportional, the micro-heater with larger dimensions will produce larger heat. Figure 6.11 shows the performance of the micro-heaters at various input powers. A maximum temperature of 406°C (measured using an IR camera) was achieved with

the micro-heater by applying a power of 8.88 W (using a Keithley meter) to the 600 μm length micro-heater.

$$R = \rho \frac{l}{a}$$

(Where, R – Resistance, ρ – Resistivity, l – Length, a – Area)

$$H = I^2RT$$

(Where I – Current, R – Resistance, T - Time)

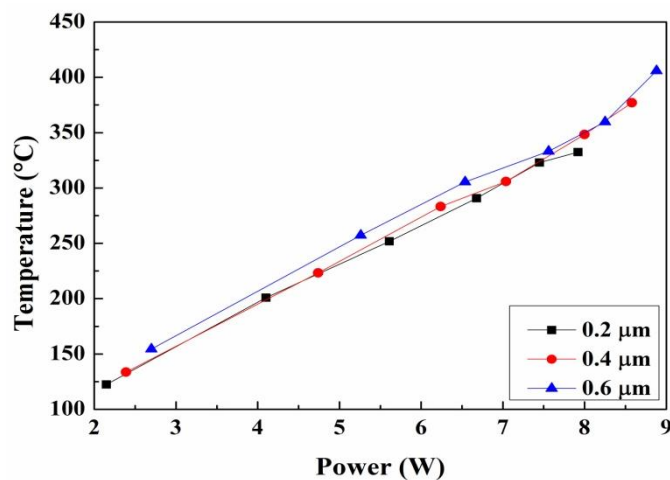


Figure 6.11: Heating performance of TiN micro-heaters at different lengths

6. 4. Micromachining of NiTiMEMS devices (Cantilevers and Wrappers) by femto second lasers

6. 4. 1. Fabrication and integration of NiTi micro-cantilevers with TiN micro-heaters

- i. An Auto CAD design of the planned micro-cantilever and micro-heater device was made to load into the femtosecond laser system software (Figure 6.12.). The contact pad (electrodes) sizes were maintained as $200 \times 200 \mu\text{m}^2$ for making the electrical contacts. The base of the NiTi micro-cantilevers was brought in touch with the TiN micro-heaters to have the maximum heating effect for the actuation to occur.
- ii. A silicon (100) wafer of 10 mm X 10 mm size was chosen as the substrate for the micro-heater fabrication. This Si wafer was pre-cleaned using standard acetone, HF cleaning procedure.

- iii.** The NiTi and TiN thin films with thicknesses of 1.3 and 0.277 μm were deposited onto this silicon using the pulsed DC magnetron sputter deposition technique. The TiN film was deposited on a selected area over the Si/NiTi stacks using a shadow mask to form Si/NiTi/TiN stacks, as shown in Figure 6.13.

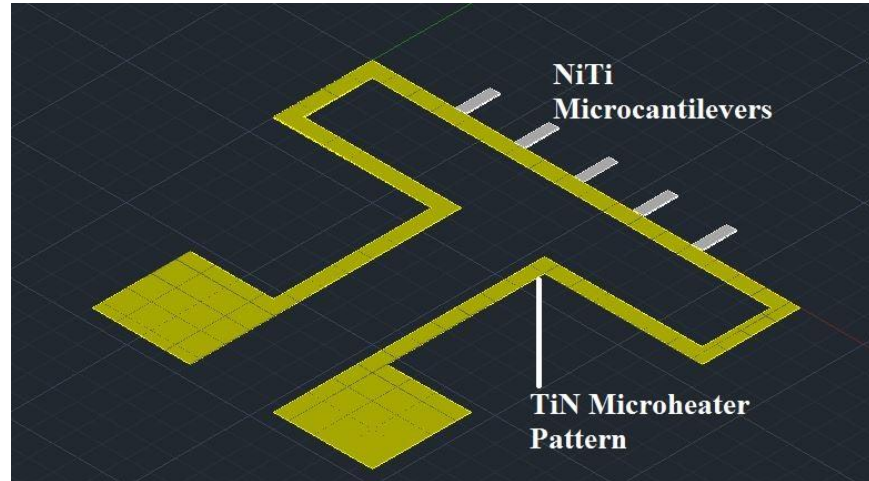


Figure 6.12: Auto CAD design of the planned NiTi micro-cantilever and TiN micro-heater structures

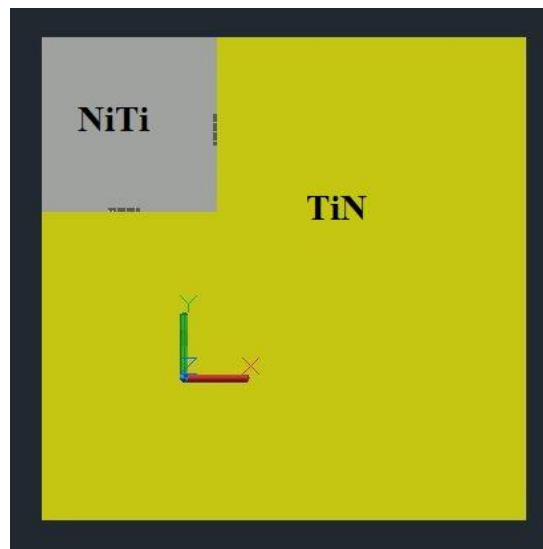


Figure 6.13: Top view of the Si/NiTi/TiN thin film stacks

- iv.** The NiTi films were micro-patterned (Figure 6.14.) using the femto second laser technique as per the Auto CAD design. The gap between the two cantilevers was kept at 50 μm to provide sufficient space for etchants to perform. The depth of the micro-patterning was set at 10 μm to ensure that the NiTi structure

remains free-standing after the bottom Si etch. The SEM image of the micro-patterned NiTi microstructure is shown in Figure 6.15.

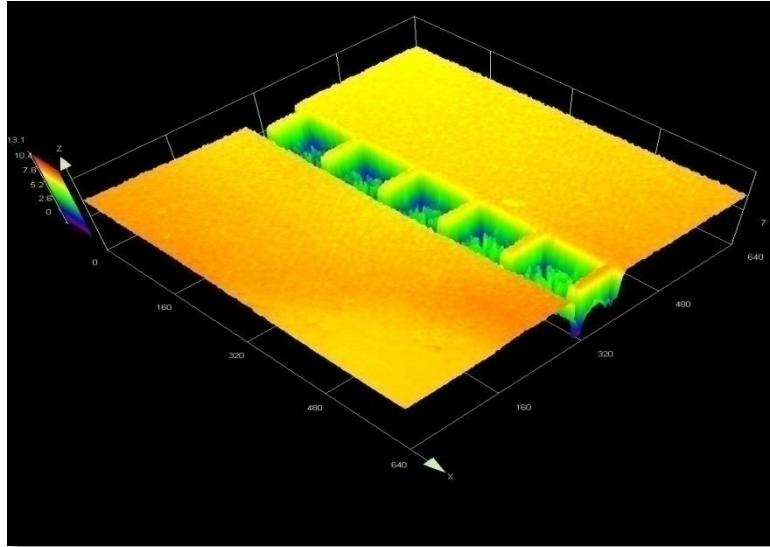


Figure 6.14: Microscopic image of the femtosecond laser micro-patterned Si/NiTi stack

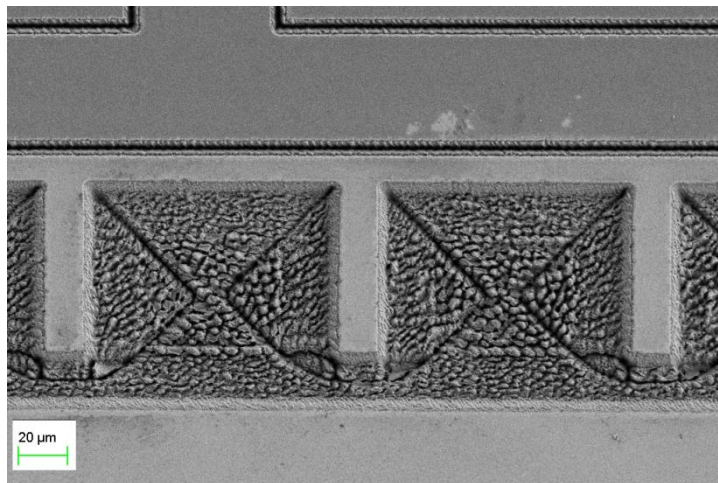


Figure 6.15: Si/NiTi stack after femtosecond laser micro-patterning (FESEM image)

- v. The micro-machined NiTi cantilevers were made to be free-standing by bottom silicon etch using Reactive Ion Etching Chlorine chemistry (RIE-Cl). The RIE-Cl technique is widely used for the etching of silicon. For anisotropic or isotropic etching, a higher etching rate is achievable for silicon with the reactive ion etching technique. The silicon etch rate was pre-optimized at 70 nm/min. Therefore, the etching was carried out for 20 min. to etch complete silicon

beneath the NiTi micro-cantilevers. The NiTi films were released after the bottom silicon etches, as shown in Figure 6.16.

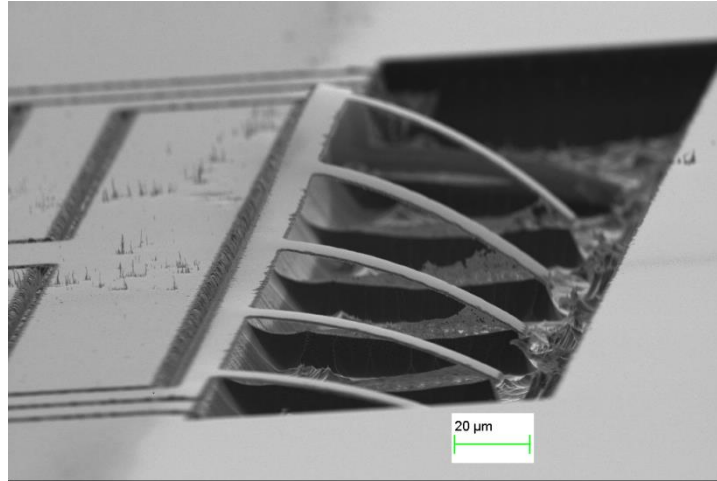


Figure 6.16: FESEM image of the released NiTi cantilever microstructures

- vi. The micro-patterning of the TiN micro-heater structures with a focused ion beam is discussed in Section 6.3.1. of this chapter.
- vii. The TiN micro-heaters were fabricated alongside the NiTi micro-cantilevers to provide the actuation's required temperature (Figure 6.17.).

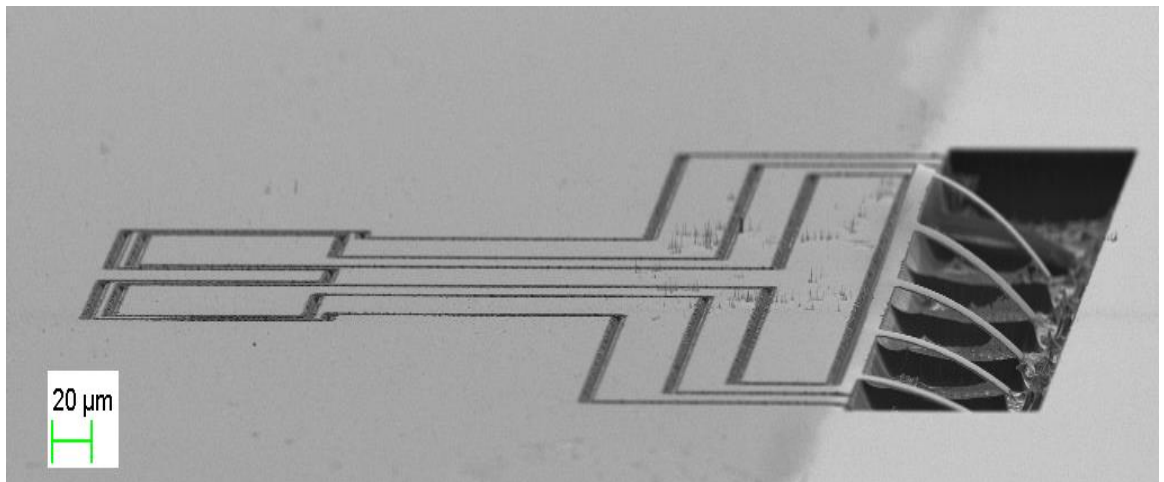


Figure 6.17: FESEM image of the micro-patterned NiTi micro-wrapper and TiN micro-heater structures

- viii. The electrical connections to the contact pads of the TiN thin film heater pattern were made using wire bonding. The heating of the TiN thin film heater was carried out through resistive heating by sending current through the contact pads. The heat generated by the TiN thin film heater was directly transferred by conduction to the base of the NiTi micro-cantilevers, which were used to actuate

them. The typical temperature observed for actuation was between 150 and 170°C. The actuation capability of the micro-cantilevers was observed with the help of an optical microscope. On heating, the reflections on the micro-cantilever bases were shifted from top to bottom. Also, the optical microscope magnification of the cantilevers was found to be changing (Figure 6.18.).

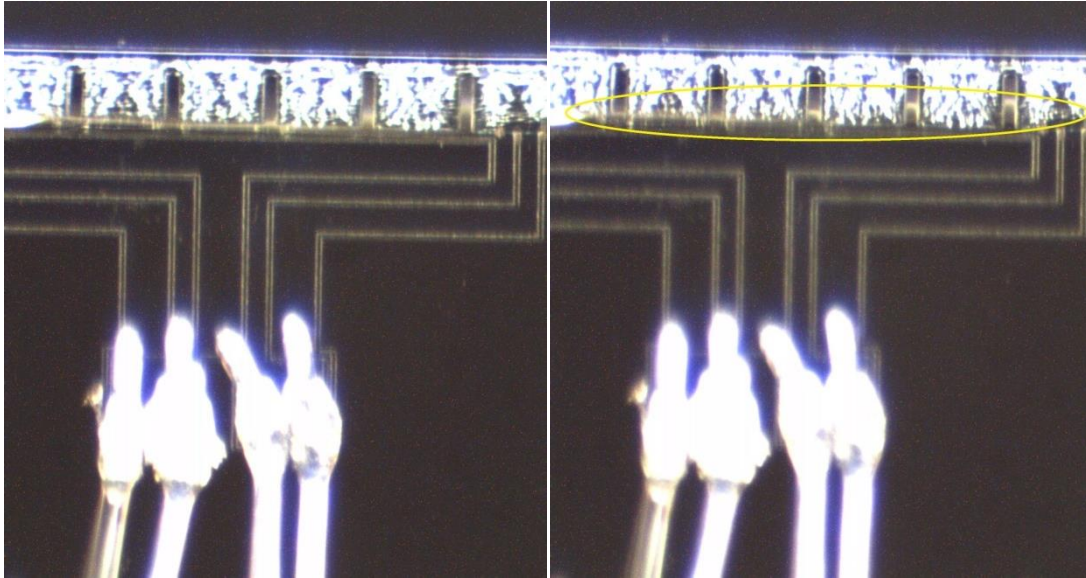


Figure 6.18: Optical images showing the actuation of NiTi cantilevers upon heating: (a) at room temperature. (b) at temperatures of 150 - 170°C.

6. 4. 2. Fabrication and integration of NiTi micro-wrappers with TiN micro-heaters

- i.** The Auto CAD design of the planned micro-wrapper and micro-heater device was drawn for loading into the femtosecond system software. The wrapper leg dimensions were fixed at 70×20 (L&W) μm . The contact pad (electrodes) sizes were maintained at $200 \times 200 \mu\text{m}^2$ for making the electrical contacts. The proposed wrapper and heater pattern structure is highlighted in Figure 6. 19.

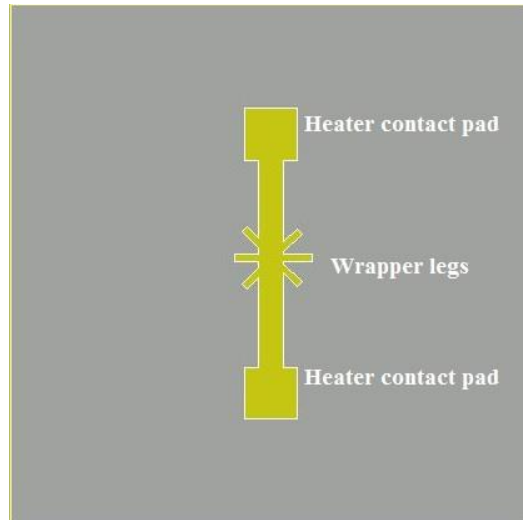


Figure 6.19: Auto CAD design of the planned NiTi micro-wrapper and TiN micro-heater structures

- ii. A silicon (100) wafer of 15 mm X 15 mm size was chosen as the substrate for the micro-heater fabrication. This Si wafer was pre-cleaned using standard acetone, HF cleaning procedure.
- iii. The NiTi and TiN thin films with thicknesses of 1.3 and 0.277 μm , respectively, have been deposited onto this silicon using the PDCMS deposition technique to form Si/NiTi/TiN (Figure 6.20) thin film stack.

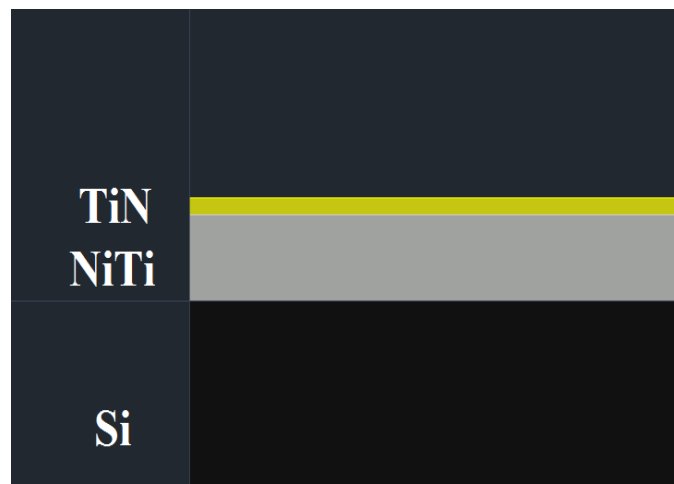


Figure 6.20: Side view of the Si/NiTi/TiN thin film stacks

- iv. The NiTi films were micro-patterned using the femto second laser technique. The depth of the micro-patterning was set at 10 μm to ensure that the NiTi wrapper legs remained free-standing after the bottom Si etch. The SEM image of the micromachined NiTi micro-wrapper structures is shown in Figure 6.21.

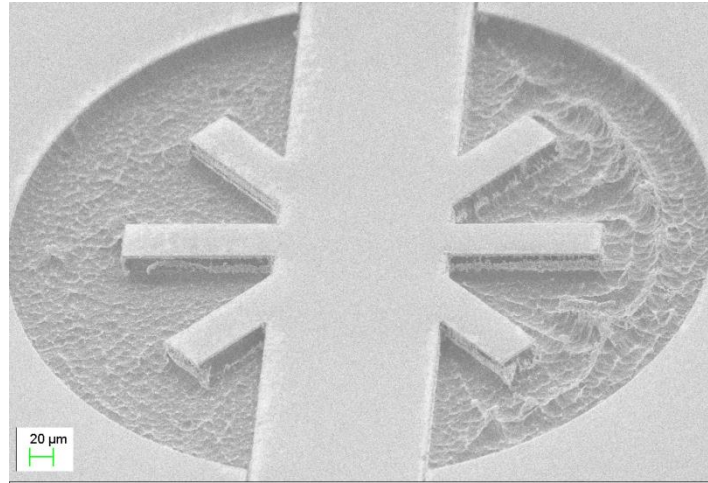


Figure 6.21:FE-SEM image of the femtosecond laser micropatterned Si/NiTi stack

- v. The micromachined NiTi wrappers were made to be free-standing by bottom silicon etch using Reactive Ion Etching Chlorine chemistry (RIE-Cl). The silicon etch rate was pre-optimized at 70 nm/min. Therefore, the etching was carried out for 20 min. to etch silicon completely beneath the NiTi wrapper legs. After the bottom silicon etches, the NiTi films were released, as shown in Figure 6.22.

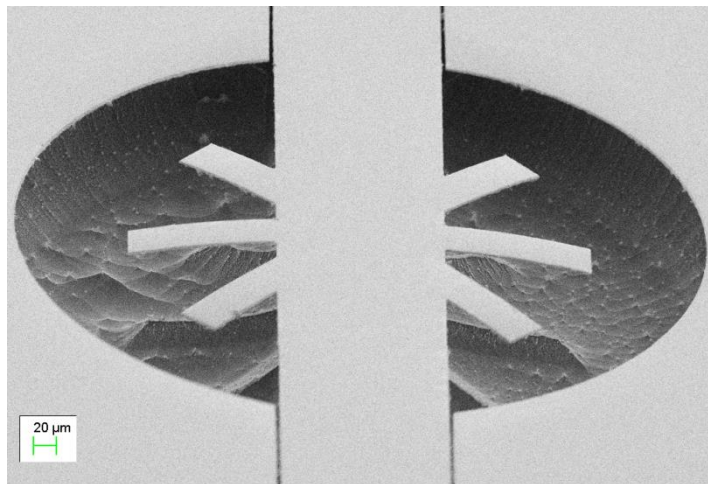


Figure 6.22: FE-SEM image of the released NiTi wrapper microstructures

- vi. The TiN micro-heater was fabricated alongside the NiTi micro-wrapper legs to provide the temperature required for the actuation (Figure 6.23).

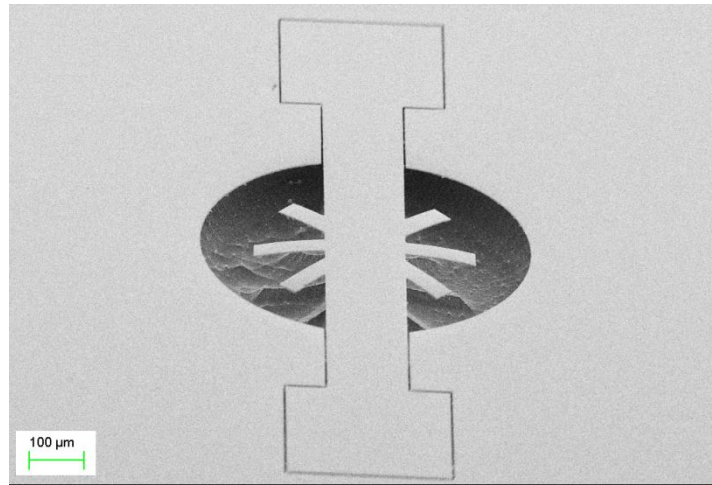


Figure 6.23: FE-SEM image of the micro-patterned NiTi micro-wrapper and TiN micro-heater structures

- vii.** The electrical connections to the contact pads of the TiN thin film heater pattern were made using wire bonding. The heating of the TiN thin film heater was carried out by resistive heating by supplying current through the contact pads. The heat generated by the TiN thin film heater was directly transferred by conduction to the base of the NiTi micro-wrapper legs, which were used to actuate the wrappers.

6. 5. Other NiTi microdevices fabricated using laser micromachining

6. 5. 1. Fabrication of NiTi micro-mesh by laser engraving technique

The Auto CAD design (Figure 6.24) of planned micromesh structures was drawn for loading into the laser system software. The micro-mesh structures' mesh dimension (diameter) was fixed at 1 μm .

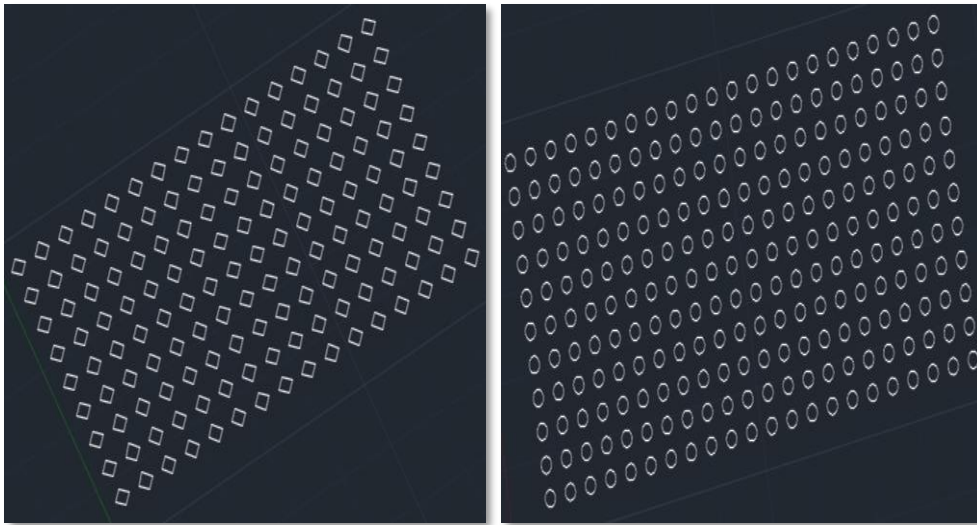


Figure 6.24: Auto CAD design of the planned NiTi micro-mesh structures

- i. A silicon (100) wafer of 15 mm×15 mm size was chosen as the substrate for the micro-mesh fabrication. This Si wafer was pre-cleaned using standard acetone, HF cleaning procedure.
- ii. The NiTi film of 1.2 μm thick was deposited using the PDCMS technique onto this Si wafer with the optimized process parameters to form the Si/NiTi stack (Figure 6.25).

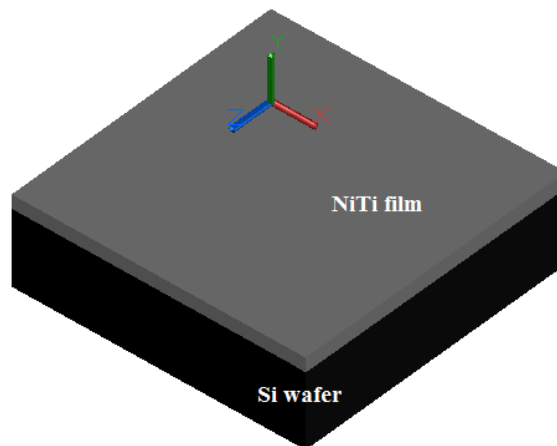


Figure 6.25: Auto CAD design of the Si/NiTi stack

- iii. In the next step, the NiTi films were micro-patterned using the laser bulk machining technique. The depth of the micropatterning was set as 10 μm to ensure that the NiTi structures would remain free-standing after the bottom Si etch.

- iv. The laser patterned NiTi micromesh structures were made free-standing by etching the bottom silicon using a chemical wet anisotropic etch process with tetramethyl ammonium hydroxide (TMAH) with an etch rate of 600 nm/min. The optical microscopic images of the free-standing NiTi micro-mesh/micro-net structures are shown in Figure 6.26. The 3D image of the same captured by the optical profiler is shown in Figure 6.27. The cyan-colored structures in the Figure indicate the NiTi micro-meshes.

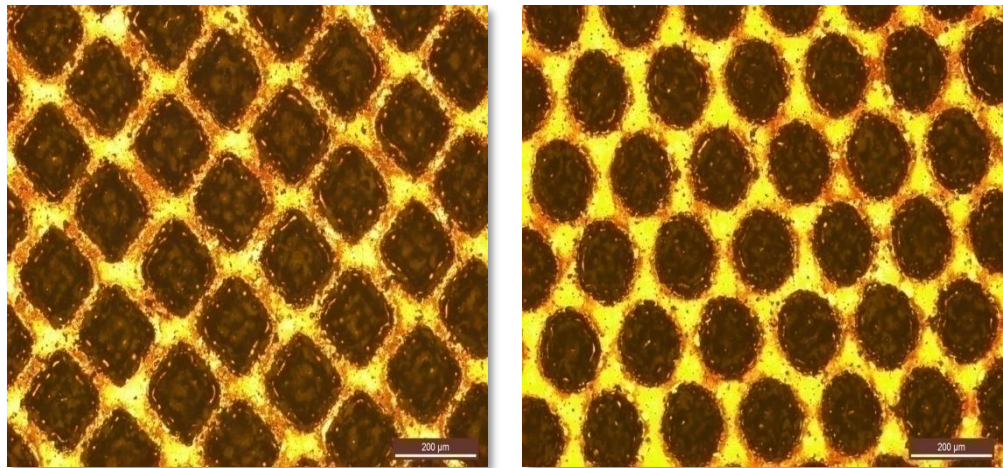
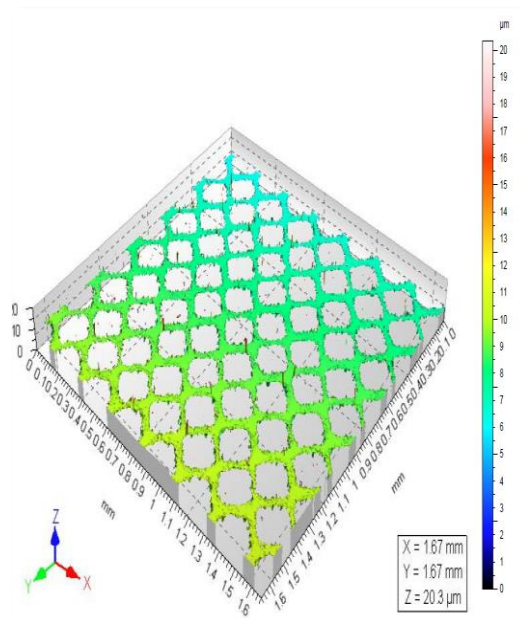


Figure 6.26: Optical microscopic images of the laser machined NiTi micro-meshes



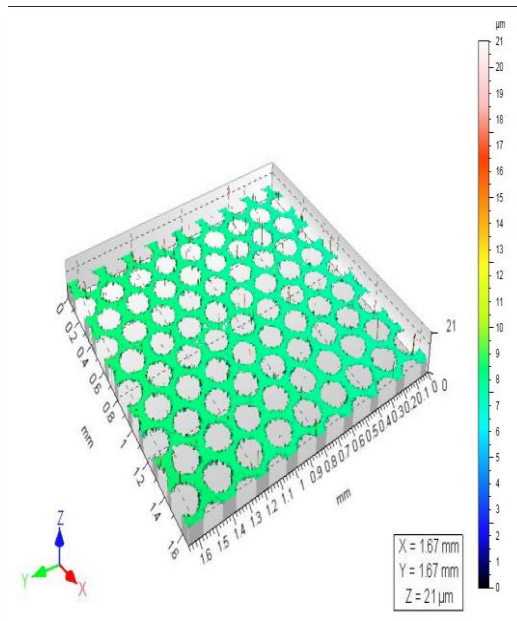


Figure 6.27: Optical profiler 3D images of the laser micro-patterned NiTi micro-meshes

6. 5. 2. *Fabrication of NiTi micro-combs by laser machining technique*

- i. Before proceeding with the fabrication, an Auto CAD design of the planned NiTi micro-comb devices was drawn (Figure 6.28). The micro-comb leg dimensions were fixed at 250×20 (L&W) μm . The contact pads dimensions were made at $500 \times 500 \mu\text{m}^2$ for taking the electrical contacts.

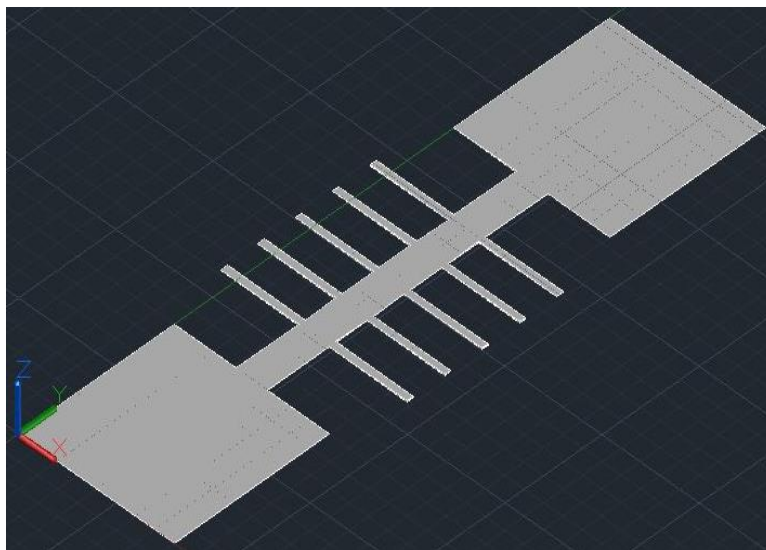


Figure 6.28: Auto CAD design of the planned NiTi micro-mesh structures

- ii. A silicon (100) wafer of 15 mm X 15 mm size was chosen as the substrate for the micro-comb fabrication. This Si wafer was pre-cleaned using standard acetone, HF cleaning procedure.
- iii. The NiTi thin films of 1.2 μm thick were deposited using the PDCMS technique onto a Si wafer with the optimized process parameters to form the Si/NiTi stack (Figure 6.25).
- iv. The NiTi films were micro-patterned using a laser machining technique. The depth of the micro-patterning was set at 10 μm . to ensure the NiTi structures would remain free-standing after the bottom Si etch.
- v. The laser patterned NiTi micro-comb structures were made free-standing by etching the bottom silicon using a chemical wet anisotropic etch process with tetramethyl ammonium hydroxide (TMAH) with an etch rate of 600 nm/min. The microscopic image of the free-standing NiTi micro-comb structures is shown in Figure 6.29.

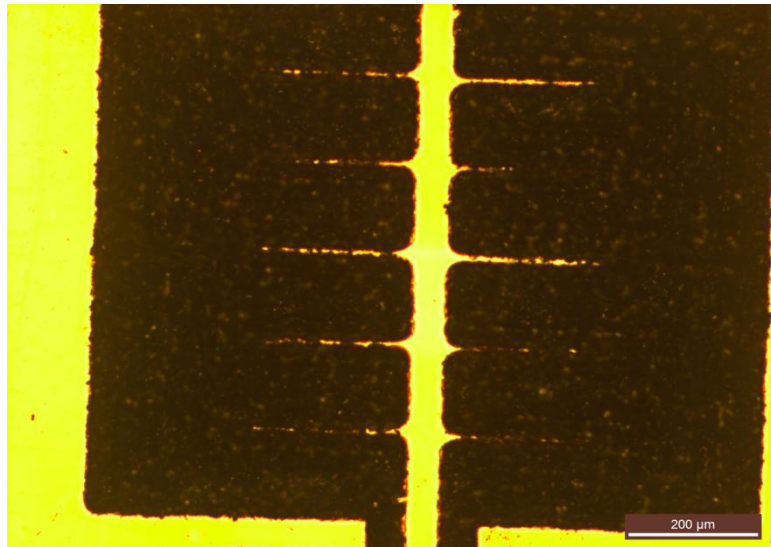


Figure 6.29: Optical microscopic image of the NiTi micro-comb structures

6. 6. Conclusions

The fabrication process for the NiTi-and TiN-based MEMS devices using laser bulk micromachining and FIB techniques has been discussed. The TiN-based micro-heaters were fabricated using focused ion beam and laser bulk micromachining techniques and tested for their heating efficiencies. A maximum temperature of $\sim 400^{\circ}\text{C}$ was achieved by applying a power of 8W to the TiN micro-heaters. This

temperature is sufficient for the actuation in NiTi MEMS devices. The NiTi-based micro-cantilevers were fabricated using femtosecond laser micromachining technique alongside these TiN micro-heaters. The heat generated by the TiN micro-heaters was utilized to actuate the NiTi micro-cantilevers. The RIE-Cl etching technique was used to etch the bottom silicon for making the NiTi free-standing structures. NiTi microstructures like micromesh and micro-comb structures were fabricated using a Ytterbium pulsed fiber laser. The fabricated structures and devices will be useful in microelectronics, optical sensing, microfluidics, and biomedical applications.

CHAPTER 7

SUMMARY, CONCLUSIONS, AND FUTURE DIRECTIONS

The conclusions of the thesis and the scope for future directions are presented in this chapter.

7.1. Summary and conclusions

- A comparative study was carried out between DCMS and PDCMS sputtered 1 – 1.2 μm thick NiTi thin films deposited at various substrate temperatures (400, 500, 600, and 650°C).
- It was observed that the films deposited at 500, 600, and 650°C were crystalline with an orientation towards the austenitic phase with a strong peak at 42.6°, corresponding to the (110) plane of NiTi at room temperature. It was also observed that the PDCMS NiTi films exhibited larger grain sizes than the DCMS. The compositional variations observed in the NiTi films deposited by both methods were significantly less.
- It was realized that the NiTi thin films deposited by the PDCMS technique were of superior quality as compared to DCMS films under the same processing conditions, such as temperature (600°C), pressure (5×10^{-3} mabr), power (100W), gas flow (25 sccm) and substrate-to-target distance (9 cm), etc. The enhanced properties of PDCMS NiTi films can be attributed to the higher plasma density in the PDCMS process as compared to the DCMS process, as observed from the *in-situ* OES analysis.
- In the next attempt, the effects of deposition pressure (2.5×10^{-3} to 1×10^{-2} mbar) and pulse frequencies (50 to 350 kHz) were investigated to improve NiTi film properties, including the martensitic phase formation at room temperature.
- The NiTi films deposited at pressures of $\sim 10^{-3}$ mbar order exhibited an austenitic phase at room temperature. On the other hand, the films deposited at a pressure of $\sim 10^{-2}$ mbar order exhibited a martensitic phase at room temperature. The OES analysis revealed that with an increase in the deposition pressures, the peak

intensities of nickel, titanium, and argon were also found to increase. When pressure increases, the mean free path decreases, affecting the adatoms' energy reaching onto the substrate. This can affect the structure of the growing NiTi films.

- The phase transformation studies of NiTi thin films deposited at 1×10^{-2} mbar was carried out using HT-XRD. It was observed that the peak corresponding to the martensitic phase (111) at 41.7° was shifted to austenite (110) at 42.6° with an increase of the stage temperature to 150°C .
- No significant changes in the structural, surface and compositional properties of NiTi films were observed in the films deposited at various pulse frequencies (50 to 350 kHz). There was only a minor increase in the nickel, titanium, and argon intensities in the OES spectra at the given target power, 100W, which was insufficient for significantly impacting the film properties.
- TiN thin films (275 ± 10 nm) were deposited onto Si and Si/SiO₂ substrates by the PDCMS technique at various substrate temperatures and nitrogen gas partial pressures. These two process conditions significantly impacted the microstructural properties of TiN films. As a result, the resistivity of TiN films was found to vary with the substrate temperature and Ar:N₂ ratio.
- The differential pumping mechanism impacted the microstructural properties of TiN thin films. The TiN films deposited with differential pumping are more oriented towards the (111) plane, whereas the TiN films deposited without the differential pumping are more oriented towards the (200) plane. The influence of differential pumping on the TiN plasma properties was *in-situ* investigated using the optical emission spectroscopy.
- The lowest electrical resistivity ($305 \mu\Omega\cdot\text{cm}$) was achieved with TiN films deposited at the substrate temperature of 300°C and an Ar:N₂ ratio of 20:5. This could be attributed to the preferred orientation of TiN thin films towards the (200) plane. The TiN films with low resistivity values were used to fabricate TiN micro-heaters, which can be used as a thermal stimulus for actuating the NiTi-based MEMS structures.
- TiN micro-heaters (length 500 μm) were fabricated on Si/SiO₂ substrates using the focused ion beam micro-machining technique. An IR thermal camera was used to measure the heat generated upon input power. A maximum temperature of

250°C was achieved within a min. by giving an input power of 2.8W. This temperature is sufficient for the actuation in NiTi-based SMA micro-structures.

- In another attempt, the TiN micro-heaters with different dimensions were fabricated using laser machining techniques. These micro-heaters were fabricated with different dimensions (length – 200, 400, 600 μm) and were optimized for their heating capabilities at the same input power. The micro-heater with a larger length (600 μm) exhibited superior heat generation at the same input powers than the other two. A maximum temperature of 400°C was achieved with power at 8W in 2 min.
- NiTi micro-cantilevers were fabricated using room temperature martensitic phase films by integrating TiN micro-heaters. The NiTi and TiN microstructures were fabricated using a combination of femtosecond bulk micromachining, FIB, and RIE-Cl.
- Actuation of NiTi micro-cantilevers was observed by varying the input power to TiN micro-heaters in the range of 0 to 2.8W.
- Microstructures, such as micro-wrapper, micro-mesh, and micro-comb, were fabricated using femtosecond laser and Ytterbium fiber laser bulk micromachining techniques.
- The fabricated structures will be useful in various MEMS applications, including optical sensing, drug delivery, fluid mechanics, etc. These devices can be used in bio-friendly environments since NiTi and TiN are biocompatible.

7. 2. Future directions

The future work in this field may focus on:

- Improving mainly the crystalline nature and other properties of the nickel-titanium thin films at lower process temperatures. These can be explored by employing the emerging high power impulse magnetron sputter (Hi-PIMS) deposition technique. This technique can produce much higher dense NiTi plasmas, facilitating crystallization at lower growth temperatures.
- The Hi-PIMS technique with a third element adding to the NiTi system can produce densely packed and thicker films that can be used in various applications,

like shape memory alloy damping application, especially with high-temperature shape memory alloys (HT-SMAs).

- The Hi-PIMS provides faster film growth rates, making the NiTi and TiN thin films suitable as corrosion-resistant coatings in gas turbine blades.
- The devices with a combination of NiTi and TiN can have a wide range of applications in biomedical/optical domains.

References

- Ahadi, A. and Sun Q. (2013) “Stress hysteresis and temperature dependence of phase transition stress in nanostructured NiTi—Effects of grain size” *Applied Physics Letters*, 103 (2), 021902
- Ainslie, K., Knick, C., Smith, G., Li, J., Troxel, C., Mehta, A. and Kukreja, R. (2019) “Physical Controlling shape memory effects in NiTi thin films grown on Ru seed layer”, *Sensors and Actuators A: Physical*, 294, 133–139
- Ao, J.-P., Naoi, Yoshik and Ohno, Yasuo (2013) “Thermally stable TiN Schottky contact on AlGaIn/GaN heterostructure” *Vacuum*, 87, 150 – 154
- Arshi, Nishat, Lu, Junqing, Joo, Yun Kon, Lee, Chan Gyu, Yoon, Jae Hong and Ahmed, Faheem, (2012) “Study on structural, morphological and electrical properties of sputtered titanium nitride films under different argon gas flow” *Materials Chemistry and Physics*, 134 (2-3) 839 – 844
- Arranz, M. A. and Riveiro, J. M. (2005) “Shape memory effect in sputtered Ti-Ni thin films” *Journal of Magnetism and Magnetic Materials*, 290–291 (PART 2) 865–867
- Ashcroft, N. W. and Mermin, M. D. (1976) “Solid state physics” Saunders College Publishing, *Harcourt College Publishers, Orlando, FL*
- Bayer, B. C., Sanjabi, S., Baehtz, C., Wirth, C.T., Esconjauregui, S., Weatherup, R.S., Barber, Z.H., Hofmann, S. and Robertson J. (2011) "Carbon nanotube forest growth on NiTi shape memory alloy thin films for thermal actuation" *Thin Solid Films*, 519(18), 6126-6129
- Belkind, A., Freilich, A., Lopez. J., Zhao, Z., Zhu, W. and Becker, K (2005) “Characterization of pulsed dc magnetron sputtering plasmas” *New Journal of Physics*, 7, 90
- Behera, A., Aich, H., Behera, A. and Sahu, A. (2015) “Processing and Characterization of Magnetron Sputtered Ni/Ti Thin Film and their Annealing Behaviour to Induce Shape Memory Effect” *Materials today proceedings*, 2 (4–5), 1183-1192

Bendahan, M., Canet, P., Seguin, J.-L. And Carchano, H. (1995) “Control composition study of sputtered NiTi shape memory alloy film” *Material Science and Engineering B*, 34 (2-3), 112–115

Bendahan, M., Seguin, J.-L., Canet, P. and Carchano, H. (1996) “NiTi shape memory alloy thin films: composition control using optical emission spectroscopy” *Thin Solid Films*, 283 (1-2), 61 – 66

Bendahan, M., Aguir, K., Seguin J. L. and Carchano, H. (1999) “TiNi thin films as a gate of MOS capacity sensors” *Sens. Actuat.*, 74, 242–245

Berg, S., Larsson, T. and Blom, H-O., (1986) “The use of nitrogen flow as a deposition rate control in reactive sputtering” *Journal of Vacuum Science & Technology A*, 4, 594 – 597

Biffi, C. A. and Tuissi, A. (2017) “Nitinol laser cutting: microstructure and functional properties of femtosecond and continuous wave laser processing”, *Smart Materials and Structures*, 26(3), 035006.

Binnig, G., Quate, C. F. and Gerber, Ch. (1986) “Atomic Force Microscope” *Phys. Rev. Lett.*, 56 (9), 930 – 933

Bogner, A., Jouneau, P.-H., Thollet, G., Basset, D. and Gauthier, C. (2007) a “A history of scanning electron microscopy developments: Towards “wet-STEM” imaging” *Micron*, 38 (4), 390 – 401

Boonyawan, D., Waruriya, P. and Suttait, K. (2016) “Characterization of titanium nitride–hydroxyapatite on PEEK for dental implants by co-axis target magnetron sputtering” *Surface and Coatings Technology*, 306, 164-170

Bourim, E.-M., Kim, H. Y. and Chung, N.-K. (2018) “Development and Characterization of Non-Evaporable Getter Thin Films with Ru Seeding Layer for MEMS Applications” *Micromachines*, 9 (10), 490

- Bradley, J. W., Backer, H., Aranda-Gonzalvo, Y., Kelly, P. J. and Arnell, R. D. (2002) “The distribution of ion energies at the substrate in an asymmetric bi-polar pulsed DC magnetron discharge” *Plasma Sources Sci. Technol.*, 11, 165–174
- Brien, J. O. U. and Kelly, P. J. (2001) “Characterization studies of the pulsed dual cathode magnetron sputtering process for oxide films”, *Surface Coating Technology*, 142 – 144, 621–627
- Briggs, J. A., Naik, G. V., Petach, T. A., Baum, B. K., Goldhaber-Gordon, D. and Dionne, J. A. (2016) “Fully CMOS-compatible titanium nitride nanoantennas” *Appl. Phys. Lett.* 108(5), 051110
- Buehler, W. J. Gilfrich, J. V. and Wiley, R. C. (1963). “Effect of Low-Temperature Phase Changes on the Mechanical Properties of Alloys near Composition TiNi” *Journal of Applied Physics*, 34 (5), 1475-1477
- Buhl, R., Pulker, H.K. and Moll, E. (1981) “TiN coatings on steel” *Thin Solid Films*, 80(1), 265 – 270
- Busch, J. D. and Johnson, A. D. (1990) “Shape-memory properties in Ni-Ti sputter-deposited film” *Journal of Applied Physics*, 68 (12), 6224-6228
- Butt, M. Z. (2014) “Laser ablation characteristics of metallic materials: Role of Debye-Waller thermal parameter” *IOP Conf. Series: Materials Science and Engineering*, 60, 012068
- Cha, J. O., Nam, T. H., Alghusun, M. and Ahn, J.S. (2012) “Composition and crystalline properties of TiNi thin films prepared by pulsed laser deposition under vacuum and in ambient Ar gas” *Nanoscale Research Letters*, 7, 37
- Chan P.M., Chung C.Y. and Ng K.C. (2008) “NiTi shape memory alloy thin film sensor micro-array for detection of infrared radiation” *Journal of Alloys and Compounds*, 449, 148–151
- Chapman, B. N. (1980) “Glow Discharge Processes: Sputtering and Plasma Etching” *Wiley-Interscience*

Chargui, A., Beainou, R. E., Mosset, A., Euphrasie, S., Potin, V., Vairac, P. and Martin, N. (2020) "Influence of thickness and sputtering pressure on electrical resistivity and elastic wave propagation in oriented columnar tungsten thin films" *Nanomaterials*, 10 (1), 81-98

Chaudhary, N. and Kaur, D. (2016) "Shape memory alloy thin films and heterostructures for MEMS applications: A review" *Sensors and Actuators A: Physical*, 242, 162-181

Chaudhary, N., Kharat, D. K. and Kaur, D. (2011) "Structural, electrical and mechanical properties of magnetron sputtered NiTi/PZT/TiO_x thin film heterostructures" *Surface and Coatings Technology*, 205(11), 3387-3396

Chawla V., Jayaganthan. R. and Chandra. Ramesh. (2009) "Microstructural characteristics and mechanical properties of magnetron sputtered nanocrystalline TiN films on glass substrate" *Bull. Mater. Sci.*, 32 (2), 117 – 123

Cheng Y. L., Wei, B. J., Shih, F. H. and Wang, Y. L. (2013) "Stability and Reliability of Ti/TiN as a Thin Film Resistor" *ECS Journal of Solid State Science and Technology*, 2 (1), Q12 – Q15.

Chopra, K. L. (1966) "Thin Film Phenomena" *McGraw Hill*, New York

Chun, S.-Y. (2013) "The Structure and Properties of Pulsed dc Magnetron Sputtered Nanocrystalline TiN Films for Electrodes of Alkali Metal Thermal-to-Electric Conversion Systems" *Journal of Nanoscience and Nanotechnology*, (13)3, 1993-1996

Chung C.Y. and Chan P.M. (2011). "NiTi shape memory alloy thin film micro-cantilevers array" *Thin Solid Films*, 519, 5307 – 5309

Cicek, H., Efeoglu, I., Totik, Y., Ezirmik, K. V. and Arslan, E. (2015) "A low temperature *in-situ* crystalline TiNi shape memory thin film deposited by magnetron sputtering" *Surf. Coatings Technol.*, 284, 90-93

- Creemer, J.F., Briand, D., Zandbergen, H.W., van der Vlist, W., de Boer, C.R., de Rooij, N.F. and Sarro, P.M. (2008) “Microhotplates with TiN heaters” *Sensors and Actuators A: Physical*, 148(2), 416 – 421
- Cuong, N. D., Kim, D.-J., Kang, B.-D. and Yoon, S.-G. (2006) “Effects of Nitrogen Concentration on Structural and Electrical Properties of Titanium Nitride for Thin-Film Resistor Applications” *Electrochemical and Solid-State Letters*, 9(9), G279 – G281
- Cullity, B. D. and Stock, S. (2014) “Elements of X-ray diffraction” *Pearson Education India*.
- Dapino, M. J. (2004) “On magnetostrictive materials and their use in adaptive structures” *Structural Engineering and Mechanics*, 17 (3- 4), 303 - 329
- Daneshvar, H., Safavi, M. S., Khalilli, V. and Khalil-Allafi, J. (2020) “Influence of aging temperature on phase transformation and mechanical behavior of NiTi thin films deposited by magnetron sputtering technique” *Journal of Ultrafine Grained and Nanostructured Materials*, 53(1), 15 - 22
- De Maayer, P. J. P. and Mackenzie, J. D. (1975) “The Electrical Properties of Thin Films of TiN_x and TiC_x” *Zeitschrift für Naturforschung A*, 30(12), 1661–1666
- Ding, Y. and Northwood, D. O. (1992) “Methods for preparation of cross-sectional scanning electron microscopy specimens and their application to corroded specimens of a zirconium alloy and TiN coated stainless steel”, *Mater. Char.*, 29, 25 – 33
- Faltermeier, C. Goldberg, C., Jones, M., Upham, A., Manger, D., Peterson, G., Lau, J., Kaloyeros, A. E., Arkles, B. and Paranjpe, A. (1997) “Barrier Properties of Titanium Nitride Films Grown by Low Temperature Chemical Vapor Deposition from Titanium Tetraiodide” *Journal of The Electrochemical Society*, 144(3), 1002
- Fang, Q. and Zhang, J.-Y. (2001) “Nano-porous TiN thin films deposited by reactive sputtering method” *International Journal of Inorganic Materials*, 3 (8), 1193 – 1196

- Fedchak, J. A., Scherschligt, J., Barker, D., Eckel, S., Farrell, A. P. and Sefa, M. (2018) "Vacuum furnace for degassing stainless-steel vacuum components" *Journal of Vacuum Science & Technology A*, 36 (2), 023201
- Fernandes, F. M. B., Martins, R., Teresa Nogueira, M., Silva, R. J. C., Nunes, P., Costa, D., Ferreira, I. and Martins R. (2002) "Structural characterisation of NiTi thin film shape memory alloys" *Sensors and Actuators A: Physical*, 99 (1-2), 55–58
- Friedensen, S., Mlack, J. T. and Drndić, M. (2017) "Materials analysis and focused ion beam nanofabrication of topological insulator Bi₂Se₃" *Sci Rep* 7, 13466
- Fu, Y., Du, H., Huang, W., Zhang, S. and Hu, M. (2004) "TiNi-based thin films in MEMS applications: a review", *Sensors and Actuators A: Physical*, 112 (2 – 3), 395 – 408.
- Fu, Y., Huang, W., Du, H., Huang, X., Tan, J. and Gao, X. (2001) "Characterization of TiNi shape-memory alloy thin films for MEMS applications", *Surface Coating Technology*, 145(1-3), 107–112
- Fu, Y. Q., Huang, W., Du, H., Huang, X., Tan, J. and Gao, X. (2001) "Characterization of TiNi shape-memory alloy thin films for MEMS applications" *Surface and Coatings Technology*, 145 (1 -3), 107 – 112
- Fu, Y.Q., Zhang, Sam, Wu, M.J., Huang, W.M., Du, H.J., Luo, J.K., Flewitt, A.J. and Milne, W.I. (2006). "On the lower thickness boundary of sputtered TiNi films for shape memory application" *Thin Solid Films*, 515 (1), 80 – 86
- Giorleo, L., Ceretti, E. and Giardini, C. (2016) "Optimization of laser micromachining process for biomedical device fabrication" *Int J Adv Manuf Technol.*, 82, 901–907
- Gao, J., Chan-Park, M. B., Xie, D., Ngoi, B. K. A. and YUE, C. Y. (2003) "Sub-Micron Patterning Titanium Nitride By Focused Ion-Beam Technique" *International Journal of Computational Engineering Science*, 4(3), 501 - 504
- Geetha Priyadarshini, B., Aich, S. and Chakraborty, M. (2010). "An Investigation on Phase Formations and Microstructures of Ni-rich Ni-Ti Shape Memory Alloy Thin Films" *Metallurgical and Materials Transactions A*, 42 (11), 3284 – 3290

- Geetha Priyadarshini, B., Esakkiraja, N., Aich, S. and Chakraborty, M. (2016). “Resputtering Effect on Nanocrystalline Ni-Ti Alloy Films” *Metallurgical and Materials Transactions A*, 1 - 10
- Giessibl, F. J. (2003) “Advances in atomic force microscopy” *Rev. Mod. Phys.*, 75 (2), 949 – 983
- Gill, J. J., Chang, D. T., Momoda L. A. and Carman, G. P. (2001) “Manufacturing issues of thin film TiNimicrowrapper” *Sens. Actuat. A*, 93(2), 148 – 156
- Giorleo, L., Ceretti, E. And Giardini, C. (2016) “Optimization of laser micromachining process for biomedical device fabrication”, *Int J Adv Manuf Technol*, 82, 901–907.
- Goldstein, J. I., Newbury, D. E., Echlin, P., Joy, D. C., Lyman, C. E., Lifshin, E., Sawyer, L. and Michael, J. R. (2003) “X-Ray Spectral Measurement: EDS and WDSIn: Scanning Electron Microscopy and X-ray Microanalysis” *Springer, Boston, MA*. 297 - 353
- Grummon, D., & Chang, L. (1992) “Effect of Concurrent Ion Bombardment on Structure and Composition of Ion Sputter-Deposited Ni-Ti Thin Films” *MRS Proceedings*, 268, 167
- Habijan, T., De Miranda, R.L., Zamponi, C., Quandt, E., Greulich, C., Schildhauer, T.A. and Koller, M. (2012). “The biocompatibility and mechanical properties of cylindrical NiTi thin films produced by magnetron sputtering” *Materials Science and Engineering: C*, 32 (8), 2523 - 2528
- Haferkamp, H., Paschko, S. and Goede, M. (2001) “New laser machining processes for shape memory alloys” *SPIE Proc.*, 4234, 94 - 101
- Hakola, A., Heczko, O., Jaakkola, A., Kajava, T. and Ullakko, K., (2004) “Ni-Mn-Ga films on Si, GaAs and Ni-Mn-Ga single crystals by pulsed laser deposition” *Applied Surface Science*, 238(1 – 4), 155–158.

- He, J. L., Won, K. W. and Chang, J. T. (2000) "TiNi thin films prepared by cathodic arc plasma ion plating" *Thin Solid Films*, 359(1), 46 – 54
- Herman, I. P. (1996) "Optical Diagnostics for Thin Film Processing", *Academic Press*, 157 – 208
- Hou, H., Hamilton, R. F., Horn, M. W. and Jin, Y. (2014) "NiTi thin films prepared by biased target ion beam deposition co-sputtering from elemental Ni and Ti targets" *Thin Solid Films*, 570(A), 1 - 6
- How, S. R., Nayan, N. and Lias, J. (2017) "The influence of N₂ flow rate on Ar and Ti Emission in high-pressure magnetron sputtering system plasma", *AIP Conference Proceedings*, 1824 (1), 030024
- How, S. R., Nayan, N., Lias, J., Ahmad, M. K., Sahdan, M. Z., Mamat, M. H., Mahmood M. R. and Aldalbahi, A. (2018) "Plasma diagnostic by optical emission spectroscopy on reactive magnetron sputtering plasma –A Brief Introduction", *Journal of Physics: Conference Series*, 1027, 012005
- Hung, C.-H., Chang, F.-Y., Chang, T.-L., Chang, Y.-T., Huang, K.-W., Liang, P.-C. (2015) "Micromachining NiTi tubes for use in medical devices by using a femtosecond laser" *Optics and Lasers in Engineering*, 66, 34-40
- Irudayaraj, A. A., Kuppusami, P. and Kalainathan, S. (2008) "Structural properties and electrical resistivity of TiN_x and Ti_{1-x}Al_xN films prepared by reactive dc magnetron sputtering: effect of nitrogen flowrate" *Journal Surface Engineering*, 24(1), 28 - 35
- Ishida, A., Sato, M., Takei, A., Nomura, K. and Miyazaki, S. (1996). "Effect of aging on shape memory behavior of Ti-51.3 at pct Ni thin films" *Metall. Mater. Trans.*, 27 (12), 3753–3759
- Ishida, A. and Sato, M. (2003) "Thickness effect on shape memory behavior of Ti-50.0at.% Ni thin film" *Acta Materialia*, 51 (18), 5571 - 5578

- Ishida, A., Takei, A. and Miyazaki, S. (1993) “Shape memory thin film of TiNi formed by sputtering” *Thin Solid Films*, 228, 210–214
- Ismail, M. H., Goodall, R., Davies, H. A. and Todd, I. (2012) “Formation of microporous NiTi by transient liquid phase sintering of elemental powders” *Materials Science and Engineering:C*, 32 (6), 1480 – 1485
- Jansen, H., Gardeniers, H., de Boer, M., Elwenspoek M. and Fluitman, J. (1996) “A survey on the reactive ion etching of silicon in microtechnology”, *Journal of Micromechanics and Microengineering*, 6(1), 14 – 28.
- Jin, S., Zhang, Y., Wang, Q., Zhang, D. and Zhang, S. (2013) “Influence of TiN coating on the biocompatibility of medical NiTi alloy” *Colloids Surfaces B Biointerfaces*, 101, 343–349
- Johnson, A. D., (1999) “NiTi thin film three dimensional devices-fabrication and 3-D TiNi shape memory alloy actuators” *Micromachine Devices*, 4, 1
- Kabla, M., Seiner, H., Musilova, M., Landa, M. and Shilo, D. (2014) “The relationships between sputter deposition conditions, grain size, and phase transformation temperatures in NiTi thin films” *Acta Mater.*, 70, 79 – 91
- Kaufmann, G. B. and Mayo, I. (1997) “The Story of Nitinol: The Serendipitous Discovery of the Memory Metal and Its Applications” *Chem. Educator*, 2, 1–21
- Kearneya, B. T., Jugdersuren, B., Culbertson, J. C., Desario, P. A. and Liu, X. (2018) “Substrate and annealing temperature dependent electrical resistivity of sputtered titanium nitride thin films” *Thin Solid Films*, 661, 78-83
- Kaur, N. Choudhary, N., Goyal, R. N., Viladkar, S., Matai, I., Gopinath, P., Chockalingam, S. and Kaur, D. (2013) “Magnetron sputtered Cu₃N/NiTiCu shape memory thin film heterostructures for MEMS applications” *J. Nanoparticle Res.*, 15, Article 1468
- Kelly, P. J., Abu-Zeid, O. A., Arnell, R. D. and Tong, J. (1996) “The deposition of aluminium oxide coatings by reactive unbalanced magnetron sputtering” *Surface and Coatings Technology*, 86–87 (Part 1), 28-32

Kelly, P. J., Beevers, C. F., Henderson, P. S., Arnell, R. D., Bradley, J. W. and Backer, H. (2003) "A comparison of the properties of titanium-based films produced by pulsed and continuous DC magnetron sputtering" *Surface and Coatings Technology*, 174–175, 795-800

Kelly P. J. and Bradley, J. W. (2009) "Pulsed magnetron sputtering - process overview and applications" *Journal of Optoelectronics and Advanced Materials*, 11, 1101-1107

Kelly, P. J., vomBraucke, T., Liu, Z., Arnell, R. D. and Doyle, E. D. (2007) "Pulsed DC titanium nitride coatings for improved tribological performance and tool life" *Surface and Coatings Technology*, 202 (4–7), 774-780

Khojier, K., Savaloni, H., Shokrai, E., Dehghani, Z. and Dehnavi, N. Z. (2013) "Influence of argon gas flow on mechanical and electrical properties of sputtered titanium nitride thin films" *Journal of Theoretical and Applied Physics*, 7(1), 37

Kiihamäki J. and Franssila S., (1999) "Pattern shape effects and artefacts in deep silicon etching", *Journal of Vacuum Science & Technology A*, 17(4), 2280-2285

Kim, H. T., Park, J. Y. and Park, C. (2012) "Effects of nitrogen flow rate on titanium nitride films deposition by DC facing target sputtering method" *Korean J. Chem. Eng.*, 29(5), 676–679

Koker, M.K.A., Schaab, J., Zotov, N. and Mittemeijer, E.J. (2013). "X-ray diffraction study of the reverse martensitic transformation in NiTi shape memory thin films" *Thin Solid Films*, 545, 71 - 80

Kong, M. C. and Wang, J. (2014) "Surface Quality Analysis of Titanium and Nickel-based Alloys Using Picosecond Laser" *Procedia CIRP*, 13, 417-422

Krulevitch, P., Lee, A. P., Ramsey, P. B., Trevino, J. C., Hamilton, J. and Northrup, M. A. (1996) "Thin film shape memory alloy microactuators" *Journal of Microelectromechanical Systems*, 5(4), 270–282

- Kumar, A., Singh, D., Goyal, R. N. and Kaur, D. (2009) "Fabrication and nanoindentation properties of TiN/NiTi thin films and their applications in electrochemical sensing" *Talanta*, (78) 3, 964-969
- Kumar, A., Singh, D. and Kaur, D. (2009) "Grain size effect on structural, electrical and mechanical properties of NiTi thin films deposited by magnetron co-sputtering" *Surface Coating Technology*, 203(12), 1596–1603
- Kumar, A., Singh, D. and Kaur, D. (2012) "Variation in phase transformation paths of NiTi films as a function of film thickness" *Sensors and Actuators A: Physical*, 178, 57-63
- Kumar, A., Singh, D., Kumar, A. and Kaur, D. (2009) "Effect of crystallographic orientation of nanocrystalline TiN on structural, electrical and mechanical properties of TiN/NiTi thin films" *Journal of Alloys and Compounds*, 479 (1–2), 166-172
- Kumar, P., M. A., Jithin, Mohan, S. and Avasthi, S. (2020) "Hundred-fold reduction in Iron diffusivity in titanium nitride diffusion barrier on steel by microstructure engineering" *Thin Solid Films*, 716, 138416
- Li, C., Nikumb, S. and Wong, F. (2006) "An optimal process of femtosecond laser cutting of NiTi shape memory alloy for fabrication of miniature devices", *Optics and Lasers in Engineering*, (44)10, 1078-1087.
- Li, Y., Zhao, T., Wei, S., Xiang, Y. and Chen, H. (2010) "Effect of Ta₂O₅/TiO₂ thin film on mechanical properties, corrosion and cell behavior of the NiTi alloy implanted with tantalum" *Materials Science and Engineering: C*, 30(8), 1227-1235
- Lima, M. S. F., Folio, F. and Mischler, S. (2005) "Microstructure and surface properties of laser-remelted titanium nitride coatings on titanium" *Surface and Coatings Technology*, 199 (1), 83-91
- Lin, J., Wu, Z. L., Zhang, X. H., Mishra, B., Moore, J. J. and Sproul, W. D. (2009) "A comparative study of CrN_x coatings Synthesized by dc and pulsed dc magnetron sputtering" *Thin Solid Films*, 517(6), 1887–1894

- Lindquist, J. M., Young, R. J. and Jaehnig, M. C. (1993) “Recent advances in application of focused ion beam technology” *Microelectronic Engineering*, 21(1-4), 179-185
- Loger, K., Engel, A., Haupt, J., de Miranda, R. L., Lutter, G. and Quandt, E. (2016) “Microstructured nickel-titanium thin film leaflets for hybrid tissue engineered heart valves fabricated by magnetron sputter deposition” *Cardiovascular Engineering and Technology*, 7, 69–77
- Lou, H. Q., Axen, N., Somekh, R. E. and Hutchings, I. M. (1997) “Effect of deposition conditions on the characteristics of reactively sputtered titanium nitride thin films” *Surface and Coatings Technology*, 90 (1 – 2), 123 – 127
- Lu, L., Luo, F., Huang, Z., Zhou, W. and Zhu, D. (2018) “Influence of the nitrogen flow rate on the infrared emissivity of TiN_x films” *Infrared Phys Technol.*, 88, 144–148
- Maissel, L. I. and Glang, R. (1970) “Handbook of thin film technology” *McGraw-Hill, New York*, 3-33
- Maissel, L. I. and Glang, R. (1970) “Handbook of thin film technology” *McGraw-Hill*, 3-33
- Makino, E. Uenoyoma, M. and Shibata, T. (1998) “Flash evaporation of TiNi shape memory thin film for microactuators” *Sensors and Actuators A: Physical*, 71(3), 187-192
- Mamat, H., Aldalbahi, A., Mahmood, M. R., Nayan, N., How, S. R., Ahmad, M. K., Lias, J. and Sahdan, M. Z. (2018) “Plasma diagnostic by optical emission spectroscopy on reactive magnetron sputtering plasma –A Brief Introduction”, *Journal of Physics Conference Series*, 1027, 012005
- Martins, R.M.S., Schell, N., Beckers, M., Mahesh, K.K., Silva, R.J.C. and Fernandes, F.M.B. (2006). “Growth of sputter-deposited Ni-Ti thin films: Effect of a SiO₂ buffer layer” *Applied Physics A*, 84 (3), 285 - 289

- Mary, R., Choudhary, D. and Kar, A. K. (2014) “Applications of Fiber Lasers for the Development of Compact Photonic Devices” *IEEE Journal of Selected Topics in Quantum Electronics*, 20, 72 – 84
- Massl, S., Thomma, W., Keckes, J. and Pippan, R. (2009) “Investigation of fracture properties of magnetron-sputtered TiN films by means of a FIB-based cantilever bending technique”, *Acta Materialia*, 57(6), 1768-1776.
- Mehrpouya, M. and Bidsorkhi, H. C. (2016) “MEMS Applications of NiTi Based Shape Memory Alloys: A Review” *Micro and Nanosystems*, 8(2), 79-91
- Melo, L.L., Vaz, A.R., Salvadori, M.C. and Cattani, M. (2004) “Grain Sizes and Surface Roughness in Platinum and Gold Thin Films” *Journal of Metastable and Nanocrystalline Materials*, 20–21, 623–628
- Meng, L.J., Azevedo, A . and dos Santos, MP ., (1995) “Deposition and properties of titanium nitride films produced by dc reactive magnetron sputtering” *Vacuum*, 46 (3), 233 – 239
- Meng, L. J. and Dos Santos, M. P. (1997) “Characterization of titanium nitride films prepared by d.c. reactive magnetron sputtering at different nitrogen pressures”, *Surface Coatings Technology*, 90(1-2), 64–70
- Miyazaki, S., Fu, Y. Q. and Huang, W. M. (2009) “Overview of sputter-deposited TiNi based thin films” *Thin Film Shape Memory Alloys: Fundamentals and Device Applications*, Cambridge University Press, New York
- Miyazaki, S., Fu, Y. Q. and Huang, W. M. (2009) “Thin Film Shape Memory Alloys” *Cambridge University Press, New York*
- Momeni S., Tillmann, W., Pohl, M. (2016) “Composite cavitation resistant PVD coatings based on NiTi thin films” *Materials & Design*, 110, 830-838
- Momeni S., Biskupek, J. and Tillmann, W. (2017) “Tailoring microstructure, mechanical and tribological properties of NiTi thin films by controlling *in-situ* annealing temperature” *Thin Solid Films*, 628, 13-21

Morozov, I. A., Gudovskikh, A. S., Kudryashov, D. A. and Kotlyar, K. P. (2017) “Influence of dry etching condition to geometry of vertically aligned silicon nanostructures”, *Journal of Physics: Conf. Series*, 917, 052030.

Muhammad, N., Whitehead, D., Boor, A., Oppenlander, W., Liu, Z. and Li, L. (2011) “Picosecond laser micromachining of nitinol and platinum–iridium alloy for coronary stent applications” *Applied Physics A*, 106, 607–617

Murray, J. L. (1987) “Phase Diagrams of Binary Titanium Alloys”, ASM International Metals Park.

Musil, J., Baroch, P., Vicek, J., Nam, K. H. and Han, J. G. (2005) “Reactive magnetron sputtering of thin films: present status and trends”, *Thin Solid Films*, 475 (1 - 2), 208-218

Nafarizal, N., Takada, N. and Sasaki, K. (2009) “Investigations of production processes of Ti+ in high pressure magnetron sputtering plasmas” *Japanese Journal of Applied Physics*, 48, 126003-1 - 126003-7

Nakano, T., Hoshi, K. and Baba, S. (2008) “Effect of background gas environment on oxygen incorporation in TiN films deposited using UHV reactive magnetron sputtering” *Vacuum*, 83 (3), 467 - 469

NIST Atomic Spectra Database <http://www.nist.gov/pml/data/asd.cfm>, (Access date: 17.3.2019)

Noh, H. Y., Lee, K. H., Cui, X. X. and Choi, C. S. (2000) “The composition and structure of TiNi thin film formed by electron beam evaporation” *Scripta Materialia*, 43(9), 847-852

Oettel, H., Wiedemann, R. and Preißler, S. (1995) “Residual stresses in nitride hard coatings prepared by magnetron sputtering and arc evaporation” *Surface and Coatings Technology*, 74 – 75 (1), 273 – 278

Olabi, A. G. and Grunwald, A (2008) “Design and application of magnetostrictive materials” *Materials & Design*, 29 (2), 469-483

- Ohring, M. (1992) “The material science of thin films” *Academic Press*, 79 – 144
- Ohta, A., Bhansali, S., Kishimoto, I. and Umeda, A. (2000). “Novel fabrication technique of TiNi shape memory alloy film using separate Ti and Ni targets” *Sensors and Actuators A: Physical*, 86 (3), 165 – 170
- Osellame, R., Cerullo, G. and Ramponi, R. (2012) “Femtosecond Laser Micromachining: Photonic and Microfluidic Devices in Transparent Materials” *Springer, Berlin, Heidelberg*
- Otubo, J., Rigo, O. D., Coelho, A. A., Neto, C. M. and Mei, P. R. (2008) “The influence of carbon and oxygen content on the martensitic transformation temperatures and enthalpies of NiTi shape memory alloy” *Materials Science and Engineering: A*, 481–482, 639-642
- Otsuka, K. and Ren, X. B. (2005) “Physical metallurgy of Ti-Ni based shape memory alloys” *Progress in Materials Science*, 50 (5), 511-678
- Ou, Y. X., Lin, J., Tong, S., Che, H. L. Sproul, W. D. and Li, M. K. “Wear and corrosion resistance of CrN/TiN superlattice coatings deposited by a combined deep oscillation magnetron sputtering and pulsed dc magnetron sputtering” *Applied Surface Science*, 351, 32-343
- Pathan, F. S., Khan, Z., Semwal, P., George, S., Raval, D. C., Thankey, P. L., Manthena, H., Yuvakiran P. and Dhanani, K. R. (2012) “Study of Residual Gas Analyser (RGA) Response towards Known Leaks” *Journal of Physics: Conference Series*, 390, 012024
- Patsalas, P., Kalfagiannis, N., Kassavetis, S. (2015) “Optical Properties and Plasmonic Performance of Titanium Nitride” *Materials*, 8(6), 3128-3154
- Patsalas, P., Kalfagiannis, N., Kassavetis, S., Abadias, G., Bellas, D. V., Lekka, Ch. and Lidorikis, E. (2018) “Conductive nitrides: Growth principles, optical and electronic properties, and their perspectives in photonics and plasmonics” *Materials Science and Engineering: R: Reports*, 123, 1-55

- Pelleg, J., Zevin, L. Z., Lungo, S. and Croitoru, N. (1991) “Reactive-sputter-deposited TiN films on glass substrates”, *Thin Solid Films*, 197(1-2), 117–128
- Peng, Z., Miao, H., Qi, L., Yang, S. and Liu, C. (2003) “Hard and wear-resistant titanium nitride coatings for cemented carbide cutting tools by pulsed high energy density plasma” *Acta Materialia*, 51(11), 3085-3094
- Penilla, E. and Wang, J. (2008) “Pressure and Temperature Effects on Stoichiometry and Microstructure of Nitrogen-Rich TiN Thin Films Synthesized via Reactive Magnetron DC-Sputtering”, *Journal of Nanomaterials*, 2008(5), 267161
- Perron, A., Politano, O. and Vignal, V. (2008) “Grain size, stress and surface roughness” *Surface and interface analysis*, 40(3-4), 518–521
- Phelps, A. V. (1990) “Cross Sections and Swarm Coefficients for H^+ , H_2^+ , H_3^+ , H , H_2 , and H^- in H_2 for Energies from 0.1 eV to 10 keV” *Journal of Physical and Chemical Reference*, 19, 653
- Philip, T. V. and Beck, P. A. (1957) “CsCl-type ordered structures in binary alloys of transition elements” *Trans AIME*, 9, 1269–1271
- Ponon, N. K., Appleby, D. J. R., Arac, E., King, P. J., Ganti, S., Kwa, K. S. K. and O'Neill, A. (2015) “Effect of deposition conditions and post deposition anneal on reactively sputtered titanium nitride thin films” *Thin Solid Films*, 578, 31 – 37
- Quintino, L., Liu, L., Miranda, R. M., Silva, R. J. C. Hu, A. and Zhou, Y. (2013) “Cutting NiTi with Femtosecond Laser”, *Advances in Materials Science and Engineering*, 2013, 198434.
- Rao., G. M., (1990) “Ph.D. thesis, Indian Institute of Science”, Bangalore, India.
- Rao, J., Roberts, T., Lawson, K. and Nicholls, J. (2010) “Nickel titanium and nickel titanium hafnium shape memory alloy thin films” *Surface Coatings Technology*, 204 (15), 2331–2336

- Reddy, B. N. K. and Udayashnkar, N. K. (2016) "The effect of annealing temperature on the structural, morphological, mechanical and surface properties of intermetallic NiTi alloy thin films" *Surfaces and Interfaces*, 5, 62-71
- Reddy, B. N. K. and Udayashnkar, N. K. (2017) "Influence of annealing temperature on the structural, morphological, mechanical and surface properties of near equiatomic NiTi thin films" *Vacuum*, 142, 186-196
- Reddy, B. N. K. and Udayashnkar, N. K. (2017) "Aging time correlation in DC magnetron sputtered Ni₆₀Ti₄₀ thin films" *Vacuum*, 135, 124-134
- Reddy, B. N. K. (2020) "Aging time correlation for near-equiatomic NiTi thin films deposited through direct current magnetron sputtering" *Results in Physics*, 17, 103075
- Robbins, H., Liu, C., Hu, S., Bui, T. and Aoyagi, M., (2016) "Integration of a microfluidic chip with multiplexed optical fluorescence detector through anisotropic etching of Si using Tetramethylammonium hydroxide (TMAH)," *6th Electronic System-Integration Technology Conference (ESTC)*, 46280234, 1 - 6.
- Rohde, M. and Schüssler, A. (1997) "On the response-time behaviour of laser micromachined NiTi shape memory actuators" *Sensors and Actuators A: Physical*, 61 (1-3), 463-468
- Rosli, S. A., Aziz A. A. and Hamid, H. A. (2006) "Highly Chemical Reactive Ion Etching of Silicon in CF₄ Containing Plasmas," *IEEE International Conference on Semiconductor Electronics*, 856-860.
- Roquiny, Ph., Bodart, F. and Terwagne, G. (1999) "Colour control of titanium nitride coatings produced by reactive magnetron sputtering at temperature less than 100°C" *Surface and Coatings Technology*, 116-119, 278-283
- Saburi, T. and Nenno, S. in: I. Tamura (Ed.), (1986) Proceedings of the International Conference on Martensitic Transformations, Japan: *The Japan Inst Metals, Japan*, pp. 671.

Salhi, M., Abaidia, S. E. K., Mammeri, S. and Bouaouina B. (2017) “Sputter deposition of Titanium and Nickel thin films in radio frequency magnetron discharge characterized by optical emission spectroscopy and by Rutherford backscattering spectrometry” *Thin Solid Films*, 629, 22 -27

Saoula, N., Henda, K. and Kesri, R. (2009) “Influence of Nitrogen Content on the Structural and Mechanical Properties of TiN Thin Films”, *Journal of Plasma Fusion Research*, 8, 1403–1407

Sharma, A., Mohan, S. and Suwas, S (2016) “The influence of deposition temperature on the structure, microstructure, morphology and magnetic properties of sputter deposited nickel thin films”, *Thin Solid Films*, 619, 91 – 101

Sharma, S., Mohan, S. (2013) “Influence of annealing on structural, morphological, compositional and surface properties of magnetron sputtered nickel–titanium thin films” *Applied Surface Science*, 282, 492-498

Shin, D. D., Lee, D. G., Mohanchandra, K. P. and Carman, G. P. (2006) “Thin film NiTi microthermostat array” *Sens. Actuat. A*, 130 - 131, 37–41

Shiva, S., Palani, I. A., Mishra, S.K., Paul, C.P., Kukreja, L.M. (2015) “Investigations on the influence of composition in the development of Ni–Ti shape memory alloy using laser based additive manufacturing”, *Optics & Laser Technology*, (69) 44-51.

Smith, H. A. and Elhamri, S. (2018) “Epitaxial titanium nitride on sapphire: Effects of substrate temperature on microstructure and optical properties” *Journal of Vacuum Science & Technology A*, 36 (3), 03E107

Smith, K. C. A and C W Oatley C. W. (1955) “The scanning electron microscope and its fields of application” *British Journal of Applied Physics*, 6 (11), 391 – 399

Smits, F. M. (1958). "Measurement of sheet resistivities with the four-point probe". *Bell Syst. Tech. J.*, 37, 711–718

Starosvetsky, D. and Gotman, I. (2001). "TiN coating improves the corrosion behavior of superelastic NiTi surgical alloy" *Surface and Coatings Technology*, 148 (2 – 3), 268 - 276

Stout, V. L. and Gibbons M. D. (1955) "Gettering of Gas by Titanium" *Journal of Applied Physics*, 26 (12), 1488

Sugawara, T., Hirota, K., Watanabe, M., Mineta, T., Makino, E., Toh, H. and Shibata, T. (2006) "Shape memory thin film actuator for holding a fine blood vessel" *Sens. Actuat.*, 130 - 131, 461–467

Sundgren, J. (1982) "Formation and characterization of titanium nitride and titanium carbide films prepared by reactive sputtering" Ph.D. Thesis, Linköping University, Sweden

Sundgren, J.-E., Johansson, B.-O., Karlsson, S.-E., and Hentzell, H.T.G. (1983) "Mechanisms of reactive sputtering of titanium nitride and titanium carbide," *Thin Solid Films*, 105 (4), 367–384

Sundgren, J.-E. (1985) "Structure and properties of TiN coatings," *Thin Solid Films*, 128 (1-2), 21-44

Swarnalatha, V., Narasimha Rao, A. V., Ashok, A., Singh, S. S., and Pal, P. (2017) "Modified TMAH based etchant for improved etching characteristics on Si{1 0 0} wafer", *Journal of Micromechanics and Microengineering*, 27(8), 085003.

Swindells, I., Kelly, P. J. and Bradley, J. W. (2006) "Influence of substrate conditions on the temporal behavior of plasma parameters in a pulsed dc magnetron discharge" *New Journal of Physics*, 8 (4), 47

Takeuchi, S. and Shimoyama, I. (2000) "A three-dimensional shape memory alloy microelectrode with clipping structure for insect neural recording" *Journal of Microelectromechanical Systems*, 9(1), 24–31

Tang, B., Sato, K., Zhang, D. and Cheng, Y. (2014) “Fast Si (100) etching with a smooth surface near the boiling temperature in surfactant-modified tetramethylammonium hydroxide solutions”, *Micro & Nano Letters*, 9(9), 582 - 584.

Thompson, C. V. (2000) “Structure evolution during processing of polycrystalline films” *Annual Review of Material Science*, 30, 159–190

Thong, J. T. L., Choi, W. K. and Chong, C. W. (1997) “TMAH etching of silicon and the interaction of etching parameters,” *Sensors and Actuators A: Physical*, 63(3), 243-249.

Tillmann, W. and Momeni, S. (2014) “Deposition of superelastic composite NiTi based films” *Vacuum*, 104, 41-46

Tillmann, W. and Momeni, S. (2015) “*In-situ* annealing of NiTi thin films at different temperatures” *Sensors Actuators A Phys.*, 221, 9 – 14

Tillmann, W. and Momeni, S. (2015) “Influence of *in-situ* and post-annealing technique on the tribological performance of NiTi SMA thin films” *Surf. Coatings Technol.*, 276, 286 – 295

Tillmann, W., and Momeni, S. (2015) “Comparison of NiTi thin films sputtered from separate elemental targets and Ti-rich alloy targets” *Journal of Materials Processing Technology*, 220, 184-190

Uchil, J., Fernandes, F. M. B. and Mahesh, K. K. (2007) “X-ray diffraction study of the phase transformations in NiTi shape memory alloy” *Material Characterization*, 58(3), 243–248

Vasu, K., Krishna, M. G. and Padmanabhan, K. A. (2011) “Substrate-temperature dependent structure and composition variations in RF magnetron sputtered titanium nitride thin films” *Applied Surface Science*, 257(7), 3069-3074

Vaz, F., Ferreira, J., Ribeiro, E., Rebouta, L., Lanceros-Méndez, S., Mendes, J. A., Alves, E., Goudeau, P., Rivière, J. P., Ribeiro, F., Moutinho, I., Pischow, K. and de Rijk, J. (2005) Influence of nitrogen content on the structural, mechanical and

electrical properties of TiN thin films, *Surface Coatings Technology*, 191(2-3), 317–323

von Seefeld, H., Cheung, N. W., Maenpaa, M. and Nicolet M.-A. (1980) “Investigation of Titanium-Nitride Layers for Solar-Cell Contacts” *IEEE Transactions on Electron Devices*, 27(4), 873 - 876

Villiermaux, F., Tabrizian, M., Yahia, L., Meunier, M. and Piron, D. (1997) “Excimer laser treatment of NiTi shape memory alloy biomaterials” *Applied Surface Science*, 109–110, 62-66

Wang, F. E., Buehler, W. J. and Pickart, S. J. (1965) “Crystal Structure and a Unique “Martensitic” Transition of TiNi” *Journal of Applied Physics*, 36(10), 3232 - 3239

Wang, X., Li, C., Verlinden, B. and Humbeeck, J. V. (2013) “Effect of grain size on aging microstructure as reflected in the transformation behavior of a low-temperature aged Ti-50.8at.%Ni alloy” *Scripta Materialia*, 69(7), 545–548

Wang, X. and Vlassak, J. J. (2015) “Thickness and film stress effects on the martensitic transformation temperature in equiatomic NiTi thin films” *Mechanics of Materials*, 88, 50-60

Watanabe, S. and Aono, M. (1996) “Reduction of outgassing rate from residual gas analyzers for extremely high vacuum measurements” *Journal of Vacuum Science & Technology A*, 14 (6), 3261

Weng, Z., Zhang, F., Xu, C. and Zhou, J. (2020) “The effect of incident energy, incident angle and substrate temperature on surface morphology and atomic distribution of NiTi films” *Materials and Design*, 187, 108350

Winzek, Bernhard, Schmitz, Sam, Rumpf, Holger, Sterzl, Tobias, Hassdorf, Ralf, Thienhaus, Sigurd, Feydt, Jurgen, Moske, Michael and Quandt, Eckhard (2004). “Recent developments in shape memory thin film technology” *Materials Science and Engineering: A*, 378 (1 – 2), 40 - 46

- Wittmer, Marc (1985) “Properties and microelectronic applications of thin films of refractory metal nitrides” *Journal of Vacuum Science & Technology A*, 3, 1797-1803
- Wolf, R.H. and Heuer, A.H. (1995). “TiNi (shape memory) films silicon for MEMS applications” *Journal of Microelectromechanical Systems*, 4 (4), 206 – 212
- Wu, B., Kumar, A. and Pamarthy, S. (2010) “High aspect ratio silicon etch: A review”, *Journal of Applied Physics*, 108 (5), 051101
- Wu, S. K., Chen, Y. S. and Chen, J. Z. (2000) “Composition control of r.f.-sputtered Ti₅₀Ni₄₀Cu₁₀ thin films using optical emission spectroscopy” *Thin Solid Films*, 365 (1), 61 – 66
- Xie D.Z., Ngoi B.K.A., Fu Y.Q., Ong A.S. and Lim B.H. (2004). “Etching characteristics of TiNi thin film by focused ion beam” *Applied Surface Science*, 225, 54 – 58
- Xu Huang, Jiri Nohava, Bin Zhang and A.G. Ramirez (2011). “Nanoindentation of NiTi shape memory thin films at elevated temperatures” *International Journal of Smart and Nano Materials*, 2 (1), 39 – 49
- Yeh, T.-S., Wu, J.-M. and Hu, L.-J. (2008) “The properties of TiN thin films deposited by pulsed direct current magnetron sputtering” *Thin Solid Films Volume*, 516(21), 7294-7298
- Zintler, A., Kunz, U., Pivak, Y., Sharath, S. U., Vogel, S., Hildebrandt, E., Kleebe, H.-J., Alff, H. and Molina-Luna, L. (2017) “FIB based fabrication of an operative Pt/HfO₂/TiN device for resistive switching inside a transmission electron microscope” *Ultramicroscopy*, 181, 144-149

List of publications – Ph.D. work

Journal Papers - Published

1. Jithin, M. A., Ganapathi, K. L., Vikram, G.N.V.R., Udayashankar, N.K. and Mohan, S. (2018) “Pulsed DC magnetron sputtered titanium nitride thin films for localized heating applications in MEMS devices”, *Sensors and Actuators A: Physical*, 272, 199-205.
2. Jithin, M. A., Ganapathi, K. L., Ambresh, M., Nukala, P., Udayashankar, N.K. and Mohan, S. (2018) “Development of titanium nitride thin film microheaters using laser micromachining”, *Vacuum*, 197, 110795.

Journal Papers - Under Review

1. Jithin, M. A., Ganapathi, K. L., Udayashankar, N.K. and Mohan, S. “Pulsed DC sputtered phase controlled nickel titanium and titanium nitride thin film stacks for micro-actuator applications” *Materials Processing Technology*
2. Jithin, M. A., Ganapathi, K. L., Udayashankar, N.K. and Mohan, S. “Plasma characteristics and crystallization behaviors of DC and pulsed DC magnetron sputtered NiTi thin films” *Materials Processing Technology*

Conference Proceedings Paper - Published

1. Jithin, M. A., Ganapathi, K. L., Udayashankar, N.K. and Mohan, S. (2020) “Novel fabrication technique for NiTi and TiN micro-structures by femtosecond lasers”, *Published in Institute of Physics, United Kingdom, IOP Conference Series: Materials Science and Engineering (MSE)*.
2. Jithin, M. A., Sidhila, P. S. and Udayashankar, N.K. “Pulse frequency effect on the NiTi plasmas characteristics and thin film properties and fabrication of NiTi micro-comb structures” *Materials Today: Proceedings*

Conference Poster/Oral Papers

1. Jithin, M. A., Ganapathi, K. L., Udayashankar, N.K. and Mohan, S. (2017) “Design, fabrication and integration of NiTi micro-cantilevers and TiN thin film heaters”. Oral paper presentation at 8th ISSS International Conference on Smart Materials, Structures & Systems (ISSS - 2017) Bengaluru-12, Karnataka, INDIA).

2. Jithin, M. A., Ganapathi, K. L., Udayashankar, N.K. and Mohan, S. (2020) “Development of micro-combs using laser engraving with pulsed DC sputtered NiTi thin films”. Oral presentation at Instrument Society of India National Symposium on Instrumentation (NSI-42).
3. Jithin, M. A., Ganapathi, K. L., Udayashankar, N.K. and Mohan, S. (2017) “Pressure induced phase tuning of pulsed DC sputtered NiTi thin films”. Poster presentation at 9th Bengaluru India Nano 2017, Dec. (07 – 08th), 2017, Bengaluru, Karnataka, India.
4. Jithin, M. A., Ganapathi, K. L., Udayashankar, N.K. and Mohan, S. (2018) “Fabrication and characterization of MIM Capacitors with Shape Memory NiTi film as an electrode”. (Poster presentation at 4th IEEE International Conference on Emerging Electronics ICEE- 2018).

Jithin M. A.

Senior Facility Technologist - RESEARCH (PVD, Thin films, Optical Coatings)

Experienced in PVD, Optical coating, Micro-fabrication, Vacuum Systems, Vacuum System Design domains

- 15+ years of experience in PVD Thin Film Deposition & Characterization, Vacuum Technology – Vacuum System Design and Commissioning.
- Lectures on Vacuum Technology & PVD techniques — Ion Beam deposition techniques.



jithinma@iisc.ac.in
jithinphy@gmail.com

☎ +91-9611608568
+91-7012177455

📍 SF30, Centre for Nano Science and Engineering, Indian Institute of Science, Malleshwaram, Bangalore-12, Karnataka, India

SKILLS:-

Vacuum technology:

- HV & UHV
- Leak Detection

Deposition Skills (PVD):

- IBS/DIBS
- RFMS/DCMS/PDCMS /Hi-PIMS
- E-Beam Evaporation & IAD
- Glove Box with a thermal evaporator

Characterization skills:

- AFM
- SEM-EDS
- XRD
- FTIR
- Surface profiler
- Ellipsometer
- Optical profiler
- IR Camera
- Optical Emission Spectroscopy
- UV-Visible Spectroscopy

In-situ Characterizations:

- Residual Gas Analysis
- Plasma Optical Emission Spectroscopy

EDUCATION:-

- ✓ **Ph.D. – Physics:** National Institute of Technology Karnataka – (2014 -Present)
8.66 CGPA (Thesis Submitted – Viva expected in Nov. 22)
- ✓ **M.Sc. – Physics:** Bharathidasan University – (2004-2006) 68.06%

RESEARCH WORK EXPERIENCE:-

➤ **Project Assistant (2nd Apr. 2007 – 31st Oct. 2008)**

(Centre for Excellence in Nanoelectronics, Department of Instrumentation, Indian Institute of Science, Bangalore, Karnataka, India)

Assignments:

- Design and develop vacuum coating units: Three Magnetron co-sputtering system, Dual Magnetron sequential sputtering system, and Vacuum system for Gas Sensor Calibration.
- Deposition and Characterization of CeO₂, HfO₂, NiTi thin films with RFMS/DCMS techniques and characterization for specific applications.

➤ **Facility Technologist - RESEARCH (1st Nov. 2008 – 31st Mar. 2013)**

(Centre for Nano Science and Engineering, Indian Institute of Science, Bangalore, Karnataka, India)

Assignments:

- Design and develop vacuum coating units: Dual Ion Beam Sputtering System
- Deposition and Characterization of NiTiCu, Ru, TiO₂ TiN thin films with DCMS/PDCS/DIBS techniques.

➤ **Senior Facility Technologist - RESEARCH (1st Apr. 2013 – present)**

(Centre for Nano Science and Engineering, Indian Institute of Science, Bangalore, Karnataka, India)

Assignments:

- Deposition and Characterization of NiTi, TiN, TaN, Al₂O₃, TiO₂, SiO₂, Ta₂O₅, HfO₂, Cu₂O, NiO, ZnO, Si₃N₄, c-axis AlN, cBN/hBN, Mo, Nb & NbN thin films with DCMS/PDCMS/ RFMS/IBS/DIBS/ Hi-PIMS techniques.
- Execute research projects from industry and strategic sectors.
- Delivering invited talks in Vacuum, Thin-film workshops.

RESEARCH PROJECTS COMPLETED:-

Industry and Strategic Sector Projects:

1. RFMS Deposition and characterization of CeO₂ dielectric thin films for CMOS applications – **Funding agency: Tokyo Electron Limited (TEL).**
2. RFMS & DCMS Deposition and characterization of NiTiCu shape memory alloy thin films - **Funding agency: MHRD.**
3. PDCMS Deposition and characterization of TiO₂ dielectric thin films for CMOS applications - **Funding agency: Tokyo Electron Limited (TEL).**
4. PDCMS Deposition and characterization of TiN thin films for barrier layer applications - **Funding agency: PSA Project.**
5. DIBS Deposition and characterization of SiO₂ and Ta₂O₅ single-layer thin films for optical filter applications - **Funding agency: Govt Funded**
6. Production of high reflection mirrors using SiO₂ and Ta₂O₅ thin-film multilayer (36 & 38 layers) stacks by Dual Ion Beam Sputtering technique for ring laser gyros - **Funding agency: Govt Funded**
7. PDCMS Deposition and characterization of NiTi shape memory alloy thin films - **Funding Agency: MHRD, MeitY, and DST Nano Mission through NNetRA.**
8. Design, fabrication, and characterization of NiTi and TiN microdevices - **Funding Agency: MHRD, MeitY, and DST Nano Mission through NNetRA.**

Student projects:

1. DCMS Deposition and characterization of TiN thin films for CMOS electrode applications.
2. DCMS Deposition and characterization of TiN thin films for plasmonic applications.
3. RFMS Deposition and characterization of cBN & hBN thin films with DC substrate bias for low-temperature electronics applications.
4. PDCMS Deposition and characterization of Nb, Cu₂O, NiO thin films.

Equipment development projects:

1. Design (Using AutoCAD-2005), fabrication, and commissioning of **Three-target Magnetron co-sputtering system - Funding Agency: MHRD, CEN Phase I.**
2. Design (Using AutoCAD-2006), fabrication, and commissioning of a Dual Target Magnetron Sequential Sputtering system - **Funding Agency: MHRD, CEN Phase I.**
3. Vacuum system design (Using AutoCAD-2006) and development for Gas Sensor Calibration purpose - **Funding Agency: MHRD, CEN Phase I.**
4. Design (Using AutoCAD-2010), fabrication and commissioning of Dual Ion Beam Sputtering (DIBS) system having DC & End Hall ion sources - **Funding Agency: MHRD, CEN Phase I.**

5. Modification of sputter deposition systems to house the High Power Impulse Magnetron Sputtering (Hi-PIMS) power supply - **Funding agency: PSA Project.**

RESEARCH PROJECTS ONGOING:-

1. Synthesis and characterization of oriented TiN thin films using Pulsed DC Magnetron Sputter & High Power Impulse Magnetron Sputter (Hi-PIMS) deposition techniques.
2. Synthesis and characterization of nanostructured SiO₂ thin films by ion beam technique with GLAD arrangements – Future TiO₂/Ta₂O₅.
3. Synthesis and characterization of oriented Mo & AlN thin films using Pulsed DC Magnetron Sputtering technique for FBAR applications.
4. Synthesis and characterization of oriented AlN thin films using High Power Impulse Magnetron Sputter (Hi-PIMS) deposition techniques.

PUBLICATIONS:-

Journals:

1. **Pulsed DC magnetron sputtered titanium nitride thin films for localized heating applications in MEMS devices**

Jithin M. A., Lakshmi Ganapathi Kolla, Vikram G. N. V. R., Udayashankar N. K., Mohan S.
Sensors and Actuators A: Physical, Volume 272, 2018, Pages 199-205

2. **Chiro-plasmonic refractory metamaterial with titanium nitride (TiN) core-shell nanohelices**

Sruthi Venkataramanababu, Greshma Nair, Preeti Deshpande, Jithin M. A., Sangeneni Mohan, and Ambarish Ghosh
Nanotechnology, Volume 29, Number 25

3. **Novel fabrication technique for NiTi and TiN micro-structures by femtosecond lasers**

Jithin M A, Lakshmi Ganapathi Kolla, N K Udayashankar, and S Mohan
Published in Institute of Physics, United Kingdom, IOP Conference Series: Materials Science and Engineering (MSE)

4. **Hundred-fold reduction in Iron diffusivity in titanium nitride diffusion barrier on steel by microstructure engineering**

Pankaj Kumar, Jithin M. A., S. Mohan, and Sushobhan Avasthi
Thin Solid Films, Volume 716, 2020, 13841

5. **Development of titanium nitride thin film microheaters using laser micromachining**

M. A. Jithin, K. L. Ganapathi, M. Ambresh, Pavan Nukala, N. K. Udayashankar, and S. Mohan
Vacuum, Volume 197, 2022, 110795

6. **Pulse frequency effect on the NiTi plasmas characteristics and thin film properties and fabrication of NiTi micro-comb structures**

Jithin, M. A., Sidhila, P. S. and Udayashankar, N.K.

In Communication:-

1. Plasma characteristics and crystallization behaviors in DC and pulsed DC magnetron sputtered NiTi thin films and fabrication of NiTi micro-mesh structures - *Journal of Materials Processing Tech.*
2. Pulse frequency effect on the NiTi plasmas characteristics and thin film properties and fabrication of NiTi micro-comb structures - *Materials Today: Proceedings*

Selected Conference Publications:

1. **Electrical and Optical Properties of CeO₂ thin films for High-K Applications**
G. Satheesh Babu, **Jithin M. A.**, J. Bujjamma, S. Mohan
(Poster presentation at **ISSS-2008/P117 International Conference** on Smart Materials Structures and Systems at Bangalore, July 24-26, 2008)
2. **Design, Fabrication, and Calibration of Three Target Magnetron co-sputtering System for Shape Memory Alloy Thin-Films**
Sudhir Kumar Sharma, **Jithin M. A.**, Sumesh M. A., and S. Mohan
(Poster presentation at **Third National Conference** on MEMS, SMART STRUCTURES AND MATERIALS (ISSS-2009))
3. **Importance of Residual gas analysis in Ion Assisted Electron beam evaporation of Ultrathin HfO₂ films**
K. Lakshmi Ganapathi, **Jithin M. A.** and S. Mohan
(Poster presentation at Instrument Society of India **National Symposium on Instrumentation (NSI-35)**)
4. **Pulsed DC Magnetron Sputtered Rutile TiO₂ films for next-generation DRAM capacitors**
M. A. Jithin, Lakshmi Ganapathi Kolla, Navakanta Bhat, S. Mohan, Yuichiro Morozumi and Sanjeev Kaushal
(Oral presentation at **2013 MRS Spring Meeting**, Volume 1561, **MRS Online Proceeding**)
5. **Design, fabrication, and integration of NiTi microcantilevers and TiN thin-film heaters**
Jithin M. A., Lakshmi Ganapathi Kolla, Vikram G.N.V.R., Udayashankar N.K., Mohan S.
(Oral presentation at **8th ISSS International Conference on Smart Materials, Structures & Systems (ISSS - 2017)**)
6. **Pressure-induced phase tuning of pulsed DC sputtered NiTi thin films**
Jithin M. A., Lakshmi Ganapathi Kolla, Udayashankar N.K., Mohan S.,
(Poster presentation at **9th Bengaluru India Nano 2017**, Dec. (07 – 08th), 2017))
7. **Fabrication and characterization of MIM Capacitors with Shape Memory NiTi film as an electrode**
Jithin M. A., Lakshmi Ganapathi Kolla, Udayashankar N.K., Mohan S.
(Poster presentation at **4th IEEE International Conference on Emerging Electronics ICEE- 2018**)
8. **SIMS characterization of TiN diffusion barrier layer on steel substrate**
Pankaj Kumar, **Jithin M. A.**, S. Mohan, Sushobhan Avasthi
(Oral presentation at **4th IEEE International Conference on Emerging Electronics ICEE-2018**)
9. **Development of micro-combs using laser engraving with pulsed DC sputtered NiTi thin films**

Jithin M. A., K. Lakshmi Ganapathi, N. K. Udayashankar, and S. Mohan

(Oral presentation at **Instrument Society of India National Symposium on Instrumentation (NSI-42)**)

INVITED TALKS:-

1. Lecture on Vacuum Technology to the scientists from various **ISRO centers (LEOS/VSSC) – 2017.**
2. Lecture on Vacuum Technology to the scientist from **DLJ (DRDO) – 2018.**
3. Lectures on Vacuum Pumps, Vacuum Components, Vacuum Diagnose, and In-situ Plasma monitoring to the engineers from **LAM Research – 2019.**
4. Lectures on Vacuum Technology, Vacuum Components, Vacuum Diagnose, Ion Beam Deposition Techniques, and In-situ Plasma monitoring to the technical staffs **NNFC, CeNSE, IISc – 2021.**
5. Lectures on Vacuum Pumps, Vacuum Components to the engineers from **Applied Materials – 2021.**

OTHER RESPONSIBILITIES UNDERTAKEN:-

- Design & Organization of Functional Thin Films Laboratory at Centre for Nano Science & Engineering to house eight sputtering systems and utilities – 2011.
- Reorganization of the Functional Thin Films Laboratory to house the sputtering, evaporation systems, and PLDs under one umbrella – 2020.
- Deliver lectures on vacuum technology & thin film deposition techniques to the participants from industries and strategic sectors.
- Initial pieces of training to the M.S., M.Tech., Ph.D. & Project students on Vacuum Systems and Deposition Techniques.

LANGUAGES:-

1. **English** - *Full Professional Proficiency*
2. **Malayalam**- *Native or Bilingual Proficiency*
3. **Tamil** - *Full Professional Proficiency*
4. **Kannada** – *Limited working proficiency*
5. **Hindi** - *Limited Working Proficiency*

REFERENCES:-

Will be produced on request...

JITHIN M. A.

Bangalore

15-08-2022